4-2023

Med13 Degradation Defines a New Receptor-Mediated Autophagy Pathway Activated by Nutrient Deprivation

Sara E. Hanley
Rowan University

MED13 DEGRADATION DEFINES A NEW RECEPTOR-MEDIATED AUTOPHAGY PATHWAY ACTIVATED BY NUTRIENT DEPRIVATION

Sara E. Hanley, B.S.

A Dissertation submitted to the Graduate School of Biomedical Sciences, Rowan University in partial fulfillment of the requirements for the Ph.D. Degree.

Stratford, New Jersey 08084

April 2023

TABLE OF CONTENTS

ACKNOWLEDGMENTS

I would like to take this opportunity to express my heartfelt gratitude to the amazing support system that made my academic journey possible. First and foremost, I am deeply indebted to my mentor, Dr. Katrina Cooper, whose constant guidance and unwavering support have been instrumental in shaping me not only as a scientist but also as a person. Working with Dr. Cooper has been truly a remarkable experience that I will always cherish. Her exceptional knowledge and inquisitive nature have inspired me to purse my research interests with passion and dedication.

I would also like to extend my sincere thanks to Dr. Randy Strich for his invaluable mentorship and guidance. Dr. Strich's insightful feedback, thoughtful advice, and constructive criticism have played a crucial role in improving my writing, presentations, and research skills. I am extremely grateful to have him as a mentor.

I am also deeply grateful to my family, including my mother Andrea Zuppa, my father, Thomas McLaughlin, and my sister, Melissa Hanley, for their unconditional love and support throughout my academic journey. Their sacrifices and encouragement have been my driving force and I cannot thank them enough.

I am also thankful for the love and support of my husband, Justin Gilfillan, and his family. Their unwavering belief in me has been a constant source of strength and motivation.

My colleagues Stephen Willis, Brittany Friedson, Steven Doyle, and Alicia Campbell have also been an integral part of my academic journey. Working with them has been a pleasure, and I am grateful for their friendship, support, and guidance.

I would like to express my appreciation to my thesis committee members, Dr. Natalia Shcherbik, Dr. Dimitri Pestov, Dr. Ron Ellis, and Dr. Alicia Melendez, for their invaluable contributions, guidance, and support. Their expertise and mentorship have helped me grow as a researcher and a professional.

I feel incredibly blessed to have such an amazing support system, and I am eternally grateful to each and every one of you for your encouragement and unwavering support.

ABSTRACT

Cells are exposed to an enormous amount of diverse extracellular cues but have a limited arsenal of weapons for protecting and maintaining homeostasis. To overcome these restrictions, nature has engineered proteins that have multiple functions. The pleiotropy of using one protein to carry out a variety of functions allows cells to rapidly execute tailored responses to a diverse set of signals. The Cdk8 kinase module (CKM) is a conserved detachable unit of the Mediator complex predominantly known for its role in transcriptional regulation. The CKM is composed of four proteins, the scaffolding proteins Med13 and Med12, as well as the non-canonical cyclin, cyclin C, and its cognate kinase, Cdk8. Previously it has been shown that cyclin C is a multifunctional protein that performs transcriptional and stress-induced roles at the mitochondria. The localization, post-translational modifications, and different functional domains of cyclin C regulate these separate functions.

Here we show that Med13 also has dual roles in regulating stress response following nutrient depletion. In physiological conditions, Med13 works within the CKM to negatively regulate the expression of autophagy genes (ATG). Following starvation, this repression is relieved by Snx4-assisted autophagy of Med13. Moreover, we identified Ksp1 to be the autophagic receptor protein for this novel autophagy pathway. Structural analysis by others showed that Med13 has an RNA binding region. Consistent with this, we showed that once in the cytosol, Med13 localizes to ribonucleoprotein granules known as processing bodies (P-bodies) which function in mRNA silencing, decay, and storage. In addition, we show that Med13, together with Ksp1 and Snx4, are required for the autophagic degradation of conserved P-body

proteins following stress. These results illustrate the day and night jobs of Med13 in response to starvation stress.

Lastly, we illustrate that the regulation of autophagy by the CKM is evolutionarily conserved. Here we show that cyclin C promotes autophagy and proteasome activity in the murine pancreatic cancer model. Collectively, these studies demonstrate the multifunctionality and conservation of the CKM in stress response.

INTRODUCTION

Stress response mechanisms

Cells experience rapidly changing environments in which they must sense, decipher, respond, and adapt to external cues. Different cues elicit diverse cell fate decisions including the initiation of survival and repair pathways, proliferation, differentiation, quiescence, or cell death programs. The ability to promptly adapt to stress is especially important for nonmotile organisms such as yeast [13]. The budding yeast, *Saccharomyces cerevisiae* is the preferred model organism for deciphering the molecular mechanisms that control conserved stress response mechanisms [14]. External stimuli can include nutrient availability or osmolarity changes, mating pheromones, growth signals, or noxious stressors such as extreme temperatures, oxidative stress, or pathogen invasion.

The stress response pathway in all cells can be divided into distinct stages. Cells first sense stress and communicate these cues via signal transduction to the nucleus whereupon gene expression is reprogrammed. Thereafter, transcriptional and translational reprogramming alters organelle function, metabolism, and the cell cycle to meet the changing needs of the cell (Figure 1). The cell membrane contains a multitude of proteins that continuously monitor the external environment and communicate signals to the intracellular space. Receptors and transporters at the cell membrane receive information from hormones, antibodies, neurotransmitters, enzymes, ions, and nutrients and transmit these signals to intracellular protein networks [14]. These networks include secondary messengers, kinases, and phosphatases that form complex signal transduction pathways that decipher and disseminate this

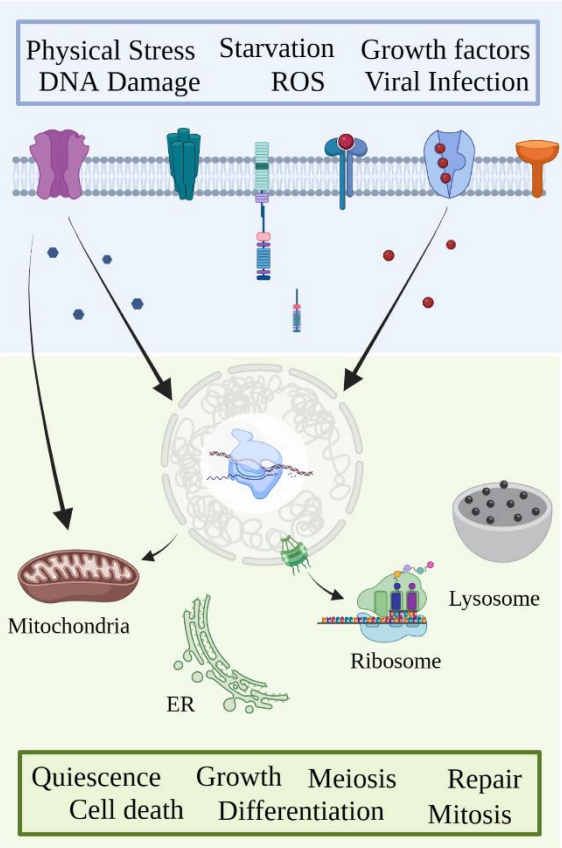

Figure 1. Cells sense, decipher, respond, and adapt to different environmental cues. Cells first sense changes via receptors and transporters at the cell membrane (top blue panel). Signal transduction pathways then transmit these cues to the nucleus and appropriate organelles. Transcriptome and proteome changes then result with adaptations in organelle function, metabolism, and cell cycle (bottom green panel). Different environmental cues lead to specific cell fate decisions and the breakdown of this communication is the etiology of aging and disease.

information to the nucleus and other organelles. One example of a highly conserved stress response pathway is the SNF1/AMPK pathway. In yeast, Snf1 is a ubiquitous protein kinase that plays many roles in response to stress [15]. In nutrient-rich conditions when extracellular glucose levels are high Snf1 is inactive. Glucose depletion triggers a signal transduction cascade that activates Snf1 through phosphorylation. Activated Snf1 enters the nucleus and regulates the transcription of over 400 genes [15]. Snf1-mediated transcriptional and metabolic changes allow cells to utilize other carbon sources, inhibit anabolic pathways, activate catabolic pathways, and store carbohydrates. These pathways are employed individually or in combination to adequately respond to the appropriate extrinsic stress cue.

Transcriptional and translational reprogramming is essential for cells to respond to changes in cellular homeostasis. Changes in the transcriptome rapidly adjust gene

expression to meet the changing needs of the cell. In addition to transcriptome changes, modifying mRNA accessibility and protein synthesis allows cells to promptly execute changes in cell function. In addition to changing protein levels, post-translational modifications such as phosphorylation, lipidation, ubiquitination, or acetylation are mechanisms used by the cell to rapidly alter protein function. Transcriptome and proteome reprogramming can fine-tune cellular function to respond promptly and accurately to infinite variations of environmental conditions.

Lastly, structural and functional changes within the cell are critical for stress response and adaptation. These cellular adaptations can include changes in the cell cycle, organelle function, metabolism, morphology, or cellular organization. For example, stress restricts cell cycle progression. Rapidly inhibiting the cell cycle and anabolic pathways allows cells time and energy to upregulate reparative mechanisms and mitigate damage. In periods of nutrient exhaustion cells enter quiescence to reserve energy [16]. In addition, the quantity and morphology of organelles such as mitochondria and peroxisomes can change during stress. During periods of nutrient deprivation or rapid growth mitochondria form highly fused matrix networks to maximize energy production [17]. The quantity of peroxisomes in the cell fluctuates depending on the cell's need for detoxification or energy supply [18]. Collectively, the cell utilizes and coordinates a variety of processes to adequately sense, respond, and adapt to stress. These multiple layers of regulation are held in place to avoid incorrect cell fate decisions as the etiology of many diseases is associated with the dysregulation of stress response pathways. For example, cancer cells evade cell death pathways and

neurodegenerative diseases result from neuronal cell death which is attributed to the attenuation of survival and repair mechanisms [19].

Multifunctional proteins

Cells are exposed to an enormous amount of diverse extracellular cues but have a limited arsenal of weapons for protecting and maintaining homeostasis. To overcome these restrictions, nature has engineered proteins that have multiple functions. The pleiotropy of using one protein to carry out a variety of functions allows cells to rapidly execute highly selective response mechanisms to a diverse set of signals. This emerging theme of proteins having two very different functions has been coined "day and night jobs" [20] [21]. The different jobs are induced by different external or intrinsic stimuli. Importantly, there are many ways in which protein function can be regulated. Protein function can be activated, amplified, inhibited, or changed through various mechanisms such as post-translational modifications, changes in subcellular localization, or interactions with other proteins or molecules such as cAMP or calcium (Figure 2).

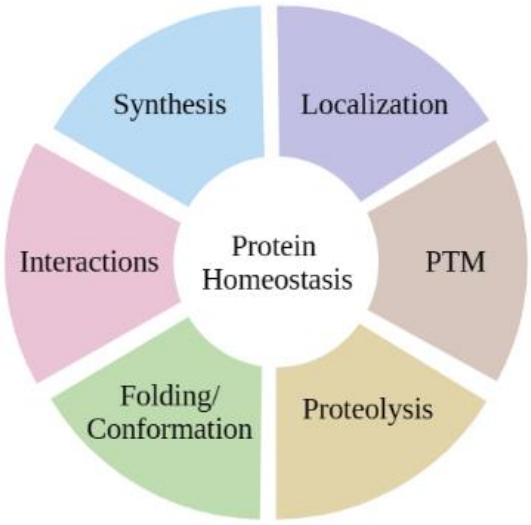

Figure 2. Mechanisms of protein homeostasis. Protein levels, post-translational modifications (PTM), conformation, and localization contribute to regulating protein function.

Post-translational modifications

There are over 350 types of known post-translational modifications that are used to alter protein function [22]. These events are dynamic, reversible, and in some cases very rapid. Post-translational modifications are thought to be the front line of stress-responsive mechanisms because they propagate and govern signals throughout the cell to promptly modify cellular function. For example, kinases within MAPK pathways phosphorylate specific targets but are also usually substrates of phosphorylation themselves. These cascades amplify and integrate signals to elicit the appropriate tailored response. In addition, acetylation and methylation of histones result in changes to chromatin accessibility and stress-induced gene expression [22]. Along with post-translational modifications, multi-faceted roles for proteins can be achieved through the utilization of multiple functional domains within a single protein. Protein domains are independent regions within a protein that can perform a specific function. Some prominent examples are the RING and BH3 domains found within ubiquitin ligases and pro-apoptotic proteins respectively. There are over 1,000 known protein domains within the proteome that help categorize proteins into different functional groups [22].

Protein localization

The subcellular localization of proteins is a key component of regulating protein function in stress response pathways. The localization of a protein determines if this protein is accessible to other proteins or molecules that can alter its function. For instance, following extracellular ligand binding, the integral membrane protein, Notch1 undergoes multiple proteolytic cleavage steps in which a fragment of the full-length protein can enter the nucleus and regulate transcription. The function of Notch1 is

therefore dependent on its subcellular localization within the cell [23]. To build upon these concepts in many cases these domains or localization sequences are not recognized or accessible until post-translational modifications occur. These mechanisms apply multiple layers of regulation and functionality to a seemingly limited number of proteins.

Proteolysis

The ubiquitin-proteasome system (UPS)

The timely expression and function of proteins are vital in coordinating cellular processes and stress responses. Proteolysis is irreversible and therefore provides a complete, rapid, and sustained termination of cellular mechanisms. Proteins are continually synthesized and degraded under normal physiological conditions. Protein turnover rates vary depending on their function. Regulatory enzymes usually have a much faster turnover rate compared to structural proteins [24]. For example, the turnover of kinases can range from minutes to hours whereas structurally proteins such as hemoglobin or albumin can range from days to weeks [25].

In addition to steady-state turnover, proteins can be actively degraded. Balancing high levels of protein synthesis with degradation allows for robust changes in cellular processes and organization. The two evolutionarily conserved proteolysis pathways within the cell are the ubiquitin-proteasomal system (UPS) and the lytic organelle known as the lysosome in metazoan and the vacuole in yeast. Metazoans also utilize cytosolic proteases such as calpains and caspases for stress-induced proteolysis [24]. One of the best examples of strictly orchestrated synthesis and degradation of proteins occurs during the cell cycle. Cyclins are regulatory proteins that activate the

activity of their cognate partners known as cyclin-dependent kinases (CDKs). The oscillation of cyclin protein levels regulates the timely activity of CDKs which allows cell cycle progression. Proteolysis is therefore tightly coupled with cell cycle progression and uncoupling of these processes can result in checkpoint evasion and uncontrolled proliferation. It is therefore not surprising that dysregulation of cyclin and CDK protein levels have been associated with many cancer types including breast and colon [26].

The predominant mode of proteolysis in the cell occurs via the UPS as it accounts for 80% of all protein degradation [24]. The UPS pathway is highly specific and uses the polypeptide co-factor, ubiquitin to mark proteins for degradation. Tagging proteins with ubiquitin requires a three-step process in which E1 enzymes activate ubiquitin, E2 enzymes then conjugate the primed ubiquitin tags to E3 enzymes which ligate ubiquitin to the specified target. There is only one known E1 protein in mammalian systems, 30-40 E2 enzymes, and over 1,000 known E3 ligases demonstrating that E3s are the defining factor for substrate specificity [24].

Ubiquitin modifications are not unique to UPS-mediated degradation, ubiquitin tags can also mark proteins for re-localization, internalization, or degradation via the lysosome [27]. Thus the number and branching patterns of ubiquitin chains can play a variety of different roles within the cell [28]. Ubiquitin chains that target substrates for UPS-mediated degradation are recognized by the 19S subunit of the 26S proteasome. Substrates are fed into the body of the proteasome for degradation and ubiquitin is removed for recycling by deubiquitinating proteins. As a substrate arrives at the proteasome it is bound, unfolded, and linearized by high-powered ATPases [24]. The

denatured protein is then fed through the central channel and hydrolyzed into small peptides.

Autophagy and lysosomal-mediated degradation

Contrary to UPS-mediated degradation which feeds individual denatured proteins through its catalytic core, lysosomal-mediated degradation requires substrates to be incorporated into membrane vesicles such as endosomes and autophagosomes [29]. These vesicles then fuse with the lysosome and its contents are degraded via luminal hydrolases. Endosomal-lysosomal networks primarily regulate secretory and membrane proteins whereas the autophagy-lysosomal pathway is a catabolic pathway required for the degradation and recycling of internal cellular components [30]. The sorting nexin protein family is a large, diverse group of trafficking proteins that function in both the endosomal-lysosomal and autophagy pathways. These proteins are key regulators in the sorting and localization of protein cargo. In the endosomal-lysosomal pathway sorting nexins direct the internalization, recycling, and degradation of membrane proteins. These proteins are also required for many selective autophagy pathways including pexophagy, mitophagy, and autophagic degradation of large multi-subunit complexes such as ribosomes, proteasomes, and the fatty acid synthase complex [30].

A. Overview of autophagy

Autophagy occurs at low levels in physiological conditions but is upregulated in periods of stress. Autophagy-mediated degradation requires the formation of double-membrane vesicles known as autophagosomes which engulf substrates and deliver them to the lysosome [29]. The field of autophagy has expanded to encompass

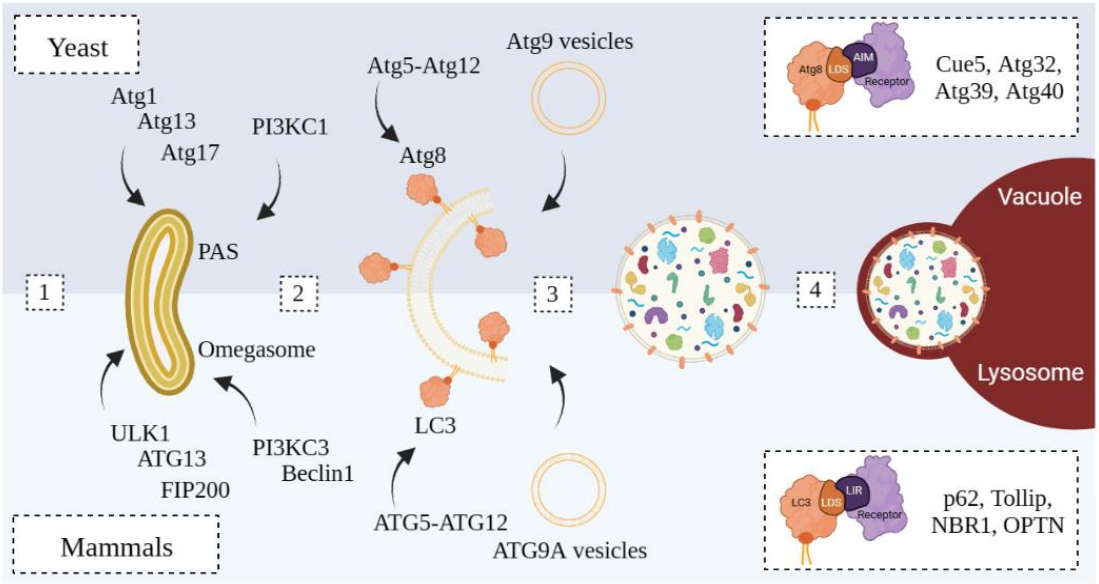

Figure 3. Autophagy in yeast (top panel) and mammalian (bottom panel) cells (adapted from [2]). Autophagy is divided into various stages that define autophagosome biogenesis. These steps include the initiation of the PAS (1), expansion of the phagophore (2), maturation of the autophagosome (3), and fusion of autophagosomes with the lytic organelle (4). Non-selective autophagy randomly sequesters and degrades cytosolic components. Selective autophagy requires receptors that exclusively bind and tether cargo to the phagophore. Autophagy receptors contain Atg8-interacting motifs (AIM/LIR) that bind to the LC3-docking site (LDS) of Atg8/LC3 (outlined in boxes on the right).

regulatory roles and degradation of a wide array of macromolecules such as nucleic acids, lipids, and proteins, as well as larger multi-subunit complexes and organelles [31]. The term “autophagy” was first coined by Christian de Duve who won the Nobel Prize in 1974 for his discovery of lysosomes. Ground-breaking work by Yoshinori Oshumi in 1993 identified genes essential for autophagy using a genetic screen in the yeast model organism. Many of these genes are evolutionarily conserved and have orthologues in humans. Yoshinori Oshumi was awarded the Nobel Prize in 2016 for his work delineating the basis of autophagy [32] [33]. The lysosome was once thought of as a dumpsite within the cell, degrading only damaged or excess cellular debris. In

more recent years, sophisticated regulatory roles of autophagy, that were once underappreciated and hidden in the limelight of the UPS, have taken center stage in the field of proteolysis.

B. Bulk vs selective autophagy

There are slight variations in the machinery required for bulk and selective autophagy pathways. Bulk also known as non-selective or macroautophagy randomly sequesters cytosolic components and delivers them to the lytic organelle for degradation during periods of stress. The phagophore assembly site (PAS), the site of autophagosome biogenesis, forms contact sites with both the lysosome and ER [34]. Following the initiation of the phagophore, the isolation membrane expands and seals around its cargo. The outer membrane of the autophagosome then fuses with the lysosome, and the contents within the autophagic body are degraded in the lumen of the lysosome (Figure 3) [34]. Bulk autophagy is induced following TORC1 inactivation and subsequent activation of the Atg1 kinase complex. The Atg1 kinase complex is required for PAS initiation and includes Atg1, Atg13, Atg17, Atg29, and Atg31 [35].

In selective autophagy such as mitophagy, pexophagy, ER-phagy, or nucleophagy autophagosomes are built at the site of the substrate organelle and these organelles or portions of these organelles are then sequestered into autophagosomes and delivered to the lysosome [36]. These forms of selective autophagy utilize a diverse set of receptor proteins that bind to unique targets and tether them to the autophagic machinery. Autophagy receptor proteins contain Atg8-interacting motifs (AIMs), also known as LC3-interacting regions (LIRs) in mammalian systems, that interact with the LC3-docking site (LDS) found within the Atg8 protein family [36] (Figure 3, boxes on

the right). These domains are essential for selective autophagy and are required for tethering specific substrates to the autophagic membrane. In addition to the growing number of receptor proteins, selective autophagy can also utilize unique scaffolding machinery such as Atg11 which is required for PAS formation of autophagosomes engulfing receptor-bound cargo [35].

C. Transcriptional, post-transcriptional, and post-translational regulation of autophagy

In the model system *S. cerevisiae*, there are over 40 autophagy-related genes (*ATG*) that are highly conserved and encode proteins required for orchestrating autophagosome biogenesis and substrate recruitment [34]. Nutrient depletion triggers a robust induction of *ATG* transcription and translational. To prevent aberrant or excess autophagy cells have multiple layers of regulation including transcriptional, post-transcriptional, and post-translational mechanisms. Major transcriptional regulators controlling *ATG* expression in yeast include repressors such as Ume6, Rph1, and Pho23, as well as activators namely Rim15, Gcn4, Gln3, and Gat1 (Figure 4) [37]. Our laboratory has shown that the CKM functions as a negative regulator of *ATG* expression. Deletion of CKM components results in a significant increase in *ATG8*, *ATG1*, and *ATG14* expression following TORC1 inhibition or nutrient deprivation [38] [3]. In addition to directly repressing transcription, cyclin C/Cdk8-mediated phosphorylation of Rim15 inhibits its activity and is required for the repression of stress response genes including *ATG8* [39].

Post-transcriptional regulation of *ATG* expression via RNA decay pathways is another layer of regulation employed by the cell to rapidly adjust autophagy levels. The helicase and decapping enzymes, Dhh1 and Dcp2, negatively regulate *ATG* expression by degrading *ATG* transcripts in unstressed conditions (Figure 4) [37]. In addition, Xrn1 is an exonuclease that degrades *ATG* transcripts in both yeast and mammalian systems. Under physiological conditions, Dhh1, Dcp2, and Xrn1 downregulate *ATG* mRNA levels. Following starvation, these three proteins are inhibited or degraded which allows for the translation and upregulation of autophagy proteins [37].

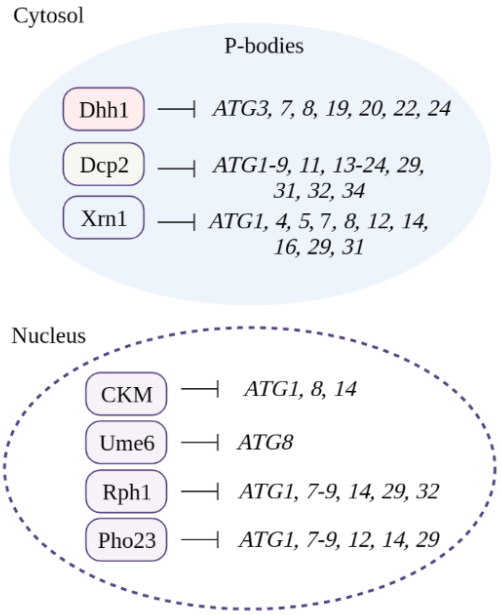

Figure 4. Transcriptional and post-transcriptional regulation of *ATG* expression.

Dhh1, Dcp2, and Xrn1 are core components of the evolutionarily conserved class of ribonucleoprotein (RNP) granules known as processing bodies (P-bodies). P-bodies form as RNA and protein condense and separate from the surrounding diluted phase in a process known as liquid-liquid phase separation (LLPS) [40]. These membrane-less organelles regulate gene expression by rapidly adjusting mRNA accessibility [41]. Under physiological conditions, P-bodies sequester and degrade mRNAs encoding proteins required for stress response such as *ATG* transcripts [42]. Following starvation, *ATG* transcripts are recycled into the cytosol, and biosynthetic mRNA transcripts required for metabolism and amino acid biogenesis are then

sequestered and degraded. This allows cells to promptly shut down anabolic pathways and conserve nutrient pools while upregulating catabolic processes [43]. RNP networks and autophagy are closely associated as RNP granules regulate *ATG* transcripts and autophagy is essential in maintaining the homeostasis of RNP granules [44,45].

Lastly, post-translational modifications such as phosphorylation, ubiquitination, lipidation, and proteolytic cleavage are also essential for autophagy induction and autophagosome biogenesis. For example, under nutrient-rich conditions Atg13, a regulatory unit of the Atg1 complex, is inactive in its hyper-phosphorylated state. Following TORC1 inhibition, Atg13 is rapidly dephosphorylated by two protein phosphatases, Rts1 and Cdc55. In its dephosphorylated state, Atg13 forms a complex with Atg1, Atg17, Atg29, and Atg31 and initiates autophagosome biogenesis [46]. In addition, Atg8 also undergoes multiple post-translational modifications during autophagy induction. Atg8 is first processed by the protease Atg4, Atg8 is then activated by Atg7 and Atg3, the E1-like and E2-like enzymes respectively. Finally, the Atg5-Atg12 complex is required for the conjugation of Atg8 with phosphatidylethanolamine (PE). The lipidation of Atg8 is required for its association with the isolation membrane of the growing phagophore [47].

CKM in cellular homeostasis and stress response

At the crossroads of stress response and homeostasis is the Cdk8 kinase module (CKM) [48]. The CKM is a detachable unit of the Mediator complex known in yeast to predominantly negatively regulate the transcription of stress-responsive genes (SRG) such as *SPO13*, *SPO11*, *CTT1*, *ATG8*, and the *HSP70* family member *SSA1* (Figure 5, left panel) [49]. This complex is comprised of four conserved proteins: the scaffolding

proteins Med13 and Med12, as well as the non-canonical cyclin, cyclin C, and its cognate kinase, Cdk8. Cyclins mediate the activity of their exclusive CDK partner and can be categorized into functional subtypes including cell cycle regulatory or transcriptional cyclins. Cyclin C/Cdk8 was the first cyclin/Cdk pair to be identified as transcriptional regulators. Protein levels of cyclin C and Cdk8 do not fluctuate during the cell cycle but remain constant in physiological conditions [50]. Med12 functions as a scaffolding component within the CKM and mediates the kinase activity of Cdk8 [51]. Interestingly, Med13 was recently identified as a potential member of the Argonaute/PIWI protein family. Based on sequence analysis Med13 shares similar structural features to Ago proteins which function in RNA silencing [51].

In *S. cerevisiae*, the CKM predominantly functions to negatively regulate SRG transcription under physiological conditions. Following stress, this repression is relieved through the disassembly of the CKM [52]. Localization and degradation of the CKM components are highly regulated and dependent upon stress cues. In response to cell death cues (triggered by increased oxidative stress) the stress signal is communicated to Med13 by the conserved MAPK signal transduction pathway. This triggers ubiquitin-mediated destruction of Med13 by nuclear 26S proteasomes [53] [54] [55]. Med13 functions as the nuclear anchor for cyclin C, therefore degradation of Med13 allows for the re-localization of cyclin C from the nucleus to the cytosol [53]. Once in the cytosol cyclin C promotes mitochondrial fragmentation and initiates programmed cell death pathways (Figure 5, center red panel) [52]. These studies serve to illustrate the day and night jobs of cyclin C. Importantly these roles are conserved as discussed below. In contrast, following cell survival cues that are triggered by

nitrogen starvation stress, cyclin C is degraded via nuclear UPS proteolysis to relieve the repression of autophagy-related genes (ATG) (Figure 5, right green panel) [29]. [38]. Nuclear retention and degradation of cyclin C during starvation stress prevents mitochondrial fragmentation and cell death.

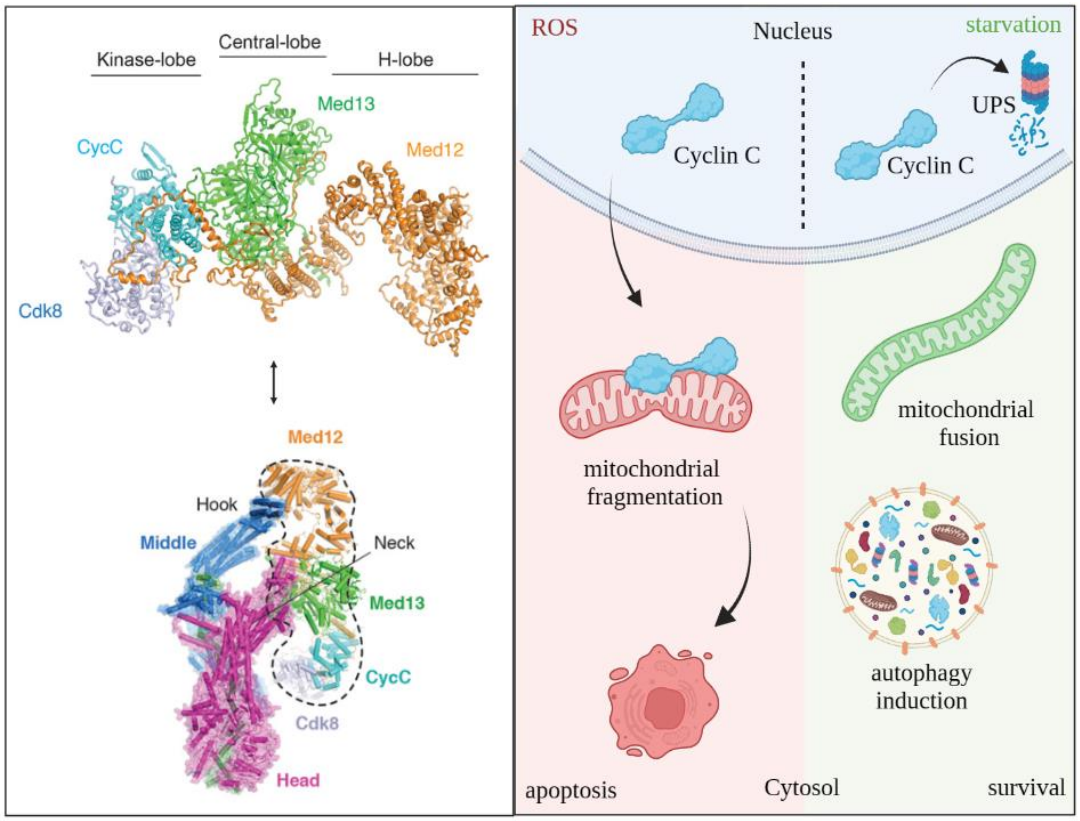

Figure 5. The CKM has dual roles. The CKM is composed of four proteins: Med13, Med12, cyclin C and its cognate Cdk8. This complex functions as a detachable unit of the Mediator complex (pink and blue regions denoted Head and Middle in the bottom left panel) In unstressed conditions, the CKM regulates the transcription of ~ 3000 genes. Following oxidative stress, cyclin C localizes to the cytosol. In the cytosol cyclin C induces mitochondrial fragmentation and initiates programmed cell death pathways (red panel). During starvation, cyclin C is degraded within the nucleus via the UPS. This promotes survival by preventing mitochondrial fragmentation and upregulating autophagy (green panel).

The CKM is highly conserved from yeast to mammalian systems. The preliminary studies in *S. cerevisiae* outlining the roles of the CKM in stress response pioneered further studies in mammalian cell culture.

Transcriptional control - CKM day job

The transcriptional control imposed by the CKM in mammalian systems is very dynamic as it depends on many factors including kinase activity, loci, and stress. The CKM can both negatively and positively regulate transcription through the recruitment or removal of this complex at specific target promoters [56]. In general, in physiological, unstressed conditions the CKM promotes the transcription of genes required for cellular homeostasis and represses the transcription of SRG. Following stress, the CKM activates the transcription of SRG either through the removal of inhibition or activation through promoter recruitment [56].

Stress-induced mitochondrial role – CKM night job

Similar to yeast, following oxidative stress, a small subset of the nuclear cyclin C population is exported from the nucleus and localizes to the mitochondria [12]. At the mitochondria, cyclin C promotes mitochondrial fragmentation and initiation of programmed cell death pathways through interactions with Drp1 and Bax, respectively [57,58]. Further studies in both yeast and mammalian models revealed that aberrant localization of cyclin C can alter stress sensitivity and viability. Premature cyclin C mitochondrial localization hypersensitizes cells to oxidative stress and chemotherapeutics and decreases viability [38] [53], whereas cells devoid of cyclin C are more resistant to stress [12,52]. It is therefore not surprising that cyclin C has been identified as a tumor suppressor in both solid and hematological cancers [59,60].

Cyclin C exemplifies multifunctionality as being a regulator of transcription, mitochondrial dynamics, and cell fate decisions. Cyclin C protein levels, localization, and structural domains orchestrate these separate functions and dictate how cells will respond to different stress cues (ROS vs starvation). Given that the degradation of Med13 is highly regulated during oxidative stress and that the function, localization, and degradation of cyclin C is dependent upon stress, the next logical question to address is how Med13 is regulated following other forms of stress. Surprisingly, I discovered that in *S. cerevisiae* Med13 localizes to the cytosol where it performs a secondary stress-induced cytoplasmic role prior to its autophagic degradation. This cytosolic role is independent of the CKM and is important for cell survival during starvation stress. The data supporting this model are reported in the chapters below. In short, Chapter 2 describes a new selective autophagy mechanism that is used to deliver Med13 to autophagosomes for vacuolar proteolysis. In Chapter 3 the autophagic receptor protein for this pathway is described. In Chapter 4, the stress-induced cytosolic role of Med13 is discovered and explained. Lastly, in Chapter 5 the role of cyclin C in regulating autophagy in the murine Kras pancreatic cancer model is delineated.

RATIONALE

The Cdk8 kinase module (CKM) is an evolutionarily conserved dissociable unit of the Mediator complex known to regulate the transcription of stress response and meiotic genes. The CKM comprises four proteins: the two scaffolding proteins Med13 and Med12, as well as the transcriptional cyclin/Cdk8 pair, cyclin C/Cdk8. In yeast, the CKM functions predominantly as a negative regulator of transcription. During periods of stress or exposure to developmental cues, transcriptional repression is relieved through CKM disassembly. After CKM disassociation, noxious stress triggers cyclin C localization to the cytosol where it promotes mitochondrial fragmentation and initiation of programmed cell death pathways [52]. By contrast following starvation cues, cyclin C is retained in the nucleus and rapidly degraded [38]. The localization and degradation of the CKM components are pivotal as aberrant localization of cyclin C results in defects in stress response pathways and deleterious effects on viability [53] [38,54].

The CKM coordinates multiple stress response mechanisms including transcription, organelle dynamics, and cell fate decisions. Early studies in *S. cerevisiae* guided subsequent studies that identified cyclin C as a regulator of both mitochondrial fission machinery and pro-apoptotic proteins in mammalian cells [12]. In periods of oxidative stress, cyclin C interacts with the GTPase and pro-apoptotic factor, Drp1 and Bax respectively, to induce programmed cell death pathways [57,58]. In addition to oxidative stress, our laboratory has also shown that the CKM regulates stress response mechanisms following starvation stress [38]. Nutrient deprivation induces autophagy, a conserved catabolic pathway required for the turnover of cytosolic components.

During physiological conditions, the CKM functions to negatively regulate autophagy. Following starvation cues, the CKM is dissolved allowing for the upregulation of autophagy.

The etiology of a variety of pathologies including cancer [61], cardiovascular diseases [62], osteoporosis [63], developmental disorders [64], as well as inflammatory and autoimmune diseases [65] [66] is associated with CKM dysregulation. In addition, defects in autophagy are closely associated with neurodegenerative diseases [67] and cancer [68]. Understanding how CKM components are regulated and how they regulate autophagy is therefore fundamental in delineating their role in pathogenesis.

CHAPTER 1

Materials and Methods

1. Yeast

Strains and plasmids

Experiments were primarily performed with endogenously labeled proteins in the S. cerevisiae W303 background (*leu2-3,112 trp1-1 can1-100 ura3-1 ade2-1 his3-11,15*) [110] or from the Research Genetics yeast knockout collection derived from BY4741 strain background (MATa *his3Δ1 leu2Δ met15Δ ura3Δ*). In accordance with the Saccharomyces Genome Database members of the CDK8 module, SSN8/CNC1/UME3/SRB11, SSN3/CDK8/UME5/SRB10, SRB8/MED12/SSN5 and SSN2/MED13/UME2/SRB9, will use CNC1, CDK8, MED12, and MED13 gene designations, respectively. All strains were constructed using replacement methodology [111]. In short, primers were made using specific regions of homology depending on the desired genomic manipulation (knocking out a gene, N-terminal tag, or C-terminal tag). These primers were then used to PCR the knock-out or epitope cassette from the pYM plasmids. There are a few special fluorophore plasmids such as mNeongreen, mRuby3, mCardinal, and mNeptune that share a different open reading frame compared to the pYM plasmids. For these plasmids use the protocol for making S2 reverse primers and for the forward primer (S3) use the extension sequence CGGATCCCCGGGTTAATTAA following 45-55 bases before the STOP-codon (excluding STOP) of the gene of interest.

The presence and size of the PCR product were confirmed using a 1% agarose gel. The PCR product was prepared using the PCR clean-up kit (Omega catlog#

D6492). The PCR product was transformed into mid-log yeast cultures using the LiAc TRAFO transformation protocol. A 25mL mid-log yeast culture in YPDA is spun down at 5000 rmp for 5 mins. The pellet is washed with 5 mL of sterile water and spun down. The pellet is resuspended in 1 mL of sterile 100 mM LiAc and transferred to a microfuge tube. The cells are pelleted at 1,400 rmp for 30 seconds and the supernatant is removed. The cells are resuspended in 200 uL of 100 mM LiAc and 50 uL of this cell suspension is transferred into new microfuge tubes. This cell suspension is then spun down and the supernatant is removed. The pellet is resuspended in 240 uL of 50% PEG, 36 uL of 1M LiAc, 25 uL of 2 mg/mL salmon sperm DNA, and 25 uL of DNA (0.1-10 ug). The cell suspension is vortexed until the pellet is completely resuspended. The cells are incubated at 30 ºC for 30 minutes, then heat shocked at 42 ºC for 20 minutes. The cells are pelleted at 7000 rpm for 30 seconds and gently resuspended in 1 mL of YDPA. Allow the cells to recover overnight at 30 ºC prior to plating on selective media.

The GLE1- and NUP159-Auxin-inducible depletion strains (Chapter 2 - Figure 4E) were a gift from K. Cunningham (John Hopkins University) [114]. The doxycycline-inducible Crm1 N-end rule degron strain (Chapter 2) was generated by integrating pMK632 [115] into the CRM1 locus in the presence of the pCM188 TET activator plasmid to create RSY2348 (Ubi-Leu-3 HA-CRM1::NATMX) as described in detail in [20].

Genes were amplified from wild-type genomic DNA, digested with restriction enzymes, and ligated into indicated vectors. All constructs were verified by sequencing. Commonly used vectors include RSB2619: pRS316, $ADH1_{prom}$-MCS-GFP-$ADH1_{term}$,

RSB2154: pAS2, *GAL4*$_{prom}$-binding domain-HA-MCS-*GAL4*$_{term}$, RSB2486: pACT2, *GAL4*$_{prom}$-activating domain-T7-MCS-*GAL4*$_{term}$. Mutations were introduced using site-directed mutagenesis (Quick Change Kit, New England Biolabs).

Cell growth

Yeast cells were grown in either rich, nonselective medium (YPDA: 2% [w:v] glucose, 2% w:v Bacto peptone, 1% w:v yeast extract, 0.001% w:v adenine sulfate) or synthetic minimal dextrose medium (SD: 0.17% w:v yeast nitrogen base without amino acids and ammonium sulfate, 0.5% w:v ammonium sulfate, 1x supplement mixture of amino acids, 2% w:v glucose) allowing plasmid selection as previously described [22]. For nitrogen-starvation experiments, cells were grown to mid-log (5-7 x 10^6 cells/mL, cells counted using hemocytometer) in SD medium spun down (1,400 rpm for 5 minutes), washed in 2x volume of water, and resuspended in SD-N media for indicated time points [113]. Rapamycin was used at the indicated concentration (low levels permitting growth = 2.5 nM or high levels 200 nM) and durations. Rapamycin (Biovision) was dissolved in 90% Tween, 10% ethanol, and stored at -20 ºC. Oxidative stress was induced using hydrogen peroxide (Millipore Sigma HX0635-3) (0.4-1 mM). For the Auxin-inducible depletion strains live cells were treated with 250 μM auxin (Indole-3-acetic acid; GoldBio, I-110) dissolved in ethanol 30 min before and during nitrogen starvation. For the doxycycline-inducible N-end rule degron studies cells were treated with 2 μg/mL of doxycycline (Sigma Aldrich, D9891) for 1 h before and during nitrogen starvation (these concentrations and incubation times are unique to Crm1, optimization will be needed depending on protein of interest and N-terminal amino acid being used).

Western blot assays

Protein extracts for western blot studies were prepared using a NaOH lysis procedure exactly as described in [55]. Pellets were flash-frozen in liquid nitrogen and stored at -80 ºC. Pellets are resuspended in 500 µL 2 M LiAC and incubated for 5 minutes on ice. Cells are spun down, the supernatant is removed, and the pellet is fully resuspended in 200 µL of 0.4 M NaOH. The cell suspension is incubated for 5 minutes on ice, then spun down and the supernatant is removed. The pellet is then resuspended in 100 µL freshly made 2X loading buffer with 1M DTT and boiled for 5 minutes. Lysates were spun down for 2 minutes, the supernatant are transferred to a new tube, and 10-30 µL of lysate was loaded onto an SDS-PAGE gel. Proteins were separated on 6–12% SDS polyacrylamide gels depending upon their size using the Bio-Rad Mini-Trans Blot cell. For proteins ran on 6% gels, input controls were run on a separate 10% gel. To detect proteins, 1:5000 dilutions of anti-MYC (UpState/EMD Millipore Corp.,05–724), anti-HA (Abcam, ab9110), anti-GFP (Invitrogen, A11122), or anti-Pgk1 (Invitrogen, 459,250) antibodies were used. Western blot signals were detected using 1:5000 dilutions of either goat anti-mouse (Abcam, ab97027) or goat anti-rabbit (Abcam, ab97061) secondary antibodies conjugated to alkaline phosphatase and CDP-Star chemiluminescence kit (Invitrogen, T2307). Signals were quantified relative to Pgk1 or Tubulin (Developmental Studies Hybridoma Bank, University of Iowa) controls using the iBright FL1500 imaging system (Thermo).

All degradation assays were performed in triplicate. Standard deviation and significance were calculated from the mean ± standard deviation using GraphPad Prism 7. For quantification of degradation kinetics band intensities of each time point were

first divided by unstressed, T=0 band intensity. These values were then divided by Pgk1 loading band intensity values which were also normalized to their T=0 intensities. Depending on the experiment either T-tests or 2-way ANOVA analysis was performed. Two-way ANOVAs were performed to determine the significance between every genotype and time point. The P-values shown are relative to wild-type T=4 time points. Protein half-life was extrapolated using linear regression analysis, where 1.7 (log of 50, half of 100%) was plugged into the y value in the slope-intercept form equation.

Cleavage assays

Cleavage assays were performed in indicated strains harboring GFP-fusion proteins. Cells were grown to mid-log in SD, washed, and resuspended in SD-N for indicated time points (usually T=0 and T=4). Protein extracts were prepared using NaOH as described above (25 mL/time point). Proteins were separated using Invitrogen BlotTM 4–12% Bis-Tris Plus gradient gels with 1X MOPS SDS running buffer (NW04122BOX) (20X: 50mM MOPS, 50 mM Tris Base, 0.1% SDS, 1mM EDTA, pH 7.7). Proteins were transferred to PVDF membranes in 1X BlotTM transfer buffer for 1 h 30 min (BT00061) (20X: 25 mM Bicine, 25mM Bis-Tris [free base], 1mM EDTA, pH 7.2). GFP-tagged proteins were detected using 1:5000 dilution of anti-GFP (FUJIFILM Wako Pure Chemical Corp., 012–20,461 for Med13, Invitrogen, A11122 for all other GFP-fusion proteins) antibodies and goat anti-mouse (WAKO) or anti-rabbit (Invitrogen) secondary antibodies conjugated to alkaline phosphatase Quantification of free GFP was calculated exactly as previously described [17]. In short, the free GFP band intensity of the final timepoint (T=4) was quantified and

normalized to Pgk1 protein levels. The P-values and significance shown are relative to wild-type T=4 timepoints.

Co-Immunoprecipitation

For co-immunoprecipitation experiments, 1 L of cells were grown to mid-log, washed, and resuspended in SD-N media (500 mL/timepoint, 125 mL per 5 mL Falcon tube). Protein extracts were prepared using a glass bead lysis method. An equal volume of glass beads and 400 µL RIPA V buffer (50 mM Tris, 150 mM NaCl, 1% NP-40, 0.5% deoxycholate, pH 8.0 HCl supplemented with 1.4 M BME, 0.1 M PMSF, 1 mg/mL Pepstatin, 10 mg/mL Leupeptin, and ProBlock Gold Protease Inhibitor) was added to each sample. Cells were vortexed 8 times for 30 seconds and kept on incubated for 1 minute on ice between vortex cycles. Cell suspensions were centrifuged at 3,500 rmp for 5 minutes and the supernatants were transferred to 1.5 mL microfuge tubes. Lysates were spun again at 4º C for 15 minutes at 1,400 rmp (could use ultra-centrifuge if needed – 50,000 rmp for 45 minutes) and supernatants were transferred to a new 1.5 microfuge tube.

Protein concentrations were determined using the Bradford (Bio-Rad) protein assay and the spectrophotometer readings at OD_{595}. Protein levels were normalized among samples, 1 mg of protein extract was measured, and the final volume was brought to 500 µL using the lysis buffer. One µL of neat antibody was added to each sample except for the negative antibody control and tubes were left at 4 ºC overnight with gentle agitation. Indicated antibodies (anti-GFP Invitrogen, anti-HA, anti-Myc, or anti-T7 Novagen,69,522) were used for immunoprecipitations. Antibodies were then precipitated using protein A beads (GoldBio, P-400-5) that were pre-washed with IP

wash solution (500 mM NaCl, 25 mM Tris, pH 7.4) for 1 hour at 4 ºC with gentle agitation. Beads were then washed twice with IP wash buffer. Beads were resuspended in 20 µL of 2x loading buffer with 1M DTT, boiled for 5 minutes, and centrifuged for 2 minutes at 1,400 rmp. The total volume of supernatant was then loaded onto an SDS-PAGE gel. The coimmunoprecipitation blot was probed with antibodies against the indicated epitopes. Due to the drastic difference in size between Med13-3xHA and GFP-tagged proteins (Snx4 and Atg17), input controls were run on separate gels. For all input controls 500 µg of protein was immunoprecipitated from whole-cell lysates and separated on either 6% (Med13-3 HA) or 10% (GFP-Snx4 and Atg17-GFP) SDS polyacrylamide gels. All co-immunoprecipitation experiments were performed in *pep4*Δ *prb1*Δ*.1* strains to enhance protein concentration.

Fluorescence microscopy

For all microscopy experiments, cells were grown to mid-log, washed, and resuspended in SD-N for the time points indicated. Deconvolved images were obtained using a Nikon microscope (Model E800) with a 100x objective with 1.2x camera magnification (Plan Fluor Oil, NA 1.3) and a CCD camera (Hamamatsu Model C4742). Data were collected using NIS software and processed using Image Pro software. All images of individual cells were optically sectioned (0.2-µM slices at 0.3 µM spacing) and deconvolved, and slices were collapsed to visualize the entire fluorescent signal within the cell. 3D imaging was obtained using the Image Pro software. The nuclei were visualized in live cells using Hoechst staining (Cayman Chemical, 15,547). Hoechst (5 µM), dissolved in water, was added to cells growing in either SD or SD-N (5 µM) 30 minutes before they were visualized by microscopy. The vacuole was visualized in live

cells using FM4-64 (Invitrogen, T3166) and phenylmethanesulfonylfluoride (PMSF; Sigma, P7626) treatment of cells was executed exactly as described [116]. The vacuoles were also visualized in live cells using CMAC (Thermo, C2110) (100μM) staining. Prior to their visualization, cells were spun down and resuspended in HEPES/glucose buffer (10mM HEPES pH 7.4, 5% glucose) with 100μM CMAC and incubated at room temperature for 15 minutes [69].

The Keyence BZX710 fluorescence microscope with a 100x objective with 1.0x camera magnification (PlanApoλ Oil, NA 1.45) and a CCD camera was also used because of its high sensitivity CCD and high-speed autofocus and sectioning. When indicated cells were optically sectioned (0.2-μM slices at 0.4 μM spacing) and Z-stack images were collapsed, and haze reduction processing (deconvolution) was performed. Data were collected using BZ-X Analyzer software. Quantification of Med13-mNeongreen fluorescence within the vacuole was obtained using the Hybrid cell count function within the analyzer software (300 cells were counted per sample). For analysis single extraction settings were used. Red (vacuole, Vph1-mCherry) was set as the target area and green (Med13-mNeongreen) was set as the extraction area. The percentage of cells with vacuolar Med13-mNeongreen was calculated using Area ratio (1st) (ratio of the total area of the extracted areas to the target area) and cell count values. Percentages represent a ratio of the extraction area to the target area.

For monitoring processing bodies (P-bodies) via microscopy special care should be used to reduce centrifugation and handling times as changes in P-bodies can occur rapidly (less than 10 minutes). For P-body microscopy experiments cells were centrifuged for 1 minute, the supernatant was aspirated, and cells were placed on the

cover slip and monitored immediately. Only prepare slides one at a time and when you can image them immediately. If cells need to be washed, wash using the SD-N media instead of sterile water and keep cells resuspended with continuous flicking to maintain aeration (doi:10.1016/S0076-6879(08)02625-6).

Yeast two-hybrid analysis

Yeast two-hybrid assays were performed in the Matchmaker Gold Yeast Two-Hybrid System (*AUR1-C, ADE2, HIS3, and MEL1*) (Takara Cat# 630489). The pAS2 (RSB2154, $GAL4_{prom}$-binding domain-HA-MCS-$GAL4_{term}$) and pACT2 (RSB2486, $GAL4_{prom}$-activating domain-T7-MCS-$GAL4_{term}$) vectors were used. Plasmids expressing the bait protein fused to the Gal4 DNA-binding domain and the prey protein fused to the Gal4 activation domain were transformed into the Y2H gold strain. Plasmids were selected for on synthetic minimal dextrose medium lacking leucine and tryptophan (SD: 0.17% w:v yeast nitrogen base without amino acids and ammonium sulfate, 0.5% w:v ammonium sulfate, 1x supplement mixture of amino acids, 2% w:v glucose). Interactions between the bait and prey proteins were monitored using the *ADE2*, *HIS3*, and *AUR1-C* reporter genes. Single colonies were plated to media lacking leucine, tryptophan, adenine, and histidine and supplemented with 200ng/mL Aureobasidin A (Takara Cat# 630466). Autoactivation or weak interactions were removed by supplementing selective media with 40ug/mL of X-alpha-Gal (GoldBio Cat# XA250) and/or 3-aminotriazole (3-AT, Simga, Cat.#A8056-100G).

Cell viability and growth assays

The population of dead cells in a yeast population was determined using flow cytometry. Cells are grown to mid-log (~5 x 10^6 cells/mL), 5 mL were used for the

unstressed T=0 control, and the rest (20 mL) is spun down, washed, and resuspended in SD-N. 5 mL cultures were allocated from the 20 mL of cells resuspended in SD-N media and put on the wheel for the indicated time points (usual time course was 0, 3, 6, 9 days in SD-N). The aseptic technique is critical as contamination is more likely with longer incubation periods. For analysis, cells are spun down and transferred to a sterile 1.5 mL microfuge tube. Cells were washed in 1 mL of 1X PBS, stained with phloxine B (Acid Red, Millipore Sigma P2759) at 5ug/mL (1X diluted in PBS), and incubated in the dark for 15 minutes. Cells were washed twice, diluted, and ran through the flow cytometer. phloxine B is a fluorescent dye that can only penetrate cells that have a permeable membrane such as necrotic cells.

Samples were performed in biological triplicate and 30,000 cells were counted per time point. The percentage of phloxine B-positive (dead cells) was quantified using parameters determined by an unstained control. In addition to viability assays performed with the flow cytometer, serial dilution plating assays can also be performed to determine changes in viability over time or between different genotypes. In these assays, cells are grown to mid-log in replete SD liquid culture and then plated (3 uL) in ten-fold serial dilutions following indicated treatments to YPDA plates. Cells were then grown at 30º C for 48 hours and plates were imaged.

For cell growth assays, cells were grown overnight in YPDA media and back diluted to ~1 x 10^5 cells/mL the following day. Cells were then grown for at least 4 hours at 30 and then aliquoted into 96 well plates. Growth rates were analyzed in the Gen5 microplate reader using the Brewing Yeast 24 h program in biological triplicate and technical duplicates. For growth recovery assays (monitoring quiescence exit)

saturated yeast cultures were diluted to ~1 x 10^5 cells/mL and aliquoted into 96 well plates and growth rates were immediately analyzed using the plate reader.

Statistical analysis

All representative results included at least two independent biological experiments. P values were generated from Prism GraphPad using unpaired Student's t-tests or ANOVA tests; NS $P \geq 0.05$; *$P \leq 0.05$, **$P \leq 0.005$; ***$P \leq 0.001$; ****$P \leq 0.0001$. All error bars indicate mean ± SD.

2. Mammalian

Cell Culture

Experiments were primarily performed in cell lines derived from *Pdx1*-cre*;* LSL-*KrasG12D* or *Pdx1*-cre; LSL-$Kras^{G12D}$; $Ccnc1^{f/f}$ murine models generated by Dr. Kerry Campbell's group at the Fox Chase Cancer Institute in Philadelphia. Clonal populations were obtained from single-cell dilutions and clonal expansion of homogenized pancreatic tissue. The two cell lines ($Kras^{G12D}$ $Ccnc^{+/+}$ or $Kras^{G12D}$ $Ccnc^{-/-}$) used in all experiments were single clone populations chosen based on the cuboidal morphology most comparable to known PDAC cell line models. The #470 clone 4 *Pdx1*-cre*;* LSL-*KrasG12D* ($Kras^{G12D}$ $Ccnc^{+/+}$) cell line was derived from a 15.5-month-old mouse with a nodular pancreas. Pathology showed extensive acinar-ductal metaplasia (ADM) and pancreatic intraepithelial neoplasia (PanIN) lesions with areas of sarcomatous stroma, but late-stage PDAC was not found. This cell line was used as the control for all experiments. The #163 clone 8 *Pdx1*-cre; LSL-$Kras^{G12D}$; $Ccnc1^{f/f}$ ($Kras^{G12D}$ $Ccnc^{-/-}$) cell line was derived from a 15-week-old female mouse. The pancreas had a malignant neuroendocrine tumor with areas of hemorrhage and adjacent ADM lesions. The PDAC

cell lines were cultured in low Ca^{+2} media with 5% chelated horse serum (FCCC, #40720) (DMEM/F12 1:1 Gibco special formula #90-5212EF, Antimycotic Gibco #15240-062, 100 ng/ml Sigma #C-8052 Choleratoxin, 20 ng/ml EGF, 5% chelated horse serum Gibco #16050-122, 27 μg/ml insulin Sigma #1-5500, 0.5 mg/L hydrocortisone Sigma #H-4001, 0.04 mM calcium chloride dihydrous, 2.438 g/L sodium bicarbonate, pH 7.2) purchased from the cell culture facility at the Fox Chase Cancer Institute. at 37 °C and 5% CO2.

Cultures were detached from flasks or wells using 1X TrypLE (Gibco Ref. #A12177-01, diluted using DPBS Ref. #14190-144 and 1mM EDTA) for 15 minutes followed by dilution in twice the volume of culture grade 1X PBS. Cells were pelleted at 700 g for 5 minutes. Cells are stored in liquid nitrogen in media containing 10% DMSO and located in boxes G8 and H8. The $Kras^{G12D}$ $Ccnc^{-/-}$ cell line was cell sorted at Fox Chase and single clones were isolated and expanded. Single clonal expansions were categorized as slow growers (SG), medium growers (MG), and fast growers (FG). We retrieve various clones of each, and they have been expanded and frozen away for later use. Any other cell lines have been described in the table below.

Cell Line	*#470 Kras^{G12D} Ccnc$^{+/+}$*	*#163 Kras^{G12D} Ccnc$^{-/-}$*
Genotype	*Pdx1*- cre; LSL-*Kras^{G12D}*	*Pdx1* -cre; LSL-*Kras^{G12D}*; *Ccnc1$^{f/f}$*
Media	Low Ca^{+2}	Low Ca^{+2}
Description	PDAC murine model at Fox Chase	PDAC murine model at Fox Chase
Instructions	Detach using 1X TrypLE for 15 min	Detach using 1X TrypLE for 15 min

Cell Line	Pancreatic Epithelial	Mpt 2b	#697
Genotype	untransformed pancreatic epithilium	*Pdx1* -cre; LSL-*Kras^{G12D} p53$^{+/-}$*	*Pdx1*- cre; LSL-*Kras^{G12D}*
Media	Low Ca^{+2}	RPMI	Low Ca^{+2}
Description	immortlized with SV40 T anitgen	female mouse aged 16 weeks	male mouse aged 49 weeks
Instructions	Detach using 1X TrypLE for 5 min		

Table 1. Cell culture conditions. The cell line, genotypes, media, and passaging conditions for the indicated genotypes are described.

For viability assays or Western blot analysis, cells were grown to 75% confluency and treated with the following. An autophagy inhibitor (100 μM) of chloroquine (Caymen, #14194) for 24 hours, an autophagy inducer 250 nM of Torin1 (Santa Cruz Biotechnology; CAS: 1222998-36-8) for 24 hours, indicated concentrations of the proteasome inhibitors Bortezomib (usually used at 100 nM) for 24 hours, or 250 nM of MG-132 (Calbiochem; CAS: 133407-82-6) for 24 hours before analysis. For Cdk8 kinase inhibition, cells were pretreated with 1 μM Sel120-34A (Caymen, #27906) for 24 hours, or 1 μM Senexin A (Tocris; CAS: 1780390-76-2) for 24 hours. Cells were treated again when the other drugs were administered to ensure that Cdk8 kinase activity would remain inhibited.

Western blot assays

For mammalian cells, protein extracts were prepared for Western blot analysis using RIPA V buffer (50 mM Tris, 150 mM NaCl, 1% NP-40, pH 8.0 HCl) made fresh with the addition of 1.4 M BME, 0.1 M PMSF, 1 mg/mL Pepstatin, 10 mg/mL Leupeptin, and sigma protease inhibitor cocktail (1:100 dilution). Pellets are harvested and flash

frozen in liquid nitrogen and stored at -80º C. Cells harvested at ~75% confluency from a 6-well dish are lysed in 30 µL of lysis buffer, and cells harvested from a 100 m dish are lysed in 100 µL of the buffer. Fully resuspend the pellet until the cell suspension is homogenous and mixed thoroughly. Tubes are then incubated at 4º C with gentle agitation for 30 minutes. Lysates are then spun down at 4º C at full speed for 15 minutes. The supernatant is then transferred to a new 1.5 microfuge tube and protein concentrations are determined using the Bradford (Bio-Rad) protein assay reagent and the spectrophotometer. Depending on the protein being monitored load between 30-50 µg of protein with equal volumes of 2x loading buffer made fresh with 1M DTT. Lysates are then boiled and run on an SDS-PAGE gel. The antibodies used can be found in Table 3 of the appendix. β-Actin (1:2500 dilution) (Abcam-ab8227) was used as the loading control. Secondary antibodies and imaging are exactly as described in the yeast methods Western blot assays section.

Fluorescence microscopy

Harvest cells as described above and dilute cells at low confluency to obtain an evenly spread, single-cell distribution. If cells are clumped or highly confluent it will be difficult to get representative images. For $Kras^{G12D}$ $Ccnc^{+/+}$ cells 100 µL of the 3mL cell/trypsin/PBS suspension was diluted into 5 mL of fresh media and for the $Kras^{G12D}$ $Ccnc^{-/-}$ cells 200 µL of the cell suspension was diluted into 5 mL of fresh media. From this dilute cell suspension, 500 µL was pipetted directly onto coverslips. Cells were allowed to settle for ~30 minutes in the incubator and then 2.5 mL of fresh media was added to each well. Cells were then grown overnight or until ~50-60% confluent. For microscopy cells were treated with the same concentration of drugs as described above

but for 4 hours instead of 24 hours. For monitoring mitochondrial morphology, Mito Tracker Red CMXRos was added 30 minutes prior to fixing.

After treatment, cells were washed twice with cold 1X PBS. Cells were then fixed using 1 mL of 4% paraformaldehyde and incubated for 10 minutes at RT. Cells were washed twice and permeabilized using 1 mL of 0.2% Triton and incubated on the shaker for 10 minutes at RT. Cells were washed and non-specific interactions were blocked using 1 mL of 2% BSA (diluted in PBS) and incubated on the shaker for 1 hour at RT. The 2% BSA was then removed, and the primary antibody was added and mixed on the shaker for 5 minutes and then incubated at 4º C overnight. For the cyclin C and LC3 antibodies, I used the same antibodies as those used for Western blots except at a 1:500 dilution (diluted in 2%BSA/PBS solution). The following day the primary antibody was removed, and cells were washed and incubated with the secondary antibody (anti-rabbit Alexa Fluor 488; Invitrogen; A-11008) at a 1:2,000 dilution (diluted in 2% BSA/PBS solution) for 1 hour on the shaker in the dark. The secondary antibody was removed, and cells were washed with 1X PBS. Coverslips were then mounted using 3 μL of the DAPI mounting solution. Cells were then visualized using the Keyence BZX710 fluorescence microscope with a 40x or 100x objective with 1.0x camera magnification (PlanApoλ Oil, NA 1.45) and a CCD camera. Images were processed using the BZ-X Analyzer software.

Flow cytometry analysis

Cells were grown in 12-well dishes to ~75% confluency and treated with the indicated drugs as described above. Media was transferred to sterile 1.5 mL microfuge tubes (dead cells are usually detached and floating within the media so it is important to

collect both the media and cells) and cells were harvested as described above. Cells were carefully collected and pelleted at 700 g for 2 minutes. The supernatant was removed by decanting (would not use aspiration) and pellets were washed with 1X cold PBS. Cells were resuspended in the indicated dye or stain and analyzed using the BD AccuriTM C6 flow cytometer (BD Biosciences). 30,000 events were counted per sample and experiments were performed in biological triplicates. Cells can vary in size between genotypes so be sure to gate correctly. For Annexin V viability assays, cells were resuspended in 100 µL of the Annexin V Ca^{+2} buffer (10X: 100 mM HEPES pH 7.4, 1.4M NaCl, 25 mM $CaCl_2$) and 1 µL of the Cy5 Annexin V reagent (BD Biosciences, Cat. #559933) and 1 µL of 100 µg/mL propidium iodine stock was added to the cell suspension. Cells were then incubated for 15 minutes in the dark at RT. Cells were then analyzed immediately (does not need to be washed). The percentage of Annexin V positive cells was quantified and graphed.

For quantifying reactive oxygen species concentrations, cells were incubated with 1 mM dihydroethidium (DHE), 250 nM tetramethyl rhodamine methyl ester (TMRM), or 5 µM of MitoSox for 30 minutes at RT in the dark. Fluorescent profiles were then analyzed and graphed. For monitoring the cell cycle and aneuploidy, cells were harvested as described above. The number of cells will affect the quality of staining, therefore $0.5x10^6$ cells/mL were spun down and washed in 1X PBS. The cells were then resuspended in 1 ml of ice-cold PBS and vortexed gently. The cells were then fixed by adding the cell suspension drop-wise slowly into 9 mL of 70% ethanol in a 15 mL conical tube. Cells were stored at 4º C for 24 hours (can be stored up to 2 years before staining). After fixation, cells were spun down at 200 g for 10 minutes at 4º C

and washed in cold PBS. Cells were resuspended in freshly made 500 µL PI/Triton staining solution (1% v/v Triton X-100 in PBS, 2 mg of DNAse-free RNAse A, 400 µL of 500 µg/ml PI). The cell suspension was incubated at RT for 30 minutes in the dark and then analyzed using the flow cytometer.

Proteasome Assays

To determine proteasome activity cells were grown to ~75% confluency in 100m dishes and harvested as previously described (protein concentrations can be low due to the gentle lysis methodology therefore 100m dishes were used). Cells were lysed using lysis buffer A (25 mM Tris, pH 7.4, 10 mM $MgCl_2$, 10% glycerol) supplemented with fresh 1mM ATP, 1 mM DTT, and 5 µL (for 500 µL of buffer) of protease inhibitor and phosphatase inhibitor. Cells were spun down, resuspended in 75 µL of lysis buffer A, and incubated at 4º C with gentle shaking for 30 minutes (gentle to not disrupt proteasome complexes). Cells were spun at full speed for 4 minutes at 4º C and lysates were transferred to a new tube. Bradford protein assays were used to determine protein concentrations. Each reaction required 25 µg of protein which was brought up to a total volume of 50 µL using lysis buffer and pipetted into one well a 96-well dish. To monitor proteasomal-independent fluorescence 72.5 µM MG132, the proteasome inhibitor was added to each control lane. Finally, the substrate buffer (lysis buffer A, 200 µM Suc LLVY, 1 mM DTT, and 1 mM ATP) was added to each well. Fluorescence was immediately monitored via the plate reader. Fluorescent readings (excitation = 360, emission = 400) were taken every 5 minutes for 90 minutes at 37º C with gentle shaking.

CHAPTER 2

Snx4-assisted vacuolar targeting of transcription factors defines a new autophagy pathway for controlling *ATG* expression

This chapter is based on a research paper published in the journal *Autophagy* in 2021.

Abstract

Autophagy, in part, is controlled by the repression and activation of autophagy-related (*ATG*) genes. Here, we describe a new selective autophagy pathway that targets functional transcriptional regulators to control their activity. This pathway is activated in response to nitrogen starvation and recycles transcriptional activators (Msn2 and Rim15) and a repressor (Med13) of *ATG* expression. Further analysis of Med13 vacuolar proteolysis revealed that this pathway utilizes the core autophagic machinery. However, it is independent of known nucleophagy mechanisms, receptor proteins, and the scaffold protein Atg11. Instead, Med13 exits the nucleus through the nuclear pore complex (NPC) and associates with the cytoplasmic nucleoporin Gle1, a member of the RNA remodeling complex. Dbp5 and Nup159, that act in concert with Gle1, are also required for Med13 clearance. Med13 is retrieved from the nuclear periphery and degraded by Atg17-initiated phagophores anchored to the vacuole. Efficient transfer to phagophores depends on the sorting nexin heterodimer Snx4/Atg24-Atg20, which binds to Atg17 and relocates to the perinucleus following nitrogen starvation. To conclude, this pathway defines a previously undescribed autophagy mechanism that targets select transcriptional regulators for rapid vacuolar proteolysis, utilizing the RNA remodeling complex, the sorting nexin heterodimer Snx4-Atg20, Atg17, and the core autophagic machinery. It is physiologically relevant as this Snx4-assisted vacuolar

targeting pathway permits cells to fine-tune the autophagic response by controlling the turnover of both positive and negative regulators of *ATG* transcription.

Introduction

Macroautophagy (hereafter autophagy) is a controlled catabolic process critical for maintaining homeostasis and cellular survival during adverse conditions, such as starvation or cytotoxic stress. Initially, identified as a mechanism to recycle superfluous cytosolic proteins [70], it is apparent that autophagy is also a critical regulator of specific cargos, including misfolded proteins and aggregates, damaged organelles, lipids, and pathogens [71]. As such, autophagy pathways have been reclassified as being either nonselective or selective autophagy [72]. In budding yeast, nonselective autophagy is upregulated in response to starvation or cytotoxic stress and triggers the formation of autophagosomes that capture superfluous cytosolic proteins [73],[74]. It is initiated by TORC1 (target of rapamycin kinase complex) inhibition [75] that triggers a cascade of events, resulting in the pentameric Atg1 kinase complex being recruited to the phagophore assembly site (PAS). Atg1 activates the Atg17 scaffold complex [76] to capture Atg9 vesicles independent of cargo, which are needed to nucleate phagophores anchored to the vacuole by Vac8 [77]. Upon the formation of the double-membraned phagophores, cytosolic cargos are randomly sequestered into these structures, and following the closure, the autophagosome cargos are subsequently degraded by vacuolar proteolysis [78],[32].

Selective autophagy pathways operate both in normal vegetative conditions to maintain homeostasis [72] and in response to stress such as starvation and cytotoxic stress [71]. They share 19 “core autophagy proteins” with nonselective autophagy and

also use receptor proteins to coordinate the tethering of specific cargos, including damaged organelles and protein aggregates to Atg8 at phagophores [32]. Receptor proteins also bind to the selective autophagy scaffold protein Atg11 [79] resulting in the nucleation of phagophores in the direct vicinity of the cargo [80]. The relationship between Atg11, Atg17, and Atg9 changes between nutrient-rich and deplete conditions [79]. In nutrient-rich conditions, receptor proteins activate and dimerize Atg11, which allows them to outcompete Atg17 for Atg9 vesicles. Furthermore, Atg17 is maintained in an inactive state by forming a constitutive Atg17–Atg31–Atg29 subcomplex [77]. Upon nitrogen starvation, Atg11 is degraded by the ubiquitin-proteasome system (UPS) and the Atg1 kinase activates Atg17. These two events permit Atg17 to sequester Atg9 vesicles to nucleate phagophores independent of cargo.

Nuclear autophagy or nucleophagy is the least well-understood of the selective autophagy mechanisms. Underscoring its importance, various pathologies namely cancer and neurodegeneration are linked with perturbed nucleophagy [81]. It is best characterized in yeast where macronucleophagy utilizes a receptor protein and involves the sequestration of a portion of the nucleus into autophagosomes [82]. In contrast, micronucleophagy (piecemeal autophagy of the nucleus), is autophagosome-independent and forms nuclear-vacuole junctions that pinch off portions of the nucleus directly into the vacuolar lumen [83]. Recently, an autophagic mechanism has been described that removes defective nuclear pore complexes (NPCs) [84,85].

In yeast, 43 unique autophagy-related (ATG) genes have been identified that control this highly coordinated and complex process [37]. Accordingly, these genes are tightly regulated at multiple levels. Recently we have shown that the Cnc1-Cdk8 kinase

negatively regulates *ATG8* expression within the Ume6-Rpd3 HDAC axis [38,86]. This kinase, together with Med13 and Med12, form the evolutionarily conserved CDK8 kinase module (CKM) of the Mediator complex. In budding yeast, the CKM predominantly represses transcription of a diverse set of meiosis and stress response genes [49,86] by interacting with DNA-bound transcription factors and RNA polymerase II [87-89].

Activation of genes controlled by the CKM is achieved by disrupting its association with the Mediator [90]. Studies from our group revealed that this is achieved by CKM disassembly. However, we observed that the mechanisms used to disassemble the CKM are dependent upon environmental cues (outlined in Figure 1A) [52]. In short, oxidative stress triggers cyclin C translocation to the cytoplasm [91] where it mediates stress-induced mitochondrial fission and regulated cell death (RCD) in both yeast [52] and mammalian cells [12,57][[58]. Its nuclear release is dependent upon Med13's destruction by the UPS [53,54]. In contrast, following a survival cue (nitrogen starvation), Cnc1 is rapidly destroyed by the UPS before its nuclear release which prevents mitochondrial fission [38].

This study reveals that the transcriptional repressor Med13 is degraded by vacuolar proteolysis via a previously undescribed autophagic pathway. Similar to known selective autophagic pathways, it requires the core autophagic machinery, but, surprisingly, does not use the known nucleophagy mechanisms or the scaffold protein, Atg11. Instead, this pathway utilizes the nucleoporin Gle1, the sorting-nexin heterodimer Snx4-Atg20, and Atg17-initiated autophagosomes. Moreover, two transcriptional activators that regulate ATG expression also utilize this pathway upon

nitrogen starvation. This suggests that Snx4-assisted vacuolar targeting of transcriptional regulators defines a new autophagy pathway for controlling *ATG* expression, that allows for fine-tuning of the autophagic response.

Experimental Results

Med13 is actively degraded following nitrogen starvation

We started this investigation by addressing if Med13 was expressing endogenous Med13-9xMYC were starved for nitrogen (SD-N), and western blot analysis showed that Med13 protein levels decreased with a half-life of 2.6 h (Figure 1B, D). Similarly, Med13 was rapidly degraded in replete medium containing rapamycin, a drug that mimics nitrogen starvation by inhibiting TORC1 [92] (Figure 1B and S1A). As the half-life of Med13 is >6 h in unstressed cultures [53], and *MED13* mRNA increased following 4 h in SD-N (Fig. S1B), these results indicate that Med13 is actively degraded following TORC1 inhibition.

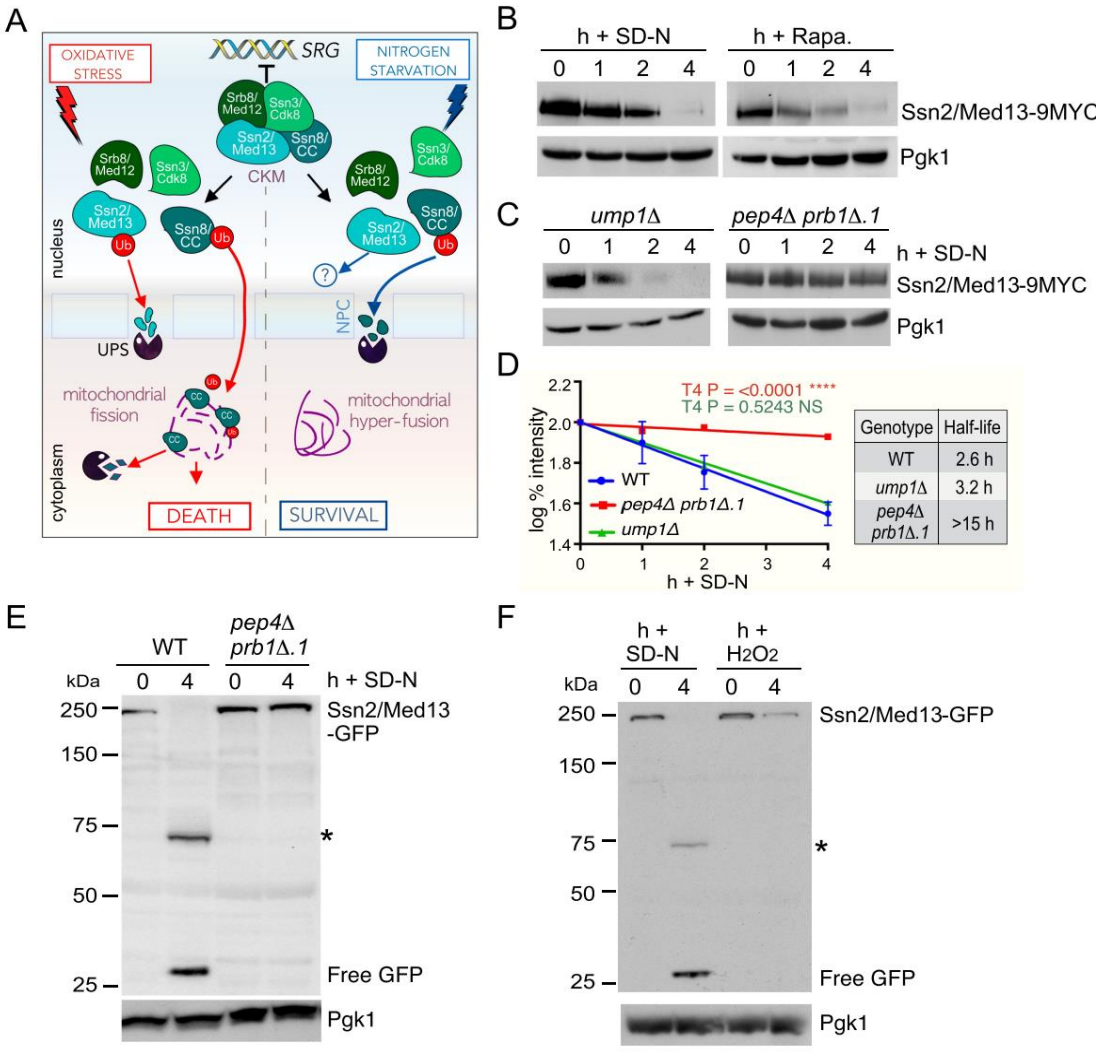

Figure 1. Med13 is degraded via vacuolar proteolysis following nitrogen starvation. **(A)** Model outlying how the CKM is disassembled following stresses that mediate cell death or survival pathways. **(B)** Western blot analysis of extracts prepared from wild-type cells expressing endogenous Med13-9xMYC resuspended in nitrogen starvation medium (SD-N) or treated with 200 ng/ml rapamycin for the indicated times. **(C)** As in B except that endogenous Med13 protein levels were monitored in *ump1*Δ and *pep4*Δ *prb1*Δ*.1* strains. **(D)** Degradation kinetics and half-life of Med13 protein levels obtained in B and C. Error bars indicate S.D., N = 3 of biologically independent experiments. **(E)** Wild-type or *pep4*Δ *prb1*Δ*.1* cells expressing Med13-GFP were starved for nitrogen for indicated times. GFP accumulation was monitored by western blot analysis using anti-GFP antibodies. An asterisk indicates a nonspecific proteolytic fragment. **(F)** As in E except that wild-type cells were resuspended in SD-N or treated with 0.8 mM H2O2. Pgk1 levels were used as loading controls.

Med13 degradation following nitrogen starvation is mediated by the vacuole

Med13 levels were next monitored in *ump1*Δ, a mutant deficient in 20S proteasome assembly [35], and no change in degradation kinetics was observed (Figure 1C, D). In contrast, in *pep4*Δ *prb1*Δ*.1*, a vacuolar protease mutant [70,93], Med13 was stable in SD-N (Figure 1C, D) with a half-life >15 h. This indicates that Med13 degradation requires vacuolar proteolysis. Confirming this, the same results were obtained in wild-type, *ump1*Δ, and *pep4*Δ *prb1*Δ*.1* cells harboring a low copy, functional Med13-3xHA plasmid [54] (Fig. S1C and D). Moreover, we found that after nitrogen starvation GFP accumulated in Med13-GFP cleavage assays. This indicates that Med13-GFP is degraded in the vacuole as the compact fold of GFP renders it resistant to vacuolar hydrolases [94]. Accordingly, repeating these cleavage assays in *pep4*Δ *prb1*Δ*.1* cells abolished the formation of free GFP and stabilized full-length Med13-GFP (Figure 1E, quantified in Fig. S1E). As anticipated from our previous studies [53], Med13-GFP was destroyed following 0.8 mM H_2O_2, and no GFP accumulation was seen (Figure 1F and S1E). These results show that the proteolysis machinery employed to degrade Med13 is dependent upon environmental cues.

To visualize Med13 vacuolar degradation, we used live-cell imaging of endogenous Med13-mNeongreen in *pep4*Δ *prb1*Δ*.1.* In SD media, Med13-mNeongreen is nuclear (Figure 2A) but after 4 h in SD-N, Med13 accumulated in the vacuole (Figure 2B). The deconvolved collapsed images in Figure 2C also captured Med13-mNeongreen transitioning between these organelles. After 24 h in SD-N, Med13-mNeongreen is predominantly vacuolar (Fig. S2A), and similar results were obtained when endogenous Med13-YFP was expressed in wild-type cells treated with

PMSF that blocks the activity of vacuolar serine proteases (Fig. S2B) [70]. We also monitored the transition of Med13-mNeongreen to the vacuole in *pep4*Δ *prb1*Δ*.1* over time (Figure 2D). After 1h, Med13 foci are seen (yellow arrow) localizing to the nuclear membrane. After 3h, Med13 is visualized in the vacuole (pink arrows), with the vacuolar pool being easier to capture at later time points (orange arrow, Figure 3D and see Figure 5). These results are consistent with a model in which nitrogen starvation triggers Med13 vacuolar proteolysis.

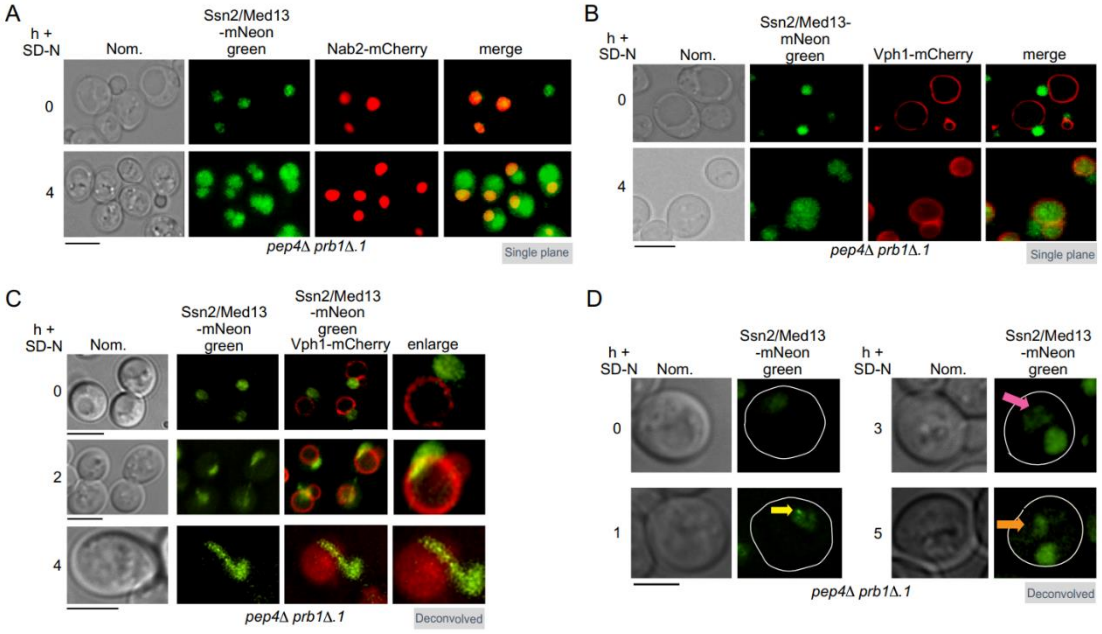

Figure 2. Med13 translocates from the nucleus to the vacuole in nitrogen starvation. **(A)** Endogenous Med13-mNeongreen localization was monitored in *pep4*Δ *prb1*Δ*.1* cells expressing Nab2-mCherry (a nuclear marker) before (growing in SD) and after 4 h in SD-N. Representative single-plane images are shown. **(B)** As in A, except cells expressed a vacuolar marker (Vph1-mCherry). **(C)** As in B, except that slices were taken through the whole cell which was then collapsed and deconvolved. Representative deconvolved images are shown. Scale bar: 5 µm. **(D)** Fluorescence microscopy of Med13-mNeonGreen for the time points indicated.

Med13 degradation requires core autophagy machinery

Next, we investigated if Med13 degradation was dependent upon proteins required for autophagosome biogenesis (outlined in Figure 3A). Med13 was significantly stabilized following nitrogen starvation in mutants defective in induction (*atg1*Δ*)* and phagophore assembly (*atg8*Δ) [95] (half-lives >15 h, Figure 3B, C). Likewise, GFP accumulation from Med13-GFP was abolished in autophagy mutants (*vps34*Δ*, atg9*Δ*, atg4*Δ, and *vam3*Δ) required for different stages of the pathway (Figure 3A, D, and S1E). We did observe some turnover of full-length Med13-GFP, which we attribute to a combination of Med13 being expressed from the *ADH1* promotor rather than the endogenous locus used for degradation assays and UPS activity. Consistent with this, Med13-GFP was more stable in *atg1*Δ *ump1*Δ than in *atg1*Δ cells (Fig. S2C). Therefore, both the vacuole and core autophagy proteins are needed for Med13 degradation.

Med13 colocalizes with the autophagy machinery after nitrogen starvation

If the degradation of Med13 requires autophagic machinery, we would expect Med13 to accumulate outside of the vacuole in mutants defective in autophagic cargo delivery. Consistent with this model, we observed Med13 accumulating on the surface of the vacuole in *atg8*Δ mutants (yellow arrow, Figure 3E, F). Here it colocalizes with Atg2-mCherry and Atg7-mCherry, two components of the phagophore (Figure 4A, B, and S2D). In *vam3*Δ*,* a fusion deficient t-SNARE mutant [96,97], Med13 colocalizes with Atg8-mCherry which conjugates to inner autophagosome membranes [98] (Figure 4C). Using this series of colocalization studies in null mutants, we were able to demonstrate the sequential movement of Med13 from the nucleus (Nab2) to the PAS (Atg2 and Atg7), followed by sequestration within autophagosomes (Atg8), and ultimately

degraded within the vacuole (Vph1). Despite this, Med13 and Atg8 do not interact in a two-hybrid assay (Fig. S2E and see Fig. S2F for Y2H control of Atg8 interaction with Atg7). Furthermore, co-immunoprecipitation experiments of endogenously tagged proteins suggest that Med13 and Atg8 do not interact in *pep4*Δ *prb1*Δ*.1* cells. In these experiments, the GFP-Atg8 affinity isolation of Med13-HA was not significantly above the background (Fig. S2G). This result was surprising as Med13 contains 33 potential Atg8-interacting motifs (AIMs), including 13 located within its large 700 amino acids intrinsically disordered region (IDR) (Fig. S2H). However, while AIMs are well-defined, potential motifs require experimental confirmation [99,100][[101]. Given the large number found in Med13, coupled with the negative Y2H and coimmunoprecipitation results, we felt that this approach was outside of the scope of this report. Moreover, the results are more consistent with a model in which another mechanism targets Med13 to Atg8.

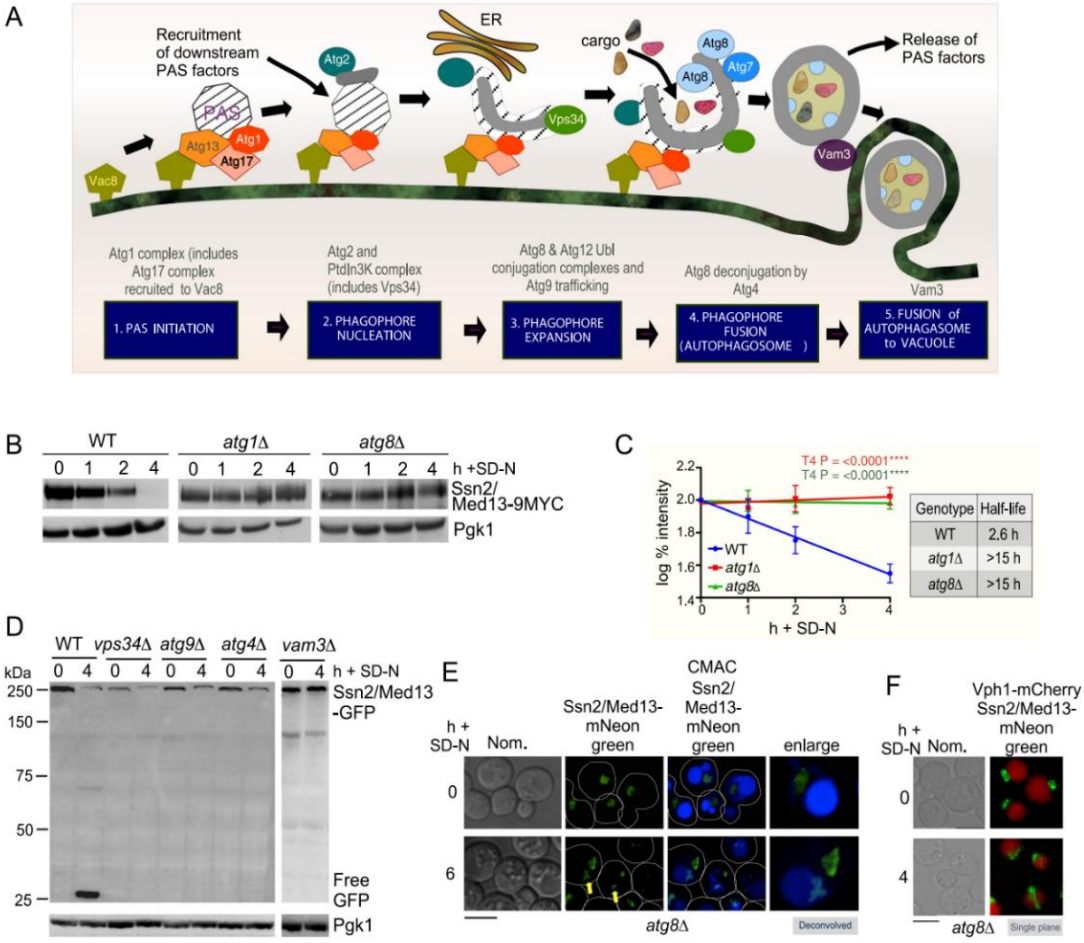

Figure 3. (A) Schematic depicting the five stages of autophagy. **(B)** Western blot analysis of extracts prepared from wild-type, *atg1*Δ, and *atg8*Δ cells expressing endogenous Med13-9xMYC resuspended in SD-N media for the indicated times. **(C)** Degradation kinetics and half-life of Med13 protein levels obtained in B. Error bars indicate S.D., N = 3 of biologically independent experiments. **(D)** Med13-GFP cleavage assays were performed in the indicated genotypes. For all experiments, Pgk1 protein levels were used as a loading control. **(E and F)** Endogenous Med13-mNeongreen localization was monitored in *atg8*Δ cells following SDN. Vacuoles were visualized with either CMAC (E) or using a vacuolar marker, Vph1-mCherry (F). Representative images are shown. Scale bar: 5 µm.

Med13 degradation does not use known selective autophagy pathways

Selective autophagy relies on cargo receptors that bind to both Atg8 and exclusive cargo [71,102]. Deletions of known receptor proteins (Cue5, Atg19, Atg34, Atg36, Atg32), including the newly defined Ubx5 [103] and the redundant Atg19 Atg34 receptors [104] did not influence the autophagic degradation of Med13 (Fig. S3A, B, and Fig. S1E). Moreover, the receptors required for micro-and macro- nucleophagy (Nvj1, Atg39, and Atg40, Figure 5A) [82,105] do not mediate Med13 degradation (Figure 5A). We also did not observe Med13 forming large protein aggregates after nitrogen starvation although very occasionally small foci were observed at early time points (see Figure 2D, 5D). Consistent with this, the deletion of Hsp42 or Hsp104, two chaperones known for sequestration of protein aggregates [106,107][[108] did not affect Med13 degradation following nitrogen starvation (Fig. S3C). Taken together, these results show that Med13 vacuolar degradation is independent of the known receptor proteins.

Med13 degradation requires the Atg17 scaffold complex

Selective autophagy of excess or damaged cellular components in physiological conditions requires the scaffold protein Atg11 to build phagophores at the site of the cargo [109]. During nitrogen starvation, Atg11 is destroyed by the UPS [79] and Atg17 tethers Atg1 and other Atg proteins to the PAS [110] located at the vacuole [78]. Analysis of the autophagic degradation of Med13-GFP (Figure 5B and S1E) and the degradation of endogenous Med13-9xMYC (Fig. S3D and E) revealed that Atg17 but not Atg11 is required for Med13 destruction. These results suggest that the autophagic degradation of Med13 is mediated by phagophores tethered to the vacuole.

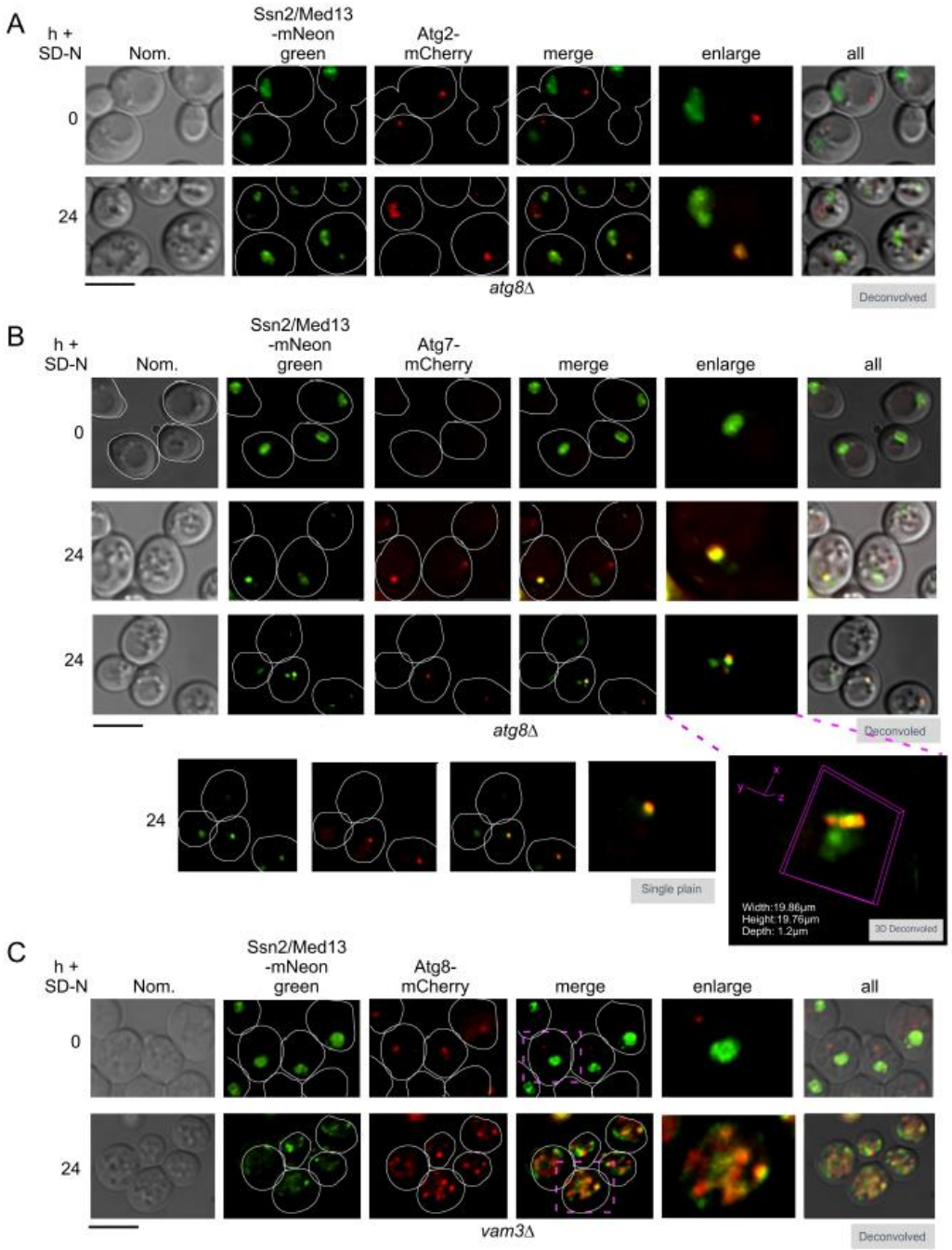

Figure 4. Med13 colocalizes with autophagic machinery following nitrogen starvation. Localization of endogenous Med13-mNeongreen and Atg2-mCherry were monitored in *atg8*Δ cells **(A)**, Atg7-mCherry in *atg8*Δ cells **(B)**, or Atg8-mCherry colocalization was monitored in *vam3*Δ cells **(C)** following 24 h. Representative deconvolved or single-plane images are shown. Scale bar: 5 µm.

Consistent with this, we observed a significant reduction in the appearance of GFP in *vac8*Δ cells (Figure 5B and S1E). As one role of Vac8 is to tether the Atg17-initiated PAS complex to the vacuole [78], these results suggest that Med13 is transported to Atg17-built phagophores located on the vacuole membrane for autophagic destruction.

The cytoplasmic nucleoporin Gle1 associates with Med13 after nitrogen starvation

To further define components of the Med13 degradative pathway, a pull-down approach of Med13-3xHA followed by mass-spectroscopy was used (Fig. S4A and B and Table SI for a list of candidate interactors). The conserved, essential nucleoporin Gle1, which localizes to the cytoplasmic filament of the nuclear pore complex (NPC) was identified [111]. Co-immunoprecipitation analysis revealed that Med13-3xHA and endogenous Gle1-GFP interacted following 1h SD-N, confirming this association (Figure 5C). Y2H analysis showed that the large central IDR of Med13, which provides a flexible interaction hub for multiple partners [54,112], interacts with Gle1 (Figure 5D and S5). Live-cell imaging of endogenous Med13-mNeongreen and Gle1- RedStar shows Med13 moves from being diffuse nuclear to associating with the punctate Gle1-RedStar that surrounds the nucleus after nitrogen starvation (Figure 5E).

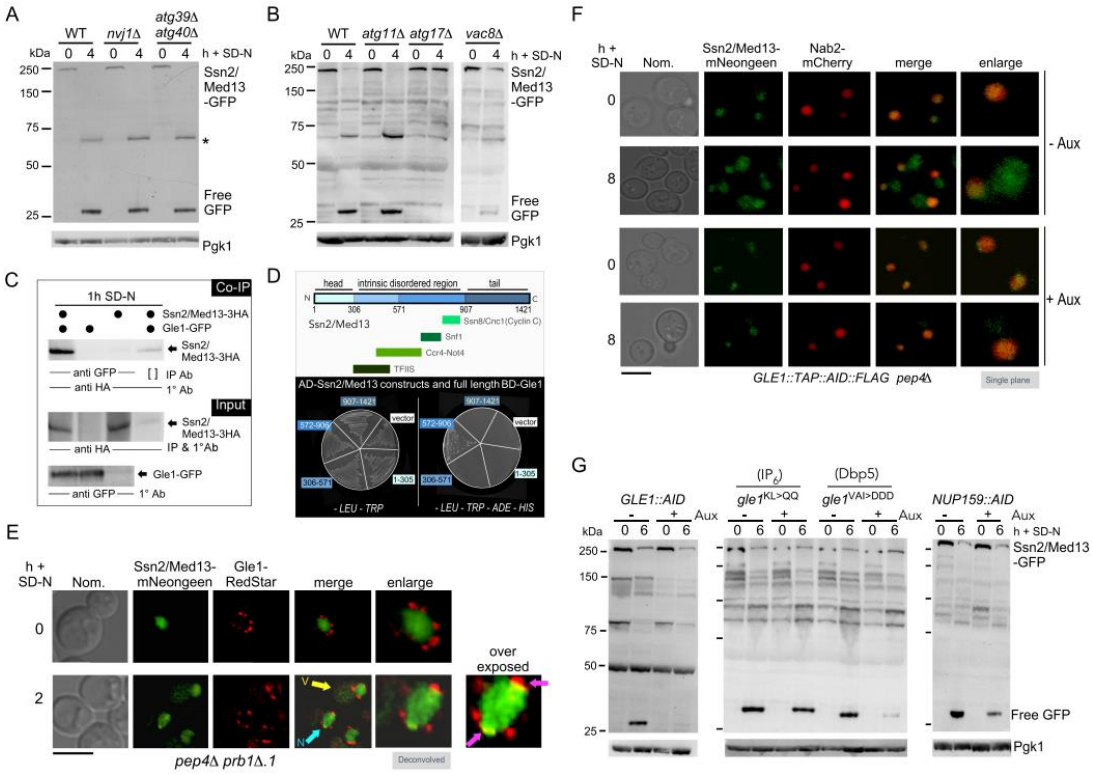

Figure 5. The autophagic degradation of Med13 requires the nucleoporin Gle1 and is independent of known autophagy pathways. **(A and B)** Western blot analysis of Med13-GFP cleavage assays after 4 h nitrogen depletion indicated genotypes. **(C)** Co-immunoprecipitation analysis of endogenous Gle1-GFP and Med13-3 HA. Whole-cell lysates were immunoprecipitated with the antibodies shown from nitrogen-starved *pep4*Δ *prb1*Δ*.1* cells expressing endogenous Gle1-GFP and Med13-3 HA or vector controls. **(D)** Map of Med13 depicting different structural regions and known interacting proteins denoted by amino acid positions. Med13-Gle1 Y2H analysis. **(E)** Fluorescence microscopy of endogenous Med13-mNeongreen and Gle1-RedStar starved for nitrogen for 2 h in *pep4*Δ *prb1*Δ*.1*. **(F)** Fluorescence microscopy of Med13-mNeongreen localization in the Gle1 auxin-inducible degron expressing Nab2-mCherry before and after SD-N. **(G)** Med13-GFP cleavage assays in the auxin-inducible deletion strains indicated. For all blots, Pgk1 levels were used as loading controls.

Gle1, Dbp5, and Nup159 are required for Med13 nuclear export

Gle1 is an essential protein [113], therefore, the auxin-inducible degron (AID) system was used to reduce Gle1 protein levels (Fig. S4C). Deletion of Gle1 does not affect autophagy (monitored using GFP-Atg8 cleavage assays) and Gle1 does not associate with Atg8 using Y2H analysis (Fig. S4D, E, and S5). Significantly, in the auxin-treated GLE1::AID degron, Med13 was retained in the nucleus (Figure 5F) and the autophagic degradation of Med13-GFP was significantly decreased following nitrogen starvation (Figure 5G – left panel).

Gle1, the DEAD-box protein Dbp5, and phosphoinositide inositol hexaphosphate (IP6) are members of the RNA remodeling complex [57–61] [114-118]. By binding to Nup159, this complex is positioned toward the NPC's central channel, permitting it to efficiently capture proteins as they exit the NPC [119]. Mutation of the cis-acting alleles IP6 and Dbp5 on Gle1 [120] revealed that only Dbp5 is required for efficient autophagic cleavage degradation of Med13 (Figure 5G middle panel). Also, autophagic degradation of Med13 was significantly decreased in the NUP159::AID strain (Figure 5G-right panel). As the RNA remodeling complex plays additional Nup159-independent cytoplasmic roles in RNA translation [121,122] [123]. these results support a model in which Nup159-dependent positioning of Gle1 and Dbp5 in the central channel is important for the final stages of Med13 nuclear export. Intriguingly, the known β karyopherins, (Crm1, Msn5, Cse1, and Los1 [124]) are not required for Med13 transport across the NPC (Fig. S4 F-I). Dbp5 has also been found in the nucleus [125], suggesting the possibility that it might play an additional role in

enabling Med13 nuclear export. One caveat to this model is that these factors possess overlapping activities, which has been demonstrated for other cargos [126].

The sorting nexin heterodimer Snx4-Atg20 is required for efficient autophagic degradation of Med13

To further define components of this new autophagy mechanism, null alleles of candidate proteins from the mass spectroscopy were screened using Med13-GFP cleavage assays. In cells deleted for the conserved sorting nexin Snx4 (Atg24), we found that free GFP was significantly reduced (Figure 6A and S1E). Snx4 forms distinct heterodimer complexes, with either Snx41 or Atg20 (Snx42), which mediate retrograde trafficking of cargo from the vacuole and endosomes to the Golgi. This role maintains homeostasis and is dispensable for nonselective autophagy [127][[128-130]. In addition, Snx4-Atg20 promotes selective autophagy of mitochondria and peroxisomes and is required for other selective autophagy pathways, including the cytoplasm to vacuole pathway (CVT), ribophagy, and proteaphagy [74–78][131-135].

Co-immunoprecipitation analysis confirmed the interaction between Med13 and Snx4 in SD-N (Figure 6B). Med13 degradation assays revealed that Snx4 and Atg20, but not Snx41, mediate Med13 autophagic degradation (Figure 6C, D). The half-life of Med13 in these mutants was 6.5 and 7.0 h, respectively, compared to >15 h seen in core autophagic mutants. Cytosolic and vacuolar Med13-mNeongreen levels were drastically reduced in *snx4*Δ *pep4*Δ *prb1*Δ*.1* mutants compared to the *pep4*Δ *prb1*Δ*.1* control (Figure 6E, G). These data demonstrate that the Snx4-Atg20 heterodimer is required for maximal efficient Med13 autophagic degradation, but in its absence, limited autophagic degradation of Med13 still can occur.

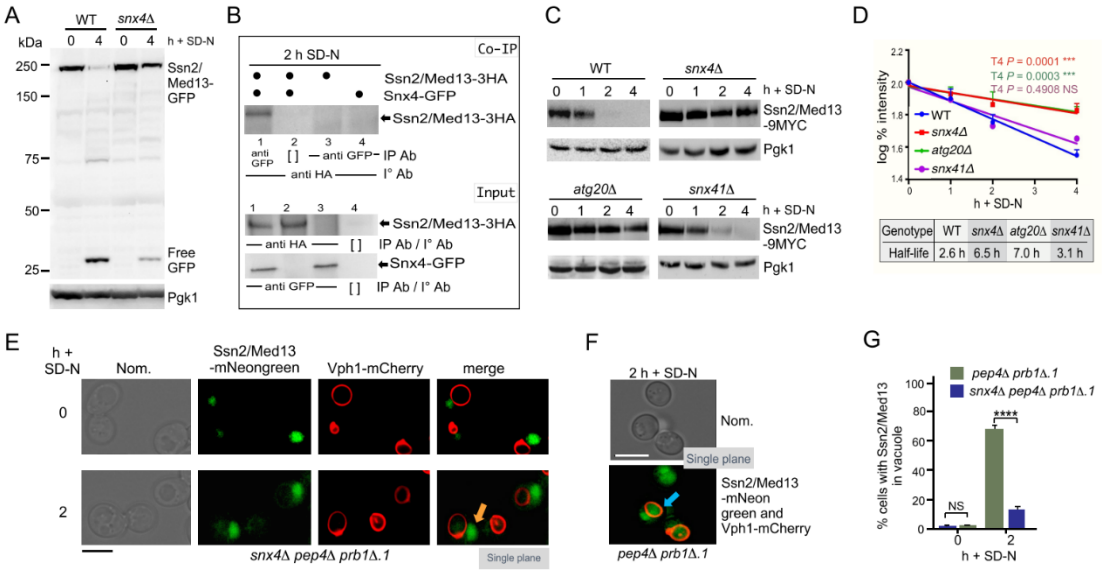

Figure 6. The Snx4-Atg20 heterodimer is required for efficient autophagic degradation of Med13. **(A)** Western blot analysis of Med13-GFP cleavage assays after 4 h nitrogen starvation in wild-type and *snx4*Δ. **(B)** Co-immunoprecipitation analysis of GFP-Snx4 and Med13-3 HA. **(C)** Western blot analysis of extracts prepared from the indicated genotypes expressing endogenous Med13-9MYC resuspended in SD-N for the indicated times. **(D)** Degradation kinetics and half-lives of Med13 protein levels obtained in C. Error bars indicate S.D., N = 3 of biologically independent experiments. **(E)** Fluorescence microscopy of endogenous Med13-mNeongreen localization in *snx4*Δ *pep4*Δ *prb1*Δ*.1* expressing the vacuole marker Vph1-mCherry. Cells were visualized before (SD) and after 2 h of SD-N treatment and representative single-plane images are shown. Scale: 5 µm. **(F)** As in E except that endogenous Med13-mNeongreen localization was followed in nitrogen-starved *pep4*Δ *prb1*Δ*.1* cells. Representative single-plane images of the results are shown. Bar: 5 µm. **(G)** Quantification of Med13-mNeongreen accumulation in vacuoles obtained from results in D and E. 100 cells counted per sample. N = 3 biological samples. **** P = >0.0001. For all blots, Pgk1 levels were used as loading controls.

Snx4 localizes to the nuclear periphery to transport Med13 to autophagosomes

Snx4 binds to the scaffold protein Atg17 [131], whose major autophagic role is binding the Atg1 kinase to the PAS [11]. Here, we report that both Snx4 and Atg17 mediate Med13 degradation (Figure 5 and Figure 6). This suggests a model in which upon nuclear export Snx4 recognizes Med13 and delivers it to the growing phagophore by Snx4-Atg17 association. Consistent with this, Med13-3xHA and endogenous Atg17-GFP coimmunoprecipitated following 2h in SD-N. This interaction was drastically decreased in the absence of Snx4 (Figure 7A). Also, endogenous Atg17-RedStar colocalized with Med13- mNeongreen after nitrogen starvation (Fig. S3F). This suggests that Snx4-Atg17 interaction promotes the efficient recruitment of Med13 to autophagosomes. Quantitative colocalization analysis of GFP-Snx4 with the nuclear marker Nab2-mCherry showed that nitrogen depletion triggers a ~ 10-fold increase in perinuclear GFP-Snx4 foci (Figure 7B, S6A, and B). Moreover, Med13- mNeongreen colocalized with both perinuclear and cytosolic Snx4 foci in SD-N (Figure 7C and S6C). Together, this suggests that Snx4 localizes to the nuclear periphery to retrieve and transport Med13 to phagophores via Atg17 association.

The above model predicts that Snx4 and Gle1 interact whilst “handing off” Med13 from the NPC to the sorting nexin complex. Live-cell imaging showed that perinuclear Snx4 foci are adjacent to, or colocalize with, Gle1 in unstressed cultures. After nitrogen starvation, an increased number of perinuclear Snx4 foci colocalize with Gle1 (Figure 7D and S6D). This is consistent with the model that Snx4 localizes to the NPC to retrieve Med13.

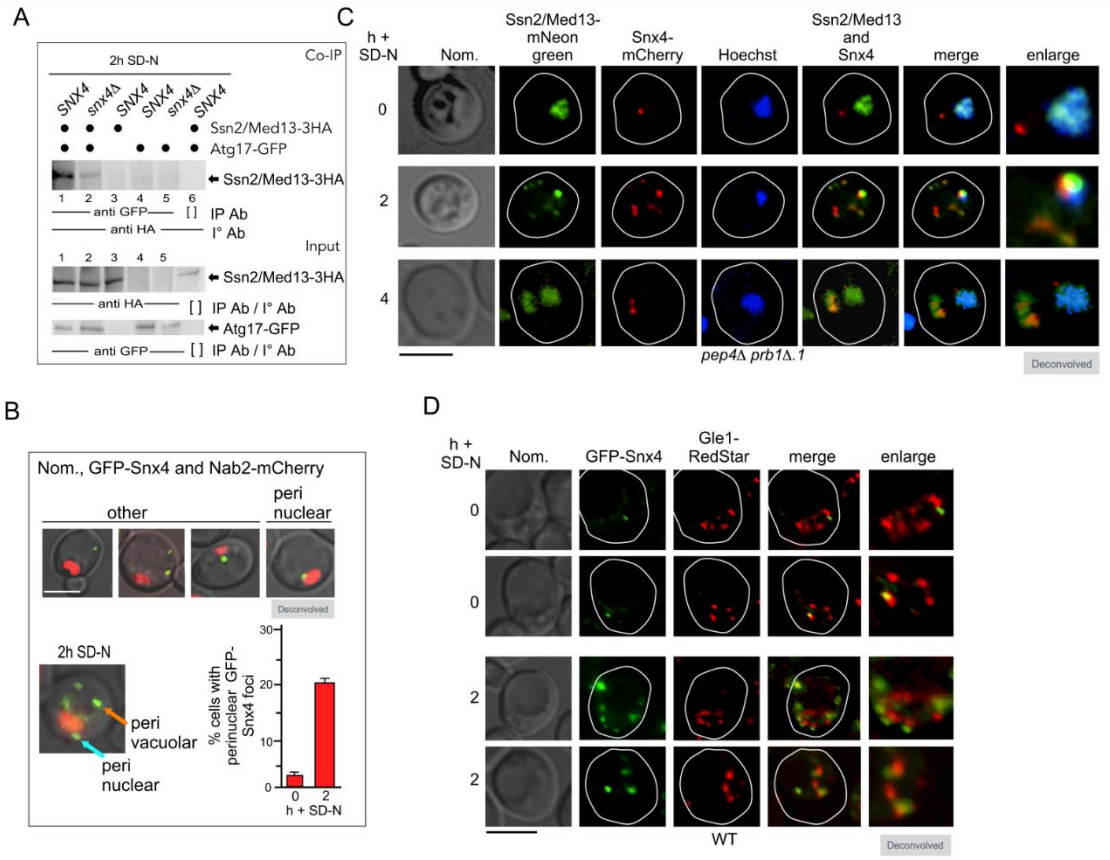

Figure 7. Snx4 localizes to the nuclear periphery to retrieve Med13. **(A)** Co-immunoprecipitation analysis of endogenous Atg17-GFP and Med13-3 HA in the presence and absence of Snx4. **(B)** Representative images showing perinuclear and perivacuolar localization of GFP-Snx4 in wild-type expressing Nab2-mCherry (nuclear marker) before and after nitrogen starvation. Bar: 5 µm. The number of perinuclear foci was counted (N = 2) before and after nitrogen starvation. At least 100 cells were counted per sample. Data are the percentage of perinuclear foci among the total number of foci. Scale: 5 µm. **(C)** Fluorescence microscopy of *pep4*Δ *prb1*Δ*.1* cells expressing endogenous Med13-mNeongreen and mCherry-Snx4 before and after nitrogen depletion. Hoechst staining was used to visualize the nucleus. Representative deconvolved images are shown. Bar: 5 µm. **(D)** GFP-Snx4 and endogenous Gle1-RedStar colocalize in wild-type cells following nitrogen starvation. Representative images are shown. Bar: 5 µm.

Snx4 specifically targets Med13 for autophagic degradation

To further understand the sequential stages of this autophagy pathway, we next asked if Med13 nuclear localization was required for retrieval and transport by Snx4. To address this, we fused Med13-GFP to the N terminus of Crn1, a protein associated with actin rafts, which relocalized Med13 to the plasma membrane [136] (Figure 8A). Autophagic degradation assays with Crn1-Med13-GFP showed that GFP accumulated in wild-type cells, and this was mostly dependent on Snx4 (Figure 8B). This suggests that Med13 can be targeted for Snx4-assisted autophagic destruction even when located outside the nucleus. To confirm specificity, we revealed that free GFP accumulation in Pgk1-GFP cleavage assays, a well-known nonselective autophagic substrate [137], is Snx4 independent (Fig. S7A). This further illustrates that Snx4 is dispensable for nonselective autophagy but mediates many forms of selective autophagy.

We next addressed whether Gle1 and Snx4 remain part of the Med13 complex delivered to the vacuole. Endogenous Snx4-6HA (Figure 8C) and Gle1-FLAG (Figure 8D) were not degraded following nitrogen starvation, suggesting that neither protein is incorporated into autophagosomes or degraded by the vacuole. Importantly, by monitoring the timing of GFP accumulation in Med13-GFP cleavage assays, we observed that the earliest detection of GFP occurred after 2h of nitrogen depletion when both Gle1 and Snx4 are present (Figure 8E). These data support the model that Gle1 and Snx4 mediate Med13 delivery to the autophagosome, but these proteins themselves are not vacuolar substrates.

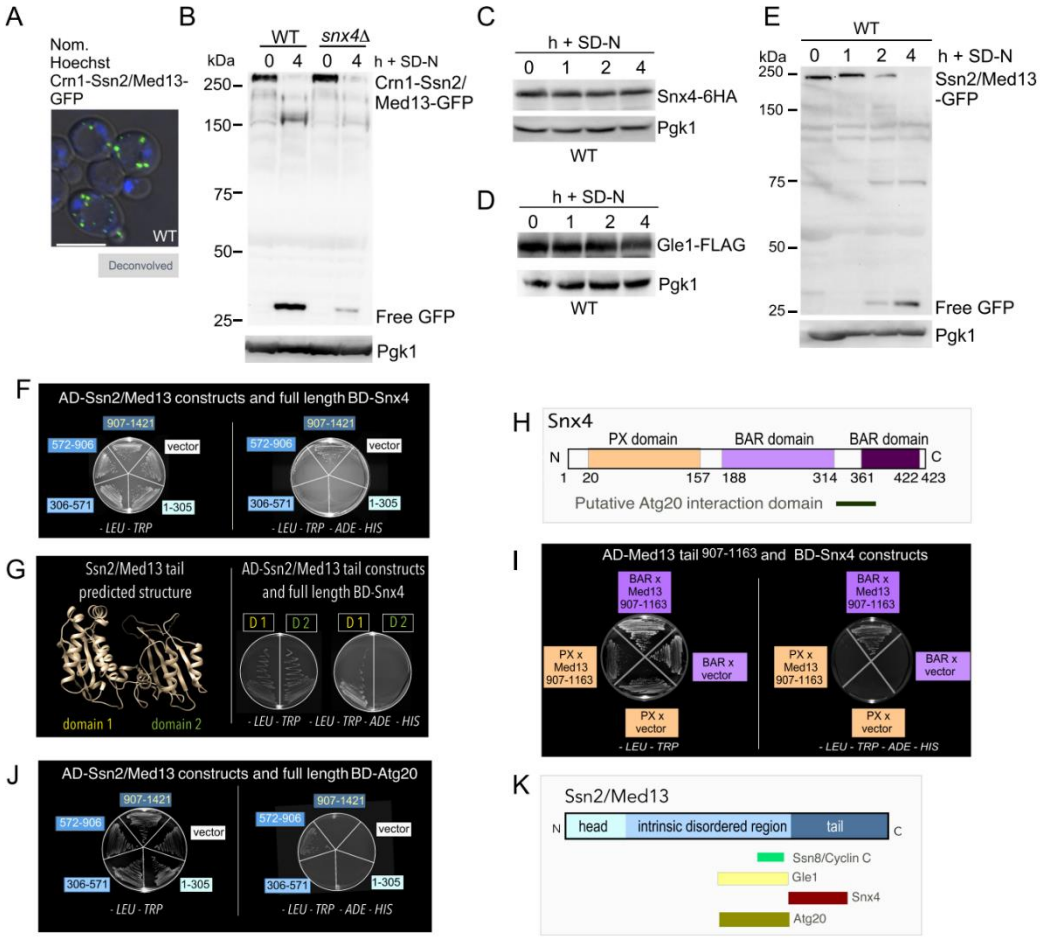

Figure 8. The BAR domain of Snx4 interacts with the C-terminal region of Med13. **(A)** Fluorescence microscopy of Crn1- Med13-GFP in wild-type cells growing in SD. Hoechst staining was used to visualize the nucleus. Bar: 5 µm. **(B)** Western blot analysis of Med13-GFP or Crn1- Med13-GFP cleavage assays performed in wild-type or *snx4*Δ cells following nitrogen starvation. **(C)** Western blot analysis of endogenous Snx4-6 HA degradation assays performed in wild-type cells following nitrogen starvation. **(D)** Western blot analysis of endogenous Gle1-FLAG degradation assays following nitrogen starvation. **(E)** Western blot analysis of Med13-GFP cleavage assays performed in wild-type cells. **(F)** Y2H Gold cells harboring Gal4- BD-Snx4 and the indicated Gal4-AD-Med13 constructs. **(G)** Predicted structural analysis of the Med13 tail region. Y2H analysis of full-length Gal4-BD-Snx4 and Gal4-AD- Med13 subclones containing either the first or second domain region of the Med13 tail. **(H)** Map of Snx4 depicting known domains. **(I)** Y2H analysis of Snx4 PX and BAR binding domain constructs with the Med13$^{907-1163}$AD construct and empty vector. **(J)** Same as in F expect Y2H Gold cells harboring Gal4-BD-Atg20 and the indicated Gal4-AD- Med13 constructs. **(K)** Map of Med13 structure depicting interactive regions between indicated proteins. For all blots, Pgk1 levels were used as loading controls.

Snx4 BAR domains interact with the C-terminal domain of Med13

To further understand the interaction between Gle1, Snx4, and Med13, we used Y2H analysis to ask if Snx4 and Gle1 associate with the same or different domains of Med13. The results show that Snx4 interacts with the structured C-terminal tail domain of Med13 (Figure 8F and S5). Phyre2 plot analysis of this region [138] revealed two potential domains of which only one, Med13[907–1163] interacted with Snx4 (Figure 8G). Therefore, Snx4 interacts with a previously undescribed region of Med13 that lies adjacent to the Gle1 interaction domain. Moreover, as Snx4 is not a nuclear protein, this interaction may be direct and define a new role for Snx4 in transporting nuclear proteins.

Snx4 is a conserved member of the SNX-BAR subfamily of sorting nexin proteins [30]. Common to all SNX family members it contains a phosphoinositide-binding phox homology (PX) domain, which binds phosphatidylinositol 3-phosphate enriched endosomal membranes. It also contains two BAR (Bin/|Amphiphysin/Rvs) domains that bind to curved membranes upon dimerization [135,139] (Figure 8H). Y2H interaction analyses between these Snx4 domains and Med13[907–1163] indicated that the Med13-Snx4 interaction occurs through the BAR domain region (Figure 8I). These results indicate that the Snx4 BAR domains recognize cargo and dimerization partners.

Atg20 interacts with a different region of Med13

We also used Y2H analysis to ask if Med13 interacts with Atg20, the heterodimer partner of Snx4 that is required for the efficient degradation of Med13 (Figure 6C, D). The results show that Atg20 also interacts with a different region of Med13, overlapping with the region that binds to Gle1, lying adjacent to the Snx4 binding

region (Figure 8J, Figure 8K, and S5D). Taken together, these data support our model that Med13 first exits the nucleus via Gle1 and then is released from NPC to the Snx4-Atg20 heterodimer for rapid delivery to the autophagic machinery. These Y2H results demonstrate a sequential hand-off mechanism from Gle1 to the Snx4-Atg20 heterodimer as Gle1 and Atg20 bind to the same region of Med13.

Med13 negatively regulates the transcription of a subset of *ATG* genes

We next explored if this newly described autophagy pathway affects viability during nitrogen starvation. Consistent with previous studies [140], efficient survival in prolonged nitrogen starvation conditions requires Snx4 (Fig. S7B). Snx4 is dispensable for nonselective autophagy but is required for many selective autophagy pathways [128]. This suggests that the role of Snx4 is essential for cellular adaptation and survival in prolonged starvation conditions. Survival during periods of nutrient depletion requires the upregulation of *ATG* genes. As Med13 destruction following H_2O_2 relieves repression on stress-responsive genes [53], we asked if a similar strategy was used following nitrogen starvation. RT-qPCR analysis of *ATG* mRNA levels in unstressed wild-type and *med13*Δ cells showed a ~ fourfold increase in *ATG8* mRNA levels (Figure 9A) that was mirrored by Atg8 protein levels (Fig. S7C). Furthermore, *ATG1* and *ATG14* mRNA levels were also elevated (Figure 9A), indicating Med13 represses the transcription of a subset of *ATG* genes. Moreover, these results are consistent with the model that the destruction of two CKM members following nitrogen starvation, Cnc1 by the UPS [38] (see Figure 1), and Med13 by autophagy are mechanisms used to relieve this repression. Snx4 assists in this autophagy program by targeting a

transcriptional repressor that provides a positive feedback loop for the autophagic response.

Snx4-assisted autophagy degrades other transcriptional regulators following nitrogen starvation

Next, we wanted to explore the idea that Snx4-assisted autophagy is a mechanism used by the cell to fine-tune the autophagic response at the level of transcription. We first examined the transcriptional activator Rim15 which also regulates *ATG* genes. During nitrogen starvation, Rim15 enters the nucleus to directly phosphorylate and inhibit the activity of the transcriptional repressors Ume6 [141] and Rph1 [142]. Surprisingly, Rim15-GFP cleavage assays revealed Rim15 is degraded via Snx4-assisted vacuolar degradation (Figure 9B).

To address if Snx4-assisted autophagy may have a more global role in degrading transcription factors that control *ATG* expression, the transcriptional activators Msn2 and Ccl1, as well as the repressor Rph1 were tested [86–88] [142-144]. Free GFP accumulated from Msn2-GFP and Rph1-GFP in wild-type cells following nitrogen starvation, illustrating that these transcription factors are degraded via the vacuole. However, only Msn2 degradation requires Snx4 (Figure 8C and S7D). These results support the conclusion that Snx4-assisted autophagy of transcriptional regulators targets a unique subset of nuclear proteins. These findings also provide the first evidence that the autophagic pathway directly targets regulatory proteins that control its own processes.

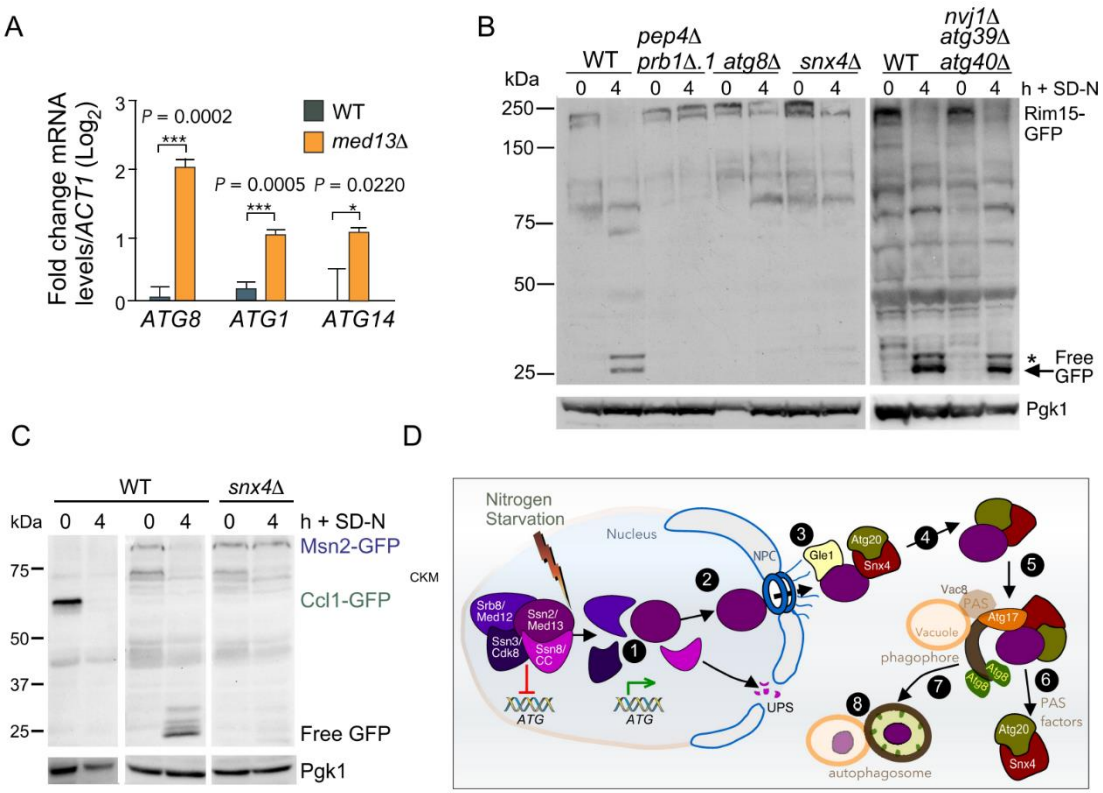

Figure 9. Transcriptional regulators controlling ATG genes are autophagy substrates. **(A)** RT-qPCR analysis of *ATG8*, *ATG1*, and *ATG14* mRNA expression in wild-type and med13Δ cells in unstressed conditions. ΔΔCt results for relative fold change (log2) values using wild-type unstressed cells as a control. Transcript levels are given relative to the internal ACT1 mRNA control. **(B)** Western blot analysis of Rim15-GFP cleavage assays in indicated mutants after nitrogen starvation. **(C)** Western blot analysis of Ccl1-GFP and Msn2-GFP cleavage assays in wild-type or snx4Δ cells. For all blots, Pgk1 levels were used as loading controls. **(D)** Summary model of the Snx4-assisted autophagy pathway.

Discussion

Here, by following Med13's fate after nitrogen starvation, we have uncovered a previously undescribed autophagy pathway in which both negative and positive transcriptional regulators of *ATG* genes are degraded following nitrogen starvation. For clarity, a list of the proteins tested, and their requirements are provided in Table 1. Our findings, together with previous studies, suggest a two-step pathway involving the NPC and Snx4 for Med13 translocation from the nucleus to the autophagic machinery (outlined in Figure 9D). First, Med13 disassociates from the CKM, shuttles through the NPC, and associates with the cytoplasmic nucleoporin Gle1. In the second step, Med13 is handed off from Gle1 to the sorting nexin heterodimer Snx4-Atg20. This heterodimer transports Med13 to Atg17-initiated phagophores located on the vacuole, by localizing to Atg17. Lastly, Snx4-Atg20 is recycled back to the cytosol, and Med13 is degraded by vacuolar proteolysis. This pathway is also utilized to degrade Rim15 and Msn2, but not Rph1 following nitrogen starvation suggesting that the cell degrades specific transcription factors following nitrogen starvation.

Snx4-assisted vacuolar degradation of transcriptional regulators is distinct from previously identified selective autophagy mechanisms for several reasons. Firstly, different from nucleophagy pathways, it does not use a blebbing mechanism to export cargo [145]. Instead, cargos are rapidly transported through the NPC to the awaiting RNA remodeling complex, with Snx4-Atg20 enabling their final passage to the vacuole. Secondly, to our knowledge, Snx4-assisted autophagy of transcriptional regulators is not used to maintain homeostasis. Instead, it rapidly responds to environmental cues such as nitrogen starvation and targets functional proteins for

autophagic degradation. Also, other selective autophagy pathways that utilize Snx4 heterodimers [131,140,146-148] predominantly operate to maintain homeostasis, by removing damaged and surplus proteins and organelles. Proteaphagy, the autophagic removal of nuclear 19S and 20S subunits, most resembles the Snx4-assisted degradation of transcription factors [140]. However, there are significant differences between the pathways, with proteaphagy being dependent upon the ß-karyopherin Crm1 for passage through the NPC and utilizing either Snx4-Atg41 or Atg20 for transport to autophagosomes [140]. Similarities include both pathways utilizing the Atg17-scaffold complex. The exception to this is the degradation of Rpn1 (19S proteasome subunit) and RNA that utilizes both scaffolds [149-151]. The requirement for Atg17 to degrade Med13 following nitrogen starvation also is consistent with the recent discovery that Atg11 is rapidly degraded by the UPS in nitrogen starvation [79]. Lastly, although nonselective autophagy of cytosolic proteins is upregulated upon nitrogen starvation, we did not observe a requirement for Snx4, in this mechanism (see Fig. S7A). However, Snx4 does recognize plasma membrane-tethered Med13 (Figure 8B), further illustrating the specificity of this pathway. Thus, to delineate this new pathway from other Snx4 pathways, we propose to call it Snx4-assisted autophagy of transcription factors.

How does Med13 find its way to the phagophore? Med13 is a large, 160-kDa protein that requires an active process to transit from the nucleus to the cytoplasm. Its unusual structure, (see Figure 5D and discussed in [54]) suggests it functions both as a scaffold protein and a communication/interaction hub [54,152]. Consistent with this, the IDR of Med13 interacts with Gle1, Atg20, Cnc1, and Cdk8 and is the target of

additional regulatory protein kinases including Slt2 and Snf1 [[54],[55]]. The established role of the Gle1-Dbp5 complex in releasing RNPs (ribonucleoproteins) from mRNPs (messenger ribonucleoprotein particles) [153] sets a precedent for Gle1 shuttling proteins through the NPC. Moreover, recent structural data places the Gle1-Dbp5 remodeling complex right over the NPC's central channel, allowing it to efficiently capture proteins as they reach the cytoplasmic side of the NPC [119]. Although speculative, a similar capture and release mechanism may be used in the Med13 transition between Gle1 to Snx4. In support of this model, both Gle1 and Dbp5 are required for the autophagic degradation of Med13, and Gle1 and Snx4 colocalize at the NPC (Figure 6D). Furthermore, Nup159, the nucleoporin that tethers Gle1 and Dbp5 to the NPC is also required for Med13 degradation (Figure 5). Recently, Nup159 has been suggested to act as a receptor protein for NPC-phagy [17,99,100] [84,154,155]. This is an Atg11-dependent process and therefore unlikely to regulate Med13 autophagic degradation. Furthermore, mass spectrometry analysis of the Atg8 interactome did not identify Gle1 as an interacting nucleoporin [68] and we show here that Gle1 does not interact with Atg8 by Y2H analysis (Fig. S4E). Lastly, the vacuolar degradation kinetics of Nup159 is significantly delayed (24 h), compared to the rapid degradation of Med13-GFP where free GFP can be seen within 2h (Figure 8E). Taken together, the role of Nup159 in Med13 autophagic degradation is most likely to be connected to its requirement for tethering the remodeling complex to the NPC.

The best-characterized cargo of Snx4-Atg20 is Snc1, a plasma membrane-directed v-SNARE [70,101][[127,156]. Similar to our results with Med13, Snc1 associates with the BAR domain of Snx4 using both co-immunoprecipitation analyses

as well as Y2H assays [157]. Likewise, SNX-BARs also directly recognize many retrograde cargos transiting the endosome in mammals [103,104] [158],[159] suggesting that this may be a common function of BAR domains. The mechanism by which Snx4 delivers Med13 to phagophores currently remains unknown. In selective autophagy, receptor proteins bind to the cargo as well as with Atg8. This is important as the phagophore in this case has to be anchored to the cargo [11]. In Snx4-assisted autophagy, the phagophores are anchored to the vacuole and Snx4 transports the cargo to the phagophore which may negate the need for a "conventional" receptor protein. Supporting this, Snx4 colocalizes with Med13 at both perinuclear and cytoplasmic locations. Our finding that efficient Med13 and Atg17 co-immunoprecipitation requires Snx4 suggests that this sorting nexin relays Med13 from the NPC to the autophagic machinery. In addition, Snx4 mediates Med13 vacuolar degradation when this nuclear protein is relocalized to the plasma membrane, illustrating that Snx4 specifically targets and transports Med13 to growing autophagosomes. Defining the Snx4 interaction motif on Med13, as well as Msn2 and Rim15, may result in a common "Snx4 recognition motif" that could be used to identify additional transcriptional regulators that are degraded by this mechanism. This would be useful because, despite the recent discovery of additional Snx4 cargos [156], no consensus Snx4-dependent sorting signal has been identified [130]. This is important as Snx4 is evolutionarily conserved [160], with recent discoveries that Snx4 dysregulation is now associated with the etiology of many diseases, including, cancer, Parkinson's disease, and Alzheimer's disease [161].

The most unexpected finding from this research was that the complex process of autophagy is used to degrade transcriptional regulators. More unexpectedly, was that

two transcriptional activators of *ATG* genes are also regulated by this pathway. The molecular details of how these transcriptional regulators are initially targeted and then transported through the NPC are unknown. These details will define the nuclear components required for this pathway. This work also provides developing information on how autophagy is regulated at the level of transcription. The process is selective as Rph1, which is also degraded by vacuolar proteolysis following nitrogen starvation, but does not require autophagic machinery (Fig. S7D). Likewise, the zinc-deficiency triggered vacuolar degradation of RNA polymerase I is autophagy-independent [162]. Taken together, Snx4-assisted autophagy may shed light on how other nuclear proteins are regulated following stress. This is important as nucleophagy is the least well-defined of all the autophagy pathways and in recent years links between deficiencies and human disease are starting to emerge [145]. For example, a mutation in human Gle1 has recently been linked to amyotrophic lateral sclerosis [163]. Given the highly conserved nature of both Med13 and Snx4 [160],[164] these studies are likely to be relevant to mammalian systems.

CHAPTER 3

Ksp1 is an autophagic receptor protein for Snx4-assisted autophagy of Med13

This chapter is based on a research paper in revision for publication in the journal *Autophagy*.

Abstract

Ksp1 is a casein II-like kinase that contributes to negatively regulating non-specific autophagy in yeast. Here we describe a kinase-independent role of Ksp1 as a novel autophagic receptor protein for Med13, a known cargo of Snx4-assisted autophagy. In this pathway, a subset of conserved transcriptional regulators, Med13, Rim15, and Msn2 are selectively targeted for vacuolar proteolysis, assisted by the sorting nexin heterodimer Snx4-Atg20 following nitrogen starvation. Here we show that characteristic of autophagic receptor proteins, Ksp1 is engulfed by autophagosomes alongside its cargo for vacuolar proteolysis. It is also directly associated with Atg8 following nitrogen starvation at the interface of two Atg8 (LC3)-interacting motifs (AIM/LIR) in Ksp1 and the LIR docking site (LDS) in Atg8. Mutation of either the AIMs or LDS sites prevents the autophagic degradation of Med13. Ksp1 is recruited to the perivacuolar phagophore assembly site (PAS) by Atg29, a member of the trimeric scaffold complex. This interaction is independent of Atg8 and Snx4, suggesting that Ksp1 is recruited early to phagophores with Snx4 delivering Med13 thereafter. Lastly, the autophagic receptor role of Ksp1 is not required for the execution of non-selective autophagy, however, the degradation of Ksp1 cargos may promote cell survival. Together, these studies define a kinase-independent role for Ksp1 as an autophagic

receptor protein for Med13. Moreover, they also suggest that phagophores built by the trimeric scaffold complex are capable of receptor-mediated autophagy.

Introduction

It is well established that maintaining protein homeostasis is essential in preserving normal cellular function. Macro-autophagy (hereafter autophagy) is a highly conserved catabolic process that promotes homeostasis [165,166]. As such, autophagy is protective against a wide variety of diseases including neurodegeneration, cancer, infections, and cardiovascular disorders [167-169].

Autophagy recycles intracellular material sequestered by the double membrane of autophagosomes. The cargo is delivered to vacuoles (in yeast and plants) or lysosomes (in metazoans) by fusion of the outer autophagosomal membrane with vacuoles. Thereafter the inner structure, an autophagic body, is released into the vacuolar lumen and degraded by resident hydrolases [170,171]. Depending on the cargo, cytoplasmic material is recycled by either bulk (non-selective) or selective autophagy pathways. Non-selective autophagy is characterized by portions of the cytoplasm being captured indiscriminately by growing phagophores located at perivacuolar sites. The phagophore assembly site (PAS) for these *de novo* autophagosomes is built on the outer vacuolar membrane and is seeded by the constitutive Atg17 scaffold complex (Atg29, Atg31, and Atg17) [11]. Non-selective autophagy is triggered by starvation-induced inactivation of the TORC1 pathway [172], leading to the upregulation of genes required to execute the autophagy signaling cascade. In *S. cerevisiae*, the model organism used in this current study, many of the autophagy-related genes (*ATG*) identified to date are highly conserved [166,173].

By contrast, selective autophagy is active in both physiological and stress conditions being required for maintaining the number and integrity of cellular organelles, as well as protecting cells from pathogen invasions [101,166,174]. Two unifying concepts define selective autophagy. First, a receptor protein is required that links cargo to the autophagy machinery, through interaction with Atg8 (Atg8 in plants and yeast, LC3/GABARAP in mammals) [71,103,166,175,176]. Second, autophagosomal membrane expansion occurs along the surface of degradation targets mediated by receptor proteins binding to the Atg11 scaffold [102,177]. In yeast, an exception to this is the Cue5 receptor that targets aggregated proteins and dysfunctional proteasomes [178,179].

Our recently published studies in the model organism *S. cerevisiae* have defined a new autophagy mechanism [3], coined Snx4-assisted autophagy of transcription factors (SAA-TF). SAA-TF targets transcriptional regulators that both positively (Msn2 and Rim15) and negatively (Med13) regulate *ATG* transcription. Med13 is a conserved member of the Cdk8 kinase module (CKM) that in yeast predominantly negatively regulates the transcription of stress response genes including *ATG8* [3,39,180]. Following nitrogen starvation, the removal of the CKM from the Mediator contributes to *ATG8* upregulation. This is mediated by the vacuolar degradation of Med13 [3] alongside the UPS-mediated destruction of Ssn8/cyclin C [3,48,180].

The autophagic degradation of Med13 (outlined in Figure 1A) utilizes the core autophagic machinery but is independent of known nucleophagy mechanisms, known receptor proteins, and Atg11. In short, following nitrogen starvation, Med13 exits the nucleus through the nuclear pore complex (NPC) mediated by the cytoplasmic

nucleoporin Gle1, a member of the RNA remodeling complex [114]. Med13 is retrieved from the nuclear periphery and degraded by Atg17-initiated phagophores anchored at the vacuole. Efficient transfer of Med13 to phagophores requires the sorting nexin heterodimer Snx4/Atg24-Atg20, which binds Atg17 [3,30,131].

To meet the criteria of selective autophagy, SAA-TF requires an autophagy receptor protein that exclusively tethers Med13 to the autophagic machinery through interactions with Atg8. Previously, using a yeast two hybrid (Y2H) screen, Ksp1 was identified as one of 34 new putative autophagic receptor proteins in the budding yeast [103]. We also identified Ksp1 as a protein that interacts with Med13 after nitrogen starvation using mass spectroscopy studies [3]. Taken together, this suggests that Ksp1 could be an autophagic receptor for SAA of Med13. Ksp1 is a serine/threonine-protein kinase in the casein kinase II subfamily. This kinase was first identified as a high copy suppressor of a temperature-sensitive allele of Srm1/Prp20, a nucleotide exchange factor for Ran/GSP1 proteins [181]. Transcriptional profiling identified that Ksp1 signaling affects a wide variety of genes including those required for pseudohyphal filamentation, amino acid biosynthesis, and metabolism [182-184]. How Ksp1 exerts this control remains unclear but proteomic studies identified Ksp1 to be a component of cytoplasmic stress granules in response to glucose starvation [185,186]. Other studies suggest that Ksp1 functions as a negative regulator of autophagy in physiological conditions. In these studies, the authors conclude that PKA-mediated phosphorylation of Ksp1 in replete media activates this kinase, which contributes to autophagy inhibition by activating the TORC1 pathway [187-191]. In support of this

mechanism *in vitro* studies have shown that PKA directly phosphorylates Ksp1 [192,193]. In contrast, other studies postulate that dephosphorylation of Ksp1 at the same PKA sites hyper-activates Ksp1 in response to glucose starvation, which permits it to directly phosphorylate the translation initiation factor eIF4G1 (encoded by *TIF4631*) [194]. These studies serve to demonstrate that Ksp1 has multifaceted regulatory roles that may vary depending on the stress. Here we define a kinase-independent role of Ksp1, demonstrating that it serves as a receptor protein for the Snx4-assisted autophagy of Med13.

Results

Ksp1 and Med13 interact following nitrogen starvation.

To further define components of the SAA pathway we used a mass spectroscopy screen to identify proteins that interact with Med13-HA following nitrogen starvation (SD-N) [3]. In this screen, we identified Ksp1 as a potential interactor. Co-immunoprecipitation analysis between Med13-HA and endogenous Ksp1-MYC both before (lane 2) and following 1 h (lane 1) in SD-N confirmed that the interaction between these two proteins is significantly enhanced following nitrogen starvation (Figure 1B). We next asked if Med13 and Ksp1 interacted using yeast 2 hybrid (Y2H) analysis. As described previously, full-length Med13 fused to the Gal4-activating domain represses transcription [3]. Therefore for all Y2H assays, we used a set of Med13 constructs that span the length of the protein (Figure 1C, left-hand panel [54]). Y2H analysis showed that the structured tail domain of Med13 interacts with Ksp1 (Figure 1C right-hand panel). Taken together these results suggest that Ksp1 and Med13 can interact following nitrogen starvation.

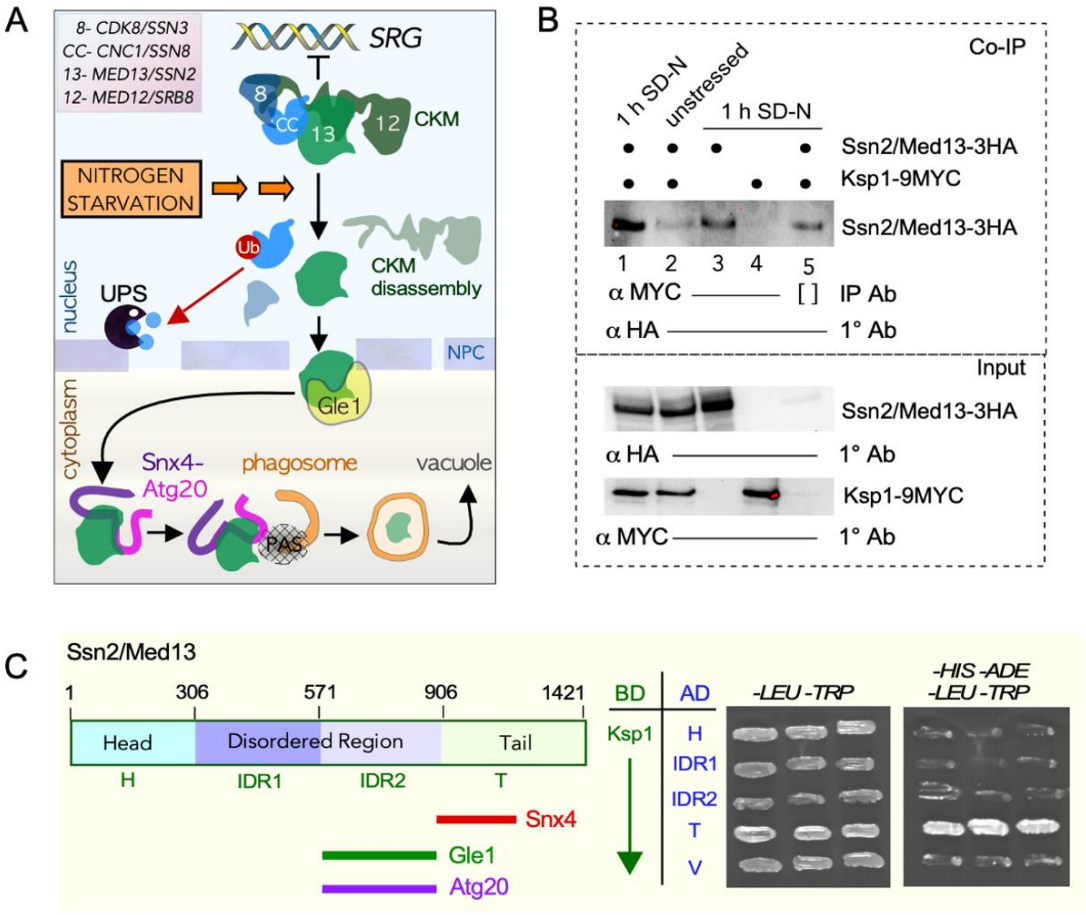

Figure 1. Ksp1 interacts with Ssn2Med13. **(A)** Schematic of Snx4-assisted autophagy (SAA) of Ssn2Med13 following nitrogen starvation. [3]. **(B)** Co-immunoprecipitation analysis of Ssn2Med13-HA and Ksp1-9MYC before and after nitrogen starvation. Cells harboring Ssn2Med13-3HA and Ksp1-MYC (lanes 1, 2, & 5) or respective vector controls (lanes 3 & 34) were immunoprecipitated from whole cell lysates obtained from *pep4*Δ *prb1*-Δ*.1* cells before and following 1 hour of nitrogen starvation. [] represents a no antibody control (lane 4). For input controls, Ssn2Med13 and Ksp1 were immunoprecipitated from lysates using the indicated antibodies. **(C)** Y2H analysis of Ssn2Med13 and Ksp1. The left panel depicts the known structural regions of Ssn2Med13 and previously identified interactors [3]. Y2H Gold cells expressing Gal4-BD-Ksp1 and the indicated Gal4-AD-Med13 subclones were plated onto medium selecting for plasmid maintenance (left panel, *-LEU -TRP*) or induction of the *ADE2* and *HIS3* reporter genes (right panel).

Med13 moves from being nuclear to associating with cytosolic components of the autophagic machinery before being destroyed in the vacuole [3].To determine where Ksp1 and Med13 interact following nitrogen starvation we used live cell imaging. First, we monitored endogenous Ksp1-GFP in cells harboring Nup-49-mCherry to mark the nucleus. As previously reported [194], in SD media, Ksp1-GFP was predominantly located in the cytoplasm although some nuclear staining is also observed upon quantification (Figure S1, upper panels). Unlike during filamentous growth [193], Ksp1 does not accumulate in the nucleus in SD-N (Figure S1, lower panels). Next, using endogenous Ksp1-mCherry and Med13-mNeongreen (hereafter Med13-mNeon) we asked if Med13 co-localizes with Ksp1 as it transitions from the nucleus to the vacuole. These studies were executed in *pep4*Δ *prb1*Δ*.1*, *a* vacuolar protease mutant, in which autophagic bodies, are kept largely intact and accumulate in the vacuolar lumen [70,93]. As previously reported, Med13-mNeon was nuclear in unstressed cells [3] and Ksp1-mCherry was predominantly cytoplasmic [194]. Following nitrogen starvation, cytoplasmic Ksp1 foci appeared which could also be captured co-localizing with cytoplasmic Med13 as it transitions from the nucleus to the vacuole (Figure 2A). These results are in agreement with the co-IP studies, showing that the interaction between Ksp1 and Med13 occurs following starvation.

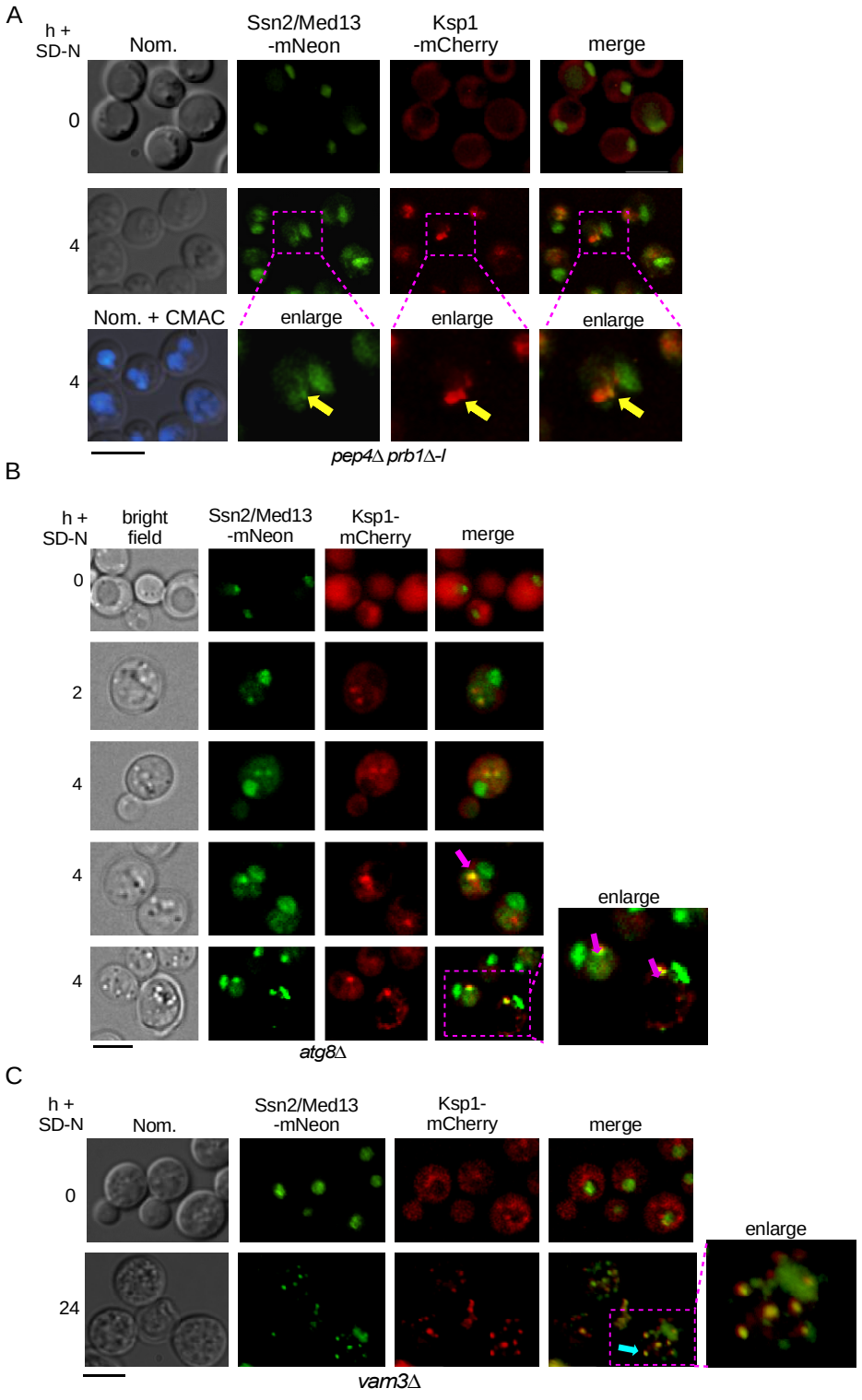
A
h +
SD-N
Nom.
Ssn2/Med13
-mNeon
Ksp1
-mCherry
merge
0
4
Nom. + CMAC
enlarge
enlarge
enlarge
4
pep4Δ prb1Δ-I
B
h +
SD-N
bright
field
Ssn2/Med13
-mNeon
Ksp1-
mCherry
merge
0
2
4
4
enlarge
4
atg8Δ
C
h +
SD-N
Nom.
Ssn2/Med13
-mNeon
Ksp1-
mCherry
merge
0
enlarge
24
vam3Δ

Figure 2. Ssn2Med13 co-localizes with Ksp1 in the cytosol following nitrogen starvation. **(A)** Fluorescence microscopy of endogenous Ssn2Med13-mNeongreen and Ksp1-mCherry in *pep4*Δ *prb1*Δ*-1* before and following nitrogen starvation. CMAC was used to visualize the vacuoles. Yellow arrows denote co-localization of Ssn2Med13 and Ksp1 puncta. **(B)** Same as in A except *atg8*Δ cells were analyzed. Pink arrows denote co-localization. **(C)** Same as in A except that *vam3*Δ cells were analyzed before and after 24 h in SD-N. Blue arrow denotes co-localization. Scale bar: 5μm.

In our previous studies, we observed Med13 accumulate outside of the vacuole in mutants defective in autophagic cargo delivery [3]. Specifically, in *atg8*Δ cells which are defective in phagophore expansion [195], we observed Med13 co-localizing with Atg2 and Atg7, two components of the phagophore [196,197]. In *vam3*Δ, a fusion deficient t-SNARE mutant, [96,97,198] Med13 colocalizes with Atg8 which conjugates to inner autophagosome membranes [98]. Similar to these studies, using live cell imaging, we also captured endogenous Ksp1-mCherry co-localizing with Med13-mNeon in both *atg8*Δ and *vam3*Δ cells (Figure 2B and C respectively) only following nitrogen starvation. Together this suggests that Med13 interacts with Ksp1 at the PAS before being delivered to vacuoles for proteolysis.

Ksp1 is required for the autophagic degradation of Med13

Med13 is actively degraded following TORC1 inhibition by vacuolar proteolysis [3]. We, therefore, asked if Ksp1 is required for the autophagic degradation of Med13. Quantitative western blot analysis of endogenous Med13-MYC revealed that Ksp1 is required for its autophagic degradation (Figures 3A, B, and S3A). The half-life of Med13 was >15 h in *ksp1*Δ compared to the 2.5 h half-life observed in wild-type cells.

These results show that Ksp1 is required for the autophagic degradation of Med13 following nitrogen depletion. Next, as Ssn8/cyclin C is also degraded in SD-N, albeit by the UPS [180], we asked if Ksp1 is required for its degradation. Quantitative western blot analysis of Ssn8/cyclin C-MYC revealed no differences in decay between WT and *ksp1*Δ (Figure S2A and S2B). This indicates that Ksp1 is only required for the degradation of autophagic substrates.

Ksp1 kinase activity is not required for the autophagic degradation of Med13

Ksp1 is a serine-threonine kinase that is activated by protein kinase A (PKA) in replete media at five consensus PKA sites (RRxS/T) [189-193]. Current models propose that this activation is required for Ksp1 to help suppress autophagy via the TORC1 pathway [188]. By using quantitative western blot analysis, we asked if Ksp1 kinase activity was required for the autophagic degradation of Med13. The results revealed no differences in the decay rate of Med13 following nitrogen starvation in *ksp1*Δ cells harboring either wild-type Ksp1 or a kinase-dead mutant ($ksp1^{K47D}$) (Figures 3C and D respectively) [181]. Taken together, this suggests that Ksp1 kinase activity is not required for its autophagic receptor function. These results also indicate that Ksp1 has dual roles in autophagy. The first is kinase-dependent and helps to suppress autophagy induction in replete media [188]. The second, is kinase-independent, being required for the autophagic degradation of Med13 and maybe other unknown substrates.

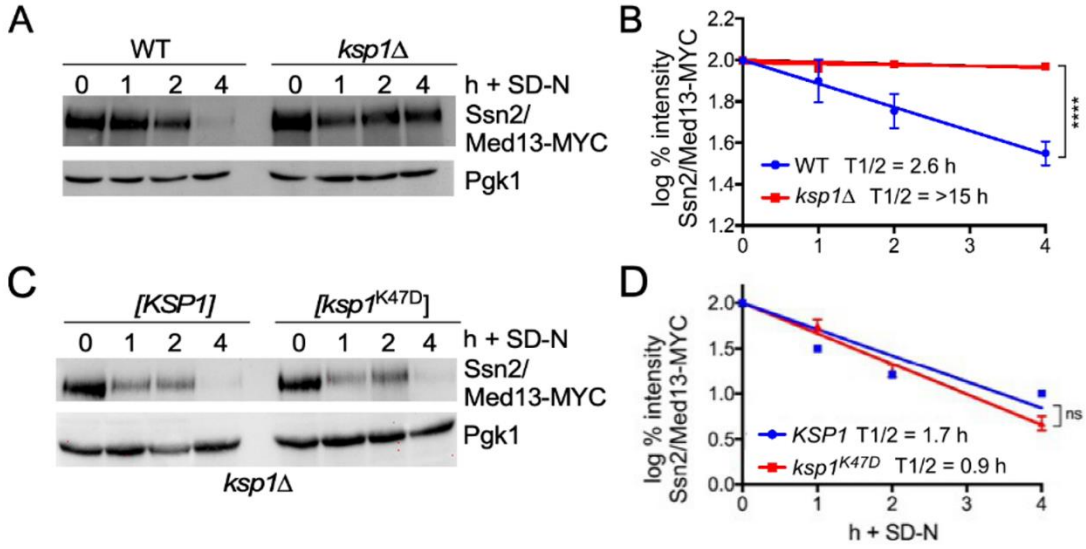

Figure 3. Ksp1 is required for the autophagic degradation of Ssn2Med13. **(A)** Western blot analysis of extracts prepared from wild-type or *ksp1*Δ expressing endogenous Ssn2Med13-9MYC resuspended nitrogen starvation medium (SD-N) for the indicated times. **(B)** Quantification of degradation kinetics and half-life of Ssn2Med13-MYC levels obtained in A. **(C)** As in A except that Ssn2Med13 in *ksp1*Δ harboring either Ksp1-GFP or a kinase-dead allele (K47D) was examined. **(D)** Degradation kinetics and half-life of Ssn2Med13-9MYC protein levels obtained from C. Pgk1 levels were used as loading controls.

Ksp1 and Atg8 co-localize following nitrogen starvation.

We next focused on determining the role of Ksp1 in cargo degradation following nitrogen starvation. Ksp1 was previously identified in a Y2H screen as one of 38 new proteins that interact directly with Atg8 [103]. In this study, the authors propose that these Atg8 interactors represent novel autophagic receptors. As Ksp1 is required for the delivery of Med13 to the vacuole, we hypothesized that Ksp1 could be a cargo receptor protein for this pathway. To test this, we asked if Ksp1 and Atg8 interact using fluorescence microscopy. In log-phase cells, growing SD media, very few GFP-Atg8 foci were observed and Ksp1-mCherry was predominantly cytoplasmic (Fig. S2C). Following 2 h in SD-N, most cells contained GFP-Atg8 foci that were observed co-

localizing with Ksp1-mCherry (Figure 4A). Also, we captured this interaction only following nitrogen starvation in *vam3*Δ where Atg8 foci accumulate in mature autophagosomes (Figure 4B and S2C) [199]. Together these results indicate that Ksp1 and Atg8 can co-localize at the PAS, indicating that Ksp1 could be the autophagic receptor for Med13.

We next used Y2H analysis to both confirm the co-localization studies as well as determine how Ksp1 interacts with its cargo and Atg8. To guide us on the design of Gal4-BD-Ksp1 constructs we used structure prediction analysis of Ksp1 using IUPred3 [8-10]. This algorithm predicts the tendency of protein regions to have negligible folded tertiary structures, called intrinsically disordered regions (IDRs). The IUPred3 analysis results (Figure 4C, red line) revealed that only the amino terminus of Ksp1, which contains the conserved kinase domain, is structured. The remaining two-thirds of Ksp1 is highly unstructured, containing multiple IDRs. We next asked if regions within these IDRs contain molecular recognition features (MoRFs) that have the potential to transition to a structured conformation by interaction with a globular protein partner [9,200]. This feature allows IDRs to interact with multiple binding partners and is observed in many proteins required for autophagy [201]. Moreover, it is significant as many Atg8 interacting motifs (AIMs) on receptor proteins lie within ANCHOR regions (see below) [5]. Using ANCHOR2 analysis [202,203] we determined that the unstructured domain of Ksp1 contains multiple potential MoRFs (Figure 4C, blue line). Together this analysis is consistent with the model that Ksp1 could be an autophagic receptor protein, possibly of multiple cargos.

Based on this structural information, three Gal4-BD-Ksp1 constructs were made, one spanning the kinase domain (KD), and two spanning the large unstructured region called disordered domain 1 (DD1) and 2 (DD2) (Figure 4C, bottom panel). Only the C-terminal construct (Gal4-BD-DD2, amino acids 681-1029) interacted with the Gal4-AD-Atg8 but not vector controls (Figure 4D). We also observed that the same domain of Ksp1 interacts with Med13 (Figure S4A). Together, these results are congruous with the model that Ksp1 is an autophagic receptor protein for this CKM member. As would be anticipated by this model, Y2H analysis revealed that Med13 does not associate with Gal4-BD-Atg8 [3]. To alleviate concern that DD2 interactions may be non-specific due to its high IDR content we showed that it does not interact by Y2H analysis with two other miscellaneous proteins (human cyclin C and yeast Ume6) fused to Gal4-AD (Figure S4B). Together these results show that Ksp1 can interact with both Atg8 as well as Med13, supporting the model that Ksp1 is the receptor protein for Med13.

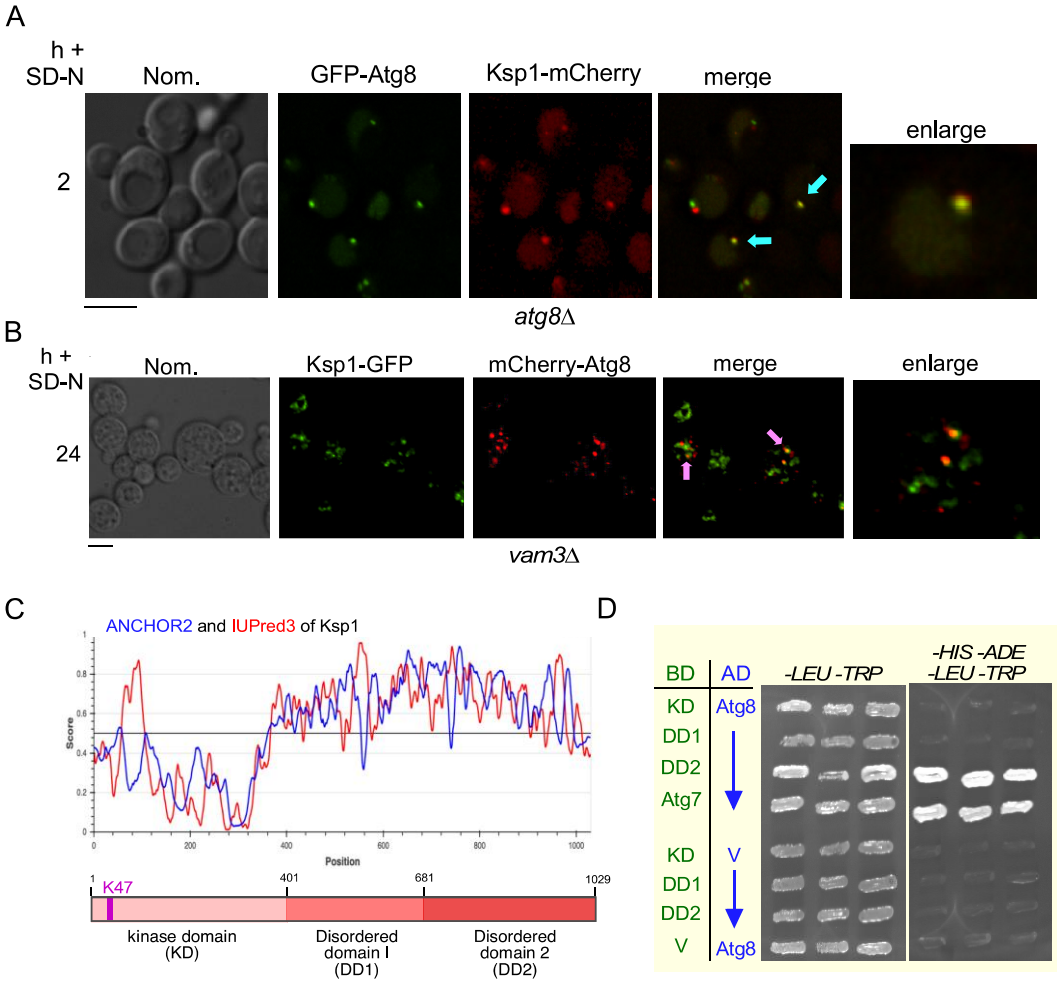

Figure 4. Ksp1 interacts with Atg8 following nitrogen starvation. **(A)** Fluorescence microscopy of endogenous Ksp1-mCherry in *atg8*Δ harboring GFP-Atg8 after 2 h nitrogen depletion. The blue arrow denotes the co-localization of Atg8 and Ksp1. **(B)** As in A except the experiment was conducted in *vam3*Δ cells after 24 h in SD-N. The pink arrow denotes co-localization. Scale bar: 5 µm. **(C)** IUPred3-long [8-10] (red) analysis of Ksp1. The score corresponds to the probability of the given residue being part of a disordered region (IUPred3-long). Residues with a predicted score above 0.5 are considered disordered, while residues with lower scores are considered to be ordered. Overlayed in blue is the ANCHOR2 plot which assesses the probability of disordered binding regions transitioning between structured and unstructured states. Underneath the profile, a schematic of full-length Ksp1 divided into the three domains used in Y2H analysis is shown. **(D)** Y2H Gold cells harboring the indicated Gal4-BD-Ksp1 subclones and Gal4-AD-Atg8. Gal4-BD-Atg8 and Gal4-AD-Atg7 were used as a positive control. V = vector. The cells were plated to medium selecting for plasmid maintenance (left panel, *-LEU -TRP*) or induction of the *ADE2* and *HIS3* reporter genes (right panel).

Ksp1 is degraded by autophagy following nitrogen starvation.

A hallmark of receptor proteins is that they are engulfed in autophagosomes alongside their cargos, being finally degraded by vacuolar proteolysis [166]. To test if Ksp1 is degraded by vacuolar proteolysis, we first used quantitative western blot analysis of endogenous Ksp1-MYC. The results showed that Ksp1 levels were reduced following nitrogen starvation with an apparent half-life of 2.6 h (Figure 5A, B, and S3B). Using cycloheximide translation inhibition assays, we found that the half-life of Ksp1 is ~7 h in unstressed cells (Figure S4C) arguing that Ksp1 is actively degraded in SD-N. Moreover, upon repeating these assays in *pep4*Δ and *atg8*Δ *strains*, we discovered that the decay rate of Ksp1 in SD-N was significantly slower with half-lives of over 15 h and 6.3 h respectively (Figure 5A and B). The faster decay rate of Ksp1 observed in *atg8*Δ compared to *pep4*Δ suggests that if Ksp1 cannot reach the vacuole then it may be subjected to proteolysis by the UPS. However, Ksp1 was still degraded in *ump1*Δ cells that are defective in 26S proteasome assembly [204-207] and its rate of decay in *ump1*Δ *atg1*Δ was not significantly different from *atg8*Δ (Figures 5C and 5D). Together, this indicates that following nitrogen depletion Ksp1 is subjected to autophagic degradation in the vacuole.

To confirm these results, we tried to measure the autophagic flux of Ksp1-GFP by western blot analysis. This assay is based on the finding that GFP is protected from rapid degradation in the vacuole compared to its fusion partner [208-210]. Unfortunately, we were unable to visualize Ksp1-GFP by this method. However, by using fluorescence microscopy we observed Ksp1-GFP in the vacuole in *pep4*Δ after 18 h in SD-N whereas it remained predominantly cytoplasmic in *atg8*Δ (Figure 5E).

Moreover, kinase-dead Ksp1-GFP which is predominantly cytoplasmic in unstressed cells (Figure S4D) is also observed in the vacuole in *pep4*Δ following SD-N treatment (Figure 5F), supporting the idea that Ksp1 kinase activity is not required for its autophagic degradation. Taken together, these results are consistent with Ksp1 being an autophagic receptor.

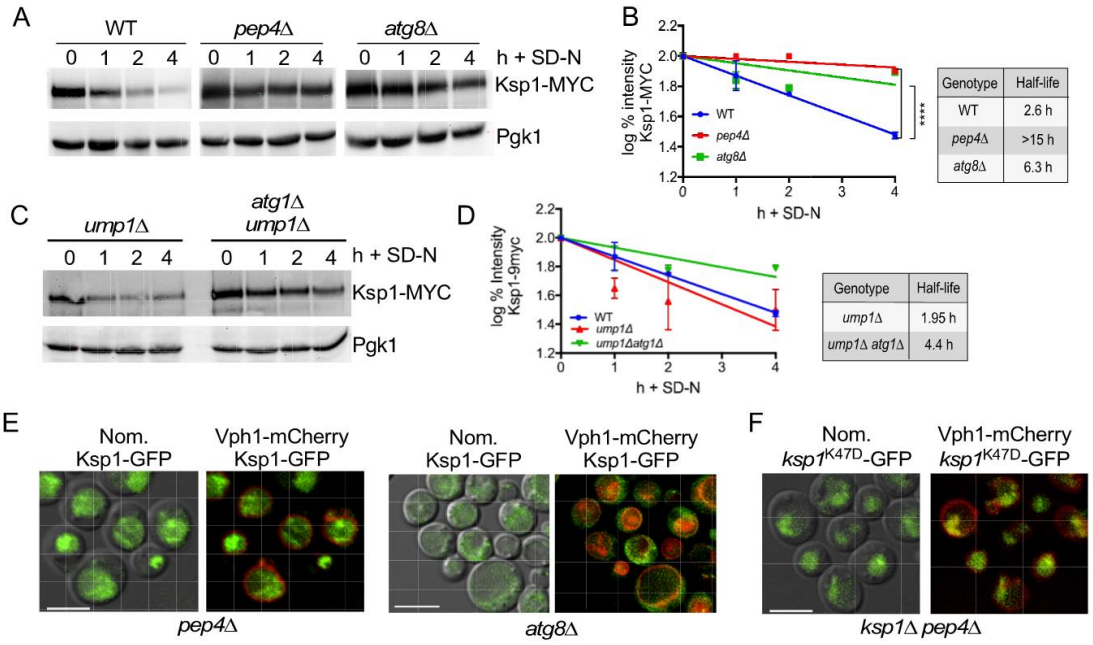

Figure 5. Ksp1 is an autophagic substrate. **(A)** Western blot analysis of protein extracts made from endogenous Ksp1-9MYC following nitrogen starvation in the genotypes indicated. **(B)** Degradation kinetics of Ksp1-9MYC in A. Pgk1 protein levels were used as the protein loading control. **(C)** Same in A, expect experiments were performed in the indicated genotypes. **(D)** Quantification of C. Ksp1-9MYC degradation kinetics in WT cells (blue line) was obtained from 5B and used as a comparison in 5D. **(E)** Fluorescence microscopy of endogenous Ksp1-GFP in either *pep4*Δ or *atg8*Δ cells following nitrogen starvation. Vph1-mCherry was used to mark the vacuoles. **(F)** As in E except *ksp1*Δ *pep4*Δ harboring *ksp1*^{K47D}-GFP was monitored. Scale bar = 5 μM.

Ksp1 interacts with the conserved receptor protein docking site on Atg8.

Selective autophagy receptors interact with Atg8 through a conserved Atg8-interacting motif (AIM), also known as LC3-interacting region (LIR), that tightly fits into two conserved hydrophobic pockets on Atg8 known as the LIR/AIM docking site (LDS) [4,211]. The hydrophobic pockets are named the W and L-sites since they interact with tryptophan and leucine residues in AIMs, respectively [4,211,212]. One prediction of Ksp1 being an autophagy receptor is that it requires functional W and L-sites on Atg8 for its autophagic degradation. To test this, we monitored the autophagic degradation of Ksp1 in *atg8*Δ harboring mutations in both sites (Y49A and L50A – named Atg8^{LDS}). The results show that Atg8^{LDS} significantly stabilized Ksp1 protein degradation in SD-N compared to the WT allele (Figure 6A), mirroring the half-life seen in *atg8*Δ (Figure 6B and S3C).

Similar to previous studies [212], we observed GFP-Atg8^{LDS} localization at the PAS after 4 h in nitrogen starvation and accumulation in vacuoles to be significantly decreased in *atg8*Δ cells harboring GFP-Atg8^{LDS} compared to GFP-Atg8 in SD-N (Figures 6C-E, S5A-C). Similarly, the vacuolar accumulation of Ksp1 in Atg8^{LDS} was severely impaired (Figure 6C, quantified in 6F and S5B, C). These results agree with a previously published report in which *in vitro* dot blot binding assays were used to show that Ksp1 interacts with processed Atg8 (amino acids 1-116), [213] but not with the processed Atg8^{LDS} mutant [103]. This is significant as the processing of Atg8 by removal of its C-terminal by Atg4 is required for its recruitment to the PAS [214]. Together these results support the model that Ksp1 is a receptor protein and directly interacts at the Atg8 docking site.

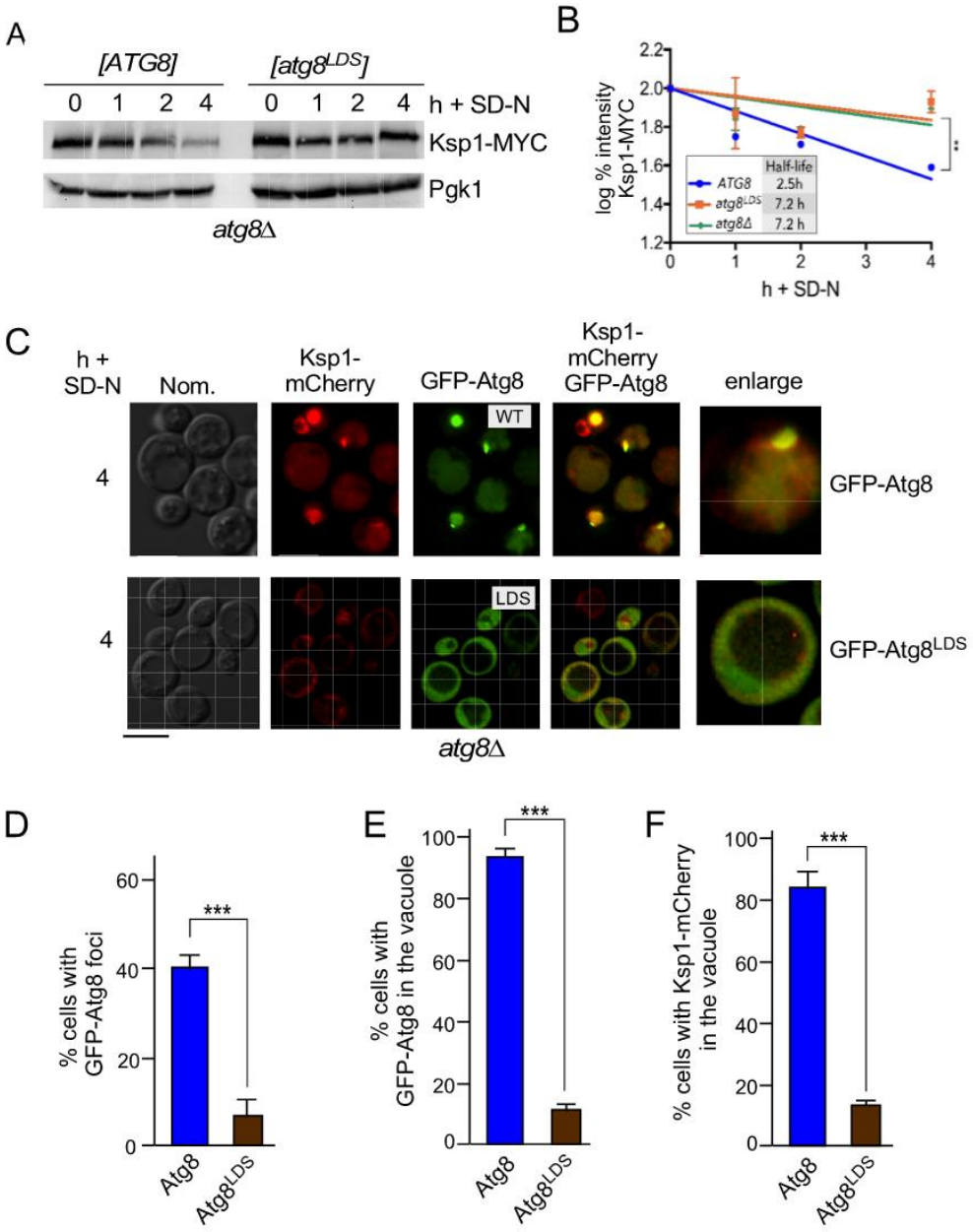

Figure 6. (A) Western blot analysis of endogenous Ksp1-9MYC protein in *atg8*Δ cells expressing either WT or LDS alleles of GFP-Atg8 following nitrogen starvation. Pgk1 protein levels were used as the protein loading control. **(B)** Degradation and half-life of Ksp1-9MYC protein levels in the genotypes indicated. Ksp1-9MYC degradation kinetics in *atg8*Δ cells (blue line) obtained from Figure 5B were used as a comparison in 6B. **(C)** Fluorescence microscopy of endogenous Ksp1-mCherry in *atg8*Δ harboring either the WT or *LDS*Δ allele of GFP-Atg8. (**D)** Quantification of foci GFP-Atg8 and GDP-Atg8^{LDS} foci observed in *atg8*Δ after 4 h in SD-N. **(E)** Quantification of cells observed with GFP-Atg8 or GDP-Atg8^{LDS} in the vacuole in *atg8*Δ after 4 h in SD-N. **(F)** Quantification of cells observed with Ksp1-mCherry in the vacuole after 4 h in SD-N in Atg8 harboring either GFP-Atg8 or GFP-Atg8^{LDS}.

Ksp1 contains a functional Atg8-interacting motif (AIM).

We next asked if Ksp1 contains a functional Atg8 interacting motif (AIM). These domains were originally described as a conserved four amino acid motif ([**W/F/Y**]xx[**L/I/V**]) [4]. More recently, based on in silico analysis of multiple experimentally verified functional AIMs, this domain has been redefined to include two additional upstream amino acids (outlined in Figure S6A) where residues 3 and 6 correspond to the required aromatic and hydrophobic residues of the original central core motif [5-7]. Also, these studies identified two additional criteria:–Firstly, the interaction with Atg8 depends strongly on acidic residues surrounding the central core motifs; Secondly, an AIM motif that overlaps with MoRFs that have the potential to transition to an ordered state is a reliable predictor of binding to LDS domains in Atg8 [5]. Using the iLIR database that incorporates all of these requirements we identified 9 putative AIMs within the Ksp1 (Figure S6B). The AIM found at the carboxy-terminal of Ksp1 (NN**W**LI**L**$^{1022\text{-}1025}$) lies within an ANCHOR region and has the highest position-specific scoring matrix (PSSM score). In other words, this AIM (coined Ksp1^{AIM1}) has the highest conservation of pattern alignment when compared to verified AIM/LIR motifs, indicating that it may be a functional AIM.

Next, using computer modeling algorithms (ClusPro, Alpha fold) [215-218] and the published Atg8 structure [211], we discovered that Ksp1^{AIM1} fits with high confidence into the hydrophobic LDS pocket of Atg8 (Figure 7A -one representative model and see Figure S7A for ribbon model). The enlarged image clearly shows that the AIM residues sit directly in the pocket and interact with LDS Atg8 residues [212]. Using computer modeling determined the potential ability of the various configurations

of the mutated AIM1 (W1022A, L1025A, W1022A & L1025A, and WLIL-AAAA) to fit into the hydrophobic pocket of Atg8. The results (Figure 7B) clearly show that, compared to the WT AIM, the mutants are significantly less able to fit into the pocket (orange scores). Instead, they lie either above (pink) or below (cyan) this interface. These results are also consistent with previous computer modeling of the LDS region of Atg8. In these studies, a mutation in the hydrophobic pocket (Y49A/L50A) prevented the conserved tryptophan residue found in $Atg19^{AIMs}$ from binding to the first hydrophobic pocket in Atg8 [212]. Taken together, our results indicate that $Ksp1^{AIM1}$ is a strong candidate to be a functional AIM.

Previous studies have shown that other receptor proteins harboring changes of either tryptophan or leucine or both residues to alanine fail to interact with Atg8 using Y2H [4,211,219]. Confirming the computer modeling prediction, the mutation of $leucine^{1025}$ to an alanine residue in the DD2 binding domain construct ($DD2^{L1025A}$) negatively affected the Ksp1-Atg8 interaction (Figure 7C). However, as this mutant did not completely eliminate activation of the reporter genes, we tested if the double mutant $DD2^{W1022A,L1025A}$ gave a cleaner result. Although significantly less growth was observed compared to DD2 on the reporter plates, $DD2^{W1022A,L1025A}$ was unable to completely eliminate the interaction (Figure 7D). As $Ksp1^{DD2}$ contains no other AIMs, (see Fig. S6A & B) we decided to rely upon *in vivo* assays to address if AIM1 is a functional Atg8 interacting motif.

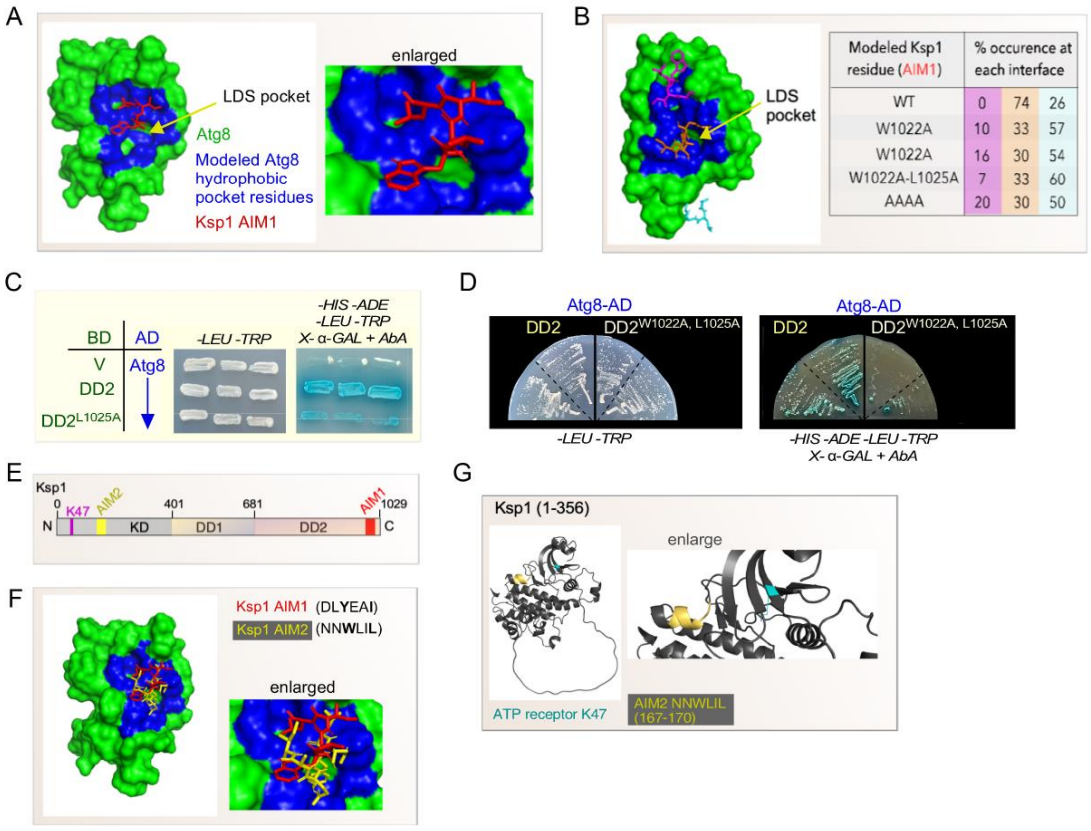

Figure 7. Ksp1 contains two functional AIM motifs. **(A)** Left panel: A representative image from computer modeling of Ksp1^{AIM1} with Atg8 showing that it can associate with the hydrophobic LDS pocket (yellow arrow). The green denotes Atg8, the red Ksp1^{AIM1}, and the blue correlates with the hydrophobic pocket (LDS) of Atg8 (see material and methods for details). Right panel: enlarged image demonstrating that the AIM1 residues engage with the LDS pocket. **(B)** Left panel. Representative image showing the interfaces on the hydrophobic pocket of Atg8 where wild type and mutant Ksp1 AIM could lie. Right panel: the % occurrence of the mutation shown in Ksp1^{AIM1} was modeled onto the hydrophobic pocket region of Atg8. The orange position is the interacting region favored by WT AIM whereas the pink and cyan positions that lie above and below the pocket are predominantly favored by the mutant alleles. **(C**) Y2H analysis of Gal4-BD constructs shown with Gal4-AD-Atg8. Three biological replicates were plated on medium selecting for plasmid maintenance *(-LEU, -TRP*, left) or interaction by induction of all four reporter genes, *ADE2*, *HIS3*, *MEL1*, and *AUR1-C* (right). **(D)** As in C except that Ksp1-DD2^{W1022A,L1022A} was analyzed. Two biological replicates are shown**. (E)** A map outlining the location of AIM1 and AIM2 with respect to other structural domains on Ksp1. **(F)** As in A except both Ksp1^{AIM1} and Ksp1^{AIM2} were modeled onto Atg8. **(G)** Modeling of structured N terminal domain (amino acids 1-356) of Ksp1 showing the position of AIM2 and the kinase pocket (K47).

Ksp1 interaction with Atg8 is required for the autophagic degradation of Med13. We next assessed the biological repercussions of disrupting Ksp1^{AIM1}. Surprisingly, endogenous *KSP1* deleted for this AIM (*ksp1*$^{AIM\Delta 1}$) was still degraded following nitrogen starvation (Figures S6C and D). This suggests that more than a single AIM may be utilized for the interaction of Ksp1 with Atg8. This idea is not without precedent, as multiple Atg8 interaction sites have also been observed for Atg19, a receptor protein for the cytoplasm-to-vacuole-targeting (Cvt) pathway [104,220,221]. The AIM with the second highest PSSM score, DLYEAI$^{169\text{-}172}$ (*ksp1*^{AIM2}, Figure S6B) can also be modeled into the hydrophobic LDS pocket of Atg8, fitting with high confidence into the same interface as AIM1 (Figure S7B). This was more apparent when both AIMs were mapped simultaneously onto Atg8 (Figure 7E and S7C). Although AIM2 lies within the more structured kinase domain of Ksp1, modeling of the N terminal domain (1-356) revealed that AIM 2 is exposed which would allow Atg8 access to the motif (Figure 7G).

We next determined the degradation kinetics of Ksp1 degradation in SD-N in *ksp1*Δ harboring the deletion of both AIMs (*ksp1*$^{D167\text{-}I172\Delta,\ W1022\text{-}L1025\Delta}$, called *ksp1*$^{AIM\Delta 1\&2}$). Cycloheximide chase assays showed that the protein is slightly less stable than its endogenous wild type counterpart with half-lives of 6 and 7 h respectively (Figure S8A and B). Western blot analysis revealed that *ksp1*$^{AIM\Delta 1\&2}$ was stabilized following nitrogen starvation (Figure 8A, quantified in 8B) demonstrating that both AIMs are required for interaction with the LDS interface of Atg8. Moreover, endogenous Med13 was also significantly stabilized following nitrogen starvation in *ksp1*$^{AIM\Delta 1\&2}$ (Figures 8C and D). Similarly, vacuolar accumulation of endogenous

Med13-mNeon in SD-N was drastically reduced in *ksp1*$^{AIM\Delta1\&2}$ (Figure 8E, quantified in 8F). They also validate that Ksp1 functions as the autophagy receptor mediating the degradation of Med13.

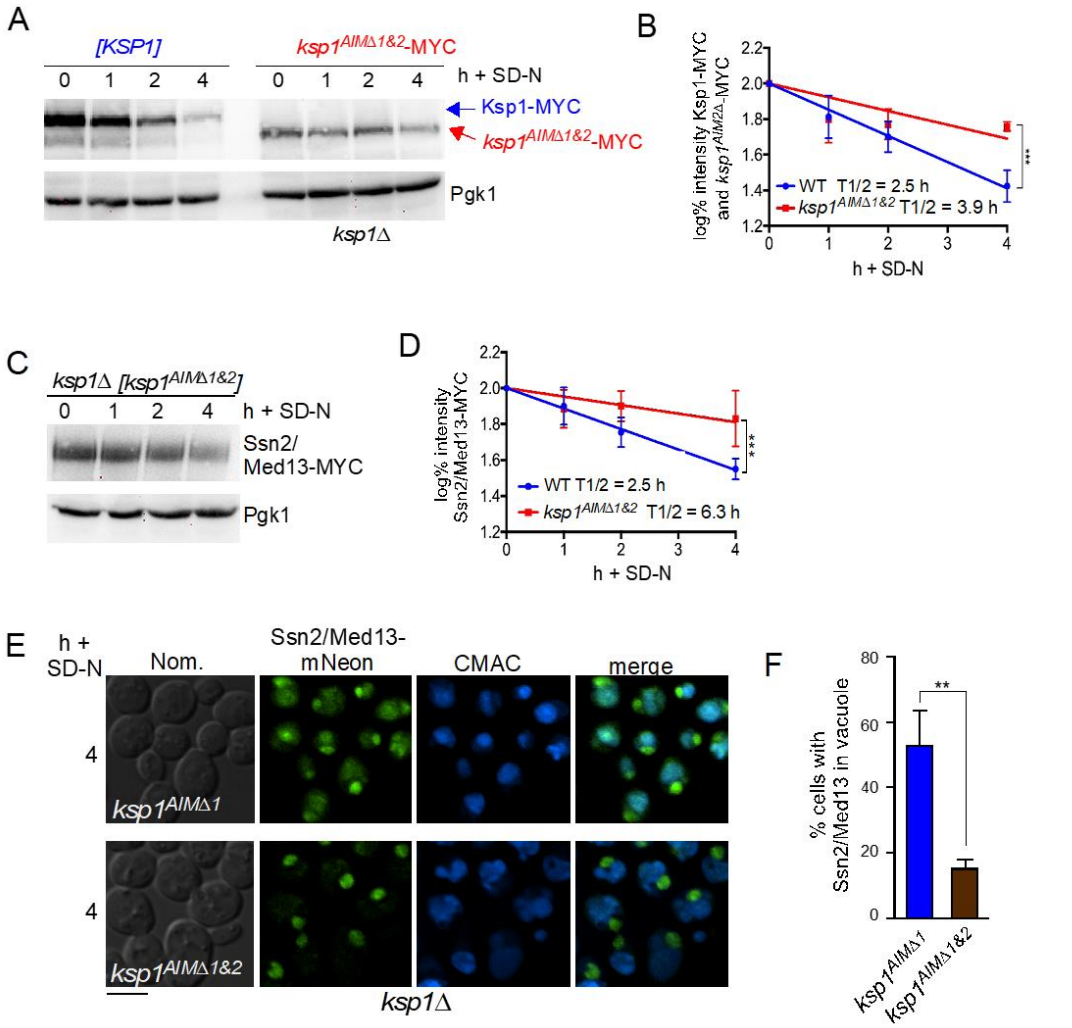

Figure 8. (A) Western blot analysis of endogenous Ksp1-9MYC and *ksp1*$^{AIM\Delta1\&2}$-9MYC following nitrogen starvation. **(B)** Degradation kinetics and half-life of indicated Ksp1 alleles. **(C)** Western blot analysis of endogenous Ssn2/Med13-9MYC protein levels in *ksp1*Δ harboring *ksp1*$^{AIM\Delta1\&2}$-GFP. **(D)** Degradation kinetics and half-life of Ssn2/Med13-9MYC in *ksp1*Δ harboring *ksp1*$^{AIM\Delta1\&2}$-GFP compared to previously observed wild type. For all blots, Pgk1 was used as the protein loading control. **(E)** Fluorescence microscopy of Med13-mNeon in *ksp1*Δ harboring either Ksp1$^{AIM\Delta1}$-9MYC or Ksp1$^{AIM\Delta1\&2}$-9MYC. Vacuoles were visualized by staining with CMAC. Scale bar = 5 μM. **(F)** Quantification of H, showing the number of cells with Ssn2/Med13 found in vacuoles.

The Atg17-Atg31-Atg29 complex interacts with Ksp1.

In yeast, the PAS is initiated during selective autophagy by the formation of cargo-receptor complexes, which are recruited to the vacuole by Atg11. This provides a local clustering platform for Atg13 recruited Atg1 leading to trans-autophosphorylation and activation of Atg1 [109,129,222]. In contrast, bulk autophagy is initiated by the formation of a supramolecular structure of Atg13 and Atg1 with the trimeric Atg17-Atg31-Atg29 complex (17C) [223,224]. Similar to the selective degradation of Cue5 cargos (ubiquitinated aggregated proteins and dysfunctional proteasomes [178,179]) the autophagic degradation of Med13 requires the 17C scaffold [3]. Therefore, using Y2H analysis, we asked if Ksp1 can interact with a member of the trimeric scaffold. As reported by others, Y2H analysis revealed that none of the trimeric scaffold complex members interacted with Atg8 [225] (Figure S9A). However, the carboxy terminus of Ksp1 interacted with both Atg29 and Atg31 (Figure S9B and C). Usage of 3-aminotriazole (3-AT), in Y2H analysis, allows for differing levels of stringency when histidine-based growth selection is used, as it competitively inhibits the *HIS3* gene product [226]. The addition of 50 mM 3-AT still permitted the Ksp1 interaction with Atg29 but not Atg31 (Figure 9A, upper panels). These results suggest that Ksp1 interacts with 17C. Previous studies have shown that mutation of the AIM in receptor proteins does not affect their interaction with scaffold proteins [146,219]. Likewise, the C-terminal Ksp1 Y2H construct harboring the L1025A mutation still interacted with Atg29 using Y2H analysis (Figure 9A, lower panels). Together, these results support the model that Ksp1 interacts with both Atg8 and the scaffold complex, with only the Ksp1-Atg8 interaction being dependent on an AIM.

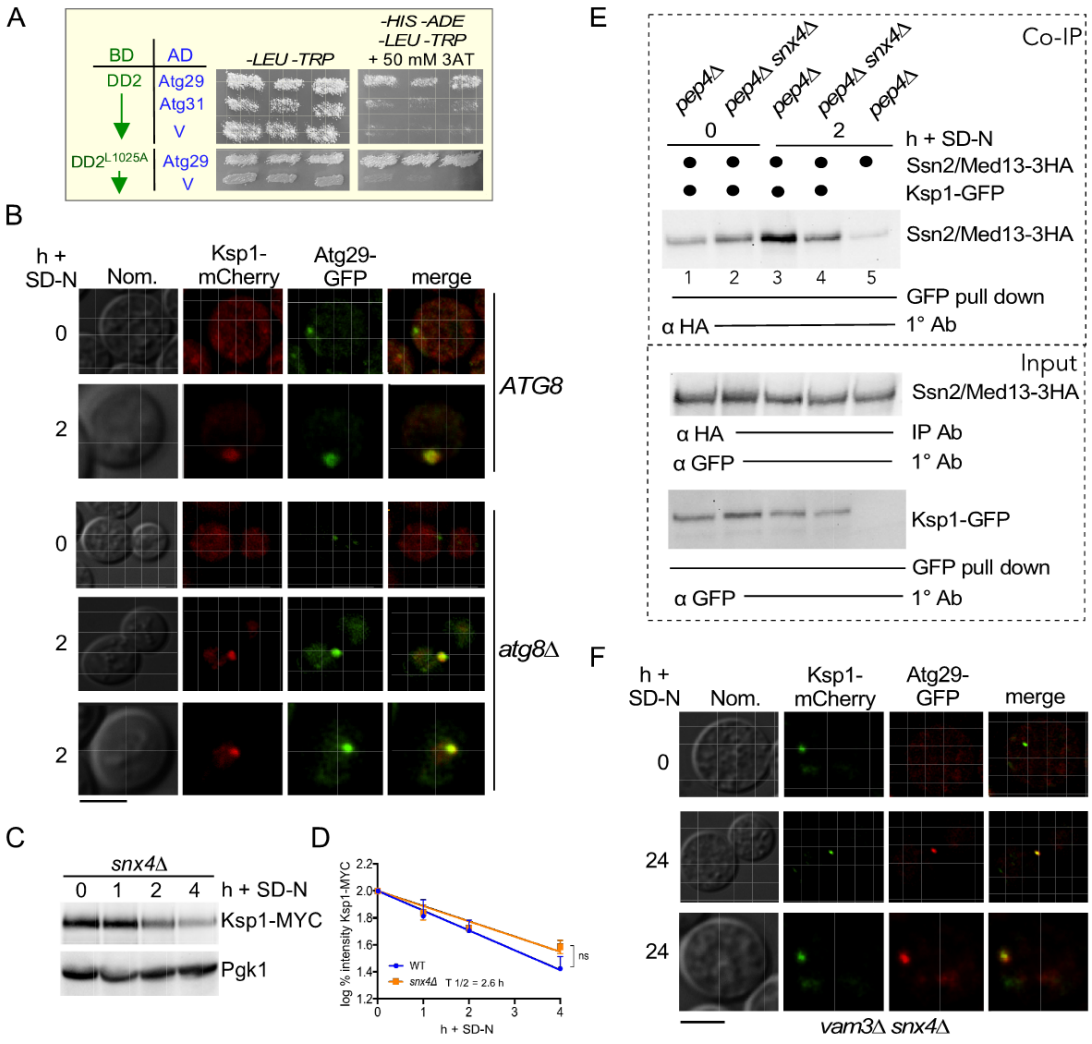

Figure 9. (A) Y2H analysis. Upper panels; Gal4-BD-Ksp1^{DD2} with either Gal4-AD-Atg29, Gal4-AD-Atg31 or a vector control. Lower panels; Gal4-BD-Ksp1$^{DD2\text{-}L1025A}$ with either Gal4-AD-Atg29 or a vector control. Cells were streaked on medium selecting for plasmid maintenance (left) or induction of reporter genes (right) by Y2H interaction. **(B)** Single-plane fluorescence microscopy images of Ksp1-mCherry and Atg29-GFP before and following nitrogen starvation in wild-type and *atg8*Δ cells respectively. Bar = 5 µM. **(C)** Western blot analysis of Ksp1-9MYC following nitrogen starvation. protein levels in *snx4*Δ. Ksp1-9MYC degradation kinetics in WT cells (blue line) was obtained from Figure 5A and used as a comparison in B. **(D)** Quantification of B. Ksp1-9MYC degradation kinetics in WT cells (blue line) was derived from Figure 5A. **(E)** GFP pull-down analysis of Ksp1-GFP and Ssn2/Med13-HA in the presence and absence of Snx4. **(F)** Single plane fluorescence microscopy images of Ksp1-mCherry and Atg29-GFP before and following nitrogen starvation in *vam3*Δ *snx4*Δ cells. Bar = 5 µM.

The Atg17-Atg31-Atg29 scaffold complex recruits Ksp1 to the PAS.

We next confirmed the Ksp1-Atg29 Y2H interaction using co-localization studies of live cells. Congruous with the Y2H results, we observed that endogenous Ksp1-mCherry colocalized with Atg29-GFP foci only following 2 h in SD-N (Figure 9B). In the hierarchy of autophagy proteins loading onto the PAS, 17C arrives at the PAS found at perivacuolar sites before Atg8 [224,227]. Therefore, we asked if Ksp1-mCherry was able to interact with the PAS (marked by Atg29-GFP) in the absence of Atg8 using fluorescence microscopy. The results showed that Ksp1 co-localized with Atg29-GFP in *atg8*Δ cells after 2 h in SD-N (Figure 9B). These studies strongly support a model in which after autophagy initiation, Ksp1 is anchored at the perivacuolar PAS by Atg29. They also define Ksp1 to be an autophagic receptor protein that works in conjunction with expanding phagophores most commonly associated with non-selective autophagy. However, instead of packaging indiscriminate parts of the cytoplasm, here we show that these phagophores also can recruit targeted cargos.

Snx4 is not required for the recruitment of Ksp1 to the PAS.

The sorting nexin heterodimer Snx4-Atg20 assists cargo degradation in many selective pathways including mitophagy, pexophagy, and ribophagy [131-135]. In addition, the recruitment of a subset of transcriptional regulators including Med13 to phagophores is aided by this heterodimer [131]. In this model, Med13 directly binds to Snx4-Atg20, and the complex is recruited to the PAS by Snx4-Atg17 interaction [131]. Consistent with this, in the absence of Snx4, co-IP analysis between Atg17 and Med13 is diminished [3]. To ask if Snx4-Atg20 also recruits Ksp1 to the PAS we monitored the autophagic degradation of endogenous Ksp1 in *snx4*Δ. The results (Figures 9C and

quantified in D) show that Ksp1 is still degraded following nitrogen starvation. This suggests that Snx4 is not required for delivering Ksp1 to the PAS. Consistent with this Ksp1-GFP pulldowns of Med13-3HA were significantly enhanced following nitrogen starvation in *pep4*Δ but not in *pep4*Δ *snx4*Δ (Figure 9E). Lastly, using fluorescence microscopy we also observed Atg29-GFP foci co-localizing with Ksp1-mCherry in *vam3*Δ *snx4*Δ cells following nitrogen starvation (Figure 9F) Collectively, these results support the model that Snx4-Atg20 delivers cytoplasmic Med13 to growing autophagosomes but is not required for the recruitment of Ksp1 to the PAS.

The Ksp1 interaction with Atg8 is not required for general autophagy.

Previous studies suggest that Ksp1 is not required for selective autophagy or Atg9 trafficking. Instead, Ksp1 kinase activity contributes to suppressing the induction of non-selective autophagy by activating the TORC1 pathway [188]. To assess if *ksp1*$^{AIM\Delta1\&2}$ also affects autophagy induction we examined the phosphorylation status of Atg13, a substrate of TORC1. This assay correlates with the induction of autophagy and serves as a readout for the functionality of upstream signaling cascades that affect bulk autophagy [95,228,229]. Similar to a kinase-dead mutant [188], we observed a reduction in the phosphorylation status of Atg13 in unstressed *ksp1*$^{AIM\Delta1\&2}$ cells (Figure 10A). These results suggest that *ksp1*$^{AIM\Delta1\&2}$ acts like a kinase-dead mutant with regards to inactivating the TORC1 pathway. Similar to this, using GFP-Atg8 cleavage assays we observed a statistically significant amount of free GFP in unstressed *ksp1*$^{AIM\Delta1\&2}$ cells compared to wild type. Also using Pgk1-GFP cleavage assays that monitor bulk autophagy [137] free GFP appeared slightly earlier in *ksp1*$^{AIM\Delta1\&2}$ (Figure S10A and S10C).

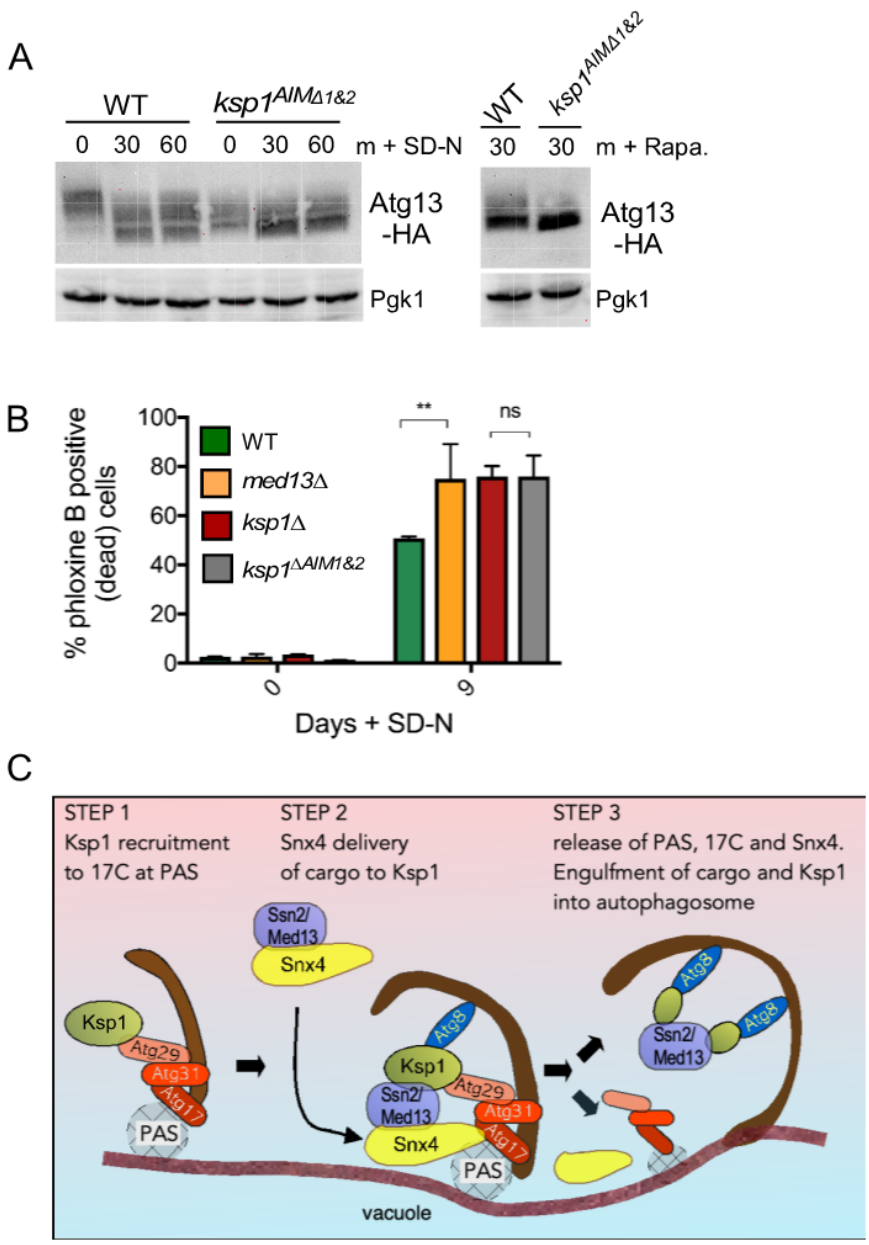

Figure 10. (**A)** Western blot analysis of Atg13-HA in the genotypes shown after 30 and 60 m in SD-N (left) and 30 m after treatment with 200 ng/ml rapamycin (Rapa) for the indicated times in SD (right). **(B)** Survival assays of the strains shown before and after 9 days in SD-N. **(C)** Model outlining the receptor protein role of Ksp1 in the autophagic degradation of Ssn2/Med13. Ksp1 is recruited to perivacuolar phagophore assembly sites (PAS) by Atg29 of the trimeric scaffold complex. Ssn2/Med13 is recruited to the PAS by Snx4-Atg20. Thereafter the trimeric complex, PAS factors, and Snx4-Atg20 are released from autophagosomes [3,11] whereas the interaction of Ksp1 with the LDS region of at least two Atg8 sites, delivers its cargo, Ssn2/Med13, to autophagosomes for eventual degradation

Taken together, these results suggest that *ksp1*$^{AIM\Delta1\&2}$ acts like a kinase-dead mutant with regards to autophagy induction.

As AIM2 lies close to the ATP receptor site, its deletion could potentially affect the kinase domain. Using modeling we observed no obvious structural differences in the kinase domain of Ksp1 and *ksp1*$^{AIM2\Delta}$ (Figure S8C). Together, these results indicate that *ksp1*$^{AIM\Delta1\&2}$ is acting like a kinase-dead mutant with respect to promoting autophagy induction and execution. However, unlike the kinase-dead mutant, *ksp1*$^{AIM\Delta1\&2}$ is unable to associate with Atg8 preventing delivery of Med13 to the PAS. This suggests a model in which Ksp1 interaction with Atg8 may disable the kinase activity of Ksp1. This would be an efficient way to switch between the opposing kinase-dependent and independent roles of Ksp1.

Ksp1 is required for survival following nitrogen starvation.

We next asked if deletion of the AIMs in Ksp1 has a physiological significance. Thus we tested if wild-type, *med13*Δ, *ksp1*Δ, and *ksp1*$^{AIM\Delta1\&2}$ cells exhibited viability differences following nitrogen starvation using a standard autophagy survival assay [230]. Mid-log cells were switched to nitrogen starvation medium and after 9 d viability was determined by using phloxine B staining that identifies dead cells. As previously reported, cell death was significantly elevated in *med13*Δ mutants compared to wild-type cells [39,180]. We also observed elevated levels of cell death in *ksp1*Δ and *ksp1*$^{AIM\Delta1\&2}$. Importantly, there was no significant difference between *ksp1*Δ and *ksp1*$^{AIM\Delta1\&2}$ strains (Figure 10B). This suggests that the destruction of Med13 and/or other potential Ksp1 cargo is important for cell survival upon starvation. As we have already identified Rim15 and Msn2 to be cargos of SAA, we tested whether these

transcription factors also use Ksp1 as an autophagic receptor. However, using autophagic GFP cleavage assays we observed free GFP cleaved from both Rim15-GFP and Msn2-GFP following nitrogen starvation in both wild -type and *ksp1*Δ cells (Figure S10D). This suggests that the autophagic degradation of these transcriptional activators may be mediated by an unknown receptor protein, possibly by one of the 34 putative Atg8 interactors previously identified [103]. These results also suggest that Snx4 transports selective substrates including transcription factors, RNA, ribosomes, and proteasomes to the autophagic machinery [3], and Ksp1 functions as a receptor protein at the PAS for only a subset of these proteins.

Discussion

In its infancy, the field of autophagy depicted the lysosome as a major non-selective dumpsite within the cell. Since then, the pool of autophagic substrates has expanded from excess or damaged organelles and protein aggregates to fully functional multi-subunit complexes and single proteins. In the last decade, a strong focus has been on discovering autophagic receptor proteins, as they provide substrate specificity, thereby acting as decision-makers in autophagy pathways [166,175,231]. In this report, we show that Ksp1 is the receptor protein for the autophagic degradation of a transcriptional regulator, Med13 (summarized in Figure 10E). This role is independent of its kinase activity, demonstrating the dual functionality of this kinase. Moreover, our results suggest a model in which Ksp1 plays dual but opposing functions in regulating autophagy. During unstressed conditions Ksp1 negatively regulates autophagy and this role is kinase-dependent, however following starvation Ksp1 promotes the autophagic degradation of specific substrates and this is kinase-independent. How these different

roles of Ksp1 are regulated remains unclear however it is possible that Ksp1 association with autophagy machinery may function as the molecular switch. Data presented in this study suggests a model in which Ksp1 is first recruited to the PAS, binding to 17C and Atg8. Next, Snx4-Atg20 delivers Med13 to PAS-bound Ksp1. Lastly, PAS factors and Snx4-Atg20 are removed from growing phagophores [3,11] and Med13 and Ksp1 are engulfed in autophagosomes. This finding supports the model that the autophagic degradation Med13 is highly discriminating. Firstly, Med13 is not only exclusively targeted from other transcription factors associated with chromatin but also from within the CKM itself [3,48]. Secondly, following its nuclear export, the engulfment of cytoplasmic Med13 by autophagosomes is not random but assisted by Snx4-Atg20, with Ksp1 acting as a receptor protein. Outlining its importance, the degradation of either Med13 and/or other Ksp1 cargos by this mechanism contributes to the survival of *S. cerevisiae* following nitrogen starvation.

Cargo receptors are characterized by their ability to both bind cargo and facilitate the recruitment of autophagic machinery through the binding of Atg8 and a scaffolding subunit of the Atg1 complex. Thereafter, cargo receptors are captured within autophagosomes, being finally degraded by vacuolar proteolysis alongside their cargos [166,231]. Here we report that Ksp1 fulfills these functions. Ksp1 specifically binds to Med13 and is required for its autophagic degradation. Ksp1 itself is also degraded by vacuolar proteolysis. Like other receptor proteins, Ksp1 directly binds to Atg8, and this binding is dependent upon the conserved hydrophobic LDS pocket in Atg8 and Atg8 interaction motifs in Ksp1. Taken together, these observations define Ksp1 as an autophagic receptor protein for Med13. Further studies are needed to investigate if

Ksp1 exclusively recognizes Med13 or if it can act as a cargo receptor for other proteins.

Cargo receptors in yeast also most commonly interact with the Atg11 scaffold protein leading to the nucleation of phagophores in the direct vicinity of cargo [79,82,132,146,232-235]. Thereafter cargo filled autophagosomes are delivered to the vacuole for degradation. The exception to this is Cue5, which does not require Atg11 to deliver its cargos to expanding phagophores [178,179]. Atg11 is also not required for the autophagic degradation of Med13. Instead, the trimeric Atg17-Atg29-Atg31 scaffold complex fulfills this role [3]. This is interesting as this scaffold nucleates phagophores which most commonly sequester random portions of cytoplasmic material during nitrogen starvation [35]. We now show that Ksp1 can bind to Atg29 using Y2H analysis as well as co-localizing with this complex after nitrogen starvation at the PAS. Together, these results suggest phagophores nucleated by either scaffold utilize receptor proteins to sequester specific cargo. Alternatively, as the second job of 17C is to mediate efficient autophagosome-vacuole fusion [236], our results could mean that Med13 requires this second function of the trimeric scaffold. However, we favor the first explanation as this model best fits our results. Intriguingly, the separation of jobs for Atg11 and the trimeric scaffold complex is not so clear-cut in more complex eukaryotes [79]. For example, in mammalian cells the Atg17 homolog, RB1CC1/FIP200 (FAK Family Kinase-interacting protein of 200 kDa), combines the functions of both these yeast scaffold proteins, playing a role in selective and non-selective autophagy [237,238].

In this report, we demonstrate that two sites in Ksp1 interact with Atg8 in an AIM-dependent manner. Multiple AIMs have also been observed in Atg19, a receptor protein for the selective Cvt pathway that delivers three resident enzymes to the vacuole in replete media [214,239,240]. Current models propose that this enables Atg19 to interact with multiple Atg8 proteins simultaneously, which in turn allows its cargos to be exclusively captured within autophagosomes [221]. We recently have identified other Ksp1 cargos but currently do not know if Ksp1 cargos are engulfed alone, together, and/or with non-specific cytoplasmic components. Furthermore, the induction of selective autophagy in mammalian cells also leads to bulk degradation of a portion of the cytosol. This mechanism, coined "bystander autophagy", results in autophagosomes enriched for both specific and non-specific cargos [241]. Thus, it's possible that autophagosomes enriched with Ksp1 cargos could also capture non-specific cytoplasmic material.

We also show in this study that Ksp1-mediated degradation of its cargo is required for survival during nitrogen starvation. As the cell survival assays show that Med13 is also required, this could mean that Med13 is the critical cargo. However, recently we have identified other cargos of Ksp1 that are required for translation (manuscript in preparation). Thus, it is possible that either all or a subset of Ksp1 cargo needs to be destroyed to survive long-term starvation. To date, no autophagic receptor(s) have been identified for autophagy-mediated mRNA degradation. Ksp1 is a good candidate as over 50% of the proteins identified as physically interacting with Ksp1 function in transcription, chromatin remodeling, mRNA maturation, decay, and translation. In

addition, some of these proteins are known autophagic substrates including eIF4G and Dhh1 [185,194].

Currently, we do not know why Med13 is destroyed by SAA following nitrogen starvation when it is destroyed by the UPS in the nucleus following ROS stress [53,54]. Like Ssn8/cyclin C, one possibility is that Med13 also has two cellular roles (a. k. a. day and night job). Its "day job" is transcriptional control of stress response genes [48]. Its starvation stress-induced night job occurs in the cytoplasm before it is destroyed by SAA. One possibility is that Med13 could be acting as an RNA binding protein (RBP) in this pathway, as recent structural studies have identified it to have an Agonaute-like bi-lobal architecture [51]. Argonaute proteins are highly conserved and bind to small RNA components to regulate transcription [242,243]. In short, Med13 has four global domains that are similar to nucleic acid regions found in RNA-binding proteins (RBP). This bi-lobal architecture forms a narrow central channel that binds nucleic acids in Argonaute proteins. Interestingly, Med13 contains an additional, unique alpha-helix that renders the narrow central channel inaccessible to nucleic acid binding in physiological conditions [51]. This channel lies in the same region that we have previously shown to be modified by phosphorylation following oxidative stress [54]. Thus, a possible model is that following nitrogen starvation, Med13 acts as an RBP for specific mRNAs. Med13 is then in turn recognized by Ksp1, thereby delivering the mRNAs to autophagosomes. Further studies are needed to explore this hypothesis, but the current models underline that both transcriptional and post-transcriptional gene regulation are unappreciated functions of autophagy.

To conclude, the results presented here support the model that Ksp1 defines a new type of autophagic receptor protein. This role is independent of its kinase function showing that Ksp1 has dual and opposing roles in regulating autophagy pathways. These findings not only broaden our knowledge of autophagy mechanisms but suggest that paradigms that define selective and non-selective autophagy pathways are merging. In support of this, recently it was revealed that specific RNA species that are tightly coupled with translation, are degraded by autophagy in response to stress [244]. Like SAA of transcription factors, Snx4-Atg20 assists in autophagy-mediated mRNA degradation suggesting that the pathways may have other unknown similarities [244].

CHAPTER 4

Med13 is required for proper quiescence entry and P-body autophagic degradation following starvation

Abstract

In response to stress, cells rapidly alter protein levels, functions, and interactions to mitigate damage and initiate repair pathways. The Cdk8 kinase module (CKM) is an evolutionarily conserved, detachable unit of the Mediator complex that plays a vital role in regulating transcription and communicating stress signals from the nucleus to other organelles. Previously, our laboratory has shown that following nitrogen starvation, Med13, a scaffold protein within the CKM, localizes to the cytosol where it is degraded via Snx4-assisted autophagy. This pathway utilizes the sorting nexin heterodimer Snx4-Atg20 and the autophagy receptor Ksp1. Here we show that re-localization of Med13 is required for cells to properly enter quiescence in response to starvation. This cytosolic role is independent of the CKM and occurs prior to its autophagic degradation. Interestingly, others have shown that Med13 contains similar structural features to RNA silencing Ago proteins. Here we show that Med13 localizes to RNP granules and is required for the degradation of selective RNA-binding proteins including Edc3 and Dhh1. Taken together, this suggests a model in which Med13 performs a cytosolic stress-induced role by promoting quiescence entry and selective autophagic degradation.

Introduction

Cells adapt to environmental changes by altering transcription, metabolic pathways, proteolysis, and upregulating reparative mechanisms. As the cell senses external stimuli such as starvation, hypoxia, mating cues, or toxic assaults, signals are transmitted to the nucleus where changes in gene transcription coordinate instructions for other organelles to respond to these external cues. These organelles, including mitochondria and vacuoles, then modulate their function to properly adapt to these stimuli [245]. Once these stress cues are deciphered, the appropriate cell fate decisions are executed. These decisions can include proliferation, quiescence entry, or the initiation of cell death pathways. Stress restricts cell cycle progression, allowing cells the time and energy to mitigate and repair cellular damage. During periods of starvation, cells enter quiescence (G_0), a temporary and reversible exit from the cell cycle [16] [246]. Features of quiescence include condensed chromatin, reduced translation, increased carbohydrate storage, increased autophagy, and increased stress resistance [246] [247].

A key commander in connecting stress-related cues, transcription, and organelle function is the Cdk8 kinase module (CKM). This interchangeable component of the Mediator is composed of four conserved proteins, two scaffolding proteins Med13 and Med12, as well as cyclin C and its cognate kinase, Cdk8. In yeast, CKM association with the Mediator predominantly represses transcription [248,249] [250], although positive roles have been described [251] [252]. In higher eukaryotes, the CKM can both negatively and positively regulate transcription and the mode of

regulation is dependent on different factors such as stress, chromosomal localization, and kinase activity [164] [56].

In addition to its transcriptional role, the CKM regulates cell fate decisions by modulating the sub-cellular address of cyclin C. In response to high levels of reactive oxygen species (ROS), Med13 is rapidly degraded via the ubiquitin-proteasomal system (UPS) [54]. Along with removing transcriptional repression of stress response genes, the dissolution of the CKM results in cyclin C translocation to the cytoplasm. Here it is required for stress-induced mitochondrial fission and mediates regulated cell death [52] [12]. This response is conserved, with cyclin C directly interacting with the Drp1, the GTPase involved in mitochondrial fission [57], as well as cell death factor Bax in mammalian cells [58]. This secondary night job of cyclin C is integral to promoting cell death and fits with an emerging theme that proteins can have two different functions, coined day and night jobs [20] [21].

In contrast to cell death cues such as oxidative stress, cells are also faced with survival cues such as those under starvation, in which they respond by inhibiting anabolic processes and activating catabolic pathways such as autophagy. Autophagy is a process in which cellular components are sequestered within double-membraned vesicles known as autophagosomes [74]. Autophagosomes loaded with cargoes fuse with vacuole (lysosome in metazoan), where the contents are degraded via resident proteases. Basic building blocks such as nucleic acids and amino acids are released back into the cytosol to replenish exhausted nutrient pools. Our studies in yeast have demonstrated that starvation cues also trigger the dissolution of the CKM. This results in upregulating stress response genes including a subset of autophagy-related genes

(ATG). In contrast to oxidative stress, cyclin C is degraded by nuclear proteasomes preventing mitochondrial fragmentation and removing repression of *ATG* expression [38].

Following starvation, CKM disassembly in yeast also results in Med13 translocation to the cytoplasm. Here Med13 is selectively targeted for degradation by Snx4-assisted autophagy. This novel autophagy pathway utilizes the sorting nexin heterodimer, Snx4-Atg20, and the autophagic receptor protein Ksp1 [3]. This illustrates that the cell utilizes two different proteolysis systems to degrade Med13 and these different modes of destruction are dependent upon stress. To understand why different modes of proteolysis are used, we proposed that Med13 plays a vital cytosolic role prior to its autophagic degradation.

Ribonucleoprotein (RNP) granules are membrane-less compartments that contain high concentrations of RNA molecules and RNA-binding proteins. These structures are intricately linked to the physiological condition of cells and constantly grow, shrink, fuse, and dissolve depending on levels of perceived stress [253]. More recently it has been discovered that as RNA and proteins concentrate, they condense into dense assemblies that are distinct and separate from the surrounding dilute phase. This mechanism is termed liquid-liquid phase separation (LLPS) and is caused by weak interactions between multivalent proteins and nucleic acids. [254].

In yeast, several types of RNP granules form in response to adverse changes in physiological conditions such as stress granules and processing bodies (P-bodies) [41]. Proteins constitutively associated with P-bodies are involved in translational repression and/or RNA decay. This includes the deadenylation complex Ccr4-Not, Lsm1-7, the

decapping coactivator and enzyme Dcp1/Dcp2, various decapping activators such as Edc3, Pat1, Dhh1 and the 5′-to-3′ exoribonuclease Xrn1 [40]. These proteins usually contain intrinsic disordered regions (IDRs) that function as hubs for simultaneous interactions with multiple binding partners and RNAs [255]. Furthermore, a subset of P-body constituents is targeted to autophagosomes for degradation [256] [257]. Similar to P-bodies, the initiation of the phagophore assembly structure (PAS) requires LLPS for its formation [258].

Med13 shares similar characteristics to core P-body proteins. Med13 contains one of the largest IDRs in the yeast proteome and was recently predicted to be a member of the RNA-binding Argonaute (Ago)/PIWI protein superfamily [51]. Med13 also contains a large 16 poly Q stretch (amino acids 1121-1136) within its C-terminal disordered region. Lastly, Med13 has previously been shown to interact with proteins involved in RNA metabolism such as the cytoplasmic nucleoporin required for mRNA export, Gle1 [3], and the Casein II-like kinase involved in mRNA decay and translation, Ksp1.

Here we show that Med13 mediates quiescence entry and survival following starvation stress. This cytosolic stress-induced role of Med13 is independent of the CKM. In short, we show that once in the cytosol, Med13 localizes to P-bodies and is required for the autophagic degradation of a subset of P-body proteins. As Med13 regulates both transcription and RNA binding proteins, these data support a model in which Med13 couples transcriptional and post-transcriptional mechanisms during starvation.

Experimental Results

Med13 mediates survival and quiescence entry following starvation.

In the budding yeast *Saccharomyces cerevisiae*, nutrient deprivation stimulates stress response genes (SRGs) transcription critical for entry into either quiescence or gametogenesis depending on the cell type. In yeast, this can be triggered by starvation stress including nitrogen starvation. The ability to survive is dependent upon correctly entering and exiting quiescence which is in part controlled by the conserved serine-threonine kinase Rim15 [247,259][[260]. Using plate survivor assays our studies and those of others showed that *rim15*Δ cells exhibited a dramatic loss in viability in quiescence triggered by prolonged nitrogen starvation stress, compared to the wild-type control or *cdk8*Δ mutants [38]. Likewise, our previous studies have shown that compared to WT or c*dk8*Δ, *med13*Δ cells exhibit a ~25% increase in cell death following prolonged nitrogen starvation stress (Figure 1B and [38]). Thus, here we set out to establish why *med13*Δ have decreased viability during nitrogen starvation.

Similar to mammalian cells, which arrest in G1/G0 after serum starvation, [261] the majority of wild-type yeast arrest in G1/G0 after nitrogen starvation [262]. To investigate the role of Med13 in G1/G0 arrest we monitored the budding index of cells following nitrogen starvation. During growth in YPDA, both wild-type and about 30% of both wild-type and *med13*Δ cells were in G1/G0, as quantified by the percentage of cells without buds. After 4 h, 60% of WT cells showed no buds, representative of cells in G0. This increased to over 80% after 24h. However, *med13*Δ cells were significantly slower in exiting the cell cycle, with ~40% and 60% of the cells retaining buds at 4 and 24 h respectively (Figure 1C, quantified in 1D). Similar to this, *med13*Δ cells had a

greater growth rate compared to WT cells following treatment with low concentrations of the TORC1 inhibitor, rapamycin (Figure S1A).

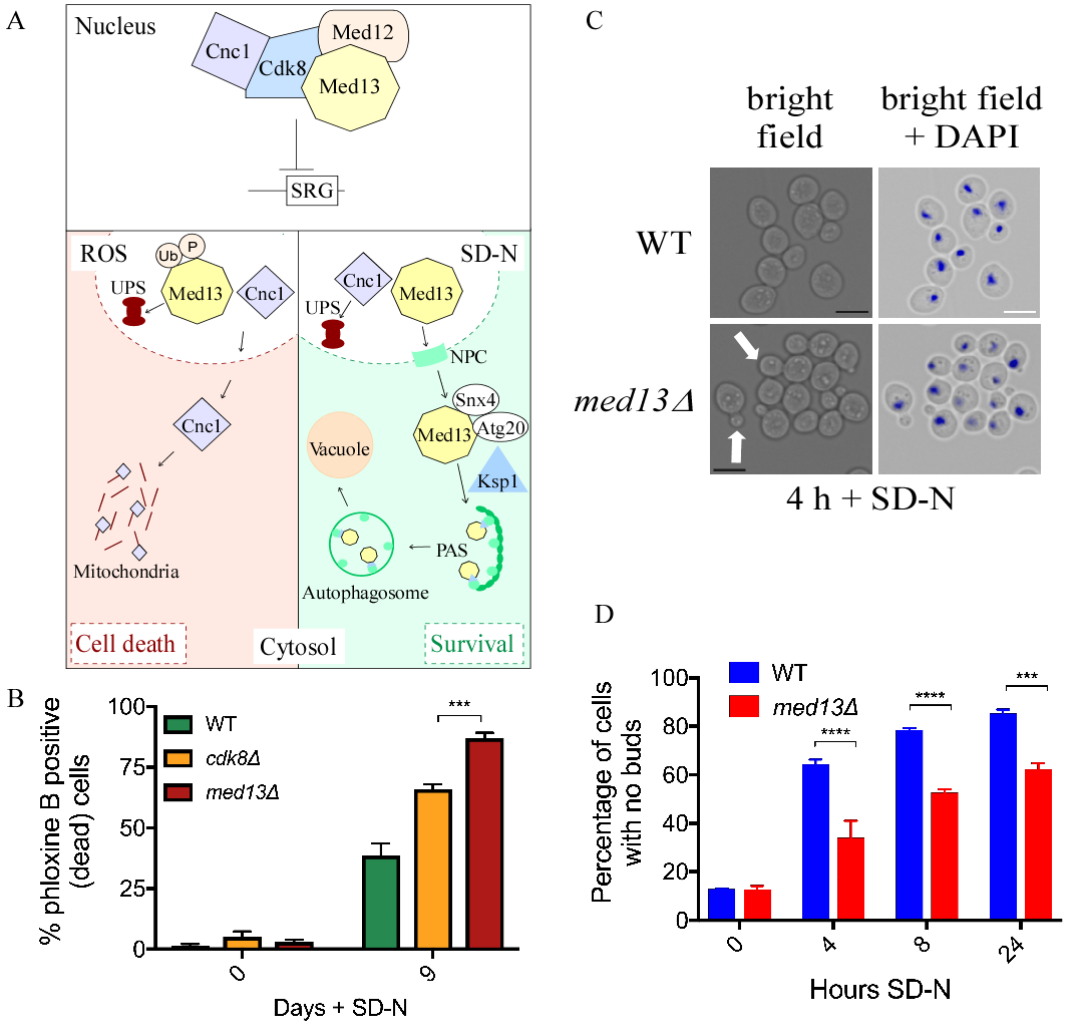

Figure 1. Med13 mediates cell survival and cell cycle arrest following nutrient deprivation. **(A)** Schematic of the role of the CKM in stress response. **(B)** The indicated genotypes were grown to mid-log, washed, and resuspended in media lacking nitrogen (SD-N) for 9 days. Cells were then stained with phloxine B and the population of phloxine B positive (dead) cells was analyzed using flow cytometry. **(C)** Representative brightfield and fluorescence microscopy images of WT and *med13*Δ cells are shown. Nuclei were visualized using DAPI. Scale bar = 5 μm. **(D)** Quantification of Figure 1C. The percentage of cells in quiescence or stationary phase (cells with no buds) was quantified in the indicated genotypes. Cells were grown to mid-log, washed, and resuspended in SD-N for the indicated time points. 200 cells were counted per biological triplicate. Error bars indicate S.D., N=3 of biologically independent experiments.

Slow nutrient exhaustion that is associated with the transition from logarithmic growth to stationary phase results in delays in cell cycle arrest and aberrant cell cycle progression in *med13*Δ cells (Figure S1B and S1C). Lastly, *med13*Δ cells were defective in glycogen accumulation which is a hallmark of quiescence entry (Figure S1D). Previously, it has been shown that *cdk8*Δ cells do not experience defects in quiescence glycogen accumulation [39], illustrating these results are unique to the loss of Med13. Taken together these data demonstrate an important secondary role for Med13 following stress that is independent of its known function within the CKM complex.

Med13 is localized to the cytosol following various starvation conditions.

Next, we asked if Med13's role in promoting cell cycle arrest occurred following other forms of stress that are known to induce cellular quiescence. Following nitrogen starvation, endogenous Med13-mNeonGreen was observed in the vacuole in *pep4*Δ *prb1*Δ*.1* cells which are deficient in a major vacuolar protease [93]. In stationary phase cells and cells depleted of a carbon source, the same fate was observed. As anticipated from our previous studies, Med13 remained nuclear following oxidative stress (H_2O_2) (Figure 2). We also observed that Med13 is degraded during stationary phase (Figure S2A and S2B), suggesting that Med13 degradation may be coupled to its cytosolic localization.

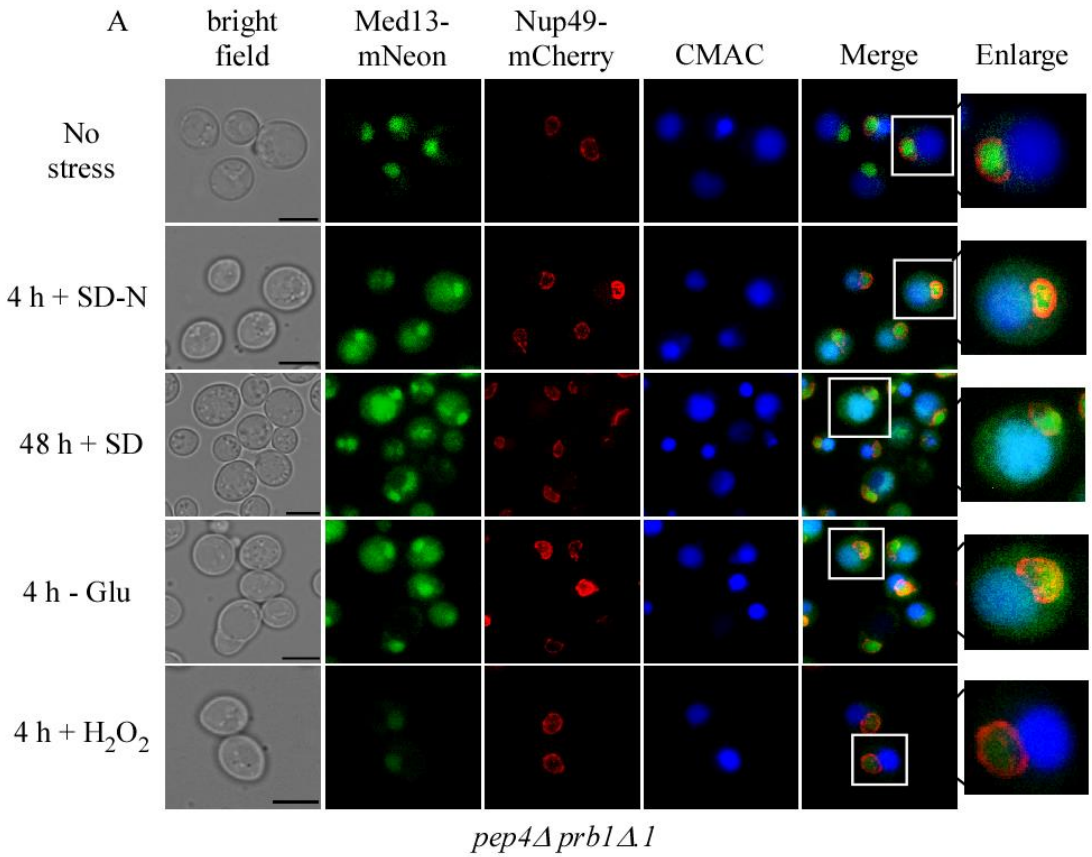

Figure 2. Med13 localizes to the cytosol in various forms of nutrient deprivation. **(A)** Fluorescence microscopy was used to monitor the localization of endogenous Med13-mNeongreen in a vacuolar protease-deficient strain. The nuclear was visualized using the nuclear marker, Nup49-mCherry, and vacuoles were observed using the vacuolar stain CMAC. Representative images are shown in various forms of stress. Scale bar = 5 μm.

To determine whether quiescence-induced cytosolic localization was unique to Med13, the localization of the cyclin C was also monitored during stationary phase. To capture transient cytosolic localization following starvation we used the autophagy-deficient strain, *atg8*Δ, which is defective in autophagosome biogenesis and allows for the cytosolic accumulation of autophagic substrates [95]. These experiments demonstrated that cyclin C was retained within the nucleus during stationary phase, whereas Med13 localized to the cytosol (Figure 3A). Interestingly, these studies also revealed that Med13 formed distinct cytosolic puncta following starvation in autophagy-deficient cells.

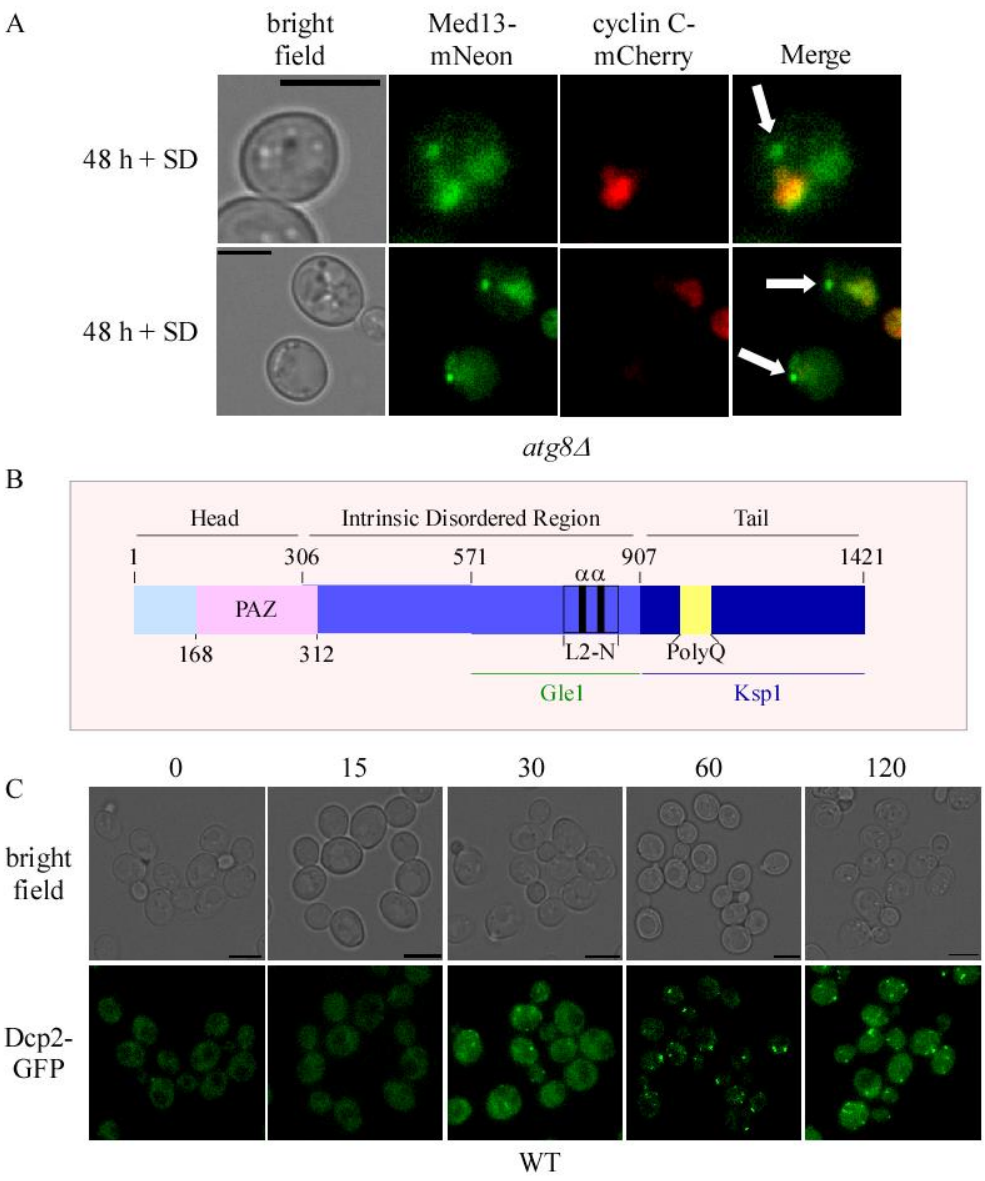

Figure 3. Processing bodies form in nitrogen starvation. **(A)** Fluorescence microscopy was used to monitor the localization of cyclin C-mCherry and Med13-mNeongreen during quiescence in *atg8*Δ cells. Representative images are shown. Scale bar = 5 μm. White arrows denote Med13 puncta. **(B)** Schematic of Med13 structural domains. Numbers denote amino acid residues and the different shades of blue signify the different structural regions of Med13. PAZ domains are shared among Argonaute/PIWI proteins and are required for nucleic acid binding. The L2-N are two small α-helices that block the RNA binding channel. The PolyQ region is a stretch of 15 glutamine residues. Interactive regions of Gle1 and Ksp1 are denoted. **(C)** Representative fluorescent microscopy images of P-body formation. WT cells expressing endogenous Dcp2-GFP were starved for nitrogen for the indicated time points. Scale bar = 5 μm.

Med13 localizes to P-bodies following starvation.

To determine if Med13 localizes to P-bodies following nitrogen starvation co-localization experiments were performed in *atg8*Δ cells expressing endogenous Med13-mNeongreen and core components of P-bodies, either Dcp2-mCherry or Edc3-mCherry [263]. The results demonstrate that Med13 and puncta overlap with both markers within the cytosol following starvation in *atg8*Δ (Figures 4A and B). Furthermore, Med13-mNeongreen also co-localized with Edc3-mCherry in stationary phase (Figure 4C), suggesting that this RNP granule role is a general response to nutrient deprivation. This is significant as it demonstrates that Med13 may perform a cytosolic stress-induced role at P-bodies.

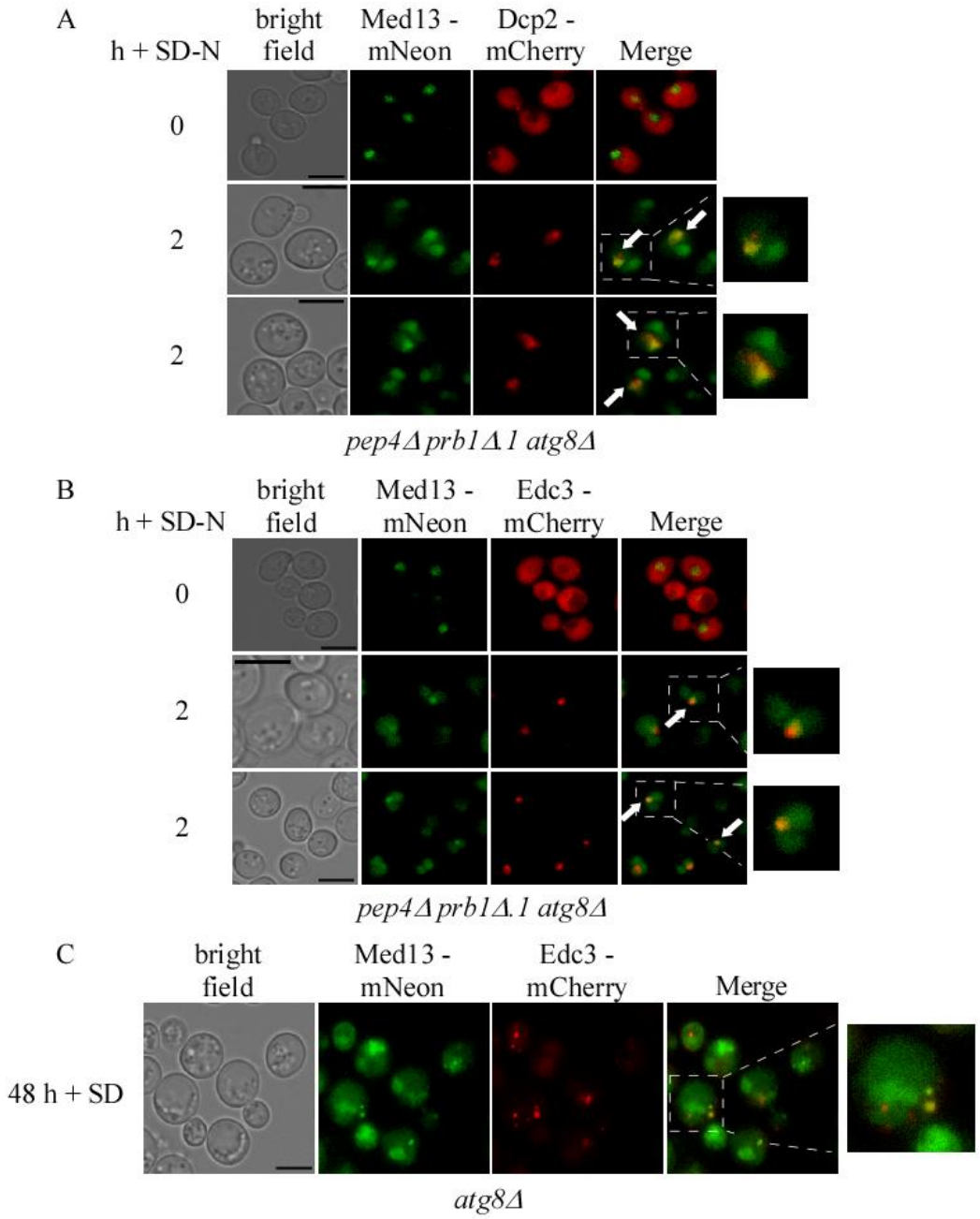

Figure 4. Med13 localizes to P-bodies following starvation. **(A-B)** Fluorescence microscopy was used to monitor the co-localization of Med13 with P-body proteins in nitrogen starvation. The autophagy and vacuolar protease deficient (*atg8Δ)* strain expressing genomically-tagged Med13-mNeongreen and harboring expression vectors encoding Dcp2-mCherry (top panel) or Edc3-mCherry (bottom panel) from their native promoters were starved for nitrogen for 2 hours. Representative images are shown. The white arrows denote the co-localization of Med13 and P-bodies. Scale bar = 5 μm. **(C)** Similar to A and B except experiments were performed in stationary phase.

Edc3 is degraded via autophagy following nitrogen starvation.

Previously, it has been shown that RNP granules are autophagic substrates in carbon starvation [257]. To determine if P-body components are autophagic substrates following nitrogen starvation, quantitative western blot analysis was performed. Endogenous Edc3-9MYC protein levels were monitored in wild-type and *atg8*Δ. These results show that Edc3 is degraded following nitrogen starvation but is stabilized in *atg8*Δ (Figures 5A and B) demonstrating that Edc3 is targeted for autophagic degradation.

Selective autophagy requires an autophagy receptor that binds exclusively to unique cargo and tethers these, substrates to the phagophore through Atg8 binding. The Atg8-interacting motif (AIM) of the receptor protein binds to the LC3-docking site (LDS) of Atg8, which results in the sequestration of cargos into autophagosomes [103,174]. Selective autophagic degradation of Med13 requires the LDS of Atg8, the sorting nexin Snx4, and the receptor protein Ksp1. To test if Edc3 is degraded using this selective autophagy mechanism, protein levels of endogenous Edc3-9MYC were monitored in *atg8*Δ cells harboring either a wild-type or LDS ($Atg8^{LDS}$) allele of Atg8. The results show that Edc3 is degraded upon nitrogen starvation with a half-life of ~2.5 h. Edc3 is actively targeted for degradation following stress as cycloheximide chase assays and revealed its half-life of Edc3 to be 9.8 h (Figure S4A, quantified in S4B). Significantly Edc3 was stabilized in $Atg8^{LDS}$ with a half-life of > 15 suggesting that Edc3 is degraded via selective autophagy (Figures 5C, quantified in 5B).

Edc3 autophagic degradation uses factors specific to Snx4-assisted autophagy of Med13

Med13 autophagic degradation is assisted by Snx4-Atg20 [3]and utilizes Ksp1 as an autophagic receptor [264] To address if Edc3 is similarly degraded, endogenous Edc3-GFP protein levels were monitored in *snx4*Δ and *ksp1*Δ following nitrogen starvation. Edc3 was significantly more stable in *snx4*Δ and *ksp1*Δ compared to wild-type cells (Figure 5D, quantified in 5E). Taken together these data show that Med13 and Edc3 are degraded in the same selective autophagy pathway.

For Ksp1 to function as an autophagy receptor for Edc3, these proteins must interact. To test if Edc3 and Ksp1 interact, yeast-two hybrid (Y2H) analysis was performed. Ksp1 is a 117 kDa protein containing a large IDR [265] therefore three Gal4-binding domain constructs that span the full-length protein was used (Figure 5F) [264]. The three Gal4-BD-Ksp1 subclones KD (kinase domain), DD1 (disordered domain 1), and DD2 (disordered domain 2) were expressed with Gal4-AD-Edc3. Y2H analysis revealed that Edc3 interacts with the C-terminal DD2 region of Ksp1 (Figure 5G). Interestingly, this is the same region that interacts with Med13 and Atg8. Previously, non-specific binding or self-activation of Gal4-BD-DD2 was ruled out using Y2H analysis with miscellaneous Gal4-AD constructs [264]. These results demonstrate that Ksp1 functions as the autophagic receptor protein for Edc3. Taken together this suggests a model (outlined in Figure 6A) in which Med13 and Edc3 co-localize in P-bodies, and they are consequently degraded by autophagy using Ksp1 as an autophagic receptor.

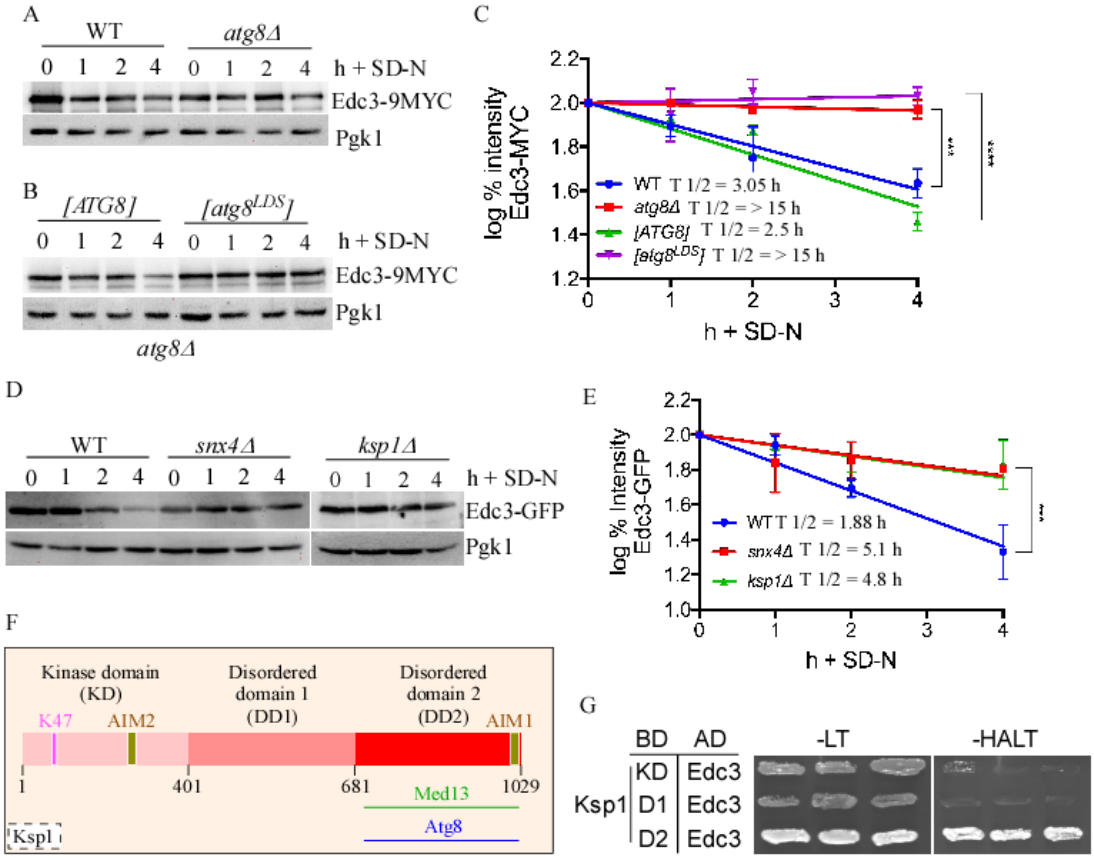

Figure 5. Edc3 is degraded via Ksp1-mediated autophagy. **(A-B)** Western blot analysis of endogenous Edc3-9MYC in WT, *atg8*Δ (top panel), or *atg8*Δ cells harboring either WT or LDS mutant alleles of Atg8 (bottom panel). Cells were grown to mid-log, washed, and resuspended in SD-N media for the indicated time points. Pgk1 protein levels were used as protein loading controls. **(C)** Quantification of A. Error bars indicate S.D. N=3 of biologically independent experiments. **(D)** Similar to A except endogenous Edc3-GFP protein levels were monitored in the indicated genotypes. **(E)** Quantification of C (**F**) Schematic of Ksp1 structural domains. Numbers denote amino acid residues. K47 denotes kinase-dead mutation and AIM mutations are shown. The interactive regions of Atg8 and Med13 are also signified. (**G**) Y2H Gold cells harboring the indicated Gal4-BD-Ksp1 subclones and Gal4-AD-Edc3. The cells were plated to medium selecting for plasmid maintenance (left panel, -LEU -TRP) or induction of the ADE2 and HIS3 reporter genes (right panel).

P-bodies form prior to their autophagic degradation

As Edc3 and Med13 localized to P-bodies before being degraded by Snx4-assisted autophagy we wanted to ask if Med13 P-bodies localization was required for its autophagic degradation. To address this, we first asked if Edc3 is required for P-body formation in nitrogen starvation. The results show that similar to other starvation conditions [266], deletion of Edc3 results in defects in P-body formation during nitrogen starvation (Figure S4C). Next, using quantitative western blot analysis we observed that Med13 was partially stabilized in *edc3*Δ compared to wild type. Together, these results suggest that as P-body assembly promotes Med13 degradation (Figure 6B, quantified in 6C) that Med13 first is a component of P-bodies, before its autophagic degradation.

Another possibility, however, is that Med13 and Edc3 co-localization is occurring at the phagophore assembly site (PAS). To test this, we asked if we could observe Edc3 foci that do not co-localize at the PAS (marked by GFP-Atg8) in cells defective in autophagosome-vacuolar fusion (*vam3*Δ) [267]. P-bodies formed prior to localizing to the PAS as Edc3-mCherry formed distinct puncta that were independent of Atg8 after 2 h in SD-N (Figure 6D). Lastly, if our predicted model is correct Med13 and Edc3 should co-localize in autophagosomes. In line with the previous results, Med13 and Edc3 puncta overlap following 24 h of nitrogen starvation in *vam3*Δ (change to Figure 6F). Taken together these data validate our model that Med13 localizes to P-bodies first, and then subsequently targeted to the PAS with Edc3 and degraded via Ksp1-mediated selective autophagy.

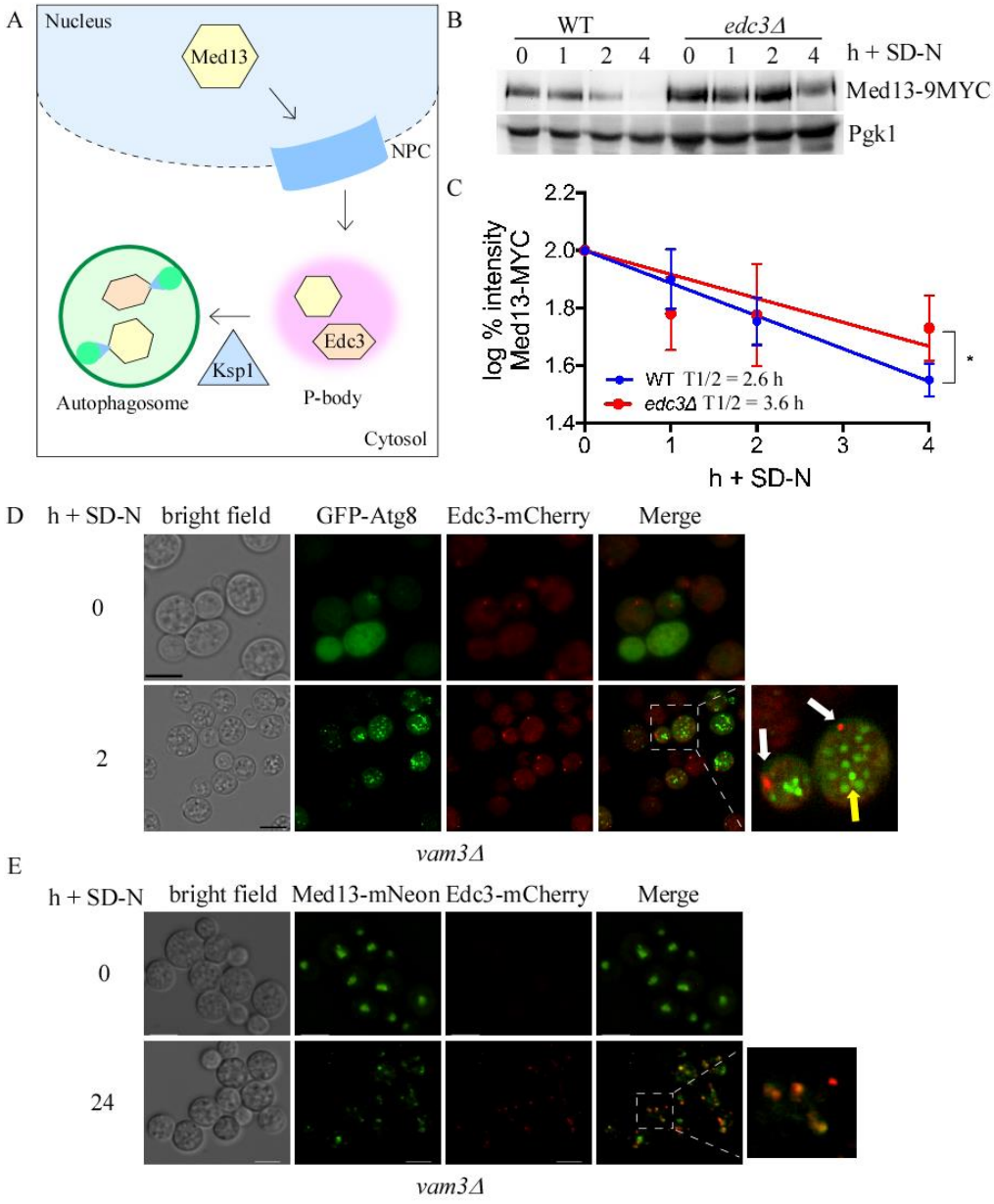

Figure 6. P-bodies form prior to localization to the PAS. (**A**) Schematic of the proposed model. Following starvation, Med13 is exported from the nucleus, localizes to P-bodies, and is subsequently degraded via autophagy with other P-body components. (**B**) Western blot analysis of endogenous Med13-9MYC protein levels in the indicated genotypes. Pgk1 was used as the protein loading control. (**C**) Quantification of B. Error bars indicate S.D. N=3 of biologically independent experiments. (**D**) Fluorescence microscopy was used to monitor the temporal formation of P-bodies and autophagosomes in a mutant defective in autophagosome-vacuole fusion (*vam3*Δ). Following 2 h of nitrogen starvation, Edc3-mCherry (white arrows) formed distinct puncta independent of GFP-Atg8 (yellow arrow). Scale bar = 5 μm.

Ksp1 selectively targets P-body components for autophagic degradation

P-bodies are composed of translationally repressed mRNAs and proteins involved with mRNA silencing and decay. Core P-body components include the decapping enzyme complex proteins Edc3 and Dcp2, as well as the helicase and exonuclease Dhh1 and Xrn1, respectively. In addition to these core components, P-bodies also contain auxiliary proteins such as the translation initiator factor eIF4G1 which is shown to localize to P-bodies following specific forms of stress such as stationary phase. Previously, Dhh1, Xrn1, Dcp2, and eIF4G1 were identified as potential components of the Ksp1 signal transduction network [194].

To determine if selective autophagy is used to degrade entire RNP granules or just selective components of P-bodies Dhh1, Dcp2, and Xrn1, protein levels were monitored following nitrogen starvation. Genomically-tagged alleles of these proteins were expressed in the indicated genotypes. Dhh1 was degraded in WT cells following 4 hours of nitrogen starvation. Interestingly like Edc3, Dhh1 was significantly stabilized in *ksp1*Δ and *snx4*Δ. Dhh1 protein half-life is 4.4 h, illustrating nitrogen starvation promotes the active degradation of Dhh1 (Figure S4D, quantified in S4E). Xrn1, Dcp2, and eIF4G1 were only partially degraded in 4 h of nitrogen starvation (Figure 7B, 7C, and 7D). This is important because this suggests that different mechanisms are used to degrade these components as their degradation kinetics vary temporally from Med13, Edc3, and Dhh1. Interestingly, Ksp1 is required for the partially autophagic degradation of Dcp2, but not Xrn1 or eIF4G. In addition, unlike granulophagy which delivers complete stress granules to autophagosomes [257] that individual proteins in P-bodies are specifically targeted for degradation.

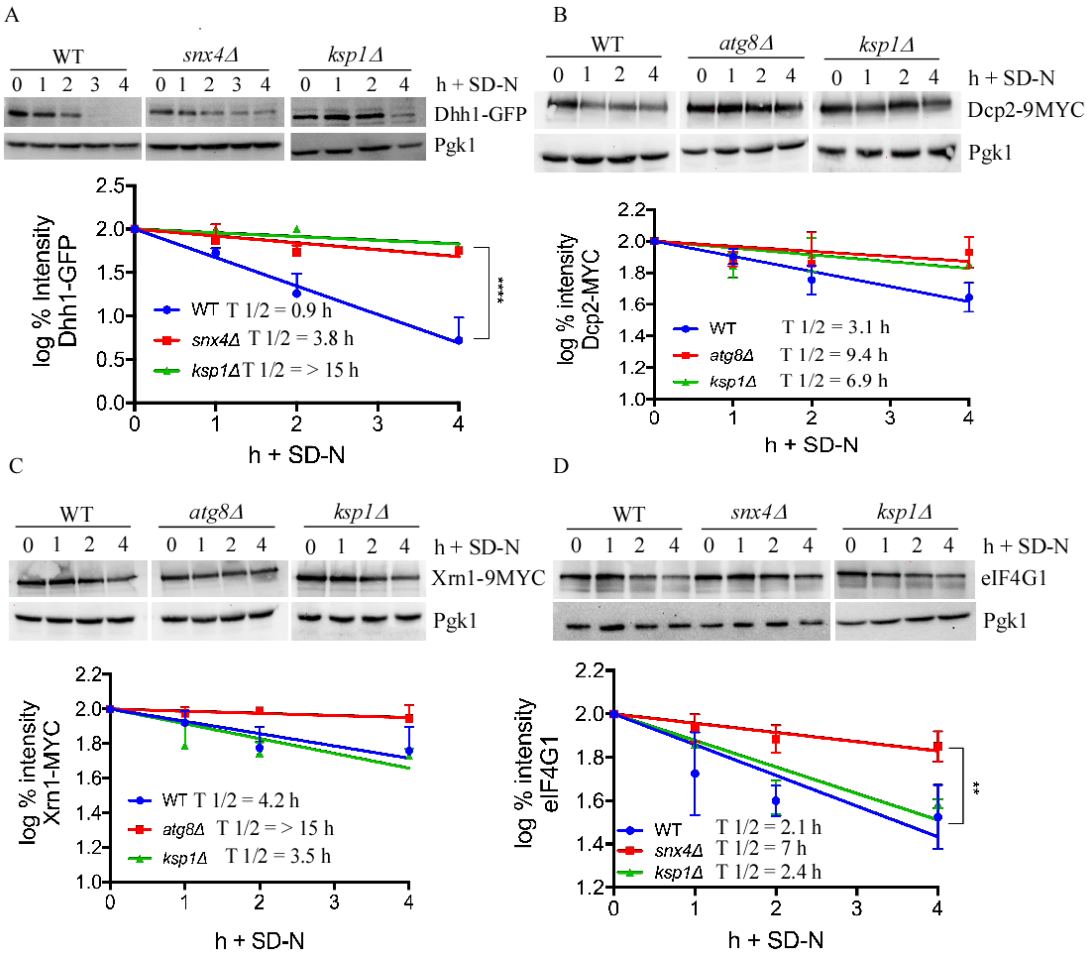

Figure 7. P-body proteins are selectively targeted for autophagic degradation**. (A)** Quantitative western blot analysis of endogenous Dhh1-GFP in the indicated genotypes following nitrogen starvation (top panel). Degradation kinetics and half-lives are shown (bottom panel). Error bars indicate S.D. N=3 of biologically independent experiments. **(B-D)** Similar to A except for protein levels of Dcp2-9MYC, Xrn1-9MYC, and eIF4G1 were monitored and quantified in the indicated genotypes following nitrogen starvation. Pgk1 was used as the protein loading control for all blots.

Selective autophagy of P-body components requires Med13

Here we have shown that selective P-body proteins, Edc3 and Dhh1, are degraded using the same Ksp1-mediated autophagy pathway as Med13. Therefore, we next asked if degradation of these P-body components requires Med13. Strikingly, Edc3-9MYC protein levels were stabilized in *med13*Δ cells (Figures 8A and 8B). In addition, GFP-fusion cleavage assays demonstrated that Dhh1-GFP autophagic degradation is drastically reduced in *med13*Δ, compared with wild-type (Figure 8C). Cleavage assays utilize the protease-resistant fold within the tertiary structure of GFP to monitor vacuolar proteolysis. Taken together, these data demonstrate that Med13 is required for the autophagic degradation of selective P-body components.

Med13 could potentially perform several roles within RNP granules. Med13 contains a large IDR which can function as a scaffolding component or mediate the formation of these granules. Med13 also contains potential RNA binding domains suggesting that Med13 can bind and sequester mRNA transcripts. To identify if Med13 is required for P-body formation, fluorescence microscopy was used to quantify Dcp2 and Edc3 foci formation in wild-type and *med13*Δ cells (Figure 8D). Interestingly, there was no difference in the quantity and size of Dcp2-GFP foci (Figure S5A-C), however, there was a significant decrease in Edc3-mCherry foci in *med13*Δ, compared to wild-type following nitrogen starvation (Figure S5D). Taken together, these data suggest that Med13 is required to concentrate a subset of P-body proteins to RNP granules or the PAS.

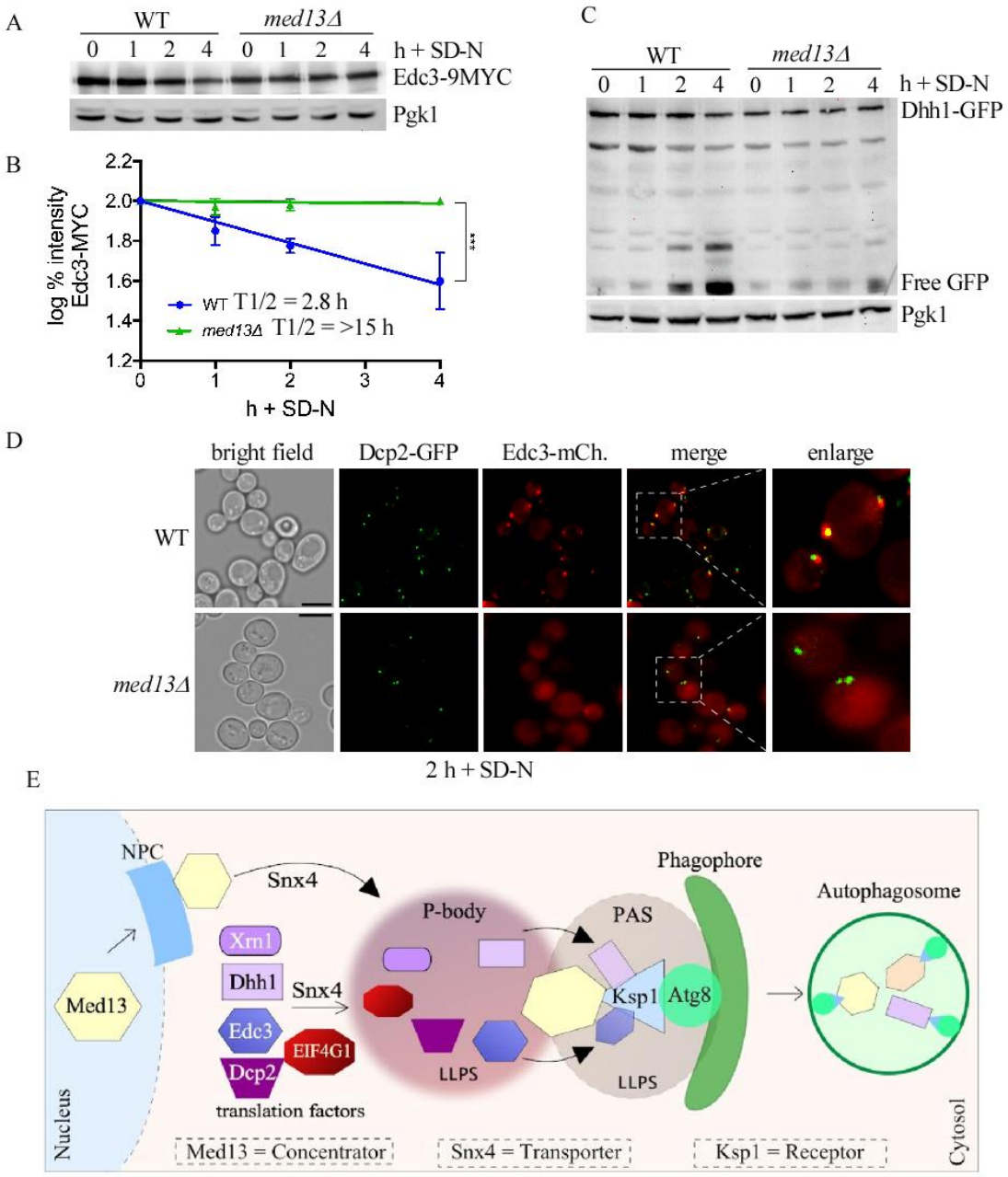

Figure 8. Med13 is required for the autophagic degradation of P-body proteins. **(A)** Western blot analysis of Ed3-9MYC protein levels in WT and *med13*Δ cells following nitrogen starvation. **(B)** Quantification of A. Error bars indicate S.D. N=3 of biologically independent experiments. **(C)** Western blot analysis of endogenous Dhh1-GFP protein levels in the indicated genotypes following SD-N. free GFP refers to the protease resistant GFP moiety that accumulates after the full-length fusion protein is degraded via the vacuole. **(D)** Fluorescence microscopy was used to monitor Dcp2-GFP and Edc3-mCHerry foci formation in WT and *med13*Δ. Scale bar = 5 μm. **(E)** Model of the cytosolic role of Med13 during starvation stress.

Discussion

Engineering proteins that can perform multiple independent functions allows cells to promptly coordinate many different cellular processes simultaneously. Here we show that Med13 plays dual roles in stress response mechanisms. In unstressed conditions, Med13 functions within the CKM as a negative regulator of *ATG* transcription [38] [3]. This control is relieved following nitrogen depletion as the CKM dissolves, and Med13 translocates out of the nucleus. Here it is consequently destroyed by Snx4-assisted autophagy, using Ksp1 as its receptor protein. Given the highly sophisticated nature of this pathway, we postulated that Med13 must have an important secondary cytoplasmic role (night job) following starvation. Here we show that Med13 is required for cell survival after nitrogen depletion, as cells deficient in Med13 have defects in quiescence entry and decreased viability during starvation. In addition, we demonstrate that Med13 localizes to P-bodies and is required for the autophagic degradation of two conserved P-body components following stress. Taken together, this supports a model in which Med13 plays a stress-induced role in the cytosol, where it mediates cell cycle arrest and is required for degradation of selective cargo.

Snx4 is required for other selective autophagy pathways including those targeting proteasomes, ribosomes, and fatty acid synthase [30]. More recently, Snx4 is required for the autophagic degradation of transcribing mRNAs encoding for amino acid biosynthesis and ribosomal proteins [244]. Here we show that Snx4 is also required for the autophagic degradation of all the P-body proteins we tested. However, Ksp1 is only required for the autophagic degradation of some of them. Taken together, this suggests a model in which Snx4 is most likely required to deliver substrates to P-

bodies. Ksp1 only acts as a receptor protein for Med13, Edc3, and Dhh1, whereas it is not required for the autophagic degradation of eIF4G1, Xrn1, or Dcp2. In addition, eIF4G1, Xrn1, and Dcp2 are degraded later, or more slowly compared to the substrates of Ksp1-mediated autophagy, suggesting different autophagy pathways are used to degrade P-body proteins.

Although these studies show that Med13 is required for Edc3 and Dhh1 degradation, how it executes this role remains unclear. Med13 contains a large IDR that can function as an interactive hub for multiple proteins. These disordered and unstructured regions are also essential features of proteins involved in LLPS [254]. LLPS has also been shown to be a fundamental component of PAS formation and pivotal in the concentration of autophagy machinery and substrates [258]. Here we show that Med13 is required for the selective autophagic degradation of P-body proteins. Only a unique subset of P-body proteins is degraded via this pathway, suggesting that there is an exclusivity factor that discriminates between different P-body components. Med13 may function as this exclusivity factor by binding and concentrating specific P-body proteins. Med13 may function as a consolidator and form dense assemblies of autophagy substrates.

As a second and not mutually exclusive model, Med13 could potentially bind to target RNAs and sequester them into RNP granules. Med13 and its bound RNA are then degraded via receptor-mediated autophagy. Along with potentially binding to RNA, Med13 also interacts with a variety of proteins involved in RNA metabolism including Gle1 and Ksp1 [148]. In favor of this model, Med13 was recently identified as a member of the Argonaute protein family, which is prominently known for its role

in RNA silencing. Med13 contains Ago-like structural features which form a narrow central nucleic acid channel [51]. Interestingly, during unstressed conditions two helices converge to cover the opening of this nucleic acid channel. The surrounding regions of these helices contain consensus sites for post-translational modifications. It can therefore be imagined that Med13's nucleic acid binding channel is inaccessible during unstressed conditions, however, during stress post-translational modifications can induce conformational changes and in turn make RNA binding accessible.

The persistence and dysregulation of RNP granules are closely associated with neurodegenerative diseases including ALS, dementia, and myopathies [268,269]. Autophagy is the prominent mode of degradation for RNP granules, however, the mechanism underlying this selective autophagy mechanism is unclear. Understanding how autophagy machinery targets and degrades RNP granules in the appropriate time and space is essential to delineating RNP granule maintenance.

CHAPTER 5

Cyclin C promotes proteolysis systems that suppress pre-pancreatic cancer progression in a murine tumor model

Abstract

The Cdk8 kinase module (CKM) regulates stress response pathways at multiple levels. Previous studies in yeast and mammalian systems demonstrate that the non-canonical cyclin within the CKM, cyclin C, plays both a transcriptional and mitochondrial role during stress. Specifically, cyclin C both represses and activates the transcription of genes involved in stress response and developmental processes. Studies in our laboratory demonstrated that cyclin C suppresses the formation of pre-cancerous lesions by 6-8-fold compared to the control group in the LSL-$Kras^{G12D}$ murine pancreatic cancer model. Interestingly, cyclin C is also required for normal pancreatic maintenance and function, as the absence of cyclin C results in islet atrophy and decreased insulin production. At the molecular level, I demonstrate that cyclin C promotes autophagy and proteasome activity in ductal lineage cell lines derived from these animals. Reduced proteolysis results in increased reactive oxygen species (ROS) and genomic instability. In addition, these cells are significantly more sensitive to the FDA-approved proteasome inhibitor Bortezomib. Given the role of autophagy in inhibiting pancreatic damage, these findings suggest a model that cyclin C suppresses pancreatic pre-cancerous lesions by preventing organ damage.

Introduction

The Cdk8 kinase module (CKM) functions as a detachable unit of the Mediator complex known to both negatively and positively regulate the transcription of ~ 3,000 genes in mouse embryonic fibroblasts (MEFs) [56]. The CKM is highly conserved and composed of four subunits: the cyclin, cyclin C (Ccnc), its cognate kinase Cdk8 or Cdk19, and one of each paralog Med12/Med12L or Med13/Med13L (Figure 1A). Previously, our laboratory has shown that transcriptional regulation via the CKM is very dynamic. CKM promoter occupancy can activate or repress transcription depending on the loci and stress conditions [56]. Many of the genes regulated by the CKM are associated with stress response, including those required for autophagy and regulated cell death pathways. In addition to transcription, the non-canonical cyclin, cyclin C, performs a stress-induced pro-apoptotic role, which involves the re-localization of a small subset of the nuclear cyclin C population to the cytosol [12]. Once in the cytosol, cyclin C interacts with mitochondrial fission machinery and pro-apoptotic factors such as Drp1 and Bax, respectively [57] [58] (Figure 1B). The duality of cyclin C as both a transcriptional and cell death regulator suggests a putative role for cyclin C as a tumor suppressor. The role of cyclin C as a tumor suppressor is exemplified in the case of T-cell-acute lymphoblastic leukemia (T-ALL) [60] and aggressive anaplastic thyroid cancer [59]. Studies investigating common mutations in human pancreatic cancer identified a small 500-kb region within the cyclin C locus that was deleted in 69% (38/55) of pancreatic cancers [270].

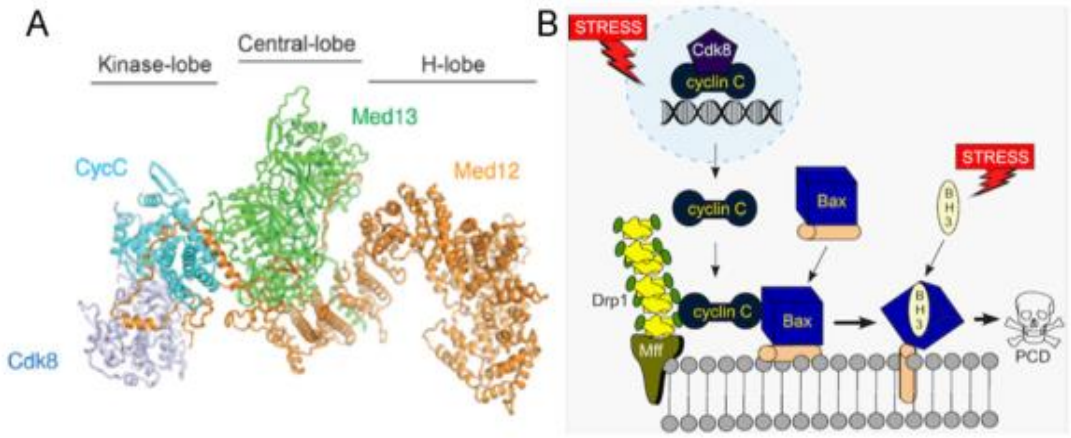

Figure 1. (A) Depiction of the Cdk8 kinase module (CKM). **(B)** Schematic of the stress-induced secondary pro-cell death role of cyclin C. Cyclin C promotes Drp1 oligomerization and mediates Bax mitochondrial localization.

Pancreatic cancer has a dismal 11.5% 5-year survival rate that is attributed to late-stage diagnosis, ineffective chemotherapy, or chemoresistance [1]. The two histological subtypes of pancreatic cancer are pancreatic ductal adenocarcinoma (PDAC) and pancreatic neuroendocrine neoplasm (PanNEN) which account for 90% and 3-5% of all pancreatic cancer cases, respectively [271]. PDAC progresses in a stepwise manner beginning with acinar-ductal metaplasia (ADM), progressing to pancreatic intraepithelial neoplasia (PanIN), and ultimately resulting in late-stage, metastatic cancer (Figure 2). The etiology of pancreatic cancer includes inherited genetic mutations, smoking or heavy drinking, diabetes, and chronic pancreatitis [1]. Acute or chronic pancreatitis can result from the dysregulation of pathways involved in zymogen activation, ER stress, and autophagy [272]. The pancreas functions as the major site of digestive protease production and secretion, therefore it is not surprising that cells within the pancreas are thought to have the highest rate of protein synthesis

compared to any other cell type. Defects in protein folding, sorting, or degradation within the pancreas can lead to aberrant zymogen activation, accumulation or aggregation of unfolded proteins, and increased levels of ROS. This results in recurrent or pro-longed injury or inflammation and increases the risk of pancreatic cancer [273].

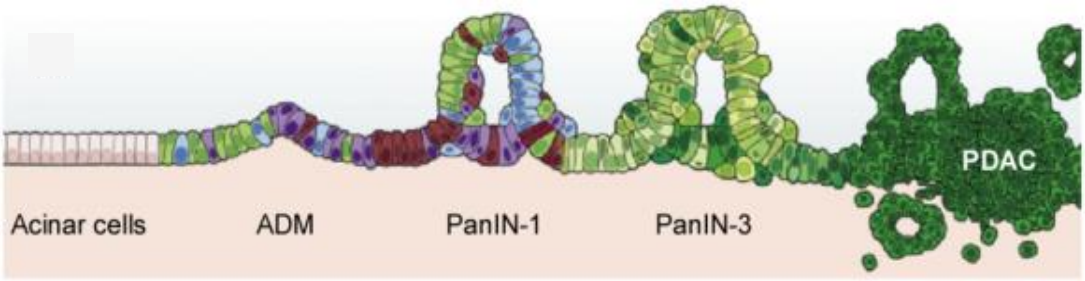

Figure 2. Depiction of pancreatic cancer progression [1].

Recent studies showed that activating mutations within *Kras* occur in 85.5% (665/775) of pancreatic tumor samples [273]. In the LSL-$Kras^{G12D}$ murine model, an oncogenic allele of *Kras* is transcribed only when Cre recombinase is expressed during pancreatic development [274]. This system is widely used and accepted within the field for inducing PDAC in mice [275]. In addition, 70% of advanced PDAC cases are associated with the inactivation of the tumor suppressor p53. The combination of oncogenic Kras activation and inactivation of p53 leads to the robust formation of pre-cancerous lesions by 10 weeks [276]. Although p53 is a common tumor suppressor in PDAC, it is not associated with all cases. Cyclin C has previously been identified as a tumor suppressor in the case of T-cell-acute lymphoblastic leukemia (T-ALL) [159] and aggressive anaplastic thyroid cancer [160]. Studies from our laboratory have shown

that the stress-induced mitochondrial role of cyclin C can alter drug sensitivity and viability in mouse embryonic fibroblasts (MEF) and thyroid cancer models [26,29].

Importantly, studies investigating common mutations in human pancreatic cancer identified a small 500-kb region within the cyclin C locus that was deleted in 69% (38/55) of pancreatic cancers [270]. In more directed studies, we in collaboration with Dr. Kerry Campbell's group, at the Fox Chase Cancer Institute found pancreatic-specific deletion of *Ccnc* in combination with oncogenic $Kras^{G12D}$ results in a 6-8-fold increase in cancerous lesions in eight-week-old mice. Strikingly, $Kras^{G12D}$ $Ccnc^{-/-}$ mice formed both PanIN and PanNEN lesions, which are rare but significant as the co-existence of these tumor types correlates with poor patient prognosis [277]. In addition, pancreatic-specific deletion of *Ccnc* alone results in significant islet atrophy and decreased insulin levels. At the molecular level, we show that cyclin C promotes proteolysis pathways such as autophagy and the ubiquitin-proteasome system (UPS). Together, we built a model in which cyclin C functions as a tumor suppressor by maintaining proteome homeostasis, thereby preventing pancreatic damage leading to pancreatic cancer.

Experimental Results

Cyclin C functions as a tumor suppressor in the LSL-$Kras^{G12D}$ pancreatic murine model and is required for normal pancreatic function.

To investigate the putative tumor suppressive role of cyclin C in this model, collaborators at the Fox Chase Cancer Institute mated LSL-$Kras^{G12D}$ mice expressing Cre recombinase under the pancreas-specific *Pdx1* promoter with *Ccnc*-floxed mice,

generating pancreas-specific homozygous *Ccnc*$^{f/f}$ knockout mice with oncogenic *Kras* (*Pdx1*-cre; LSL-*Kras*^{G12D}; *Ccnc1*$^{f/f}$ [273]. In these studies, *Kras*^{G12D} *Ccnc*$^{-/-}$ mice had a 6-8-fold increase in the appearance of pre-cancerous lesions as early as 8 weeks compared to the *Kras*^{G12D} *Ccnc*$^{+/+}$ mice (Figure 3A). Strikingly, in addition to PDAC lesions (ADM and PanIN), neuroendocrine neoplasms (NENs) were also identified in *Kras*^{G12D} *Ccnc*$^{-/-}$ animals, but not in the control group (Figure 3B). These data are significant as intermixed populations of PDAC and NEN tumor types are very rare but correlate with poor patient prognosis. Together, this demonstrates that cyclin C functions as a repressor for both PDAC and NEN tumor formation.

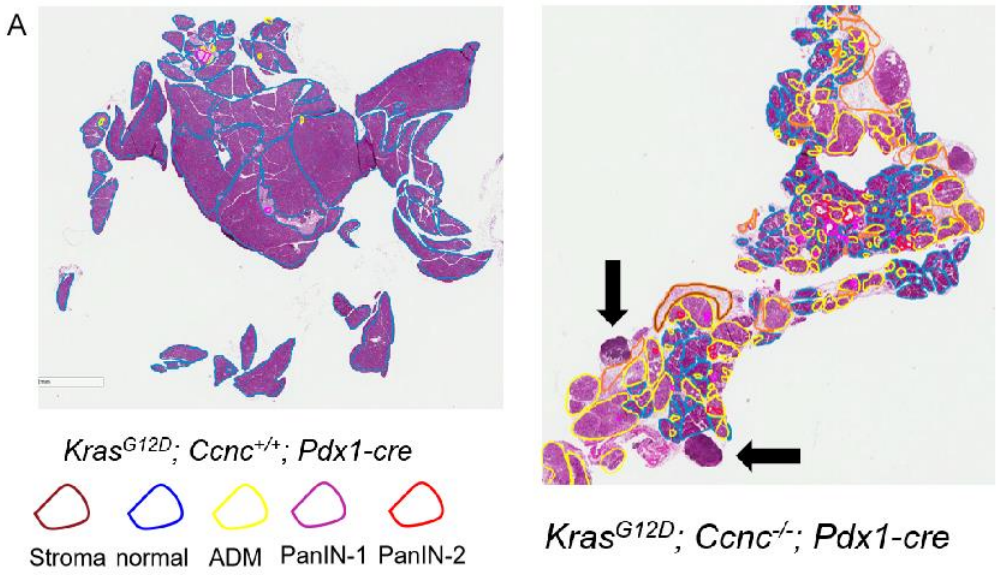

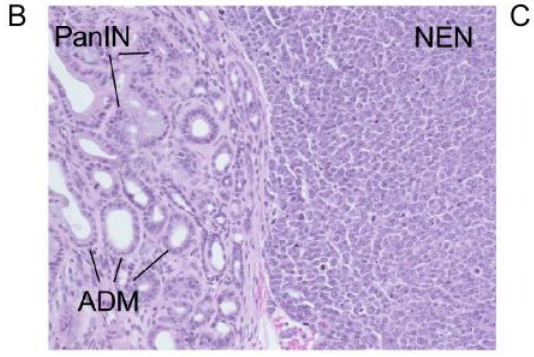

C

Genotype	weight 8 wks (g)	mM serum glucose
WT	19.0±1 (n=5)	5.15±0.22 (n=5)
Kras^{G12D+}	19.3±2.4 (p=0.9, n=3)	4.27±0.26 (p=0.02, n=6)
Ccnc$^{-/-}$; *Kras*$^{G12D+}$	17.8±0.7 (p=0.7, n=5)	5.05±0.7 (p=0.7, n=6)
Ccnc$^{-/-}$	15.1±0.8 (p=0.02, n=4)	15.5±1.8 (p=0.001, n=5)

Figure 3. Cyclin C functions as a tumor suppressor in PDAC progression. **(A)** H&E histopathology of tissue samples from indicated mice genotypes. Black arrows denote NEN regions. **(B)** H&E staining of tissue from a KrasG12D Ccnc-/- animal illustrating inter-mixed regions of ADM/PanIN and NEN. **(C)** Table outlining weight and serum glucose levels of indicated genotypes. These data were obtained from the Fox Chase Cancer Institute.

The loss of cyclin C in the pancreas alone does not promote tumorigenesis, however, pancreatic function is drastically disrupted in *Ccnc*$^{-/-}$ mice. Loss of cyclin C within the pancreas resulted in significant islet atrophy, which correlated with decreased insulin levels and hyperglycemia (Figure 3C). Interestingly, double mutant mice, *Kras*^{G12D} *Ccnc*$^{-/-}$, had similar serum glucose levels, compared to wild-type animals. One possible explanation is that cancerous cells upregulate glucose uptake and anaerobic metabolism to survive hypoxic or nutrient-deprived microenvironments. Oncogenic Kras mutations could thereby rescue the loss of cyclin C phenotype by increasing glucose uptake and reducing hyperglycemia.

Cell lines derived from the mouse models recapitulate PDAC *in vitro* systems

To determine the underlying molecular mechanisms occurring within these mice models, cell lines were derived from these animals. These cell lines were characterized using a variety of techniques to validate this *in vitro* system. PCR and western blot analysis were used to confirm the genotypes of these cell lines (Figure 4A-4C). In addition, western blot analysis was also used to monitor protein levels of Cdk8, the cognate kinase of cyclin C (Figure 4D). Lastly, to confirm that these cell lines were ductal cells, western blot analysis was used to monitor the exocrine-specific marker, cytokeratin 19 (CK19) [278] (Figure 4E). These analyses indicate that the *Kras*^{G12D} *Ccnc*$^{-/-}$ cell line is derived from a ductal lineage representing a pre-cursor to PDAC.

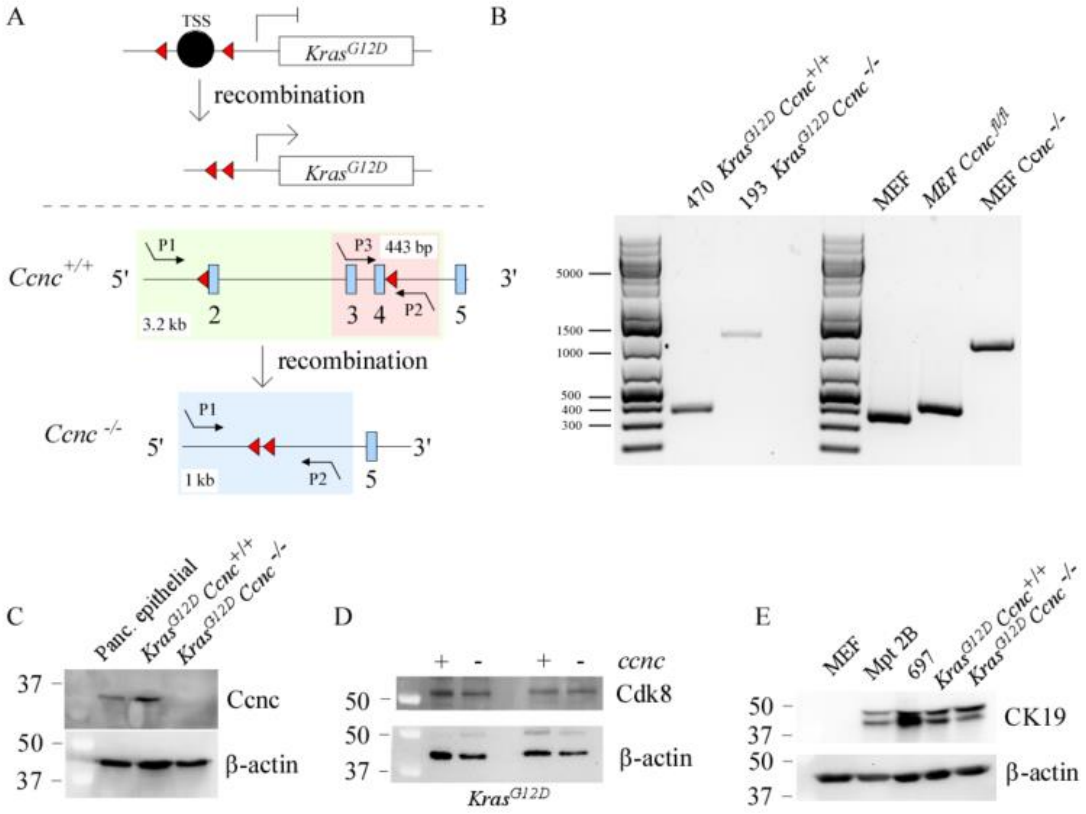

Figure 4. Characterization of PDAC cell lines. **(A)** Schematic of conditional oncogenic *Kras* and *Ccnc* knockout model [12]. The arrowheads denote loxP sites, the black circle denotes a transcriptional stop sequence, and the blue boxes denote exons. Primers used are denoted by P1, P2, and P3. The different colored boxes and numbers describe the size of different PCR products generated with the indicated primer sets. Cre-recombinase is under the control of the pancreas-specific *Pdx1* promoter and simultaneously activates transcription of oncogenic *Kras* and knocks out *Ccnc*. **(B)** PCR products of the indicated genotypes. Immortalized $Ccnc^{+/+}$, $Ccnc^{fl/fl}$, and $Ccnc^{-/-}$ MEF cell lines were used as controls. **(C)** Western blot analysis of Ccnc protein levels in the indicated cell lines. An immortalized pancreatic epithelial cell was used as a control (lane 1). **(D)** Western blot analysis of Cdk8 protein levels in the indicated PDAC cell lines. Results are shown in duplicate. **(E)** Western blot analysis of cytokeratin 19, CK19 in the indicated genotypes. An immortalized MEF cell and two other PDAC cell lines, Mpt2B and 697, were used as controls. β-actin protein levels were used as protein loading controls for all blots.

Cyclin C and its cognate kinase, Cdk8, regulate tumorigenesis through a variety of different mechanisms. Independent of its transcriptional role, cyclin C-Cdk8 mediated-phosphorylation of Stat3 and Notch intracellular domain (NICD) suppressors thyroid and leukemia tumorigenesis respectively [59,279] [280]. In addition, Smad4 inactivation through deletion or mutation occurs in over 60% of PDAC cases [281], therefore, to determine if other oncogenes or tumor suppressors were dysregulated in these PDAC models, western blot analysis was used to monitor p53, p21, Smad4, and NICD protein levels. The results indicate that these proteins were expressed at similar levels in these cell lines and suggest that cyclin C-mediated phosphorylation of these proteins is not required for PDAC suppression (Figure 5).

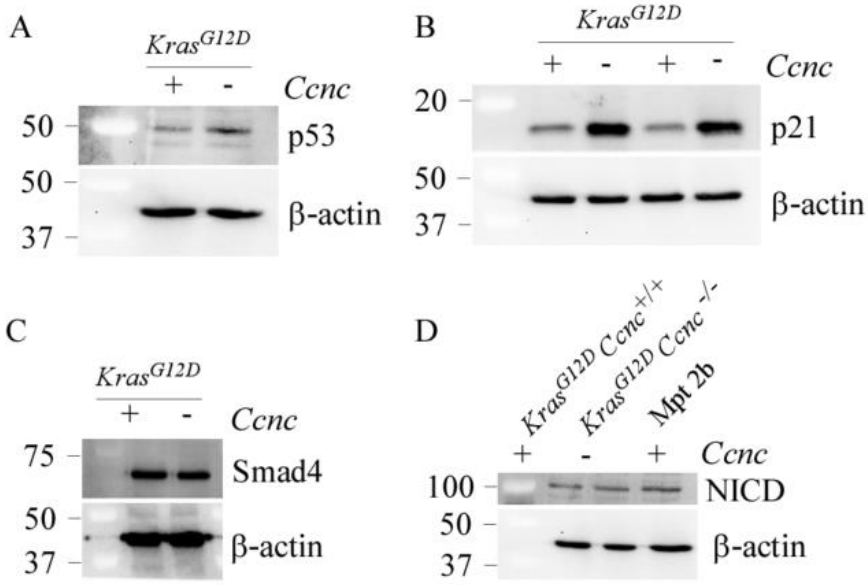

Figure 5. Other oncogenes or tumor suppressors are expressed at similar levels in PDAC cell lines. **(A)** Western blot analysis of the p53 protein levels in the indicated genotypes. **(B)** As in B except p21 protein levels are monitored. Experiments were shown in duplicate. **(C)** As in A, except SMAD4 protein levels are monitored. **(D)** As in A, except Notch intracellular domain (NICD) protein levels are monitored. The Mpt2b PDAC cell line was used as a control. β-actin protein levels were used as the protein loading control for all blots.

Cyclin C promotes autophagy in pancreatic *Kras^{G12D}* mouse model

Previously, our laboratory has shown that the CKM positively regulates the transcription of genes required for autophagy [56]. Autophagy is the catabolic mechanism necessary for the lysosomal degradation of excess, non-functional, or damaged macromolecules, organelles, and protein aggregates. Substrates degraded via autophagy are sequestered into double-membrane vesicles known as autophagosomes. The cargo within the autophagosome is degraded once the autophagosome fuses with the lysosome [282]. Defects in autophagy result in pancreatic injury, pancreatitis, and loss of pancreatic function [272].

To determine if the CKM promotes autophagy in our system, LC3 assays were performed. LC3 is a ubiquitin-like protein within the Atg8 family of proteins and is required for the maturation of autophagosomes and cargo recruitment. LC3 is first synthesized as LC3-I and quickly lipidated to form LC3-II following autophagy induction. Autophagy induction and flux can be monitored by treating cells with drugs such as Torin1 (autophagy inducer) and chloroquine (CQ, lysosomal inhibitor) and using western blot analysis to monitor LC3-I and LC3-II protein levels [283]. Torin1 promotes autophagy induction and upregulates LC3-I transcription and lipidation to LC3-II. Chloroquine inhibits lysosomal degradation of LC3-II, which allows it to accumulate within the cell. In *Kras^{G12D} Ccnc$^{+/+}$* cells LC3-II accumulates following treatment with both autophagy inducers and lysosomal inhibitors demonstrating autophagy induction and degradation can occur (Figure 6A). Interestingly, *Kras^{G12D} Ccnc$^{-/-}$* cells had drastically decreased levels of LC3-II indicating a defect in autophagy induction (Figure 6A). Similar results were also obtained by monitoring LC3 protein

levels, via indirect immunofluorescence (Figure 6B). To determine if this is a transcriptional role of cyclin C, *Kras*^{G12D} *Ccnc*$^{+/+}$ cells were pretreated with the Cdk8 kinase inhibitor, Senexin A before treatment with chloroquine and Torin1 (Figure 6C). These results showed that Cdk8 kinase inhibition mirrored *Kras*^{G12D} *Ccnc*$^{-/-}$ cells and suggests that the CKM functions as a transcriptional activator of autophagy.

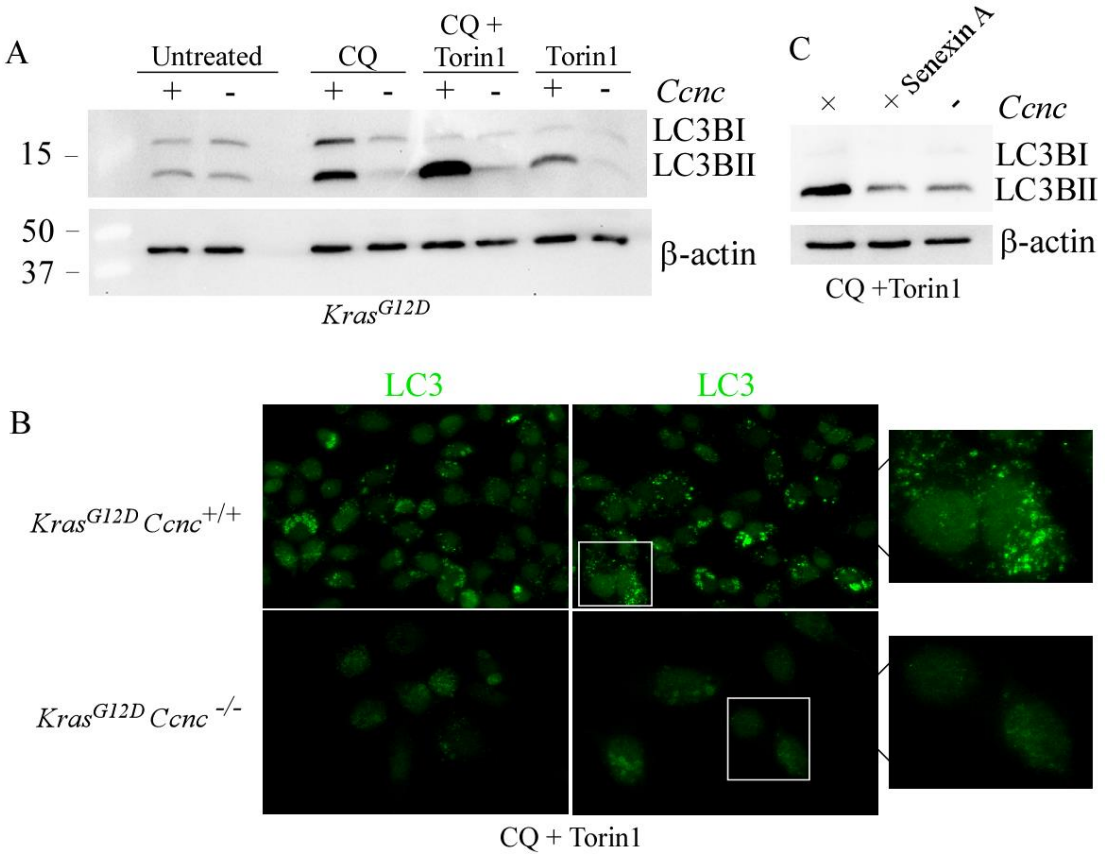

Figure 6. Cyclin C promotes autophagy in PDAC. **(A)** Western blot analysis of LC3 protein levels following 24 h treatment with Torin1 (250 nM), chloroquine (CQ, 100 μM), or both in indicated cell lines derived from the animal models. β-actin protein levels were used as protein loading controls. **(B)** Indirect IF was used to monitor LC3 protein levels in indicated genotypes following 4 h treatment of Torin1 and CQ. **(C)** Western blot analysis of LC3 protein levels following treatment with Torin1 and CQ. *Kras*^{G12D} *Ccnc*$^{+/+}$ cells were pretreated with Senexin A (0.4 mM) for 24 h.

The autophagy pathway utilizes at least 40 core proteins and multiple protein complexes. Western blot analysis was used to determine if other autophagy proteins were downregulated in *Kras*^{G12D} *Ccnc*$^{-/-}$ cells. [68]. There was no significant difference in protein levels between genotypes (Figure 7A), illustrating that the CKM upregulates a unique subset of autophagy genes.

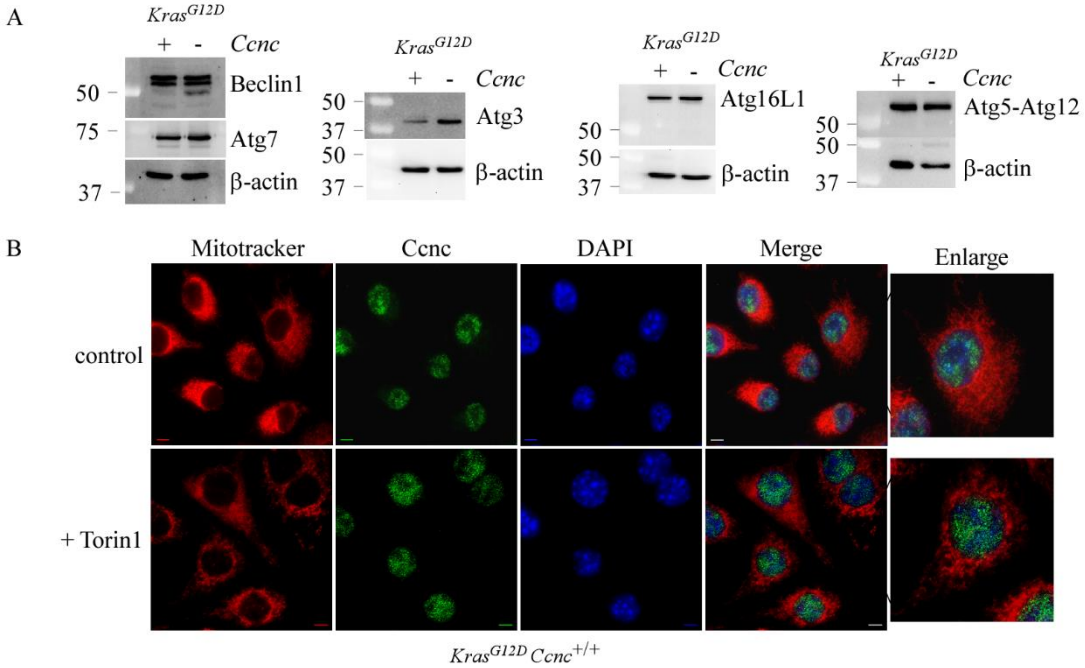

Figure 7. **(A)** Western blot analysis of the indicated autophagy proteins. β-actin protein levels were used as the protein loading control for all blots. **(B)** Indirect immunofluorescence was used to monitor cyclin C localization in unstressed conditions and following autophagy induction (250 nM Torin1 for 4 h). Nuclei and mitochondria were visualized using DAPI and mitotracker red respectively. Scale = 25 μm.

During oxidative stress a small nuclear portion of cyclin C re-localizes from the nucleus to the cytosol. In the cytosol, cyclin C promotes mitochondrial fragmentation and initiation of regulated cell death pathways [12] [57] [58]. To determine if cyclin C localizes to the mitochondria during autophagy induction, cyclin C localization, and mitochondrial morphology were monitored in unstressed conditions and following autophagy induction (Torin1 treatment). These results indicate that cyclin C is retained within the nucleus and mitochondria remain reticular, following autophagy induction (Figure 7B). Taken together these data suggest that the stress-induced mitochondrial role of cyclin C does not occur following autophagy induction.

Previously, it has been shown that defects in autophagy lead to increased ER stress, oxidative stress, proteotoxic protein aggregates, and genomic instability [284] [285]. Here we show that $Kras^{G12D}$ $Ccnc^{-/-}$ cells have increased cytosolic and mitochondrial ROS levels, compared to $Kras^{G12D}$ $Ccnc^{+/+}$ cells (Figures 8A and 8B). Minimal levels of ROS promote tumorigenesis by functioning as a signal for growth, proliferation, survival, and adaptation [286,287]. If the level of oxidative stress exceeds a certain threshold ROS becomes deleterious to the cell and perturbs cellular functions, such as mitochondrial integrity. However, mitochondrial morphology and membrane potential were similar between genotypes (Figure 8C and 8D). Similar to other PDAC studies [286,287], these data suggest that ROS levels are maintained at elevated concentrations, which may be advantageous for viability and tumorigenesis.

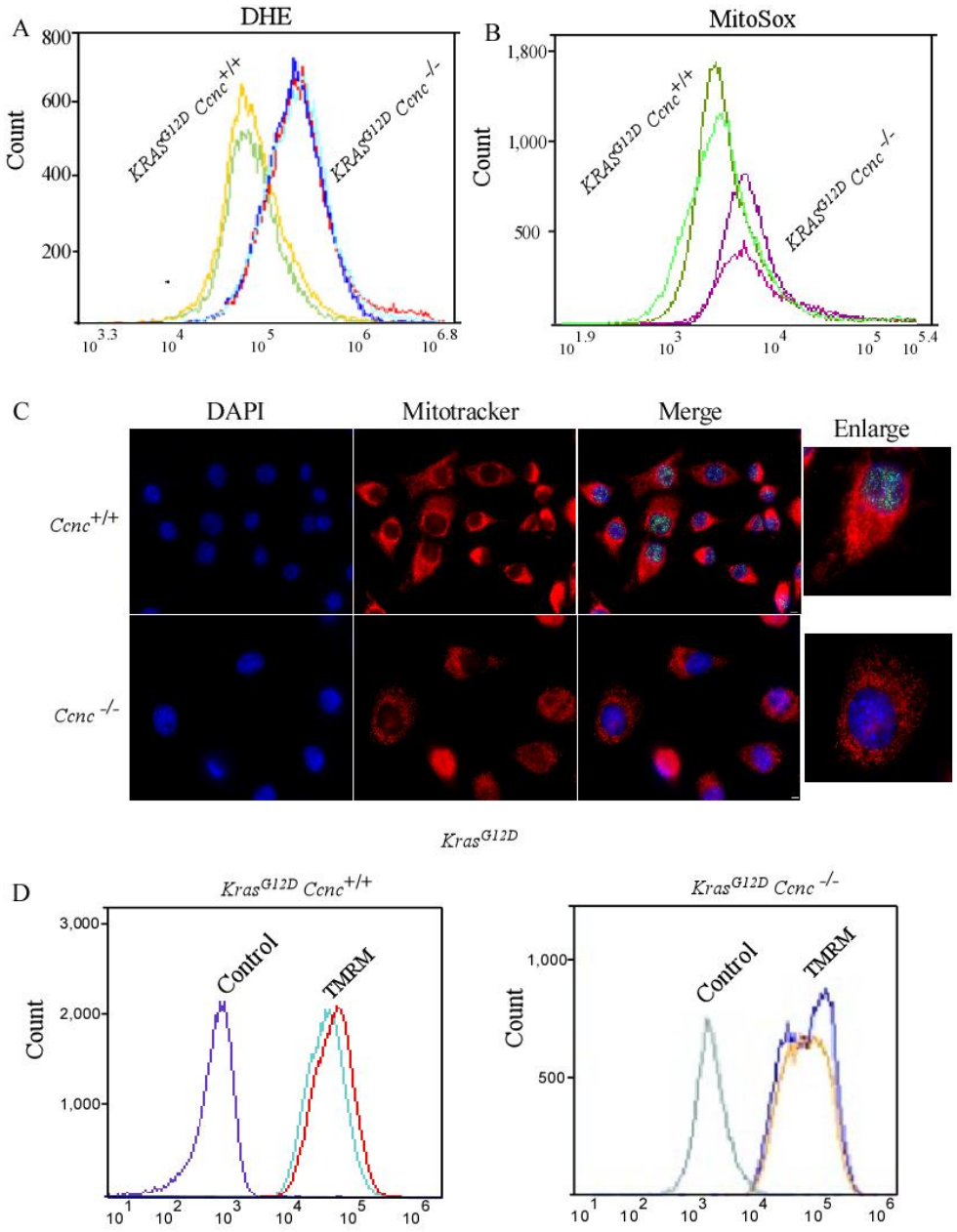

Figure 8. Decreased autophagy results in elevated levels of ROS and p62 as well as genomic instability. **(A)** Flow cytometry analysis of cytosolic ROS levels using the fluorescent redox-sensitive probe, DHE was performed in the indicated genotypes. Overlapping lines indicated biological replicates. **(B)** Similar to A except cells were dyed with the fluorogenic mitochondrial specific dye, Mitosox. **(C)** Fluorescence microscopy was used to monitor mitochondrial morphology in the indicated genotypes. Nuclei and mitochondria were visualized using DAPI and mitotracker red respectively. **(D)** Flow cytometry analysis of mitochondrial membrane potential using the fluorescent dye, TMRM. Control signifies unstained cells. Overlapping lines indicated biological replicates.

Under physiological conditions, the autophagy receptor, p62, is degraded via basal autophagy [283]. Defects in the autophagy pathway result in the accumulation of p62 in the cytosol. If not degraded, p62 can form proteotoxic aggregates which have been associated with many neurodegenerative diseases [288]. Correlating with our previous data, p62 protein levels were elevated in *Kras*^{G12D} *Ccnc*$^{-/-}$ cells compared to *Kras*^{G12D} *Ccnc*$^{+/+}$ cells (Figure 9A). Autophagy has previously been shown as a vital component of genome maintenance. Defects in autophagy result in increased DNA damage, abnormal nuclear architecture, and aneuploidy [289] [284]. *Kras*^{G12D} *Ccnc*$^{-/-}$ cells also exhibited a high degree of aneuploidy and abnormal nuclear structure (Figure 9B, 9C, and 9D). Lastly, increases in cell size correlate with increases in cellular biomass, which occurs when biosynthetic rates are greater than catabolic rates [290]. Here we show that *Kras*^{G12D} *Ccnc*$^{-/-}$ cells were significantly larger in size compared to *Kras*^{G12D} *Ccnc*$^{+/+}$ cells (Figures 9E and 9F). Taken together these data demonstrate that autophagy inhibition in *Kras*^{G12D} *Ccnc*$^{-/-}$ cells results in the accumulation of ROS, proteotoxic aggregates, aneuploidy, and an increase in cell size.

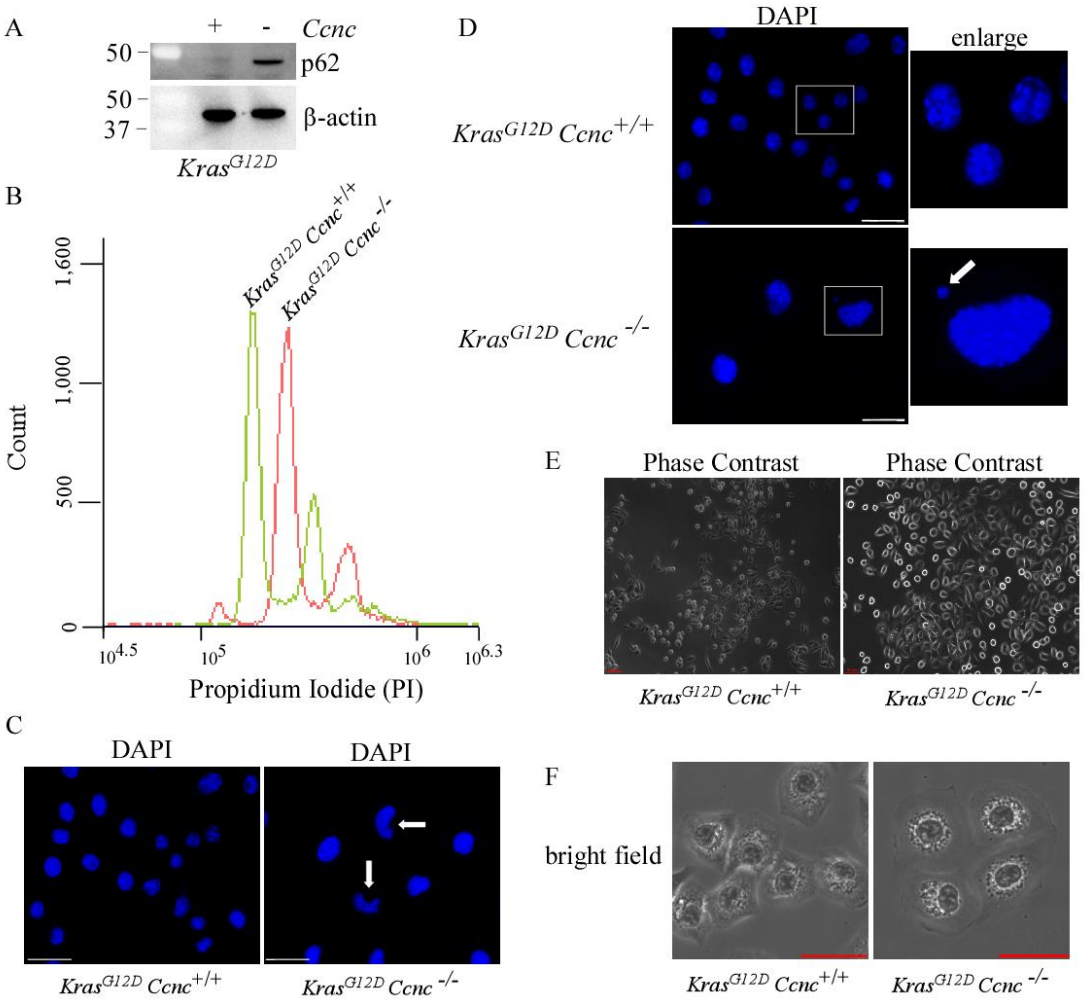

Figure 9. Decreased autophagy results in elevated levels of ROS and p62 as well as genomic instability. **(A)** Western blot analysis was used to monitor protein levels of the autophagy receptor, p62/SQSTM1. β-actin protein levels were used as the protein loading control. **(B)** The quantity of genetic material was monitored using the fluorescent stain PI and flow cytometry. Interestingly, *Kras*^{G12D} *Ccnc*$^{-/-}$ cells appear to be triploidy. **(C** and **D)** Fluorescence microscopy was used to monitor nuclear abnormalities. Cells were fixed and stained with the nuclear marker, DAPI. *Kras*^{G12D} *Ccnc*$^{-/-}$ cells have significantly larger nuclei and abnormal nuclear structure. The white arrow denotes abnormal structure and nuclear blebbing. 1000x magnification representative images are shown. Scale = 25 μm. **(F** and **F)** Phase contrast and brightfield microscopy were used to monitor cell morphology. 20x magnification representative images are shown. Scale = 50 μm.

Cyclin C is required for efficient proteasomal activity in the pancreatic *Kras^{G12D}* mouse model

Lysosomal- and proteasomal-mediated degradation are the two major modes of proteolysis within the cell. To compensate for defects in autophagy or lysosomal degradation, cells upregulate proteasome activity [291]. To monitor proteasomal degradation, whole-cell lysates were prepared and incubated with a fluorogenic substrate (Suc-LLVY-AMC) to detect chymotrypsin activity [292]. Fluorescence occurs only after the cleavage of this substrate and is measured by a plate reader every 15 minutes for a duration of 90 minutes. Proteasome inhibitors are used as controls to measure UPS-independent cleavage due to cytosolic proteases or aberrant degradation. Strikingly, *Kras^{G12D} Ccnc$^{-/-}$* cells had a significant decrease in proteasomal activity, compared to *Kras^{G12D} Ccnc$^{+/+}$* cells (Figure 10A). Taken together, these data suggest that *Kras^{G12D} Ccnc$^{-/-}$* cells have decreased proteasomal activity and are more sensitive to proteasome inhibitors.

To determine if Cdk8 kinase activity is required for upregulating proteasome activity, *Kras^{G12D} Ccnc$^{+/+}$* cells were pretreated with the Cdk8 kinase inhibitor, Senexin A. These results demonstrate that *Kras^{G12D} Ccnc$^{+/+}$* cells treated with Senexin A partially phenocopy *Kras^{G12D} Ccnc$^{-/-}$* (Figure 10B), suggesting that the CKM is a transcriptional activator of proteasomal-mediated degradation. Senexin A inhibits Cdk8 kinase activity [293], therefore kinase-independent transcriptional regulation imposed by the CKM can also be at play. Lastly, we wanted to determine if autophagy inhibition affected proteasome activity. Interestingly, treating *Kras^{G12D} Ccnc$^{+/+}$* cells with chloroquine results in a significant decrease in proteasome activity (Figure 6C).

One hypothesis for these results is that inhibition of one proteolysis system results in the inundation of the other. If the lysosome is inhibited the proteasome may be clogged with substrates that are either too big or cannot be easily denatured.

To determine if decreased proteasome activity was due to decreased quantities of proteasome subunits, western blot analysis was used to monitor protein levels of both the core (20S) and lid (19S) complexes of the 26S proteasome. Interestingly, there were no differences observed in protein levels between genotypes, suggesting that the decrease in activity was not due to fewer proteasomes (Figures 10D and 10E). The proteasomal-ubiquitin system is very complex and is regulated on multiple levels. Decreases in activity can be a result of defects in many different pathways such as autophagy, ubiquitin conjugation, ATPases, and chaperones.

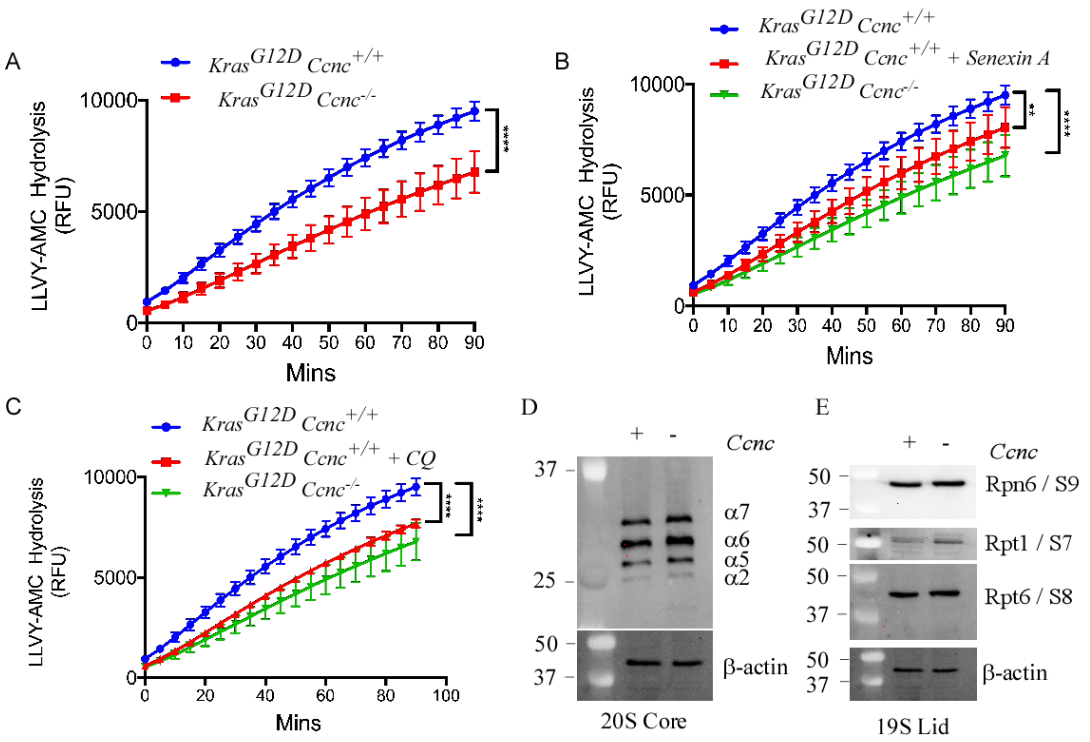

Figure 10. Cyclin C promotes UPS activity in PDAC. **(A)** Proteasome activity assays were performed using the fluorogenic substrate, Suc-LLVY-AMC. This peptide fluoresces following hydrolysis via chymotrypsin-like proteases. Whole-cell lysates were prepared from unstressed cells, normalized by protein concentration, and incubated with the fluorogenic substrate. Fluorescence (LLVY-AMC hydrolysis) was measured over time. **(B)** Similar to A except *Kras*^{G12D} *Ccnc*$^{+/+}$ cells were treated with 0.4 mM Senexin A for 24 h prior o harvesting. **(C)** Similar to A except *Kras*^{G12D} *Ccnc*$^{+/+}$ cells were treated with 100 μM CQ prior to harvesting. **(D** and **E)** Western blot analysis of the indicated proteasome subunits from unstressed *Kras*^{G12D} *Ccnc*$^{+/+}$ or *Kras*^{G12D} *Ccnc*$^{-/-}$ cells. β-actin protein levels were used as protein loading controls.

The absence of cyclin C sensitizes cells to proteasome inhibitors.

The finding that *Kras*^{G12D} *Ccnc*$^{-/-}$ cells are deficient in lysosomal and proteasomal mediated degradation prompted the question of whether these cells were sensitive to autophagy and proteasomal inhibitors. To test this, we monitored viability following treatment with autophagy inducers, autophagy inhibitors, and proteasome inhibitors. Autophagy induction did not result in cell death in either genotype. However, *Kras*^{G12D}

Ccnc$^{+/+}$ cells had increased cell death compared to *Kras*^{G12D} *Ccnc*$^{-/-}$ cells following treatment with the autophagy inhibitor chloroquine (Figure 11A). Previously it has been shown that cancer cells can become "autophagy addicted" [294]. The increased energetic demands of cancer cells can be fueled by autophagy. Cancer cells become dependent on autophagy for survival during periods of starvation, hypoxia, and toxic chemotherapy drug treatments. It has been shown that autophagy-addicted, or dependent cells are sensitive to autophagy inhibitors and a combination of autophagy inhibitors with other drug treatments results in synergistic effects [295]. These data may suggest that *Kras*^{G12D} *Ccnc*$^{+/+}$ cells are sensitive to autophagy inhibitors because they are autophagy-dependent, however, *Kras*^{G12D} *Ccnc*$^{-/-}$ cells are resistant to autophagy inhibitors.

Next, we monitored viability following treatment with proteasome inhibitors. Here we demonstrate that *Kras*^{G12D} *Ccnc*$^{-/-}$ cells have a 2-3 fold increase in cell death compared to *Kras*^{G12D} *Ccnc*$^{+/+}$ cells following treatment with proteasome inhibitors such as MG132 and the FDA-approved inhibitor, Bortezomib (Figure 11B). Before a drug can be approved for use, efficacy and toxicity studies must be conducted. To determine the concentration of Bortezomib that efficiently induce PCD *Kras*^{G12D} *Ccnc*$^{-/-}$ cells but does not affect untransformed pancreatic cells, titration curves were performed with *Kras*^{G12D} *Ccnc*$^{-/-}$ cells, *Kras*^{G12D} *Ccnc*$^{+/+}$ cells, and quiescent or dividing immortalized pancreatic epithelial cells (Figure 11C). Quiescent epithelial cells were used to best imitate cells within the body which are predominantly not divided. As expected, proliferating untransformed cells were more sensitive than quiescent cells to proteasome inhibition. Most importantly *Kras*^{G12D} *Ccnc*$^{-/-}$ cells were more sensitive to

proteasome inhibitors compared to any of the control conditions. These data show that we can target more aggressive cancer cells such as *Kras*^{G12D} *Ccnc*$^{-/-}$ cells with proteasome inhibitors.

Next, we sought to determine if we can phenocopy drug sensitivity in *Kras*^{G12D} *Ccnc*$^{+/+}$ cells using the FDA-approved Cdk8 inhibitor, Sel120. *Kras*^{G12D} *Ccnc*$^{+/+}$ cells pretreated with Cdk8 inhibitors mirror Bortezomib drug sensitivity in *Kras*^{G12D} *Ccnc*$^{-/-}$ cells (Figure 7C). Together, this provides insight into the effects of different drug combinations such as Cdk8 inhibitors, autophagy inhibitors, and proteasome inhibitors. Lastly, we asked if these drug combinations could be effective in promoting cell death in other cancer models such as the colorectal cancer model, HCT116. Strikingly, cells defective in cyclin C or Cdk8 kinase activity were more sensitive to proteasome inhibitors, compared to the control groups. These data expand the efficacy of these drug combinations to other Kras-driven cancer models.

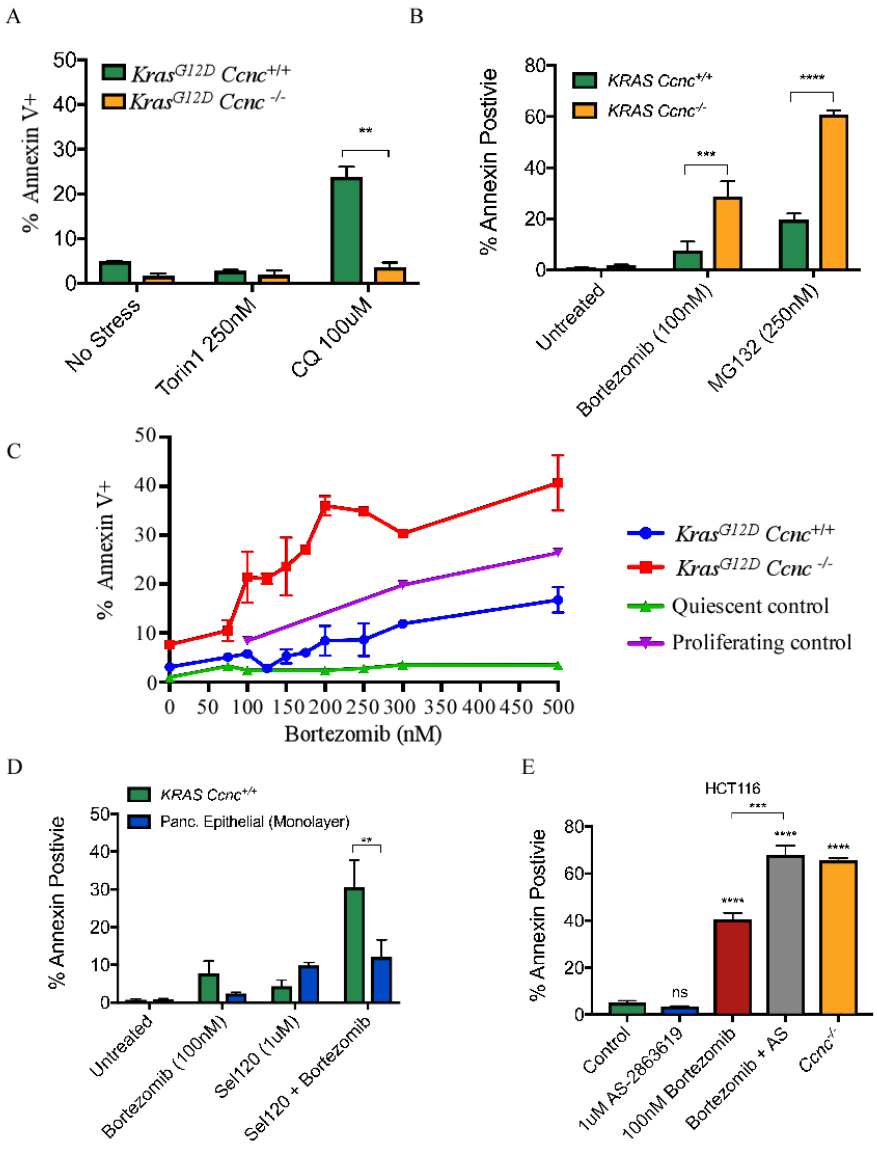

Figure 11. Cells defective in cyclin C are sensitive to proteasome inhibitors. **(A)** Flow cytometry was used to quantify annexin V positive (apoptotic) cells within the population following Torin1 (250 nM) or chloroquine (CQ, 100 μM) 24 h treatment. **(B)** Flow cytometry was used to quantify viability following 24 h treatment with the indicated proteasome inhibitors. N=3 of biologically independent experiments. **(C)** Titration curves were generated in the indicated genotypes following 24 h of treatment. Immortalized, untransformed quiescent or dividing pancreatic epithelial cells were used as a control. **(D)** Viability in the indicated cell lines was monitored using flow cytometry. Cells were pretreated with the Cdk8 inhibitor Sel120 for 24 h prior to 24 h Bortezomib treatment. **(E)** Flow cytometry was used to monitor the viability of HCT116 human colorectal cancer cells following the indicated drug treatments. AS-2863619 is a small molecule Cdk8 inhibitor. Statistical significance compared to the control is shown.

Discussion

The asymptomatic nature and rapid progression of pancreatic cancer result in poor patient prognosis and extraordinarily low survival rates. The thick, dense fibrous stromal microenvironment, and significant heterogeneity of PDAC, render current therapeutic strategies ineffective [296]. In particular, pancreatic cancer is thought to have a very high degree of inter- and intra-tumor heterogeneity, encompassing different tumor types, varying in differentiation status, proliferation rates, and drug sensitivities [297]. These factors make tailoring effective drug regimens very difficult. This is exemplified by evidence demonstrating that the co-existence of different tumor subtypes, such as pancreatic ductal adenocarcinoma (PDAC) and pancreatic neuroendocrine neoplasm (PanNEN), is associated with poorer patient prognosis [277].

This study describes the putative role of cyclin C as a tumor suppressor in the pancreatic $Kras^{G12D}$ mouse model and identifies cyclin C as a PDAC and PanNEN suppressor, and a critical component of pancreatic homeostasis and function. Data obtained by Dr. Kerry Campbell's group at the Fox Chase Cancer Institute showed that pancreas-specific deletion of *Ccnc* in the presence of oncogenic Kras resulted in the rapid formation of intermixed, heterogeneous populations of various tumor subtypes including early-stage PDAC lesions (ADM/PanIN), as well as non-functional, high and low grade, poorly differentiated NEN.

A major cause of pancreatic cancer is chronic, recurrent, or prolonged pancreatic injury and pancreatitis. Our collaborators at Fox Chase also demonstrated that the deletion of *Ccnc* alone resulted in significant metabolic disturbances reminiscent of pancreatic injury. Pancreas-specific deletion of *Ccnc* during

development resulted in islet atrophy, decreased insulin, hyperglycemia, and decreased weight in these animals.

Here, we propose a model in which the transcriptional role of cyclin C is required for tumor suppression. However, pancreas-specific deletion of Cdk8 (Figure 12), in combination with activation of oncogenic Kras, did not show an increase in pre-cancerous lesion formation compared to the control group. One explanation is that Cdk8 activity can be substituted with the closely related paralog, Cdk19. These paralogs may function redundantly and Cdk19 could activate autophagy and proteasome activity in the absence of Cdk8. The kinase domain of Cdk8 and Cdk19 share 97% sequence identity, therefore kinase inhibitors cannot discriminate between Cdk8 and Cdk19 [50]. This could explain why pharmacological inhibition of Cdk8/Cdk19 kinase activity mirrored *Ccnc*$^{-/-}$ phenotypes.

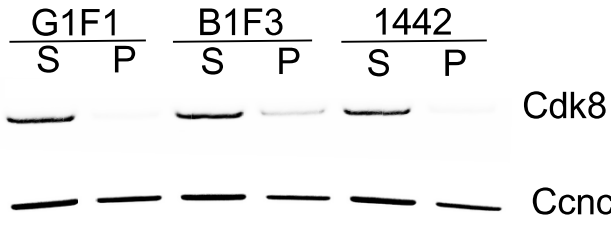

Figure 12. Confirmation of pancreas-specific deletion of Cdk8. PCR products of *Cdk8* and *Ccnc* were obtained from DNA derived from either the spleen (S) or the pancreas (P). Three biological replicates are shown.

At the molecular level, cyclin C functions to promote autophagy and proteasomal degradation (Figure 13A). In the absence of cyclin C, there is an increase in ROS and genomic instability (Figure 13B) which correlates with the defects in pancreatic function seen in the animal studies. Following pancreatic injury or inflammation, cells enter a reparative state in which cells either go through cell death or repair pathways. To reestablish homeostasis and restore healthy tissue, cells will de-differentiate and re-differentiate [21]. Oncogenic Kras mutations repress

redifferentiation pathways and promote tumorigenesis (Figure 13C). Cyclin C, therefore, functions as a tumor suppressor by maintaining proteome integrity and reducing the risk of pancreatic dysfunction.

Autophagy plays opposing roles during different stages of tumorigenesis. In the early stages of tumorigenesis, autophagy inhibits tumor formation under physiological conditions by decreasing ROS, mitochondrial defects, DNA damage, and inflammation, and promoting cell death. In later stages of tumorigenesis, autophagy promotes survival and metastasis by providing nutrients during periods of hypoxia and nutrient deprivation and decreasing stress sensitivity. In these studies, we demonstrate that autophagy may play tumor suppressive roles in the Kras pancreatic murine model, as deletion of cyclin C and subsequent autophagy inhibition results in the formation of pre-cancerous lesions as early as 8 weeks.

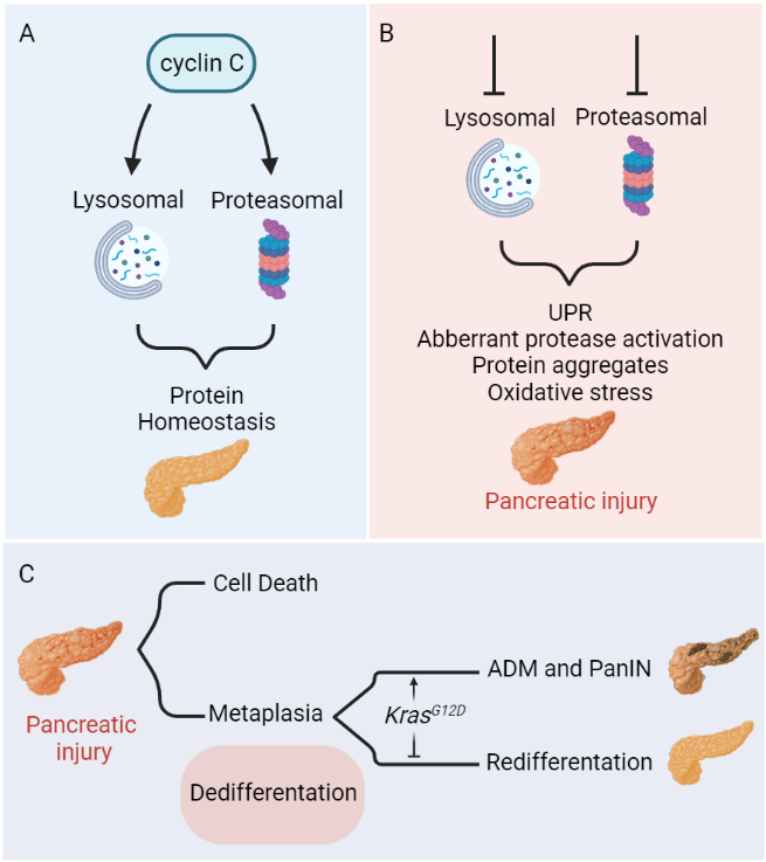

Figure 13. Cyclin C functions as a tumor suppressor in the PDAC murine model. **(A)** Cyclin C promotes autophagy-mediated lysosomal and proteasomal degradation. **(B)** Defects in these pathways result in pancreatic dysfunction, pancreatic injury, and pancreatitis. **(C)** Pro-longed or recurrent pancreatic injury or inflammation is a common cause of pancreatic cancer. To reestablish healthy tissue and restore normal function cells either go through cell death or repair pathways. These reparative mechanisms include the dedifferentiation and redifferentiation phases. Oncogenic Kras represses redifferentiation and promotes tumor formation and progression.

Further studies will need to be conducted to determine the origin of these different tumor types and distinguish if these cell types originate from a single cell lineage, or if they are expansions of functionally distinct cell types. Interestingly, the deletion of *Ccnc*, in the presence of oncogenic Kras, rescues the metabolic disturbances observed in the deletion of *Ccnc* alone. One hypothesis previously mentioned was that cancer levels upregulate glucose consumption, therefore it may be possible that the excess glucose attributed to the deletion of *Ccnc* can be taken up by oncogenic Kras-driven tumors. These tumors would then eliminate glucotoxicity and mitigate pancreatic stress (Figure 14). In addition to metabolic dysregulation, the immune system also plays a key role in pancreatitis and pancreatic injury [298]. It would be interesting to investigate the role of cyclin C in pancreatic function at the organismal level and delineate potential connections between metabolism, immunity, and tumorigenesis. The detailed function of the CKM in regulating proteasome activity remains unclear. The integrity of the ubiquitin-proteasome system is regulated and maintained at multiple levels including ubiquitin conjugation, chaperone activity, ATPase hydrolysis, proteasome assembly, and clearance [299]. The CKM can regulate one or more of these steps. Lastly, determining if the novel drug combinations identified in these studies will be translatable to animal studies will be of great significance.

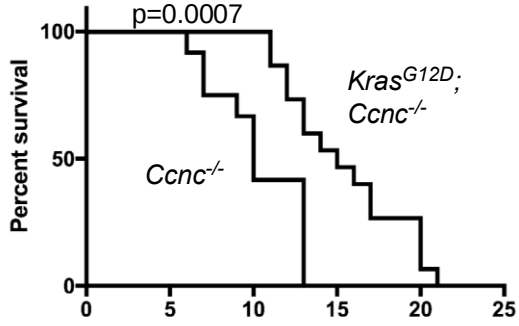

Figure 14. Kapan Meier plot of viability.

SUMMARY AND CONCLUSIONS

Summary

To summarize, multifunctionality is a characteristic of many proteins that regulate stress response mechanisms. Here, we show that Med13 and Ksp1 perform repressive roles in unstressed conditions by negatively regulating transcription and autophagy, respectively. Following starvation these proteins take on different roles, both being required for the selective autophagic degradation of processing body (P-body) proteins. These highly selective and complex mechanisms expand the underappreciated sophistication of autophagy-mediated vacuolar degradation. We show that autophagy, which was once thought of as a bulk degradative process, has elaborately coupled transcriptional and post-transcriptional regulatory mechanisms. These various levels of regulation coordinate a feedback loop in which proteins regulating autophagy are substrates for autophagic degradation themselves. These intricate regulatory networks allow cells to tightly moderate autophagy levels and promptly fine-tune the autophagic response.

These studies describe a novel receptor-mediated autophagy pathway that selectively targets transcriptional regulators such as Med13, Rim15, and Msn2 [3]. In Chapter 2 the sequential steps of this autophagy pathway were described. Med13 is exported from the nucleus via the evolutionarily conserved cytosolic nucleoporin, Gle1. At the nuclear periphery, Med13 is transported to Atg17-initiated phagophores, via the conserved sorting nexin heterodimer consisting of Snx4 and Atg20 [3]. In Chapter 3, the protein kinase Ksp1 was identified as the autophagy receptor protein required for tethering Med13 to autophagosomes through interaction with Atg8. We

describe here the first kinase-independent role of Ksp1. We discovered two functional Atg8-interacting motifs (AIMs), within Ksp1 which are required for its autophagic receptor role. After delineating the mechanistic details of this novel receptor-mediated autophagy pathway, we asked why different proteolysis pathways are used to degrade Med13 in response to different stress conditions (oxidative stress vs starvation; UPS vs autophagy) [54,265]. In Chapter 4, we demonstrate that Med13 plays an important cytosolic role before its autophagic degradation. This role is independent of the CKM and mediates cell cycle arrest and survival during periods of starvation or stationary phase. During starvation, Med13 localizes to ribonucleoprotein (RNP) granules, known as processing bodies (P-bodies). Med13 is required for the autophagic degradation of a small subset of P-bodies proteins, including Edc3 and Dhh1. Strikingly, Med13 functions as a negative regulator of bulk autophagy in unstressed conditions [38], but promotes the autophagic degradation of P-body proteins during starvation. This work has been separated into three manuscripts: Chapter 2 was published in the *Autophagy* journal; Chapter 3 is in revision for publication in the *Autophagy* journal; and Chapter 4 is in preparation for submission to an autophagy special issue in the *MBoC* journal.

In addition to work done in *S. cerevisiae*, in Chapter 5, I investigated the evolutionarily conserved roles of the CKM in regulating autophagy in the pancreatic murine model. Using cell lines derived from mice models, generated by our collaborators at Fox Chase, we show that the CKM promotes autophagy and proteasome activity in this mammalian system. These data complement work done at the Fox Chase Cancer Institute, which shows pancreas-specific deletion of cyclin C results in significant defects in pancreatic homeostasis and function. Additionally,

combining pancreas-specific oncogenic Kras mutations, with the deletion of cyclin C resulted in a 6-8 fold increase in pre-cancerous lesions. These data suggest that the role of cyclin C in regulating autophagy and proteasome activity is evolutionarily conserved, and provides insight into pathologies associated with CKM defects. This work is in preparation for submission to the *Cancer Research* journal.

Conclusions

Autophagy can be divided into two major groups: bulk (non-selective) and selective. Nitrogen starvation triggers Atg1 phosphorylation, and robust induction of bulk autophagy which randomly sequesters cytoplasmic contents in starvation-induced autophagosomes, and requires the scaffold protein Atg17 (Figure 1, right side) [300]. Bulk autophagy substrates and autophagic machinery are degraded as early as 2 h, following autophagy induction [3]. In contrast, selective autophagy pathways degrade organelles or large multisubunit complexes, such as mitochondria, peroxisomes, proteasomes, and ribosomes, and require the Atg11 scaffold protein (Figure 1, left side). Degradation of

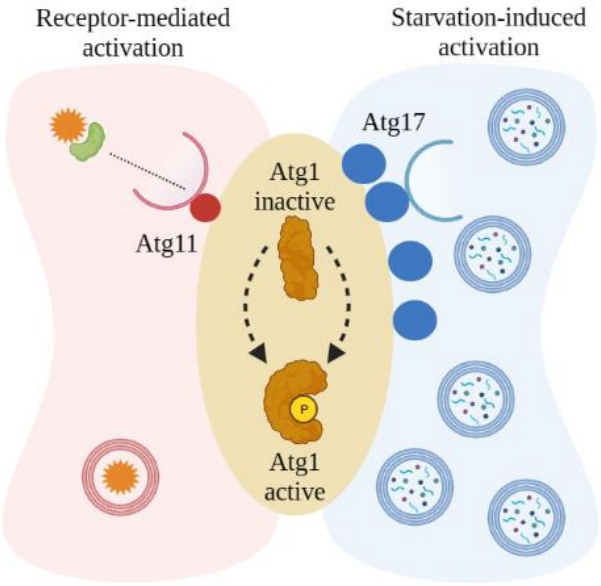

Figure 1. Activation of Atg1 in selective vs non-selective autophagy. On the left in red shows, selective autophagy is induced by receptor-mediated activation of Atg1. These selective autophagy pathways require the Atg11 scaffold protein. On the right in blue to the robust activation of the non-selective, starvation-induced autophagy pathway that requires the Atg17 scaffold protein.

these organelles and complexes requires Atg1 activation by receptor proteins [301]. These receptor proteins monitor organelle dynamics and intracellular conditions and are activated when their targeted substrates need to be degraded. For instance, Atg32, Atg39, and Atg30 are activated during conditions that stimulate mitophagy, ERphagy, and pexophagy respectively. These selective autophagy pathways are predominantly used to maintain homeostasis, but can also be induced following ER and oxidative stress [174].

The autophagic degradation of Med13 defines a new autophagy mechanism

As in the case of Med13 during oxidative stress, the timely degradation of transcription factors requires nuclear 26S proteasomes [54,55]. Remarkably, in these studies, we demonstrate that Med13 degradation following nitrogen starvation requires the trimeric Atg17 complex and starvation-induced autophagosomes. Degradation products of Med13-GFP can be identified as early as 2 h ,which correlates with Med13's observed 2.6 h protein half-life during starvation [3]. The temporal degradation of Med13 is critical, as it illustrates that Med13 is actively selected and recruited to autophagy machinery in the initial phases of the starvation stress response. If Med13 was exported from the nucleus and randomly sequestered via bulk autophagosomes it would take much longer than 4 h to sequester and degrade the entire cytosolic population of Med13 (Figure 2). Med13 autophagic degradation, therefore, requires components of both bulk and selective autophagy. Selective mRNA autophagic degradation is described using a similar mechanism that requires Snx4 and occurs following 3 hours of nitrogen starvation [244]. The autophagy-mediated degradation of targeted regulatory substrates

such as transcription factors and mRNA illustrates that these mechanisms are temporally distinct from Atg11-mediated selective autophagy pathways.

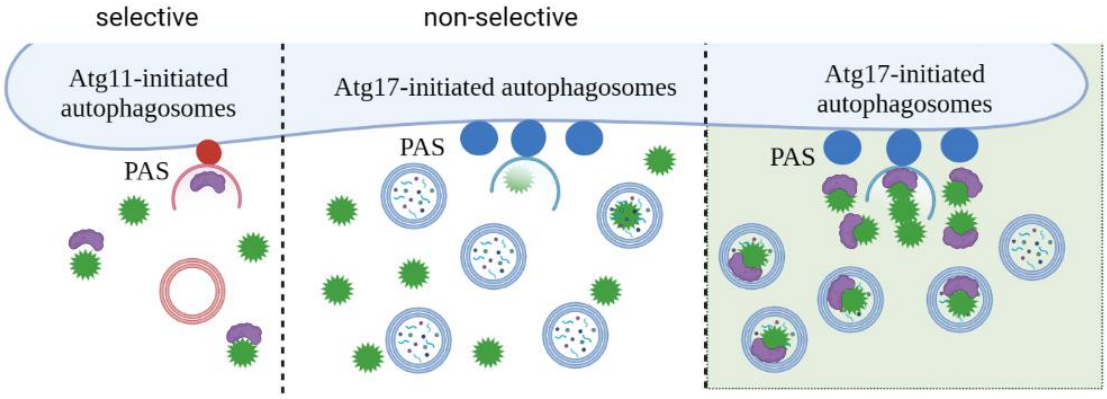

Figure 2. Mechanisms of selective vs non-selective autophagy during nitrogen starvation. The green shapes represent Med13, and the purple shapes denote autophagy receptors. The blue and red circles symbolize Atg17 and Atg11 respectively. The box on the left is a schematic of selective autophagy. The middle box is a schematic of starvation-induced non-selective autophagy. The green box on the right outlines the proposed mechanism of Med13 autophagic degradation. Med13 is concentrated at the PAS during periods of starvation through interactions with Snx4 and Ksp1. Receptor-mediated degradation allows cells to rapidly concentrate, sequester, and degraded selective cargo such as Med13.

To date, much of the literature describing selective autophagy pathways refers to the mechanisms used to degrade excess or damaged organelles or multi-subunit complexes [174]. Here we expand upon the concepts of selective autophagy and introduce a new model in which receptor-mediated autophagy can exclusively target substrates destined for vacuolar degradation. Data from these studies illustrate that starvation-induced autophagosomes which were initially thought to only sequester random cytosolic cargo can also sequester selective cargo such as transcription factors. Our work revealed that Snx4-assisted autophagy is highly exclusive as Med13 is distinguished not only from other chromatin-bound proteins, but also from the other

CKM members. Moreover, we discovered that other transcription factors regulating *ATG* transcription were also substrates of this pathway, illustrating that this pathway is a general regulatory function of autophagy. Autophagic degradation of transcriptional repressors and activators (Rim15 and Msn2) of *ATG* expression allows cells to fine-tune autophagy levels [37]. The discovery of these receptor-mediated autophagy pathways in yeast is important as it redefines paradigms that describe bulk and selective autophagy as separate and distinct. These findings also suggest that the potential pool of autophagic substrates and autophagy receptors can be much more expansive than originally thought.

Ksp1 has two opposing roles in autophagy that are kinase-dependent and independent

Selective autophagy pathways require receptor proteins that bind exclusively to cargo and tether substrates to Atg8. The Atg8-interacting motif (AIM) within the receptor interacts with the LC3-docking site (LDS) of Atg8 [103]. In these studies, we show that Med13 autophagic degradation requires the serine/threonine kinase, Ksp1, as the selective receptor protein. Here, we show that Ksp1 is an autophagic substrate with two functional AIMs required for its autophagic degradation. The AIM-LDS interface of Ksp1 and Atg8 is essential for Med13 degradation, as mutations obscuring this interaction inhibit Med13 autophagic degradation. This is significant as it demonstrates that Med13 degradation requires a specificity factor such as a receptor protein that exclusively binds to Med13 and tethers it to the autophagy machinery. The use of transporters (Snx4-Atg20) and receptors (Ksp1) allows cells to rapidly localize, sequester, and degraded specific substrates during stress.

Ksp1 functions within the TORC1 pathway and negatively regulates autophagy in unstressed conditions [188]. Following stress, Ksp1 is required for the autophagic degradation of Med13, illustrating that Ksp1 plays opposing roles in these conditions. Ksp1 is a multifunctional protein, and its duality tightly regulates autophagy, both in unstressed and stressed conditions. It has been shown that Ksp1 is hyperphosphorylated in unstressed conditions and dephosphorylation is required for these stress-induced roles [194]. Our model suggests that following autophagy induction Ksp1 localizes to the PAS and interacts with Atg29, a component of the Atg17 trimeric scaffold complex. Med13 localizes to the PAS via Snx4 [3] and interacts with Ksp1. Ksp1 then tethers Med13 to the phagophore through its interaction with Atg8. Med13 and Ksp1 are then engulfed into the autophagosome and degraded via vacuolar-mediated proteolysis.

As with cyclin C, Ksp1 is also a multifunctional protein that plays opposing roles in unstressed and stressed conditions. Under physiological, unstressed conditions Ksp1 plays its day job as a repressor of autophagy in a kinase-dependent manner [194]. However, following starvation Ksp1 plays a night job by promoting the autophagic degradation of target substrates in a kinase-independent manner. These separate roles function as a molecular switch to promptly and appropriately turn on or turn off the autophagic stress response.

Med13 mediates cell cycle arrest and autophagic degradation of P-body proteins following starvation

The studies presented in this thesis and previous studies by our group have revealed that both the mode and subcellular address of Med13 proteolysis is dependent upon the type of stress cues. In short, oxidative stress promotes Med13 proteasomal degradation

in the nucleus [54], whereas following nitrogen depletion, Med13 is exported to the cytoplasm, where it is selectively targeted for autophagic degradation [3]. Our previous studies demonstrate that following oxidative stress, cyclin C plays a critical role in promoting mitochondrial fragmentation and programmed cell death initiation [12,52]. We hypothesized that similar to cyclin C, Med13 plays an important cytosolic role prior to its autophagic degradation.

Here we provide evidence to support this model. In short, our data suggest that Med13 mediates cell cycle arrest and autophagic degradation of P-body proteins following starvation. Data presented in these studies illustrate that Med13 mediates quiescence entry and survival during starvation conditions independent of the CKM. Strikingly, Med13 localizes to cytosolic P-bodies during periods of starvation including nitrogen starvation and stationary phase. We also illustrate that a unique subset of P-body proteins is degraded via autophagy following nitrogen starvation. Significantly, degradation of these proteins requires Med13, Ksp1, and Snx4.

Med13 plays dual roles in regulating autophagy

Under physiological conditions, Med13 performs its day job as a negative regulator of autophagy (Figure 3A) [38], following starvation, the CKM is disassembled and Med13 is exported to the cytosol [3]. Here we show that once in the cytosol Med13 performs its night job by promoting the autophagic degradation of P-body proteins (Figure 3B). In the cytosol, Med13 functions as a scaffolding component required for the concentration of specific P-body proteins such as Edc3 and Dhh1. Although Med13 functions as a negative regulator of bulk autophagy under physiological conditions [3], during stress Med13 promotes the autophagic degradation of Edc3 and Dhh1. We

propose a model in which Med13 is required for the concentration and sequestration of selective autophagic substrates (Figure 3C). The large IDR of Med13 functions as an interactive hub allowing for multiple binding partners simultaneously [54]. Med13 may therefore function in binding and concentrating autophagic substrates within RNP granules or the PAS. Liquid-liquid phase separation (LLPS) is an essential process in both RNP granules and PAS formation [258].

P-bodies are ribonucleoprotein (RNP) granules that play a role in mRNA silencing, decay, and storage. Ribosomal proteins and proteins involved in cell cycle regulation have previously been identified in RNP granules demonstrating that these assemblies mediate stress-induced cell cycle arrest and translation inhibition [302],[303],[43]. These RNP granules are evolutionarily conserved attesting to their importance as regulatory storage centers. Taken together, these data suggest that defects in cell cycle arrest and quiescence observed in *med13*Δ cells could potentially be attributed to its role in regulating the P-body proteome.

The duality of regulating both transcription and RNP granule dynamics demonstrates that Med13 coordinates multiple mechanisms of stress response. Med13 post-translational modifications, localization, and degradation are pivotal in orchestrating these separate functions. These results expand upon the concepts of multifunctional proteins and broaden the roles of the CKM in stress response.

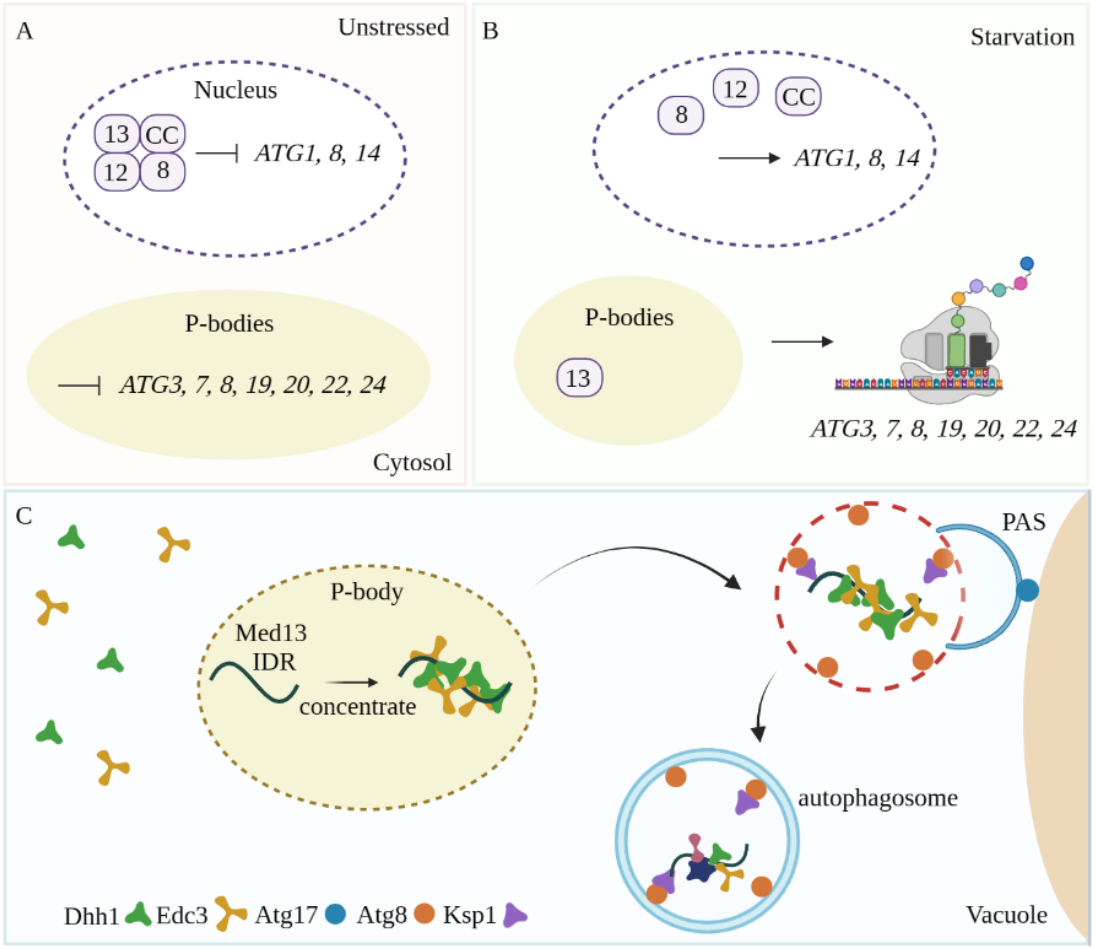

Figure 3. Multifunctionality of Med13. **(A)** Med13 is a negative regulator of *ATG* transcription and P-body proteins negatively regulate *ATG* mRNA expression in unstressed conditions. **(B)** Following stress, the CKM is disassembled and *ATG* transcription is upregulated. Med13 localizes to cytosolic P-bodies and is required to degrade selective P-body proteins. *ATG* transcripts are recycled back into the cytosol and translated. **(C)** Following starvation, Med13 functions as a scaffolding component that concentrates specific P-body proteins and is required for their autophagic degradation.

The CKM regulates autophagy in the pancreatic murine model.

Our studies have shown that cyclin C and Med13 are multifunctional and execute both day and night jobs. Their day job in unstressed cells is to maintain transcriptional control of a subset of stress response genes. In yeast, the CKM predominantly negatively regulates stress response genes whereas in mammalian cells the CKM both positively and negatively regulates these gene sets. Following stress, cyclin C and Med13 perform night jobs which are separate and distinct from their transcription roles. Both the day (transcriptional) and night (mitochondrial) roles of cyclin C are evolutionarily conserved.

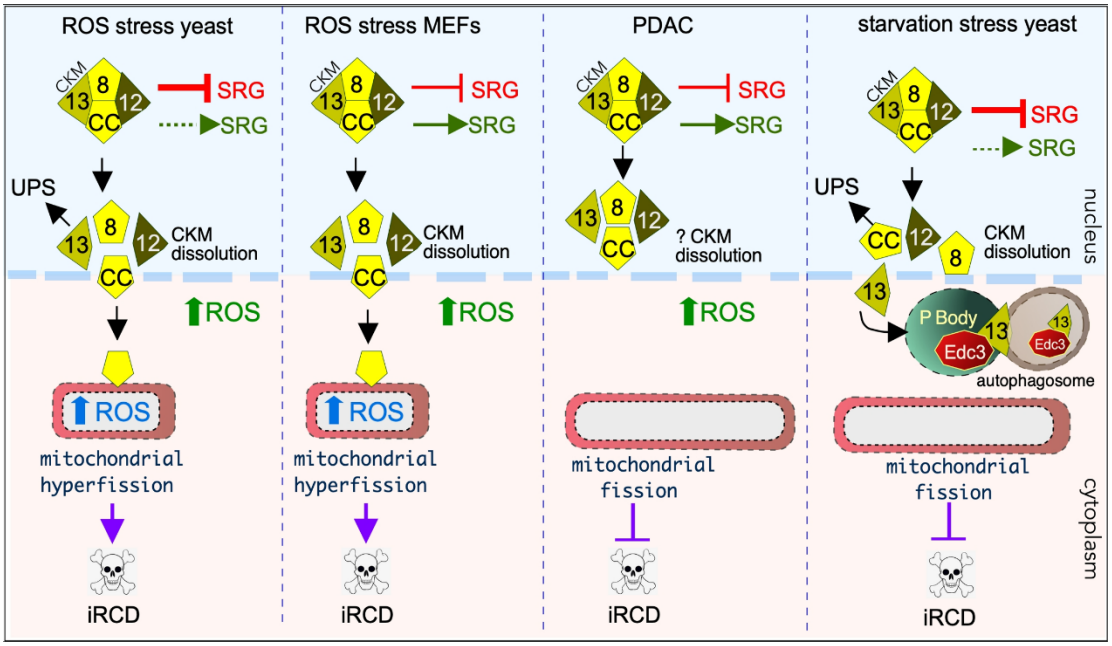

Figure 4. Evolutionarily conserved day and night jobs of the CKM. From left to right: The transcriptional (day job, negatively regulates stress response genes = SRG) and the mitochondrial (night job, inducing mitochondrial fragmentation) of cyclin C in yeast following oxidative stress. Next, these roles are evolutionarily conserved in mouse embryonic fibroblast (MEF) cells. Cyclin C both represses and activates SRGs in mammalian systems. Thirdly, the transcriptional role (day job) is conserved in the pancreatic ductal adenocarcinoma murine model. Within these cells, there are elevated levels of intrinsic ROS, but mitochondrial remain reticular. Lastly, the autophagic role (night job) of Med13 following nitrogen starvation stress in yeast.

The CKM functions as a negative regulator of *ATG* genes in *S. cerevisiae*. In mouse embryonic fibroblasts (MEFs) the CKM functions as an activator of autophagy genes such as *Gabarap*, *Beclin1*, and *Atg9b*. Although these are opposing roles, the CKM-mediated regulation of autophagy is evolutionarily conserved. In the pancreatic $Kras^{G12D}$ murine cancer model, cyclin C promotes autophagy and proteasome activity. Defects in proteolysis result in increased oxidative stress, genomic instability, and accumulation of proteotoxic proteins, such as p62. The pancreas is the site of digestive protease production and secretion, therefore defects in proteostasis can be detrimental to this cell type. Recurrent or prolonged pancreatic dysfunction is a major cause of pancreatic cancer. $Kras^{G12D}$ $Ccnc^{-/-}$ mice had a 6-8 fold increase in pre-cancerous lesions (ADM and PanINs) compared to $Kras^{G12D}$ animals. $Kras^{G12D}$ $Ccnc^{-/-}$ mice also had a significant degree of tumor heterogeneity compared to the control group. $Kras^{G12D}$ $Ccnc^{-/-}$ mice form very aggressive cancer types as large, heterogeneous tumors arise as early as 8 weeks, and by 26-29 weeks pre-cancerous lesions cover 80% of the total tissue area.

Aggressive and heterogenous cancer types make finding effective treatment difficult as these tumors are usually resistant to chemotherapy and metastasis rapidly. Identifying drug combinations that can trigger cell death within these cancer types is therefore of utmost importance. Here we show that the deletion of *Ccnc* or inhibition of Cdk8 kinase activity in the PDAC model sensitives $Kras^{G12D}$ cells to proteasome inhibitors. These results were translated to human colorectal cells as well demonstrating, that this drug combination can be effective in other aggressive cancer types such as colorectal cancer.

REFERENCES

1. Wood LD, Canto MI, Jaffee EM, et al. Pancreatic Cancer: Pathogenesis, Screening, Diagnosis, and Treatment. Gastroenterology. 2022 Aug;163(2):386-402 e1.
2. Kohler V, Aufschnaiter A, Buttner S. Closing the Gap: Membrane Contact Sites in the Regulation of Autophagy. Cells. 2020 May 9;9(5).
3. Hanley SE, Willis SD, Cooper KF. Snx4-assisted vacuolar targeting of transcription factors defines a new autophagy pathway for controlling ATG expression. Autophagy. 2021 Nov;17(11):3547-3565.
4. Noda NN, Ohsumi Y, Inagaki F. Atg8-family interacting motif crucial for selective autophagy. FEBS Lett. 2010 Apr 2;584(7):1379-85.
5. Jacomin AC, Samavedam S, Promponas V, et al. iLIR database: A web resource for LIR motif-containing proteins in eukaryotes. Autophagy. 2016 Oct 2;12(10):1945-1953.
6. Alemu EA, Lamark T, Torgersen KM, et al. ATG8 family proteins act as scaffolds for assembly of the ULK complex: sequence requirements for LC3-interacting region (LIR) motifs. J Biol Chem. 2012 Nov 16;287(47):39275-90.
7. Kalvari I, Tsompanis S, Mulakkal NC, et al. iLIR: A web resource for prediction of Atg8-family interacting proteins. Autophagy. 2014 May;10(5):913-25.
8. Dosztanyi Z, Csizmok V, Tompa P, et al. IUPred: web server for the prediction of intrinsically unstructured regions of proteins based on estimated energy content. Bioinformatics. 2005 Aug 15;21(16):3433-4.

9. Mészáros B, Erdős G, Dosztányi Z. IUPred2A: context-dependent prediction of protein disorder as a function of redox state and protein binding. Nucleic Acids Res. 2018;46(W1):W329-W337.
10. Erdős G, Pajkos M, Dosztányi Z. IUPred3: prediction of protein disorder enhanced with unambiguous experimental annotation and visualization of evolutionary conservation. Nucleic Acids Res. 2021;49(W1):W297-W303.
11. Hollenstein DM, Kraft C. Autophagosomes are formed at a distinct cellular structure. Curr Opin Cell Biol. 2020 Aug;65:50-57.
12. Wang K, Yan R, Cooper KF, et al. Cyclin C mediates stress-induced mitochondrial fission and apoptosis. Mol Biol Cell. 2015 Mar 15;26(6):1030-43.
13. Galluzzi L, Yamazaki T, Kroemer G. Linking cellular stress responses to systemic homeostasis. Nat Rev Mol Cell Biol. 2018 Nov;19(11):731-745.
14. Rutherford JC, Bahn YS, van den Berg B, et al. Nutrient and Stress Sensing in Pathogenic Yeasts. Front Microbiol. 2019;10:442.
15. Hedbacker K, Carlson M. SNF1/AMPK pathways in yeast. Front Biosci. 2008 Jan 1;13:2408-20.
16. Sun S, Gresham D. Cellular quiescence in budding yeast. Yeast. 2021 Jan;38(1):12-29.
17. Youle RJ, van der Bliek AM. Mitochondrial fission, fusion, and stress. Science. 2012 Aug 31;337(6098):1062-5.

18. Camoes F, Bonekamp NA, Delille HK, et al. Organelle dynamics and dysfunction: A closer link between peroxisomes and mitochondria. J Inherit Metab Dis. 2009 Apr;32(2):163-80.

19. Seo J, Park M. Molecular crosstalk between cancer and neurodegenerative diseases. Cell Mol Life Sci. 2020 Jul;77(14):2659-2680.

20. Gross A, Katz SG. Non-apoptotic functions of BCL-2 family proteins. Cell Death Differ. 2017 Aug;24(8):1348-1358.

21. Shamas-Din A, Kale J, Leber B, et al. Mechanisms of action of Bcl-2 family proteins. Cold Spring Harb Perspect Biol. 2013 Apr 1;5(4):a008714.

22. Lee MJ, Yaffe MB. Protein Regulation in Signal Transduction. Cold Spring Harb Perspect Biol. 2016 Jun 1;8(6).

23. Zhou B, Lin W, Long Y, et al. Notch signaling pathway: architecture, disease, and therapeutics. Signal Transduct Target Ther. 2022 Mar 24;7(1):95.

24. Lecker SH, Goldberg AL, Mitch WE. Protein degradation by the ubiquitin-proteasome pathway in normal and disease states. J Am Soc Nephrol. 2006 Jul;17(7):1807-19.

25. Troester MA, Lindstrom AB, Waidyanatha S, et al. Stability of hemoglobin and albumin adducts of naphthalene oxide, 1,2-naphthoquinone, and 1,4-naphthoquinone. Toxicol Sci. 2002 Aug;68(2):314-21.

26. Casimiro MC, Crosariol M, Loro E, et al. Cyclins and cell cycle control in cancer and disease. Genes Cancer. 2012 Nov;3(11-12):649-57.

27. Kwon YT, Ciechanover A. The Ubiquitin Code in the Ubiquitin-Proteasome System and Autophagy. Trends Biochem Sci. 2017 Nov;42(11):873-886.

28. Komander D, Rape M. The ubiquitin code. Annu Rev Biochem. 2012;81:203-29.

29. Ciechanover A. Proteolysis: from the lysosome to ubiquitin and the proteasome. Nat Rev Mol Cell Biol. 2005 Jan;6(1):79-87.

30. Hanley SE, Cooper KF. Sorting Nexins in Protein Homeostasis. Cells. 2020 Dec 24;10(1).

31. Fujiwara Y, Wada K, Kabuta T. Lysosomal degradation of intracellular nucleic acids-multiple autophagic pathways. J Biochem. 2017 Feb 1;161(2):145-154.

32. Ohsumi Y. Historical landmarks of autophagy research. Cell Res. 2014 Jan;24(1):9-23.

33. Harnett MM, Pineda MA, Latre de Late P, et al. From Christian de Duve to Yoshinori Ohsumi: More to autophagy than just dining at home. Biomed J. 2017 Feb;40(1):9-22.

34. Levine B, Klionsky DJ. Development by self-digestion: molecular mechanisms and biological functions of autophagy. Dev Cell. 2004 Apr;6(4):463-77.

35. Eickhorst C, Licheva M, Kraft C. Scaffold proteins in bulk and selective autophagy. Prog Mol Biol Transl Sci. 2020;172:15-35.

36. Zaffagnini G, Martens S. Mechanisms of Selective Autophagy. J Mol Biol. 2016 May 8;428(9 Pt A):1714-24.

37. Delorme-Axford E, Klionsky DJ. Transcriptional and post-transcriptional regulation of autophagy in the yeast Saccharomyces cerevisiae. J Biol Chem. 2018 Apr 13;293(15):5396-5403.

38. Willis SD, Hanley SE, Beishke T, et al. Ubiquitin-proteasome mediated cyclin C degradation promotes cell survival following nitrogen starvation. Mol Biol Cell. 2020 Mar 11:mbcE19110622.

39. Willis SD, Hanley SE, Doyle SJ, et al. Cyclin C-Cdk8 Kinase Phosphorylation of Rim15 Prevents the Aberrant Activation of Stress Response Genes. Front Cell Dev Biol. 2022;10:867257.

40. Luo Y, Na Z, Slavoff SA. P-Bodies: Composition, Properties, and Functions. Biochemistry. 2018 May 1;57(17):2424-2431.

41. Corbet GA, Parker R. RNP Granule Formation: Lessons from P-Bodies and Stress Granules. Cold Spring Harb Symp Quant Biol. 2019;84:203-215.

42. Delorme-Axford E, Abernathy E, Lennemann NJ, et al. The exoribonuclease Xrn1 is a post-transcriptional negative regulator of autophagy. Autophagy. 2018;14(5):898-912.

43. Hubstenberger A, Courel M, Benard M, et al. P-Body Purification Reveals the Condensation of Repressed mRNA Regulons. Mol Cell. 2017 Oct 5;68(1):144-157 e5.

44. Alberti S, Mateju D, Mediani L, et al. Granulostasis: Protein Quality Control of RNP Granules. Front Mol Neurosci. 2017;10:84.

45. Kumaran G, Michaeli S. Eating the messenger (RNA): autophagy shapes the cellular RNA landscape. J Exp Bot. 2021 Oct 26;72(20):6803-6807.

46. Yeasmin AM, Waliullah TM, Kondo A, et al. Orchestrated Action of PP2A Antagonizes Atg13 Phosphorylation and Promotes Autophagy after the Inactivation of TORC1. PLoS One. 2016;11(12):e0166636.

47. Geng J, Klionsky DJ. The Atg8 and Atg12 ubiquitin-like conjugation systems in macroautophagy. 'Protein modifications: beyond the usual suspects' review series. EMBO Rep. 2008 Sep;9(9):859-64.

48. Friedson B, Cooper KF. Cdk8 Kinase Module: A Mediator of Life and Death Decisions in Times of Stress. Microorganisms. 2021 Oct 15;9(10).

49. Cooper KF, Mallory MJ, Smith JB, et al. Stress and developmental regulation of the yeast C-type cyclin Ume3p (Srb11p/Ssn8p). EMBO J. 1997 Aug 1;16(15):4665-75.

50. Jezek J, Smethurst DGJ, Stieg DC, et al. Cyclin C: The Story of a Non-Cycling Cyclin. Biology (Basel). 2019 Jan 4;8(1).

51. Li YC, Chao TC, Kim HJ, et al. Structure and noncanonical Cdk8 activation mechanism within an Argonaute-containing Mediator kinase module. Sci Adv. 2021 Jan;7(3).

52. Cooper KF, Khakhina S, Kim SK, et al. Stress-induced nuclear-to-cytoplasmic translocation of cyclin C promotes mitochondrial fission in yeast. Dev Cell. 2014 Jan 27;28(2):161-73.

53. Khakhina S, Cooper KF, Strich R. Med13p prevents mitochondrial fission and programmed cell death in yeast through nuclear retention of cyclin C. Mol Biol Cell. 2014 Sep 15;25(18):2807-16.

54. Stieg DC, Willis SD, Ganesan V, et al. A complex molecular switch directs stress-induced cyclin C nuclear release through SCF(Grr1)-mediated degradation of Med13. Mol Biol Cell. 2018 Feb 1;29(3):363-375.

55. Willis SD, Stieg DC, Ong KL, et al. Snf1 cooperates with the CWI MAPK pathway to mediate the degradation of Med13 following oxidative stress. Microb Cell. 2018 Jun 25;5(8):357-370.

56. Stieg DC, Cooper KF, Strich R. The extent of cyclin C promoter occupancy directs changes in stress-dependent transcription. J Biol Chem. 2020 Nov 27;295(48):16280-16291.

57. Ganesan V, Willis SD, Chang KT, et al. Cyclin C directly stimulates Drp1 GTP affinity to mediate stress-induced mitochondrial hyperfission. Mol Biol Cell. 2019 Feb 1;30(3):302-311.

58. Jezek J, Chang KT, Joshi AM, et al. Mitochondrial translocation of cyclin C stimulates intrinsic apoptosis through Bax recruitment. EMBO Rep. 2019 Sep;20(9):e47425.

59. Jezek J, Wang K, Yan R, et al. Synergistic repression of thyroid hyperplasia by cyclin C and Pten. J Cell Sci. 2019 Aug 15;132(16).

60. Li N, Fassl A, Chick J, et al. Cyclin C is a haploinsufficient tumour suppressor. Nat Cell Biol. 2014 Nov;16(11):1080-91.

61. Clark AD, Oldenbroek M, Boyer TG. Mediator kinase module and human tumorigenesis. Crit Rev Biochem Mol Biol. 2015;50(5):393-426.

62. Ponce JM, Coen G, Spitler KM, et al. Stress-Induced Cyclin C Translocation Regulates Cardiac Mitochondrial Dynamics. J Am Heart Assoc. 2020 Apr 7;9(7):e014366.

63. Yamada T, Fukasawa K, Horie T, et al. The role of CDK8 in mesenchymal stem cells in controlling osteoclastogenesis and bone homeostasis. Stem Cell Reports. 2022 Jul 12;17(7):1576-1588.

64. Chang KT, Jezek J, Campbell AN, et al. Aberrant cyclin C nuclear release induces mitochondrial fragmentation and dysfunction in MED13L syndrome fibroblasts. iScience. 2022 Feb 18;25(2):103823.

65. Dannappel MV, Sooraj D, Loh JJ, et al. Molecular and in vivo Functions of the CDK8 and CDK19 Kinase Modules. Front Cell Dev Biol. 2018;6:171.

66. Wu D, Zhang Z, Chen X, et al. Angel or Devil ? - CDK8 as the new drug target. Eur J Med Chem. 2021 Mar 5;213:113043.

67. Guo F, Liu X, Cai H, et al. Autophagy in neurodegenerative diseases: pathogenesis and therapy. Brain Pathol. 2018 Jan;28(1):3-13.

68. Li X, He S, Ma B. Autophagy and autophagy-related proteins in cancer. Mol Cancer. 2020 Jan 22;19(1):12.

69. Conibear E, Stevens TH. Studying yeast vacuoles. Methods Enzymol. 2002;351:408-32.

70. Takeshige K, Baba M, Tsuboi S, et al. Autophagy in yeast demonstrated with proteinase-deficient mutants and conditions for its induction. J Cell Biol. 1992 Oct;119(2):301-11.

71. Farre JC, Subramani S. Mechanistic insights into selective autophagy pathways: lessons from yeast. Nat Rev Mol Cell Biol. 2016 Sep;17(9):537-52.

72. Suzuki K. Selective autophagy in budding yeast. Cell Death Differ. 2013 Jan;20(1):43-8.

73. Onodera J, Ohsumi Y. Autophagy is required for maintenance of amino acid levels and protein synthesis under nitrogen starvation. J Biol Chem. 2005 Sep 9;280(36):31582-6.

74. Klionsky DJ, Codogno P. The mechanism and physiological function of macroautophagy. J Innate Immun. 2013;5(5):427-33.

75. Noda T. Regulation of Autophagy through TORC1 and mTORC1. Biomolecules. 2017 Jul 7;7(3).

76. Kabeya Y, Kamada Y, Baba M, et al. Atg17 functions in cooperation with Atg1 and Atg13 in yeast autophagy. Mol Biol Cell. 2005 May;16(5):2544-53.

77. Rao Y, Perna MG, Hofmann B, et al. The Atg1-kinase complex tethers Atg9-vesicles to initiate autophagy. Nat Commun. 2016 Jan 12;7:10338.

78. Hollenstein DM, Gomez-Sanchez R, Ciftci A, et al. Vac8 spatially confines autophagosome formation at the vacuole in S. cerevisiae. J Cell Sci. 2019 Nov 14;132(22).

79. Matscheko N, Mayrhofer P, Rao Y, et al. Atg11 tethers Atg9 vesicles to initiate selective autophagy. PLoS Biol. 2019 Jul;17(7):e3000377.

80. Zientara-Rytter K, Subramani S. The Roles of Ubiquitin-Binding Protein Shuttles in the Degradative Fate of Ubiquitinated Proteins in the Ubiquitin-Proteasome System and Autophagy. Cells. 2019 Jan 10;8(1).

81. Fu N, Yang X, Chen L. Nucleophagy Plays a Major Role in Human Diseases. Curr Drug Targets. 2018;19(15):1767-1773.

82. Mochida K, Oikawa Y, Kimura Y, et al. Receptor-mediated selective autophagy degrades the endoplasmic reticulum and the nucleus. Nature. 2015 Jun 18;522(7556):359-62.

83. Roberts P, Moshitch-Moshkovitz S, Kvam E, et al. Piecemeal microautophagy of nucleus in Saccharomyces cerevisiae. Mol Biol Cell. 2003 Jan;14(1):129-41.

84. Lee CW, Wilfling F, Ronchi P, et al. Selective autophagy degrades nuclear pore complexes. Nat Cell Biol. 2020 Feb;22(2):159-166.

85. Vishnoi N, Dhanasekeran K, Chalfant M, et al. Differential turnover of Nup188 controls its levels at centrosomes and role in centriole duplication. J Cell Biol. 2020 Mar 2;219(3).

86. Cooper KF, Mallory MJ, Strich R. Oxidative stress-induced destruction of the yeast C-type cyclin Ume3p requires phosphatidylinositol-specific phospholipase C and the 26S proteasome. Mol Cell Biol. 1999 May;19(5):3338-48.

87. Nemet J, Jelicic B, Rubelj I, et al. The two faces of Cdk8, a positive/negative regulator of transcription. Biochimie. 2014 Feb;97:22-7.

88. Akoulitchev S, Chuikov S, Reinberg D. TFIIH is negatively regulated by cdk8-containing mediator complexes. Nature. 2000 Sep 7;407(6800):102-6.

89. Jeronimo C, Langelier MF, Bataille AR, et al. Tail and Kinase Modules Differently Regulate Core Mediator Recruitment and Function In Vivo. Mol Cell. 2016 Nov 3;64(3):455-466.

90. Jeronimo C, Robert F. The Mediator Complex: At the Nexus of RNA Polymerase II Transcription. Trends Cell Biol. 2017 Oct;27(10):765-783.

91. Cooper KF, Scarnati MS, Krasley E, et al. Oxidative-stress-induced nuclear to cytoplasmic relocalization is required for Not4-dependent cyclin C destruction. J Cell Sci. 2012 Feb 15;125(Pt 4):1015-26.

92. Li J, Kim SG, Blenis J. Rapamycin: one drug, many effects. Cell Metab. 2014 Mar 4;19(3):373-9.

93. Van Den Hazel HB, Kielland-Brandt MC, Winther JR. Review: biosynthesis and function of yeast vacuolar proteases. Yeast. 1996 Jan;12(1):1-16.

94. Shintani T, Klionsky DJ. Cargo proteins facilitate the formation of transport vesicles in the cytoplasm to vacuole targeting pathway. J Biol Chem. 2004 Jul 16;279(29):29889-94.

95. Kamada Y, Funakoshi T, Shintani T, et al. Tor-mediated induction of autophagy via an Apg1 protein kinase complex. J Cell Biol. 2000 Sep 18;150(6):1507-13.

96. Xu H, Jun Y, Thompson J, et al. HOPS prevents the disassembly of trans-SNARE complexes by Sec17p/Sec18p during membrane fusion. EMBO J. 2010 Jun 16;29(12):1948-60.

97. D'Agostino M, Risselada HJ, Lurick A, et al. A tethering complex drives the terminal stage of SNARE-dependent membrane fusion. Nature. 2017 Nov 30;551(7682):634-638.

98. Martens S, Fracchiolla D. Activation and targeting of ATG8 protein lipidation. Cell Discov. 2020;6:23.

99. Xie Q, Tzfadia O, Levy M, et al. hfAIM: A reliable bioinformatics approach for in silico genome-wide identification of autophagy-associated Atg8-interacting motifs in various organisms. Autophagy. 2016 May 3;12(5):876-87.

100. Birgisdottir AB, Lamark T, Johansen T. The LIR motif - crucial for selective autophagy. J Cell Sci. 2013 Aug 1;126(Pt 15):3237-47.

101. Johansen T, Lamark T. Selective Autophagy: ATG8 Family Proteins, LIR Motifs and Cargo Receptors. J Mol Biol. 2020 Jan 3;432(1):80-103.

102. Martens S, Behrends C. Molecular Mechanisms of Selective Autophagy. J Mol Biol. 2020 Jan 3;432(1):1-2.

103. Marshall RS, Hua Z, Mali S, et al. ATG8-Binding UIM Proteins Define a New Class of Autophagy Adaptors and Receptors. Cell. 2019 Apr 18;177(3):766-781 e24.

104. Sawa-Makarska J, Abert C, Romanov J, et al. Cargo binding to Atg19 unmasks additional Atg8 binding sites to mediate membrane-cargo apposition during selective autophagy. Nat Cell Biol. 2014 May;16(5):425-433.

105. Millen JI, Krick R, Prick T, et al. Measuring piecemeal microautophagy of the nucleus in Saccharomyces cerevisiae. Autophagy. 2009 Jan;5(1):75-81.

106. Specht S, Miller SB, Mogk A, et al. Hsp42 is required for sequestration of protein aggregates into deposition sites in Saccharomyces cerevisiae. J Cell Biol. 2011 Nov 14;195(4):617-29.

107. Kaganovich D, Kopito R, Frydman J. Misfolded proteins partition between two distinct quality control compartments. Nature. 2008 Aug 28;454(7208):1088-95.

108. Parsell DA, Kowal AS, Singer MA, et al. Protein disaggregation mediated by heat-shock protein Hsp104. Nature. 1994 Dec 1;372(6505):475-8.

109. Zientara-Rytter K, Subramani S. Mechanistic Insights into the Role of Atg11 in Selective Autophagy. J Mol Biol. 2020 Jan 3;432(1):104-122.

110. Mao K, Chew LH, Inoue-Aono Y, et al. Atg29 phosphorylation regulates coordination of the Atg17-Atg31-Atg29 complex with the Atg11 scaffold during autophagy initiation. Proc Natl Acad Sci U S A. 2013 Jul 30;110(31):E2875-84.

111. Lin DH, Hoelz A. The Structure of the Nuclear Pore Complex (An Update). Annu Rev Biochem. 2019 Jun 20;88:725-783.

112. Uversky VN. Multitude of binding modes attainable by intrinsically disordered proteins: a portrait gallery of disorder-based complexes. Chem Soc Rev. 2011 Mar;40(3):1623-34.

113. Murphy R, Wente SR. An RNA-export mediator with an essential nuclear export signal. Nature. 1996 Sep 26;383(6598):357-60.

114. Noble KN, Tran EJ, Alcazar-Roman AR, et al. The Dbp5 cycle at the nuclear pore complex during mRNA export II: nucleotide cycling and mRNP

remodeling by Dbp5 are controlled by Nup159 and Gle1. Genes Dev. 2011 May 15;25(10):1065-77.

115. Tran EJ, Zhou Y, Corbett AH, et al. The DEAD-box protein Dbp5 controls mRNA export by triggering specific RNA:protein remodeling events. Mol Cell. 2007 Dec 14;28(5):850-9.

116. Aryanpur PP, Regan CA, Collins JM, et al. Gle1 Regulates RNA Binding of the DEAD-Box Helicase Ded1 in Its Complex Role in Translation Initiation. Mol Cell Biol. 2017 Nov 1;37(21).

117. Alcazar-Roman AR, Tran EJ, Guo S, et al. Inositol hexakisphosphate and Gle1 activate the DEAD-box protein Dbp5 for nuclear mRNA export. Nat Cell Biol. 2006 Jul;8(7):711-6.

118. Weirich CS, Erzberger JP, Flick JS, et al. Activation of the DExD/H-box protein Dbp5 by the nuclear-pore protein Gle1 and its coactivator InsP6 is required for mRNA export. Nat Cell Biol. 2006 Jul;8(7):668-76.

119. Fernandez-Martinez J, Kim SJ, Shi Y, et al. Structure and Function of the Nuclear Pore Complex Cytoplasmic mRNA Export Platform. Cell. 2016 Nov 17;167(5):1215-1228 e25.

120. Adams RL, Mason AC, Glass L, et al. Nup42 and IP(6) coordinate Gle1 stimulation of Dbp5/DDX19B for mRNA export in yeast and human cells. Traffic. 2017 Dec;18(12):776-790.

121. Bolger TA, Folkmann AW, Tran EJ, et al. The mRNA export factor Gle1 and inositol hexakisphosphate regulate distinct stages of translation. Cell. 2008 Aug 22;134(4):624-33.

122. Bolger TA, Wente SR. Gle1 is a multifunctional DEAD-box protein regulator that modulates Ded1 in translation initiation. J Biol Chem. 2011 Nov 18;286(46):39750-9.

123. Gross T, Siepmann A, Sturm D, et al. The DEAD-box RNA helicase Dbp5 functions in translation termination. Science. 2007 Feb 2;315(5812):646-9.

124. Macara IG. Transport into and out of the nucleus. Microbiol Mol Biol Rev. 2001 Dec;65(4):570-94, table of contents.

125. Adams RL, Wente SR. Dbp5 associates with RNA-bound Mex67 and Nab2 and its localization at the nuclear pore complex is sufficient for mRNP export and cell viability. PLoS Genet. 2020 Oct;16(10):e1009033.

126. Chatterjee K, Majumder S, Wan Y, et al. Sharing the load: Mex67-Mtr2 cofunctions with Los1 in primary tRNA nuclear export. Genes Dev. 2017 Nov 1;31(21):2186-2198.

127. Ma M, Burd CG, Chi RJ. Distinct complexes of yeast Snx4 family SNX-BARs mediate retrograde trafficking of Snc1 and Atg27. Traffic. 2017 Feb;18(2):134-144.

128. Ma M, Kumar S, Purushothaman L, et al. Lipid trafficking by yeast Snx4 family SNX-BAR proteins promotes autophagy and vacuole membrane fusion. Mol Biol Cell. 2018 Sep 1;29(18):2190-2200.

129. Suzuki SW, Emr SD. Membrane protein recycling from the vacuole/lysosome membrane. J Cell Biol. 2018 May 7;217(5):1623-1632.

130. Ma M, Burd CG. Retrograde trafficking and plasma membrane recycling pathways of the budding yeast Saccharomyces cerevisiae. Traffic. 2020 Jan;21(1):45-59.

131. Nice DC, Sato TK, Stromhaug PE, et al. Cooperative binding of the cytoplasm to vacuole targeting pathway proteins, Cvt13 and Cvt20, to phosphatidylinositol 3-phosphate at the pre-autophagosomal structure is required for selective autophagy. J Biol Chem. 2002 Aug 16;277(33):30198-207.

132. Kanki T, Wang K, Cao Y, et al. Atg32 is a mitochondrial protein that confers selectivity during mitophagy. Dev Cell. 2009 Jul;17(1):98-109.

133. Shpilka T, Welter E, Borovsky N, et al. Fatty acid synthase is preferentially degraded by autophagy upon nitrogen starvation in yeast. Proc Natl Acad Sci U S A. 2015 Feb 3;112(5):1434-9.

134. Deng Y, Qu Z, Naqvi NI. The role of snx41-based pexophagy in magnaporthe development. PLoS One. 2013;8(11):e79128.

135. Popelka H, Damasio A, Hinshaw JE, et al. Structure and function of yeast Atg20, a sorting nexin that facilitates autophagy induction. Proc Natl Acad Sci U S A. 2017 Nov 21;114(47):E10112-E10121.

136. Humphries CL, Balcer HI, D'Agostino JL, et al. Direct regulation of Arp2/3 complex activity and function by the actin binding protein coronin. J Cell Biol. 2002 Dec 23;159(6):993-1004.

137. Welter E, Thumm M, Krick R. Quantification of nonselective bulk autophagy in S. cerevisiae using Pgk1-GFP. Autophagy. 2010 Aug;6(6):794-7.

138. Kelley LA, Mezulis S, Yates CM, et al. The Phyre2 web portal for protein modeling, prediction and analysis. Nat Protoc. 2015 Jun;10(6):845-58.

139. Stanishneva-Konovalova TB, Derkacheva NI, Polevova SV, et al. The Role of BAR Domain Proteins in the Regulation of Membrane Dynamics. Acta Naturae. 2016 Oct-Dec;8(4):60-69.

140. Nemec AA, Howell LA, Peterson AK, et al. Autophagic clearance of proteasomes in yeast requires the conserved sorting nexin Snx4. J Biol Chem. 2017 Dec 29;292(52):21466-21480.

141. Bartholomew CR, Suzuki T, Du Z, et al. Ume6 transcription factor is part of a signaling cascade that regulates autophagy. Proc Natl Acad Sci U S A. 2012 Jul 10;109(28):11206-10.

142. Bernard A, Jin M, Gonzalez-Rodriguez P, et al. Rph1/KDM4 mediates nutrient-limitation signaling that leads to the transcriptional induction of autophagy. Curr Biol. 2015 Mar 2;25(5):546-55.

143. Vlahakis A, Lopez Muniozguren N, Powers T. Stress-response transcription factors Msn2 and Msn4 couple TORC2-Ypk1 signaling and mitochondrial respiration to ATG8 gene expression and autophagy. Autophagy. 2017;13(11):1804-1812.

144. Zhu J, Deng S, Lu P, et al. The Ccl1-Kin28 kinase complex regulates autophagy under nitrogen starvation. J Cell Sci. 2016 Jan 1;129(1):135-44.

145. Papandreou ME, Tavernarakis N. Nucleophagy: from homeostasis to disease. Cell Death Differ. 2019 Mar;26(4):630-639.

146. Okamoto K, Kondo-Okamoto N, Ohsumi Y. Mitochondria-anchored receptor Atg32 mediates degradation of mitochondria via selective autophagy. Dev Cell. 2009 Jul;17(1):87-97.

147. Kanki T, Wang K, Baba M, et al. A genomic screen for yeast mutants defective in selective mitochondria autophagy. Mol Biol Cell. 2009 Nov;20(22):4730-8.

148. Shpilka T, Weidberg H, Pietrokovski S, et al. Atg8: an autophagy-related ubiquitin-like protein family. Genome Biol. 2011 Jul 27;12(7):226.

149. Waite KA, De-La Mota-Peynado A, Vontz G, et al. Starvation Induces Proteasome Autophagy with Different Pathways for Core and Regulatory Particles. J Biol Chem. 2016 Feb 12;291(7):3239-53.

150. Huang H, Kawamata T, Horie T, et al. Bulk RNA degradation by nitrogen starvation-induced autophagy in yeast. EMBO J. 2015 Jan 13;34(2):154-68.

151. Kageyama T, Suzuki K, Ohsumi Y. Lap3 is a selective target of autophagy in yeast, Saccharomyces cerevisiae. Biochem Biophys Res Commun. 2009 Jan 16;378(3):551-7.

152. Nagulapalli M, Maji S, Dwivedi N, et al. Evolution of disorder in Mediator complex and its functional relevance. Nucleic Acids Res. 2016 Feb 29;44(4):1591-612.

153. Folkmann AW, Noble KN, Cole CN, et al. Dbp5, Gle1-IP6 and Nup159: a working model for mRNP export. Nucleus. 2011 Nov-Dec;2(6):540-8.

154. Yin Z, Klionsky DJ. NPC-phagy: selective autophagy of the nuclear pore complexes. Autophagy. 2020 Oct;16(10):1735-1736.

155. Tomioka Y, Kotani T, Kirisako H, et al. TORC1 inactivation stimulates autophagy of nucleoporin and nuclear pore complexes. J Cell Biol. 2020 Jul 6;219(7).

156. Bean BD, Davey M, Conibear E. Cargo selectivity of yeast sorting nexins. Traffic. 2017 Feb;18(2):110-122.

157. Zhang D, Chen T, Ziv I, et al. Together, Rpn10 and Dsk2 can serve as a polyubiquitin chain-length sensor. Mol Cell. 2009 Dec 25;36(6):1018-33.

158. Simonetti B, Danson CM, Heesom KJ, et al. Sequence-dependent cargo recognition by SNX-BARs mediates retromer-independent transport of CI-MPR. J Cell Biol. 2017 Nov 6;216(11):3695-3712.

159. Kvainickas A, Jimenez-Orgaz A, Nagele H, et al. Cargo-selective SNX-BAR proteins mediate retromer trimer independent retrograde transport. J Cell Biol. 2017 Nov 6;216(11):3677-3693.

160. Zhang H, Huang T, Hong Y, et al. The Retromer Complex and Sorting Nexins in Neurodegenerative Diseases. Front Aging Neurosci. 2018;10:79.

161. Hu YB, Dammer EB, Ren RJ, et al. The endosomal-lysosomal system: from acidification and cargo sorting to neurodegeneration. Transl Neurodegener. 2015;4:18.

162. Lee YJ, Lee CY, Grzechnik A, et al. RNA polymerase I stability couples cellular growth to metal availability. Mol Cell. 2013 Jul 11;51(1):105-15.

163. Aditi, Glass L, Dawson TR, et al. An amyotrophic lateral sclerosis-linked mutation in GLE1 alters the cellular pool of human Gle1 functional isoforms. Adv Biol Regul. 2016 Sep;62:25-36.

164. Tsai KL, Sato S, Tomomori-Sato C, et al. A conserved Mediator-CDK8 kinase module association regulates Mediator-RNA polymerase II interaction. Nat Struct Mol Biol. 2013 May;20(5):611-9.

165. Dikic I. Proteasomal and Autophagic Degradation Systems. Annu Rev Biochem. 2017 Jun 20;86:193-224.

166. Gubas A, Dikic I. A guide to the regulation of selective autophagy receptors. FEBS J. 2022 Jan;289(1):75-89.

167. Levine B, Kroemer G. Biological Functions of Autophagy Genes: A Disease Perspective. Cell. 2019 Jan 10;176(1-2):11-42.

168. Hetz C, Saxena S. ER stress and the unfolded protein response in neurodegeneration. Nat Rev Neurol. 2017 Aug;13(8):477-491.

169. Gonzalez-Teuber V, Albert-Gasco H, Auyeung VC, et al. Small Molecules to Improve ER Proteostasis in Disease. Trends Pharmacol Sci. 2019 Sep;40(9):684-695.

170. Lawrence RE, Zoncu R. The lysosome as a cellular centre for signalling, metabolism and quality control. Nat Cell Biol. 2019 Feb;21(2):133-142.

171. Dikic I, Elazar Z. Mechanism and medical implications of mammalian autophagy. Nat Rev Mol Cell Biol. 2018 Jun;19(6):349-364.

172. Gonzalez A, Hall MN. Nutrient sensing and TOR signaling in yeast and mammals. EMBO J. 2017 Feb 15;36(4):397-408.

173. Delorme-Axford E, Klionsky DJ. Transcriptional and post-transcriptional regulation of autophagy in the yeast Saccharomyces cerevisiae. J Biol Chem. 2018 Jan 25.

174. Kirkin V, Rogov VV. A Diversity of Selective Autophagy Receptors Determines the Specificity of the Autophagy Pathway. Mol Cell. 2019 Oct 17;76(2):268-285.

175. Rogov V, Dotsch V, Johansen T, et al. Interactions between autophagy receptors and ubiquitin-like proteins form the molecular basis for selective autophagy. Mol Cell. 2014 Jan 23;53(2):167-78.

176. Stolz A, Ernst A, Dikic I. Cargo recognition and trafficking in selective autophagy. Nat Cell Biol. 2014 Jun;16(6):495-501.

177. Shintani T, Klionsky DJ. Autophagy in health and disease: a double-edged sword. Science. 2004 Nov 5;306(5698):990-5.

178. Lu K, Psakhye I, Jentsch S. Autophagic clearance of polyQ proteins mediated by ubiquitin-Atg8 adaptors of the conserved CUET protein family. Cell. 2014 Jul 31;158(3):549-63.

179. Marshall RS, McLoughlin F, Vierstra RD. Autophagic Turnover of Inactive 26S Proteasomes in Yeast Is Directed by the Ubiquitin Receptor Cue5 and the Hsp42 Chaperone. Cell Rep. 2016 Aug 09;16(6):1717-32.

180. Willis SD, Hanley SE, Beishke T, et al. Ubiquitin-proteasome-mediated cyclin C degradation promotes cell survival following nitrogen starvation. Mol Biol Cell. 2020 May 1;31(10):1015-1031.

181. Fleischmann M, Stagljar I, Aebi M. Allele-specific suppression of a Saccharomyces cerevisiae prp20 mutation by overexpression of a nuclear serine/threonine protein kinase. Mol Gen Genet. 1996 Mar 20;250(5):614-25.

182. Mace K, Krakowiak J, El-Samad H, et al. Multi-kinase control of environmental stress responsive transcription. PLoS One. 2020;15(3):e0230246.

183. Bharucha JP, Larson JR, Gao L, et al. Ypi1, a positive regulator of nuclear protein phosphatase type 1 activity in Saccharomyces cerevisiae. Mol Biol Cell. 2008 Mar;19(3):1032-45.

184. Mutlu N, Sheidy DT, Hsu A, et al. A Stress-Responsive Signaling Network Regulating Pseudohyphal Growth and Ribonucleoprotein Granule Abundance in Saccharomyces cerevisiae. Genetics. 2019 Oct;213(2):705-720.

185. Mitchell SF, Jain S, She M, et al. Global analysis of yeast mRNPs. Nat Struct Mol Biol. 2013 Jan;20(1):127-33.

186. Jain S, Wheeler JR, Walters RW, et al. ATPase-Modulated Stress Granules Contain a Diverse Proteome and Substructure. Cell. 2016 Jan 28;164(3):487-98.

187. Laxman S, Tu BP. Multiple TORC1-associated proteins regulate nitrogen starvation-dependent cellular differentiation in Saccharomyces cerevisiae. PLoS One. 2011;6(10):e26081.

188. Umekawa M, Klionsky DJ. Ksp1 kinase regulates autophagy via the target of rapamycin complex 1 (TORC1) pathway. J Biol Chem. 2012 May 11;287(20):16300-10.

189. Huber A, Bodenmiller B, Uotila A, et al. Characterization of the rapamycin-sensitive phosphoproteome reveals that Sch9 is a central coordinator of protein synthesis. Genes Dev. 2009 Aug 15;23(16):1929-43.

190. Oliveira AP, Ludwig C, Zampieri M, et al. Dynamic phosphoproteomics reveals TORC1-dependent regulation of yeast nucleotide and amino acid biosynthesis. Sci Signal. 2015 Apr 28;8(374):rs4.

191. Soulard A, Cremonesi A, Moes S, et al. The rapamycin-sensitive phosphoproteome reveals that TOR controls protein kinase A toward some but not all substrates. Mol Biol Cell. 2010 Oct 1;21(19):3475-86.

192. Ptacek J, Devgan G, Michaud G, et al. Global analysis of protein phosphorylation in yeast. Nature. 2005 2005/12/01;438(7068):679-684.

193. Bharucha N, Ma J, Dobry CJ, et al. Analysis of the yeast kinome reveals a network of regulated protein localization during filamentous growth. Mol Biol Cell. 2008 Jul;19(7):2708-17.

194. Chang Y, Huh WK. Ksp1-dependent phosphorylation of eIF4G modulates post-transcriptional regulation of specific mRNAs under glucose deprivation conditions. Nucleic Acids Res. 2018 Apr 6;46(6):3047-3060.

195. Xie Z, Nair U, Klionsky DJ. Atg8 controls phagophore expansion during autophagosome formation. Mol Biol Cell. 2008 Aug;19(8):3290-8.

196. Tanida I, Mizushima N, Kiyooka M, et al. Apg7p/Cvt2p: A novel protein-activating enzyme essential for autophagy. Mol Biol Cell. 1999 May;10(5):1367-79.

197. Kotani T, Kirisako H, Koizumi M, et al. The Atg2-Atg18 complex tethers pre-autophagosomal membranes to the endoplasmic reticulum for autophagosome formation. Proc Natl Acad Sci U S A. 2018 Oct 9;115(41):10363-10368.

198. Lőrincz P, Juhász G. Autophagosome-Lysosome Fusion. J Mol Biol. 2020 2020/04/03/;432(8):2462-2482.

199. Barz S, Kriegenburg F, Sánchez-Martín P, et al. Small but mighty: Atg8s and Rabs in membrane dynamics during autophagy. Biochim Biophys Acta. 2021 2021/08/01/;1868(9):119064.

200. Dyson HJ, Wright PE. Intrinsically unstructured proteins and their functions. Nat Rev Mol Cell Biol. 2005 Mar;6(3):197-208.

201. Mei Y, Su M, Soni G, et al. Intrinsically disordered regions in autophagy proteins. Proteins. 2014 Apr;82(4):565-78.

202. Meszaros B, Simon I, Dosztanyi Z. Prediction of protein binding regions in disordered proteins. PLoS Comput Biol. 2009 May;5(5):e1000376.

203. Dosztanyi Z, Meszaros B, Simon I. ANCHOR: web server for predicting protein binding regions in disordered proteins. Bioinformatics. 2009 Oct 15;25(20):2745-6.

204. Ramos PC, Hockendorff J, Johnson ES, et al. Ump1p is required for proper maturation of the 20S proteasome and becomes its substrate upon completion of the assembly. Cell. 1998 Feb 20;92(4):489-99.

205. Czabotar PE, Westphal D, Dewson G, et al. Bax crystal structures reveal how BH3 domains activate Bax and nucleate its oligomerization to induce apoptosis. Cell. 2013 Jan 31;152(3):519-31.

206. Uekusa Y, Okawa K, Yagi-Utsumi M, et al. Backbone (1)H, (1)(3)C and (1)(5)N assignments of yeast Ump1, an intrinsically disordered protein that

functions as a proteasome assembly chaperone. Biomol NMR Assign. 2014 Oct;8(2):383-6.

207. Li X, Kusmierczyk AR, Wong P, et al. beta-Subunit appendages promote 20S proteasome assembly by overcoming an Ump1-dependent checkpoint. EMBO J. 2007 May 2;26(9):2339-49.

208. Loos B, du Toit A, Hofmeyr JH. Defining and measuring autophagosome flux-concept and reality. Autophagy. 2014;10(11):2087-96.

209. Suzuki K, Kirisako T, Kamada Y, et al. The pre-autophagosomal structure organized by concerted functions of APG genes is essential for autophagosome formation. EMBO J. 2001 Nov 01;20(21):5971-81.

210. Delorme-Axford E, Guimaraes RS, Reggiori F, et al. The yeast Saccharomyces cerevisiae: an overview of methods to study autophagy progression. Methods. 2015 Mar;75:3-12.

211. Noda NN, Kumeta H, Nakatogawa H, et al. Structural basis of target recognition by Atg8/LC3 during selective autophagy. Genes Cells. 2008 Dec;13(12):1211-8.

212. Ho KH, Chang HE, Huang WP. Mutation at the cargo-receptor binding site of Atg8 also affects its general autophagy regulation function. Autophagy. 2009 May;5(4):461-71.

213. Kirisako T, Ichimura Y, Okada H, et al. The reversible modification regulates the membrane-binding state of Apg8/Aut7 essential for autophagy and the cytoplasm to vacuole targeting pathway. J Cell Biol. 2000 Oct 16;151(2):263-76.

214. Hutchins MU, Klionsky DJ. Vacuolar localization of oligomeric alpha-mannosidase requires the cytoplasm to vacuole targeting and autophagy pathway components in Saccharomyces cerevisiae. J Biol Chem. 2001 Jun 8;276(23):20491-8.

215. Kozakov D, Hall DR, Xia B, et al. The ClusPro web server for protein-protein docking. Nat Protoc. 2017 Feb;12(2):255-278.

216. Desta IT, Porter KA, Xia B, et al. Performance and Its Limits in Rigid Body Protein-Protein Docking. Structure. 2020 Sep 1;28(9):1071-1081 e3.

217. Varadi M, Anyango S, Deshpande M, et al. AlphaFold Protein Structure Database: massively expanding the structural coverage of protein-sequence space with high-accuracy models. Nucleic Acids Res. 2021;50(D1):D439-D444.

218. Jumper J, Evans R, Pritzel A, et al. Highly accurate protein structure prediction with AlphaFold. Nature. 2021 Aug;596(7873):583-589.

219. Suzuki K, Kondo C, Morimoto M, et al. Selective transport of alpha-mannosidase by autophagic pathways: identification of a novel receptor, Atg34p. J Biol Chem. 2010 Sep 24;285(39):30019-25.

220. Scott SV, Guan J, Hutchins MU, et al. Cvt19 is a receptor for the cytoplasm-to-vacuole targeting pathway. Mol Cell. 2001 Jun;7(6):1131-41.

221. Abert C, Kontaxis G, Martens S. Accessory Interaction Motifs in the Atg19 Cargo Receptor Enable Strong Binding to the Clustered Ubiquitin-related Atg8 Protein. J Biol Chem. 2016 Sep 2;291(36):18799-808.

222. Yorimitsu T, Klionsky DJ. Atg11 links cargo to the vesicle-forming machinery in the cytoplasm to vacuole targeting pathway. Molecular biology of the cell. 2005;16(4):1593-1605.

223. Kawamata T, Kamada Y, Kabeya Y, et al. Organization of the pre-autophagosomal structure responsible for autophagosome formation. Mol Biol Cell. 2008 May;19(5):2039-50.

224. Yamamoto H, Fujioka Y, Suzuki SW, et al. The Intrinsically Disordered Protein Atg13 Mediates Supramolecular Assembly of Autophagy Initiation Complexes. Dev Cell. 2016 Jul 11;38(1):86-99.

225. Kawamata T, Kamada Y, Suzuki K, et al. Characterization of a novel autophagy-specific gene, ATG29. Biochem Biophys Res Commun. 2005 Dec 30;338(4):1884-9.

226. Caufield JH, Sakhawalkar N, Uetz P. A comparison and optimization of yeast two-hybrid systems. Methods. 2012 Dec;58(4):317-24.

227. Suzuki H, Osawa T, Fujioka Y, et al. Structural biology of the core autophagy machinery. Curr Opin Struct Biol. 2017 Apr;43:10-17.

228. Kamada Y, Yoshino K, Kondo C, et al. Tor directly controls the Atg1 kinase complex to regulate autophagy. Mol Cell Biol. 2010 Feb;30(4):1049-58.

229. Torggler R, Papinski D, Kraft C. Assays to Monitor Autophagy in Saccharomyces cerevisiae. Cells. 2017 Jul 13;6(3).

230. Noda T. Viability assays to monitor yeast autophagy. Methods Enzymol. 2008;451:27-32.

231. Galluzzi L, Baehrecke EH, Ballabio A, et al. Molecular definitions of autophagy and related processes. EMBO J. 2017 Jul 03;36(13):1811-1836.

232. Farre JC, Manjithaya R, Mathewson RD, et al. PpAtg30 tags peroxisomes for turnover by selective autophagy. Dev Cell. 2008 Mar;14(3):365-76.

233. Motley AM, Nuttall JM, Hettema EH. Pex3-anchored Atg36 tags peroxisomes for degradation in Saccharomyces cerevisiae. EMBO J. 2012 Jun 29;31(13):2852-68.

234. Farre JC, Burkenroad A, Burnett SF, et al. Phosphorylation of mitophagy and pexophagy receptors coordinates their interaction with Atg8 and Atg11. EMBO Rep. 2013 May;14(5):441-9.

235. Nakatogawa H, Mochida K. Reticulophagy and nucleophagy: New findings and unsolved issues. Autophagy. 2015;11(12):2377-8.

236. Liu X, Mao K, Yu AYH, et al. The Atg17-Atg31-Atg29 Complex Coordinates with Atg11 to Recruit the Vam7 SNARE and Mediate Autophagosome-Vacuole Fusion. Curr Biol. 2016 Jan 25;26(2):150-160.

237. Hara T, Takamura A, Kishi C, et al. FIP200, a ULK-interacting protein, is required for autophagosome formation in mammalian cells. J Cell Biol. 2008 May 5;181(3):497-510.

238. Zachari M, Ganley IG. The mammalian ULK1 complex and autophagy initiation. Essays Biochem. 2017 Dec 12;61(6):585-596.

239. Harding TM, Morano KA, Scott SV, et al. Isolation and characterization of yeast mutants in the cytoplasm to vacuole protein targeting pathway. J Cell Biol. 1995 Nov;131(3):591-602.

240. Yamasaki A, Noda NN. Structural Biology of the Cvt Pathway. J Mol Biol. 2017 Feb 17;429(4):531-542.

241. An H, Harper JW. Systematic analysis of ribophagy in human cells reveals bystander flux during selective autophagy. Nat Cell Biol. 2018 2018/02/01;20(2):135-143.

242. Meister G. Argonaute proteins: functional insights and emerging roles. Nature Reviews Genetics. 2013 2013/07/01;14(7):447-459.

243. Muller M, Fazi F, Ciaudo C. Argonaute Proteins: From Structure to Function in Development and Pathological Cell Fate Determination. Front Cell Dev Biol. 2019;7:360.

244. Makino S, Kawamata T, Iwasaki S, et al. Selectivity of mRNA degradation by autophagy in yeast. Nat Commun. 2021 Apr 19;12(1):2316.

245. Kourtis N, Tavernarakis N. Cellular stress response pathways and ageing: intricate molecular relationships. EMBO J. 2011 May 17;30(13):2520-31.

246. De Virgilio C. The essence of yeast quiescence. FEMS Microbiol Rev. 2012 Mar;36(2):306-39.

247. Shi L, Sutter BM, Ye X, et al. Trehalose is a key determinant of the quiescent metabolic state that fuels cell cycle progression upon return to growth. Mol Biol Cell. 2010 Jun 15;21(12):1982-90.

248. van de Peppel J, Holstege FC. Multifunctional genes. Mol Syst Biol. 2005;1:2005 0003.

249. Kuchin S, Yeghiayan P, Carlson M. Cyclin-dependent protein kinase and cyclin homologs SSN3 and SSN8 contribute to transcriptional control in yeast. Proc Natl Acad Sci U S A. 1995 Apr 25;92(9):4006-10.

250. Holstege FC, Jennings EG, Wyrick JJ, et al. Dissecting the regulatory circuitry of a eukaryotic genome. Cell. 1998 Nov 25;95(5):717-28.

251. Hirst M, Kobor MS, Kuriakose N, et al. GAL4 is regulated by the RNA polymerase II holoenzyme-associated cyclin-dependent protein kinase SRB10/CDK8. Mol Cell. 1999 May;3(5):673-8.

252. Larschan E, Winston F. The Saccharomyces cerevisiae Srb8-Srb11 complex functions with the SAGA complex during Gal4-activated transcription. Mol Cell Biol. 2005 Jan;25(1):114-23.

253. Becker LA, Gitler AD. It's all starting to come together. Elife. 2015 Aug 5;4.

254. Garaizar A, Sanchez-Burgos I, Collepardo-Guevara R, et al. Expansion of Intrinsically Disordered Proteins Increases the Range of Stability of Liquid-Liquid Phase Separation. Molecules. 2020 Oct 15;25(20).

255. Protter DSW, Parker R. Principles and Properties of Stress Granules. Trends Cell Biol. 2016 Sep;26(9):668-679.

256. Aryanpur PP, Renner DM, Rodela E, et al. The DEAD-box RNA helicase Ded1 has a role in the translational response to TORC1 inhibition. Mol Biol Cell. 2019 Aug 1;30(17):2171-2184.

257. Buchan JR, Kolaitis RM, Taylor JP, et al. Eukaryotic stress granules are cleared by autophagy and Cdc48/VCP function. Cell. 2013 Jun 20;153(7):1461-74.

258. Noda NN, Wang Z, Zhang H. Liquid-liquid phase separation in autophagy. J Cell Biol. 2020 Aug 3;219(8).

259. Klosinska MM, Crutchfield CA, Bradley PH, et al. Yeast cells can access distinct quiescent states. Genes Dev. 2011 Feb 15;25(4):336-49.

260. Pfanzagl V, Gorner W, Radolf M, et al. A constitutive active allele of the transcription factor Msn2 mimicking low PKA activity dictates metabolic remodeling in yeast. Mol Biol Cell. 2018 Nov 15;29(23):2848-2862.

261. Zetterberg A, Larsson O. Kinetic analysis of regulatory events in G1 leading to proliferation or quiescence of Swiss 3T3 cells. Proc Natl Acad Sci U S A. 1985 Aug;82(16):5365-9.

262. Gray JV, Petsko GA, Johnston GC, et al. "Sleeping beauty": quiescence in Saccharomyces cerevisiae. Microbiol Mol Biol Rev. 2004 Jun;68(2):187-206.

263. Rao BS, Parker R. Numerous interactions act redundantly to assemble a tunable size of P bodies in Saccharomyces cerevisiae. Proc Natl Acad Sci U S A. 2017 Nov 7;114(45):E9569-E9578.

264. Hanley SEW, S. D.; Friedson, B.F.; Cooper, K, F. . Ksp1 is an autophagic receptor protein for Snx4-assisted autophagy of Ssn2/Med13. in revision Autophagy. 2023.

265. Hanley SE, Willis SD, Cooper KF. Snx4-assisted vacuolar targeting of transcription factors defines a new autophagy pathway for controlling ATG expression. Autophagy. 2021 Mar 8:1-19.

266. Xing W, Muhlrad D, Parker R, et al. A quantitative inventory of yeast P body proteins reveals principles of composition and specificity. Elife. 2020 Jun 19;9.

267. Darsow T, Rieder SE, Emr SD. A multispecificity syntaxin homologue, Vam3p, essential for autophagic and biosynthetic protein transport to the vacuole. J Cell Biol. 1997 Aug 11;138(3):517-29.

268. Ramaswami M, Taylor JP, Parker R. Altered ribostasis: RNA-protein granules in degenerative disorders. Cell. 2013 Aug 15;154(4):727-36.

269. Marcelo A, Koppenol R, de Almeida LP, et al. Stress granules, RNA-binding proteins and polyglutamine diseases: too much aggregation? Cell Death Dis. 2021 Jun 8;12(6):592.

270. Abe T, Makino N, Furukawa T, et al. Identification of three commonly deleted regions on chromosome arm 6q in human pancreatic cancer. Genes Chromosomes Cancer. 1999 May;25(1):60-4.

271. Gao HL, Wang WQ, Yu XJ, et al. Molecular drivers and cells of origin in pancreatic ductal adenocarcinoma and pancreatic neuroendocrine carcinoma. Exp Hematol Oncol. 2020;9:28.

272. Antonucci L, Fagman JB, Kim JY, et al. Basal autophagy maintains pancreatic acinar cell homeostasis and protein synthesis and prevents ER stress. Proc Natl Acad Sci U S A. 2015 Nov 10;112(45):E6166-74.

273. Luo J. KRAS mutation in pancreatic cancer. Semin Oncol. 2021 Feb;48(1):10-18.

274. Jackson EL, Willis N, Mercer K, et al. Analysis of lung tumor initiation and progression using conditional expression of oncogenic K-ras. Genes Dev. 2001 Dec 15;15(24):3243-8.

275. Herreros-Villanueva M, Hijona E, Cosme A, et al. Mouse models of pancreatic cancer. World J Gastroenterol. 2012 Mar 28;18(12):1286-94.

276. Morton JP, Timpson P, Karim SA, et al. Mutant p53 drives metastasis and overcomes growth arrest/senescence in pancreatic cancer. Proc Natl Acad Sci U S A. 2010 Jan 5;107(1):246-51.

277. Farrell AS, Joly MM, Allen-Petersen BL, et al. MYC regulates ductal-neuroendocrine lineage plasticity in pancreatic ductal adenocarcinoma associated with poor outcome and chemoresistance. Nat Commun. 2017 Nov 23;8(1):1728.

278. Cao D, Maitra A, Saavedra JA, et al. Expression of novel markers of pancreatic ductal adenocarcinoma in pancreatic nonductal neoplasms: additional evidence of different genetic pathways. Mod Pathol. 2005 Jun;18(6):752-61.

279. Bancerek J, Poss ZC, Steinparzer I, et al. CDK8 kinase phosphorylates transcription factor STAT1 to selectively regulate the interferon response. Immunity. 2013 Feb 21;38(2):250-62.

280. Fryer CJ, White JB, Jones KA. Mastermind recruits CycC:CDK8 to phosphorylate the Notch ICD and coordinate activation with turnover. Mol Cell. 2004 Nov 19;16(4):509-20.

281. Dardare J, Witz A, Merlin JL, et al. SMAD4 and the TGFbeta Pathway in Patients with Pancreatic Ductal Adenocarcinoma. Int J Mol Sci. 2020 May 16;21(10).

282. Yang Z, Klionsky DJ. Mammalian autophagy: core molecular machinery and signaling regulation. Curr Opin Cell Biol. 2010 Apr;22(2):124-31.

283. Yoshii SR, Mizushima N. Monitoring and Measuring Autophagy. Int J Mol Sci. 2017 Aug 28;18(9).

284. Hewitt G, Korolchuk VI. Repair, Reuse, Recycle: The Expanding Role of Autophagy in Genome Maintenance. Trends Cell Biol. 2017 May;27(5):340-351.

285. Vessoni AT, Filippi-Chiela EC, Menck CF, et al. Autophagy and genomic integrity. Cell Death Differ. 2013 Nov;20(11):1444-54.

286. Vaquero EC, Edderkaoui M, Pandol SJ, et al. Reactive oxygen species produced by NAD(P)H oxidase inhibit apoptosis in pancreatic cancer cells. J Biol Chem. 2004 Aug 13;279(33):34643-54.

287. Storz P. KRas, ROS and the initiation of pancreatic cancer. Small GTPases. 2017 Jan 2;8(1):38-42.

288. Bjorkoy G, Lamark T, Brech A, et al. p62/SQSTM1 forms protein aggregates degraded by autophagy and has a protective effect on huntingtin-induced cell death. J Cell Biol. 2005 Nov 21;171(4):603-14.

289. Mathew R, Kongara S, Beaudoin B, et al. Autophagy suppresses tumor progression by limiting chromosomal instability. Genes Dev. 2007 Jun 1;21(11):1367-81.

290. Lloyd AC. The regulation of cell size. Cell. 2013 Sep 12;154(6):1194-205.

291. Lilienbaum A. Relationship between the proteasomal system and autophagy. Int J Biochem Mol Biol. 2013;4(1):1-26.

292. Ott C, Tomasina F, Campolo N, et al. Decreased proteasomal cleavage at nitrotyrosine sites in proteins and peptides. Redox Biol. 2021 Oct;46:102106.

293. Porter DC, Farmaki E, Altilia S, et al. Cyclin-dependent kinase 8 mediates chemotherapy-induced tumor-promoting paracrine activities. Proc Natl Acad Sci U S A. 2012 Aug 21;109(34):13799-804.

294. Galluzzi L, Pietrocola F, Bravo-San Pedro JM, et al. Autophagy in malignant transformation and cancer progression. EMBO J. 2015 Apr 1;34(7):856-80.

295. Maycotte P, Gearheart CM, Barnard R, et al. STAT3-mediated autophagy dependence identifies subtypes of breast cancer where autophagy inhibition can be efficacious. Cancer Res. 2014 May 1;74(9):2579-90.

296. Cros J, Raffenne J, Couvelard A, et al. Tumor Heterogeneity in Pancreatic Adenocarcinoma. Pathobiology. 2018;85(1-2):64-71.

297. Evan T, Wang VM, Behrens A. The roles of intratumour heterogeneity in the biology and treatment of pancreatic ductal adenocarcinoma. Oncogene. 2022 Oct;41(42):4686-4695.

298. Elebo N, Fru P, Omoshoro-Jones J, et al. Role of different immune cells and metabolic pathways in modulating the immune response in pancreatic cancer (Review). Mol Med Rep. 2020 Dec;22(6):4981-4991.

299. Rousseau A, Bertolotti A. Regulation of proteasome assembly and activity in health and disease. Nat Rev Mol Cell Biol. 2018 Nov;19(11):697-712.

300. Cheong H, Nair U, Geng J, et al. The Atg1 kinase complex is involved in the regulation of protein recruitment to initiate sequestering vesicle formation for nonspecific autophagy in Saccharomyces cerevisiae. Mol Biol Cell. 2008 Feb;19(2):668-81.

301. Kamber RA, Shoemaker CJ, Denic V. Receptor-Bound Targets of Selective Autophagy Use a Scaffold Protein to Activate the Atg1 Kinase. Mol Cell. 2015 Aug 6;59(3):372-81.

302. Loll-Krippleber R, Brown GW. P-body proteins regulate transcriptional rewiring to promote DNA replication stress resistance. Nat Commun. 2017 Sep 15;8(1):558.

303. Wang C, Schmich F, Srivatsa S, et al. Correction: Context-dependent deposition and regulation of mRNAs in P-bodies. Elife. 2018 Aug 23;7.

304. Strich R, Slater MR, Esposito RE. Identification of negative regulatory genes that govern the expression of early meiotic genes in yeast. Proc Natl Acad Sci USA. 1989;86:10018-10022.

305. Zubenko GS, Park FJ, Jones EW. Mutations in PEP4 locus of Saccharomyces cerevisiae block final step in maturation of two vacuolar hydrolases. Proc Natl Acad Sci U S A. 1983 Jan;80(2):510-4.

306. Snyder NA, Kim A, Kester L, et al. Auxin-Inducible Depletion of the Essentialome Suggests Inhibition of TORC1 by Auxins and Inhibition of Vrg4 by SDZ 90-215, a Natural Antifungal Cyclopeptide. G3 (Bethesda). 2019 Mar 7;9(3):829-840.

307. Chu AM, Davis RW. High-throughput creation of a whole-genome collection of yeast knockout strains. Methods Mol Biol. 2008;416:205-20.

308. Kingsbury JM, Cardenas ME. Vesicular Trafficking Systems Impact TORC1-Controlled Transcriptional Programs in Saccharomyces cerevisiae. G3 (Bethesda). 2016 Jan 6;6(3):641-52.

309. Wanke V, Pedruzzi I, Cameroni E, et al. Regulation of G0 entry by the Pho80-Pho85 cyclin-CDK complex. EMBO J. 2005 Dec 21;24(24):4271-8.

310. Cebollero E, van der Vaart A, Zhao M, et al. Phosphatidylinositol-3-phosphate clearance plays a key role in autophagosome completion. Curr Biol. 2012 Sep 11;22(17):1545-53.

311. Abeliovich H, Zhang C, Dunn WA, Jr., et al. Chemical genetic analysis of Apg1 reveals a non-kinase role in the induction of autophagy. Mol Biol Cell. 2003 Feb;14(2):477-90.

312. Wade Harper J, Adami GR, Wei N, et al. The p21 Cdk-interacting protein Cip1 is a potent inhibitor of G1 cyclin-dependent kinases. Cell. 1993 1993/11/19/;75(4):805-816.

313. Graef M, Friedman JR, Graham C, et al. ER exit sites are physical and functional core autophagosome biogenesis components. Mol Biol Cell. 2013 Sep;24(18):2918-31.

314. Gari E, Piedrafita L, Aldea M, et al. A set of vectors with a tetracycline-regulatable promoter system for modulated gene expression in Saccharomyces cerevisiae. Yeast. 1997 Jul;13(9):837-48.

315. Montpetit B, Thomsen ND, Helmke KJ, et al. A conserved mechanism of DEAD-box ATPase activation by nucleoporins and InsP6 in mRNA export. Nature. 2011 Apr 14;472(7342):238-42.

316. Stephan JS, Yeh YY, Ramachandran V, et al. The Tor and PKA signaling pathways independently target the Atg1/Atg13 protein kinase complex to control autophagy. Proc Natl Acad Sci U S A. 2009 Oct 6;106(40):17049-54.

APPENDIX

Table 1. Candidate proteins that interact with Med13 after 90 min 200 ng/ml rapamycin treatment.

Select proteins obtained from mass spectroscopy where counts were greater than 2-fold after 90 min of 200 ng/mL rapamycin.			Counts	
Systematic Name	**Gene**	**Protein Function**	**T=0**	**T=90**
Other				
YER155C	*BEM2*	RhoGAP	47	203
YJL005W	*CYR1*	Adenylate cyclase	19	50
YHR016C	*YSC84*	Actin-binding protein	7	18
YNL271C	*BNI1*	Formin	5	13
YBR140C	*IRA1*	GTPase activator	1	12
YDR103W	*STE5*	MAPK scaffold	4	12
YGR032W	*GSC2*	spore wall assembly	1	9
YDL198C	*GGC1*	Mitochondrial GTP/GDP transporter	3	7
Nuclear Activity				
YPR018W	*RLF2*	Chromatin assembly	21	44
YPL155C	*KIP2*	Kinesin	6	34
YDL140C	*RPO21*	RNA polymerase II subunit	13	33
YML065W	*ORC1*	DNA replication	14	32
YNL278W	*CAF120*	Transcriptional regulation	7	27
YDR216W	*ADR1*	Transcription factor	12	26
YER040W	*GLN3*	Transcriptional activator	10	23
YDR364C	*CDC40*	mRNA Splicing	7	15
YGL045W	*RIM8*	Activates Rim101	6	13
YER088C	*DOT6*	DNA binding protein	3	12
YDL089W	*NUR1*	Mitotic exit/nuclear periphery	3	9
YDL207W	*GLE1*	Cytoplasmic nucleoporin	3	9

YDL220C	*CDC13*	Telomere capping	4	9
Vacuole				
YJL172W	*CPS1*	Vacuolar carboxypeptidase	4	18
YPR036W	*VMA13*	V-ATPase	4	12
YDR128W	*MTC5*	Vacuole/TORC1	3	8
YLL048C	*YBT1*	Vacuole fusion	2	8
Kinase/Phosphatase				
YDR283C	*GCN2*	Kinase	78	160
YHR082C	*KSP1*	Kinase	25	60
YKL168C	*KKQ8*	Kinase	13	36
YDR122W	*KIN1*	Kinase	4	28
YOR039W	*CKB2*	Kinase	8	26
YDL025C	*RTK1*	Kinase	3	18
YOR061W	*CKA2*	Kinase	5	15
YGL019W	*CKB1*	Kinase	4	13
YMR165C	*PAH1*	Phosphatase	4	13
YIL035C	*CKA1*	Kinase	5	12
YAR014C	*BUD14*	Protein phosphatase regulator	3	7
Anabolism/Catabolism				
YLR044C	*PDC1*	Pyruvate decarboxylase	57	200
YKL182W	*FAS1*	Fatty acid synthetase	35	94
YKL060C	*FBA1*	Glycolysis	26	62
YEL071W	*DLD3*	Lactate dehydrogenase	16	40
YBR196C	*PGI1*	Phosphoglucose isomerase	3	29
YLR304C	*ACO1*	Aconitase	10	25
YLR153C	*ACS2*	Acetyl-coA synthetase	8	24
YOR136W	*IDH2*	Isocitrate dehydrogenase complex	7	22
YBR208C	*DUR1,2*	Urea amidolyase	0	21
YLR355C	*ILV5*	Amino acid biosynthesis	1	19

YGL009C	*LEU1*	Leucine biosynthesis	7	17
YKL218C	*SRY1*	Amino acid catabolism	2	15
YGL245W	*GUS1*	tRNA synthetase	2	15
YER024W	*YAT2*	Acetyltransferase/mitochondria	1	11
YBR221C	*PDB1*	Pyruvate dehydrogenase	3	10
YDR341C	YDR341C	Arginyl-tRNA synthetase/mitochondria	1	9
YIL128W	*MET18*	Methionine biosynthesis/CIA complex	2	9
YGL001C	*ERG26*	Ergosterol biosynthesis	3	7
YJL060W	*BNA3*	Aminotransferase	3	7
Protein Trafficking				
YNL287W	*SEC21*	COPI vesicle coat	9	23
YBR102C	*EXO84*	Exocytosis/splicesome assembly	3	19
YBL037W	*APL3*	Intracellular protein transport	5	13
YNL049C	*SFB2*	COPII vesicle coat	5	12
YNL246W	*VPS75*	Histone chaperone	4	12
YHR103W	*SBE22*	Golgi/bud growth	2	11
YLR114C	*AVL9*	Exocytic transport	3	9
YDR483W	*KRE2*	Golgi mannosyltransferase	2	8
YJL036W	*SNX4*	Sorting nexin/CVT	2	8
YDR171W	*HSP42*	Chaperone	3	7
YDR186C	*SND1*	ER targeting	3	7
Ribosome				
YPL009C	YPL009C	Ribosome quality control complex	14	63
YKL014C	*URB1*	Ribosome biogenesis	20	47
YGR162W	*TIF4631*	Translation initiation factor	12	37
YDR333C	*RQC1*	Ribosome quality control	13	31
YMR049C	*ERB1*	Ribosome biogenesis	13	28

YJR041C	*URB2*	Ribosome biogenesis	1	11
YNL224C	*SQS1*	Ribosome biogenesis	4	9
Unknown Function				
YPL032C	*SVL3*	Unknown function/vacuole	16	59
YER047C	*SAP1*	Unknown/AAA ATPase	21	53
YGR237C	*YGR237C*	Unknown function	11	28
YLR187W	*SKG3*	Unknown function	9	19
YLR219W	*MSC3*	Unknown function	8	18
YBR007C	*DSF2*	Unknown/bud Tip	5	15
YOR093C	*YOR093C*	Unknown function	6	15
YBR225W	*YBR225W*	Unknown/cell wall	5	13
YDR251W	*PAM1*	Unknown function	2	13
YGR196C	*FYV8*	Unknown function	4	11
YDR239C	*YDR239C*	Unknown function/ribosome	2	9
Transporters/Permeases				
YDR345C	*HXT3*	glucose transporter	7	22
YKR093W	*PTR2*	Peptide transporter	6	21
YKR039W	*GAP1*	Amino acid permease	4	20
YJR152W	*DAL5*	Allantoate permease	0	15
YCL025C	*AGP1*	amino acid permease	4	11
Ubiquitin				
YBL067C	*UBP13*	Ubiquitin protease	7	19
YEL012W	*UBC8*	Ubiquitin-conjugating	7	16
YDL126C	*CDC48*	ATPase/ubiquitin binding	6	15
YDL122W	*UBP1*	Ubiquitin protease	3	11

Table 2. List of yeast strains that were used.

Strain*	Genotype	Source
RSY10*	*MAT**a** ade2 ade6 can1-10 his3-11, 15 leu2-3, 112 trp1-1 ura3-1*	[304]
RSY1812*	*MED13-yECitrine::KanMX6*	[53]
BJ5459**/RSY449	*pep4::HIS3 prb1-Δ1.6R*	[305]
RSY1961*	*ump1::HIS3 MED13-13MYC::KanMX4*	[53]
RSY2000	*gal4Δ gal80Δ LYS2::GAL1-HIS3 GAL2-Ade2 URA3-MEL1 AUR1-C MEL1*	
RSY2094*	*atg1::KanMX4*	This study
RSY2097*	*vac8::KanMX4*	This study
RSY2104*	*atg17::KanMX4*	This study
RSY2106*	*nvj1::KanMX4*	This study
RSY2144*	*atg8::KanMX4*	This study
RSY2160*	*ump1::KanMX4*	[180]
RSY2123*	*atg39::KanMX4 atg40Δ::NatNT2*	This study
RSY2202*	*atg1::KanMX4 ump1::NatNT2*	This study
RSY2211*	*MED13-9MYC::NatNT2*	This study
RSY2213*	*nvj1::KanMX4 MED13-9MYC::NatNT2*	This study
RSY2214*	*atg1::KanMX4 MED13-9MYC::NatNT2*	This study
RSY2215**	*pep4::HIS3 prb1-Δ1.6R MED13-9MYC::NatNT2*	This study
RSY2231*	*atg8::KanMX4 MED13-9MYC::NatNT2*	This study
RSY2248*	*atg11::KanMX4*	This study
RSY2157*	*PRE6-GFP::HphNT1*	
RSY2176*	*Cdk8::NatNT2*	
RSY2266*	*ksp1::KanMX4*	This study
RSY2267*	*ksp1:: KanMX4 MED13-9MYC::NatNT2*	This study
RSY2272*	*snx4::HphNT1*	This study
RSY2276*	*snx4::HphNT1 MED13-9MYC::NatNT2*	This study
RSY2277*	*atg20::KanMX4 MED13-9MYC::NatNT2*	This study
RSY2283*	*ADH-GFP-SNX4::NatNT2*	This study
RSY2299*	*pep4:: KanMX4 ADH-GFP-SNX4::NatNT2*	This study
RSY2305**	*pep4::HIS3 prb1-Δ1.6R MED13-mNeongreen::NatNT2*	This study
RSY2307*	*atg8::KanMX4 MED13-mNeongreen::NatNT2*	This study

RSY2323**	*pep4::HIS3 prb1-Δ1.6R ksp1Δ::KanMX4 MED13-mNeongreen::NatNT2*	This study
RSY2324**	*pep4::HIS3 prb1-Δ1.6R snx4Δ::HphNT1 MED13-mNeongreen::NatNT2*	This study
RSY2325*	*atg8::KanMX4 MED13-mNeongreen::NatNT2*	
RSY2348*	*PTetO7-Ubi-Leu::3HA-CRM1::NatMX4 MED13-9MYC::HphNT1*	This study
RSY2349*	*atg39::KanMX4 atg40::NatNT2 MED13-9MYC::HphNT1*	This study
RSY2373*	*atg17::KanMX4 MED13-9MYC::NatNT2*	This study
RSY2394*	*snx41::HIS3 MED13-9MYC::NatNT2*	This study
RSY2395**	*pep4::HIS3 prb1-Δ1.6R ATG17-GFP::HphNT1*	This study
RSY2396**	*pep4::HIS3 prb1-Δ1.6R snx4::KanMX4 ATG17-GFP::HphNT1*	This study
RSY2399*	*msn5::KanMX4 MED13-9MYC::NatNT2*	This study
RSY2400**	*pep4::HIS3 prb1-Δ1.6R MED13-mNeongreen::HphNT1 ATG17-RedStar::NatNT2*	This study
RSY2423**	*pep4::HIS3 prb1-Δ1.6R GLE1-GFP::HphNT1*	This study
RSY2424**	*pep4::HIS3 prb1-Δ1.6R MED13-mNeongreen::HphNT1 ADH1-mCherry-SNX4::NatNT2*	This study
RSY2444*	*MED13::HIS3*	This study
RSY2450**	*pep4::HIS3 prb1-Δ1.6R MED13-mNeongreen::NatNT2 GLE1-RedStar::KanMX4*	This study
RSY2451*	*ADH1-GFP-SNX4::NatNT2 GLE1-RedStar::KanMX4*	This study
RSY2455*	*GLE1-GFP::HphNT1*	This study
RSY2456	*his3Δ1 leu2Δ met15Δ ura3Δ GLE1-TAP-AID-FLAG::Ura3*	[306]
RSY2464	*his3Δ1 leu2Δ met15Δ ura3Δ NUP159-TAP-AID-FLAG::Ura3*	[306]
RSY2473	*his3Δ1 leu2Δ met15Δ ura3Δ GLE1-TAP-AID-FLAG::Ura3 pep4::KanMX4 MED13-mNeonGreen::NatNT2*	This study
RSY2474**	*pep4::HIS3 prb1-Δ1.6R KSP1-GFP::KanMX4*	This study
RSY2535*	*vam3::KanMX4 MED13-mNeonGreen::NatNT2*	This study
RSY2540*	*atg19::HphNT1*	This study
RSY2545*	*atg8::KanMX4 MED13-mNeonGreen::NatNT2 atg7-mCherry::HphNT1*	This study

RSY2547*	*atg8::KanMX4 MED13-mNeonGreen::NatNT2 atg2-mCherry::HphNT1*	This study
RSY2551*	*vam3::KanMX4*	This study
RSY2557*	*atg34::KanMX4*	This study
RSY2559*	*atg19::HphNT1 atg34::KanMX4*	This study
RSY2561*	*pep4::KanMX4 MED13-mNeonGreen::NatNT2 KSP1-mCherry::HphNT1*	This study
RSY2567*	*KSP1-9MYC::HphNT1*	This study
RSY2574*	*pep4::KanMX4 KSP1-9MYC::HphNT1*	This study
RSY2666*	*EDC3-GFP::KanMX4*	
RSY2687*	*DHH1-GFP::KanMX4*	
RSY2688*	*ksp1::KanMX4 DHH1-GFP::HphNT1*	
RSY2694*	*med13::HIS3 DCP2-GFP::HphNT1*	
RSY2700*	*snx4::HphNT1 DHH1-GFP::KanMX4*	
RSY2701*	*snx4::HphNT1 EDC3-GFP::KanMX4*	
RSY2704*	*atg8::KanMX4 MED13-mNeongreen::NatNT2 DCP2-mCherry::HphNT1*	
RSY2714*	*edc3::KANMX4 DCP2-GFP::HphNT1*	
RSY2715*	*atg8::KanMX4 Ksp1-GFP::HphNT1*	This study
RSY2716*	*vam3::KanMX4 Ksp1-GFP::HphNT1*	This study
RSY2725*	*ksp1::KanMX4 EDC3-GFP::HphNT1*	
RSY2737*	*atg8::KanMX4 KSP1-9MYC::HphMX6*	This study
RSY2744*	*atg8::KanMX4 pep4::HIS3 MED13-mNeonGreen::NatNT2 KSP1-mCherry::HphNT1*	This study
RSY2745*	*vam3::KanMX4 MED13-mNeonGreen::NatNT2 KSP1-mCherry::HphNT1*	This study
RSY2778*	*atg8::KanMX4 3BFP-PHO8::LEU2 KSP1-mCherry::HpHNT1*	This study
RSY2797*	*KSP1-9MYC::HphNT1 ump1::NATNT2*	This study
RSY2798*	*KSP1-9MYC::HphNT1 ump1::NATNT2 atg1::KanMX4*	This study
RSY2815*	*atg8::KanMX4 Ksp1-mCherry::HphNT1*	This study
RSY2817*	*atg8::KanMX4 EDC3-9MYC::HphNT1*	
RSY2820*	*atg8::KanMX4 XRN1-9MYC::HphNT1*	
RSY2821*	*atg8::KanMX4 DCP2-9MYC::HphNT1*	
RSY2824*	*ksp1::KanMX4 DCP2-9MYC::HphNT1*	
RSY2825*	*ksp1::KanMX4 XRN1-9MYC::HphNT1*	
RSY2826*	*edc3::KANMX4 MED13-9MYC::HphNT1*	

BY4741	*MAT**a** his3Δ1 leu2Δ met15Δ ura3Δ*	[307]
	atg4::KANMX4	
	atg9::KANMX4	
	atg19:: KANMX4	
	atg32::KANMX4	
	atg36:: KANMX4	
	cue5::KANMX4	
	hsp42:: KANMX4	
	hsp104:: KANMX4	
	los1::KANMX4	
	nup2:: KANMX4	
	ubx5::KANMX4	
	vps34::KANMX4	

*Genotype of all stains is *MAT**a** ade2 ade6 can1-10 his3-11, 15 leu2-3, 112 trp1-1 ura3-1* (W303). **Genotype of all strains is *MAT**a** his3-Δ200 can1 ura3-52 leu2Δ1 lys2-801 trp1-289* (BJ5459). The *atg19, atg36, csm1, heh1, lrs4,* and *nur1* strains are from the yeast knock out collection (Chu and Davis, 2008) and are derived from BY4741 (*MAT**a** his3Δ1 leu2Δ met15Δ ura3Δ).*

Table 3. List of plasmids that were used.

Plasmid Name	Gene	Tag	Marker	Reference
pKC801	*MED13*	3HA	*URA3*	[54]
pKC803	*MED13*	3HA	*LEU2*	[54]
pKC337	*CNC1*	MYC	*TRP1*	[49]
pDS2	*GAL4-AD-MED13*$^{1-305}$	1HA	*LEU2*	[54]
pDS4	*GAL4-AD-MED13*$^{907-1421}$	1HA	*LEU2*	[54]
pDS7	*GAL4-AD-MED13*$^{306-570}$	1HA	*LEU2*	[54]
pDS8	*GAL4-AD-MED13*$^{571-906}$	1HA	*LEU2*	[54]
pSH3	*RPH1*	GFP	*URA3*	This study
pSH4	*PGK1*	GFP	*URA3*	[3]
pSH8	*GAL4BD-SNX4*	1HA	*TRP1*	This study
pSH9	*GAL4-AD-ATG8*	T7	*TRP1*	[3]
pSH13	*GAL4BD-ATG20*	1HA	*TRP1*	This study
pSH16	*GAL4BD-SNX4*$^{1-157}$	1HA	*TRP1*	This study
pSH17	*GAL4BD-SNX4*$^{157-423}$	1HA	*TRP1*	This study

pSH18	*GAL4AD-MED13$^{907-1163}$*	1HA	*LEU2*	This study
pSH19	*GAL4AD-MED13$^{1163-1421}$*	1HA	*LEU2*	This study
pSH25	*GAL4-BD-KSP1*	1HA	*TRP1*	This study
pSH26	*KSP1*	GFP	*URA3*	This study
pSH30	*SNX4*	6HA	*TRP1*	This study
pSH32	*KSP1^{K47D}*	GFP	*URA3*	This study
pSH33 (KD)	*GAL4-BD-KSP1$^{1-401}$*	1HA	*TRP1*	This study
pSH34 (DD1)	*GAL4-BD-KSP1$^{401-681}$*	1HA	*TRP*	This study
pSH35 (DD2)	*GAL4-BD-KSP1$^{681-1029}$*	1HA	*TRP1*	This study
pSH36	*ATG8^{Y49A,L50A}*	GFP	*TRP*	This study
pSH37	*KSP1$^{1022-1029\Delta}$*	9MYC	*URA3*	This study
pSH38	*KSP1$^{167-172\Delta,1022-1029\Delta}$*	9MYC	*URA3*	This study
pSH39	*KSP1$^{167-172\Delta,1022-1029\Delta}$*	GFP	*URA3*	This study
pSW108	*GAL4-AD-CNC1*	-	*LEU2*	This study

pSW132	*GAL4AD-UME6*	-	*LEU2*	This study
pSW143	*GAL4-BD-ATG7*	1HA	*TRP1*	[3]
pSW144	*GAL4-AD-ATG8*	T7	*LEU2*	[3]
pSW155	*GAL4-AD-ATG17*	T7	*LEU2*	This study
pSW156	*GAL4-AD-ATG29*	T7	*LEU2*	This study
pSW157	*GAL4-AD-ATG31*	T7	*LEU2*	This study
pSW163	*GAL4-BD-KSP1*$^{681\text{-}1029,\ L1025A}$	T7	*TRP1*	This study
pSW217	MSN2	GFP	URA3	This study
pSW218	MED13	GFP	URA3	This study
pSW221	*VPH1*	mCherry	*URA3*	[180]
pSW230	*CCL1*	GFP	*URA3*	This study
pSW288	*CRN1-MED13*	GFP	*URA3*	This study
pSW320	*MED13*	GFP	*HIS3*	[3]
pSW337	*ATG8*	GFP	*TRP1*	[3]
Lep752	*NUP49*	mCherry	*LEU2*	Kiran Madura
pNab2-NLS	*NAB2*	mCherry	*LEU2*	[308]
pFD846	*RIM15*	GFP	*TRP1*	[309]
pYL666	*ATG8*	mCherry	*LEU2*	[310]

Atg8	*ATG8*	GFP	*TRP1*	[311]
ATG8	mCherry	*LEU2*	*CUP*	*ATG8*
pAS2	*GAL4-BD*	1HA	*TRP1*	[312]
pACT2-T7	*GAL4-AD*	1T7	*LEU2*	[3]
PHO8	*PHO8*	3xBFP	*HIS3*	[313]
pCM188	*TET*	-	*URA3*	[314]
pKW2571	*Gle1-V513D/A516D/I520D*	-	*LEU2*	[315]
pSW3345	*Gle1-K337Q/L378Q*	-	*LEU2*	[117]
pPH27427	*ATG13*	3HA	*TRP1*	[316].
pRS315	-	-	*LEU2*	CEN
pRS316	-	-	*URA3*	CEN

Table 4. Antibodies used in mammalian work.

Antibody	Dilution	Company	Catalog #
cyclin C	1:1,000	Cell Signaling	68179
Cdk8	1:1,000	Santa Cruz	SC-1521
LC3	1:1,000	Cell Signaling	3868
CK19	30:1,000	DSHB	AB_2133570
p53	1:1,000	Santa Cruz	SC-126
β-actin	1:2,500	Abcam	ab8227
Notch (NICD)	1:1,000	Millipore	07-1232
Atg7	1:1,000	Cell Signaling	8558
p62	1:1,000	Cell Signaling	5144
Hif1α	1:1,000	Cell Signaling	36169
Beclin 1	1:1,000	Cell Signaling	3495
p21	1:1,000	Abcam	ab188224
α 20 subunits	1:1,000	Enzo	PW8195
Rpn6	1:1,000	Enzo	PW8370
Rpt1	1:1,000	Enzo	PW8825
Rpt6	1:1,000	Enzo	PW9265
Atg12	1:1,000	Cell Signaling	4180
Atg3	1:1,000	Cell Signaling	3415
Atg16L1	1:1,000	Cell Signaling	8089

List of antibodies that were used to monitor proteins via western blot analysis. Reactive with mouse. DSHB: Developmental Studies Hybridoma Bank

Supplemental figures

Chapter 2

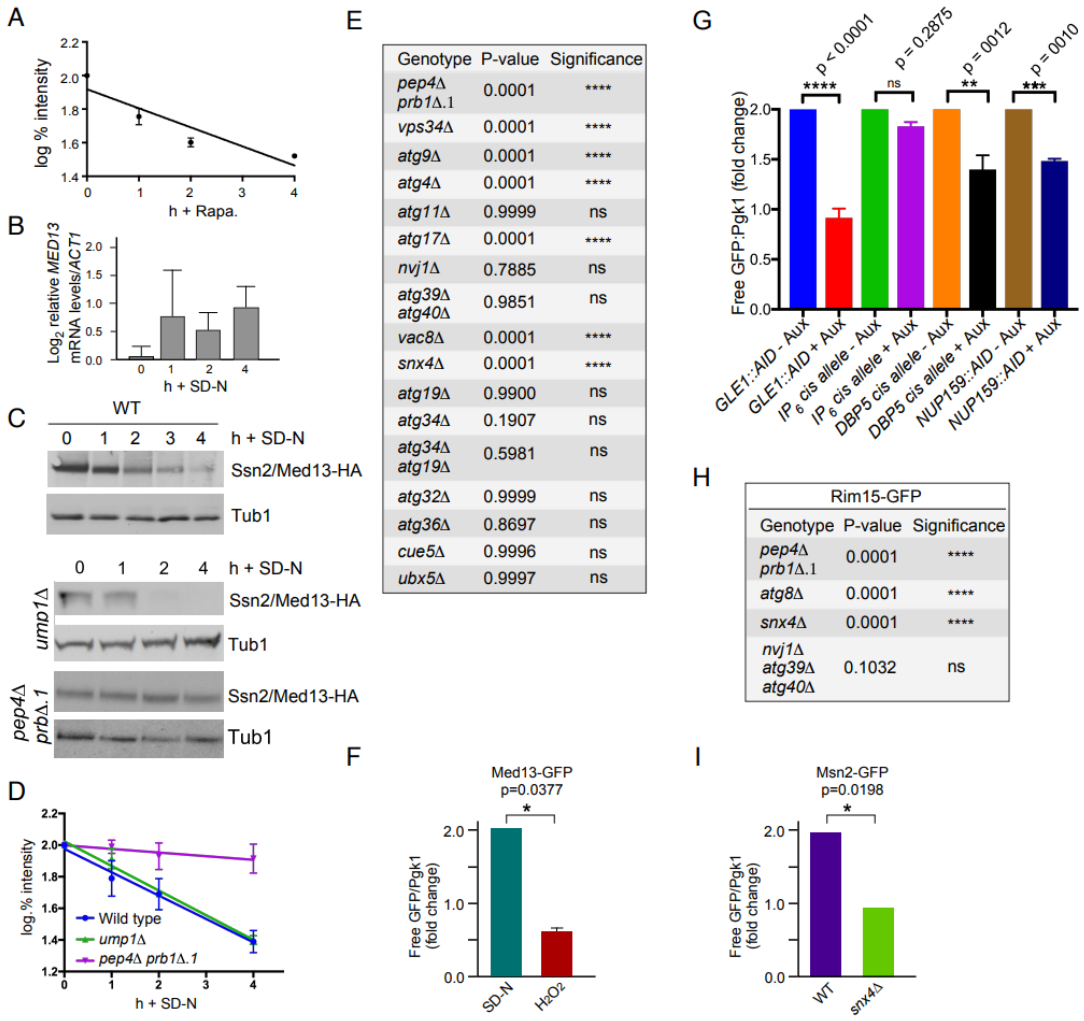

Genotype	P-value	Significance
pep4Δ prb1Δ.1	0.0001	****
vps34Δ	0.0001	****
atg9Δ	0.0001	****
atg4Δ	0.0001	****
atg11Δ	0.9999	ns
atg17Δ	0.0001	****
nvj1Δ	0.7885	ns
atg39Δ atg40Δ	0.9851	ns
vac8Δ	0.0001	****
snx4Δ	0.0001	****
atg19Δ	0.9900	ns
atg34Δ	0.1907	ns
atg34Δ atg19Δ	0.5981	ns
atg32Δ	0.9999	ns
atg36Δ	0.8697	ns
cue5Δ	0.9996	ns
ubx5Δ	0.9997	ns

Rim15-GFP

Genotype	P-value	Significance
pep4Δ prb1Δ.1	0.0001	****
atg8Δ	0.0001	****
snx4Δ	0.0001	****
nvj1Δ atg39Δ atg40Δ	0.1032	ns

Figure S1. Med13 is degraded in response to rapamycin. **(A)** Degradation kinetics of endogenous Med13-9MYC protein levels in wild-type cells treated with 200 ng/mL rapamycin. Error bars indicate S.D., N=3 biological samples. **(B)** RT-qPCR analysis probing for *MED13* mRNA expression in wild-type cells following nitrogen starvation. ΔΔCt results for relative fold change (log_2) values using wild-type unstressed cells as a control. Transcript levels are given relative to the internal *ACT1* mRNA control. **(C)** Western blot analysis of Med13-3HA protein levels, expressed from a single copy functional plasmid in wild-type, *ump1*Δ and *pep4*Δ *prb1*Δ*.1* cells following nitrogen starvation. Pgk1 levels were used as loading controls. **(D)** Quantification of Med13-3HA degradation kinetics in indicated mutants obtained from C. Error bars indicates S.D., N=3 biological samples. **(E-I)** Quantification of free GFP accumulation in cleavage assays.

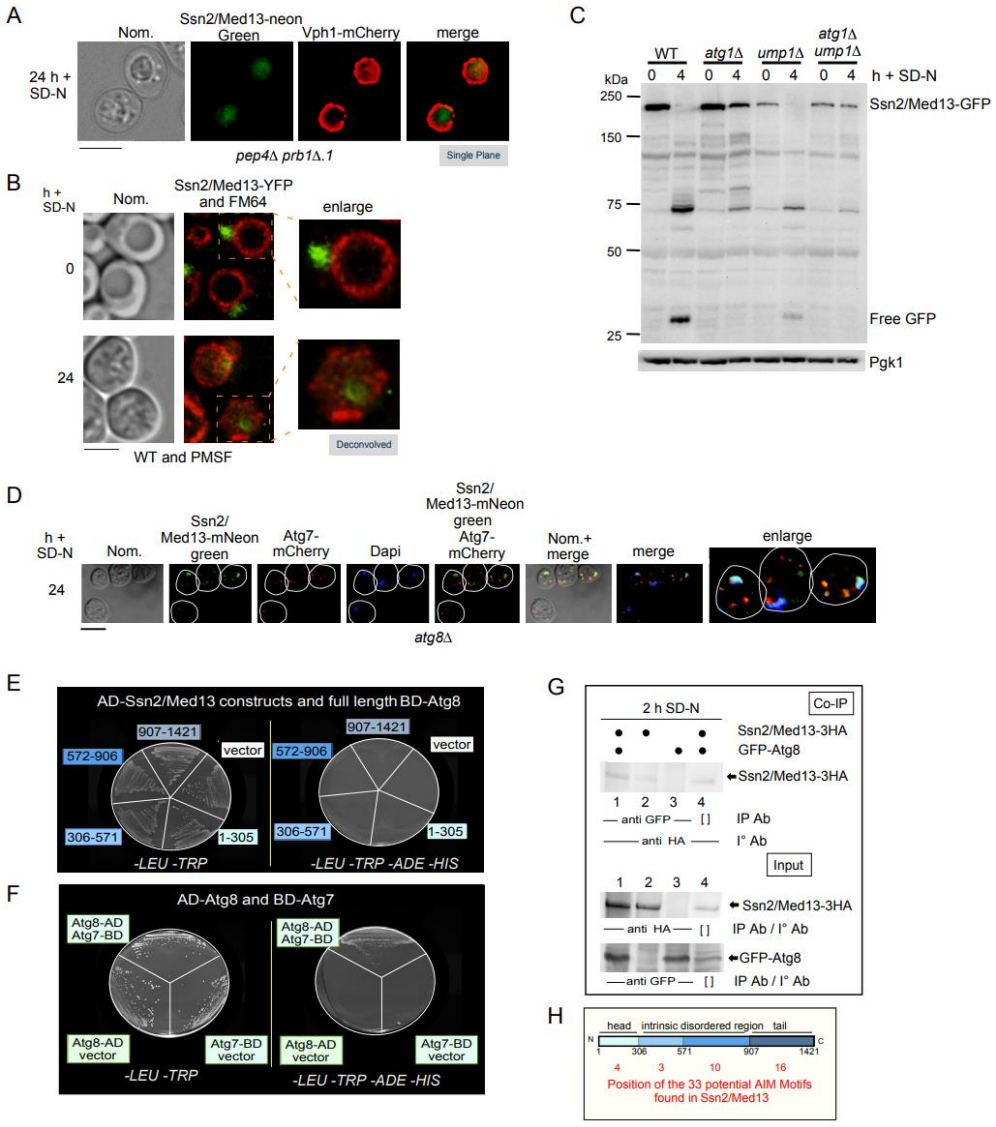

Figure S2. (A) Fluorescence microscopy of *pep4*Δ *prb1*Δ*.1* cells expressing endogenous Med13-mNeongreen and Vph1-mCherry (vacuole marker). **(B)** Fluorescence microscopy of wild-type cells expressing endogenous Med13-YFP treated with 200 mM PMSF before and after 24 h in SD-N media. FM4-64 staining was used to visualize the vacuole. **(C)** Western blot analysis of Med13-GFP cleavage assays in the indicated genotypes. Pgk1 levels were used as loading controls. **(D)** Co-localization of endogenous Med13-mNeongreen and Atg7-mCherry in *atg8*Δ cells stained with DAPI. **(E)** Y2H Gold cells harboring Gal4-BD-Atg8 and the indicated Gal4-AD- Med13 constructs or vector controls. **(F)** Y2H analysis with GAL4-AD-Atg8 and GAL4-BD-Atg7. **(G)** Co-immunoprecipitation analysis of GFP-Atg8 and Med13-3HA. Whole-cell lysates were immunoprecipitated with the antibodies shown from nitrogen-starved *pep4*Δ *prb1*Δ*.1* cells expressing GFP-Atg8 and Med13-3HA. **(H)** Schematic map of the 33 putative AIMs motifs found within the different domains of Med13.

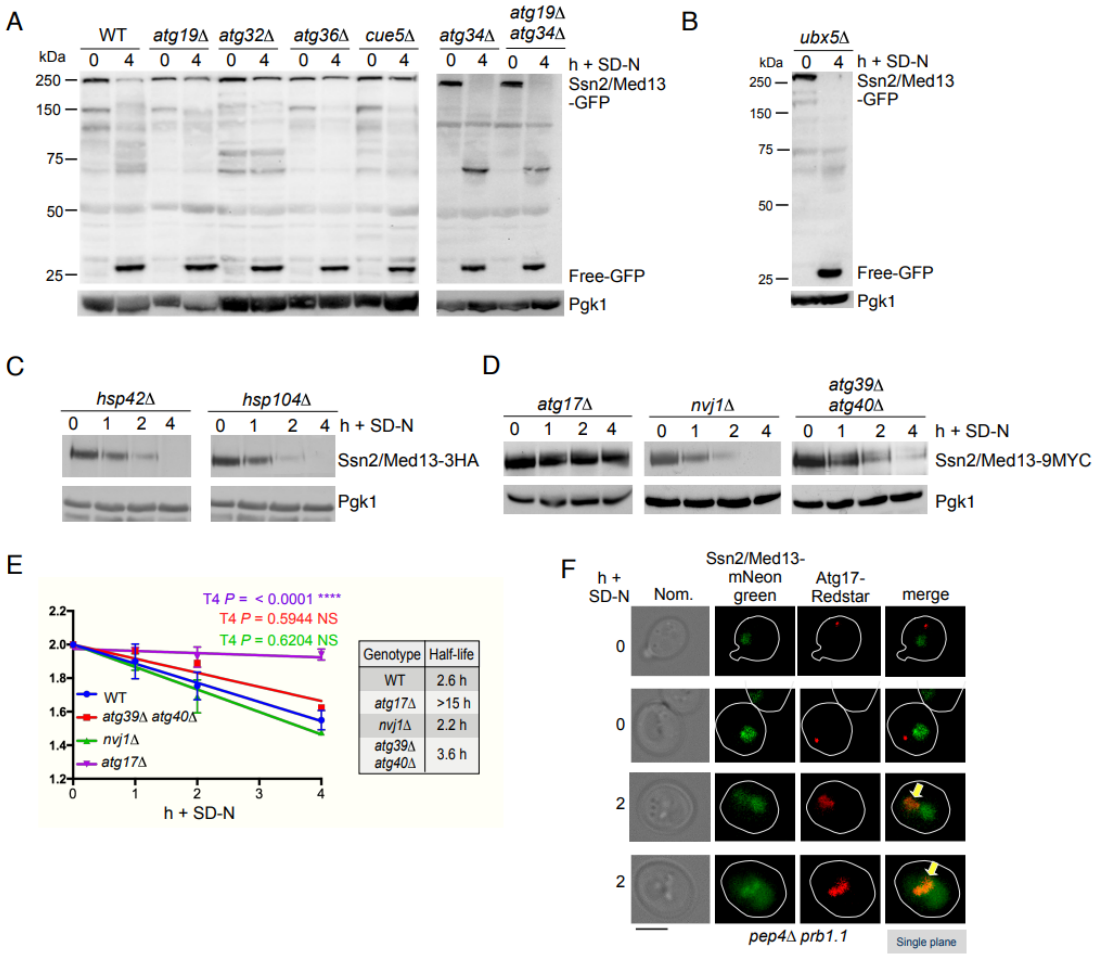

Figure S3. The autophagic degradation of Med13 does not require known selective autophagy receptor proteins. **(A)** Wild-type BY4741 cells and the indicated mutants expressing Med13-GFP were nitrogen-starved for the indicated times. **(B)** As in A except that Med13-GFP were executed in *ubx5*Δ. **(C)** Western blot analysis of Med13-3HA protein levels, expressed from a single copy functional plasmid in *hsp42*Δ and *hsp104*Δ cells following nitrogen starvation. Pgk1 was used as a protein loading control in all experiments. **(D)** Western blot analysis of endogenous Med13-9xMYC degradation in *atg17*Δ cells as well as in strains defective in known nucleophagy pathways following nitrogen starvation. **(E)** Degradation kinetics and half-life of Med13 protein levels obtained in D. Error bars indicate S.D., N=3 biological samples. **(F)** Fluorescence microscopy monitoring colocalization of endogenous Med13-mNeongreen and Atg17-Redstar after 2 h of nitrogen starvation in *pep4*Δ *prb1*Δ*.1*. Representative single-plane images are shown. Bar: 5 μm. For all blots, Pgk1 levels were used as loading controls.

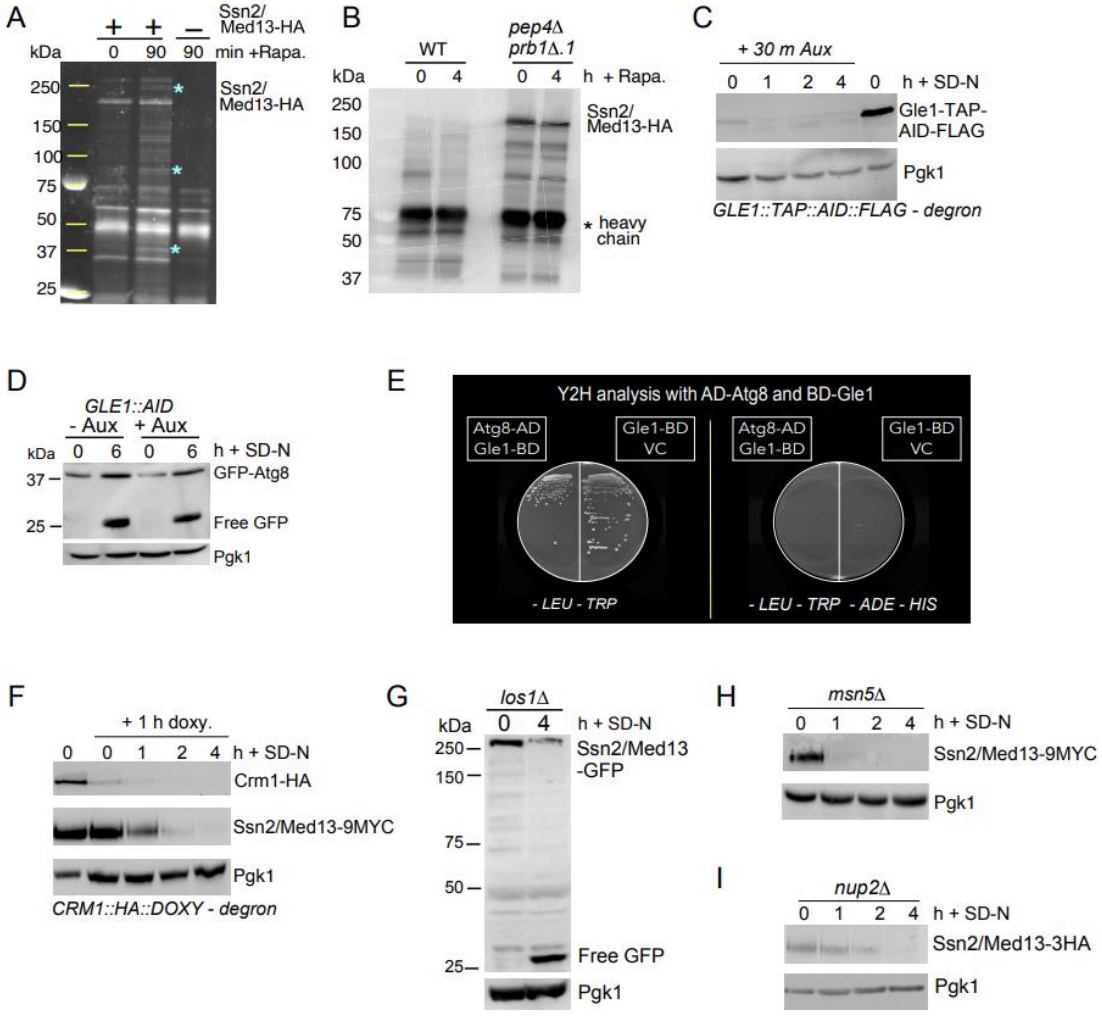
A
+ + – Ssn2/ Med13-HA
kDa 0 90 90 min +Rapa.
250
150
100
75
50
37
25
Ssn2/ Med13-HA
B
WT
pep4Δ prb1Δ.1
kDa 0 4 0 4 h + Rapa.
250
150
100
75
50
37
Ssn2/ Med13-HA
* heavy chain
C
+ 30 m Aux
0 1 2 4 0 h + SD-N
Gle1-TAP-AID-FLAG
Pgk1
GLE1::TAP::AID::FLAG - degron
D
GLE1::AID
- Aux + Aux
kDa 0 6 0 6 h + SD-N
37
25
GFP-Atg8
Free GFP
Pgk1
E
Y2H analysis with AD-Atg8 and BD-Gle1
Atg8-AD Gle1-BD
Gle1-BD VC
Atg8-AD Gle1-BD
Gle1-BD VC
- LEU - TRP
- LEU - TRP - ADE - HIS
F
+ 1 h doxy.
0 0 1 2 4 h + SD-N
Crm1-HA
Ssn2/Med13-9MYC
Pgk1
CRM1::HA::DOXY - degron
G
los1Δ
kDa 0 4 h + SD-N
250
150
75
50
25
Ssn2/Med13 -GFP
Free GFP
Pgk1
H
msn5Δ
0 1 2 4 h + SD-N
Ssn2/Med13-9MYC
Pgk1
I
nup2Δ
0 1 2 4 h + SD-N
Ssn2/Med13-3HA
Pgk1

Figure S4. Mass spectrometry screen to identify proteins required for Med13 vacuolar degradation. **(A)** Immunoprecipitation assays with Med13 in unstressed cells or cells treated with 200 ng/ml rapamycin for 90 minutes. Spyro Ruby stain was used to visualize proteins immunoprecipitated with Med13-3xHA from whole cell lysate. Asterisks denote bands that were present in stressed samples and absent in unstressed samples. **(B)** Western blot analysis of immunoprecipitation experiments performed in wild-type and *pep4*Δ*prb1*Δ*.1* cells. **(C)** Gle1 auxin-inducible degron system. The BY4741 strain harboring endogenous *GLE1-TAP-AID-FLAG* was grown to mid-log and treated with 250 μM Auxin. Cells were then washed and resuspended in SD-N media containing 250 μM Auxin for indicated time points. Gle1 protein depletion was monitored via western blot analysis using antibodies against FLAG. **(D)** Western blot analysis of Atg8-GFP cleavage assays performed in the Gle1 auxin-inducible degron system. **(E)** Y2H Gold cells harboring Gal4-BD-Atg8 and the indicated Gal4-AD-Med13 constructs or vector controls were plated on medium selecting for plasmid maintenance *(-LEU, -TRP*) (left) or interaction by induction of the *ADE2* and *HIS3* reporter genes (right). **(F)** Crn1-doxycyclin inducible degron system. Cells expressing Crm1-HA under a tetracycline repressible promoter and endogenous Med13-9xMYC were grown to mid-log. Cells were treated with doxycycline for 1 hour before switching cells to SD-N media with doxycycline. Western blot analysis was used to monitor Crm1-HA and Med13-9xMYC degradation following doxycycline and nitrogen starvation treatment. **(G)** *los1*Δ BY4741 cells Med13-GFP were nitrogen-starved for the indicated times. **(H)** Western blot analysis of Med13-9xMYC protein levels following nitrogen starvation in *msn5*Δ cells**. (I)** Western blot analysis of Med13-9xMYC protein levels following nitrogen starvation in *nup2*Δ cells**.**

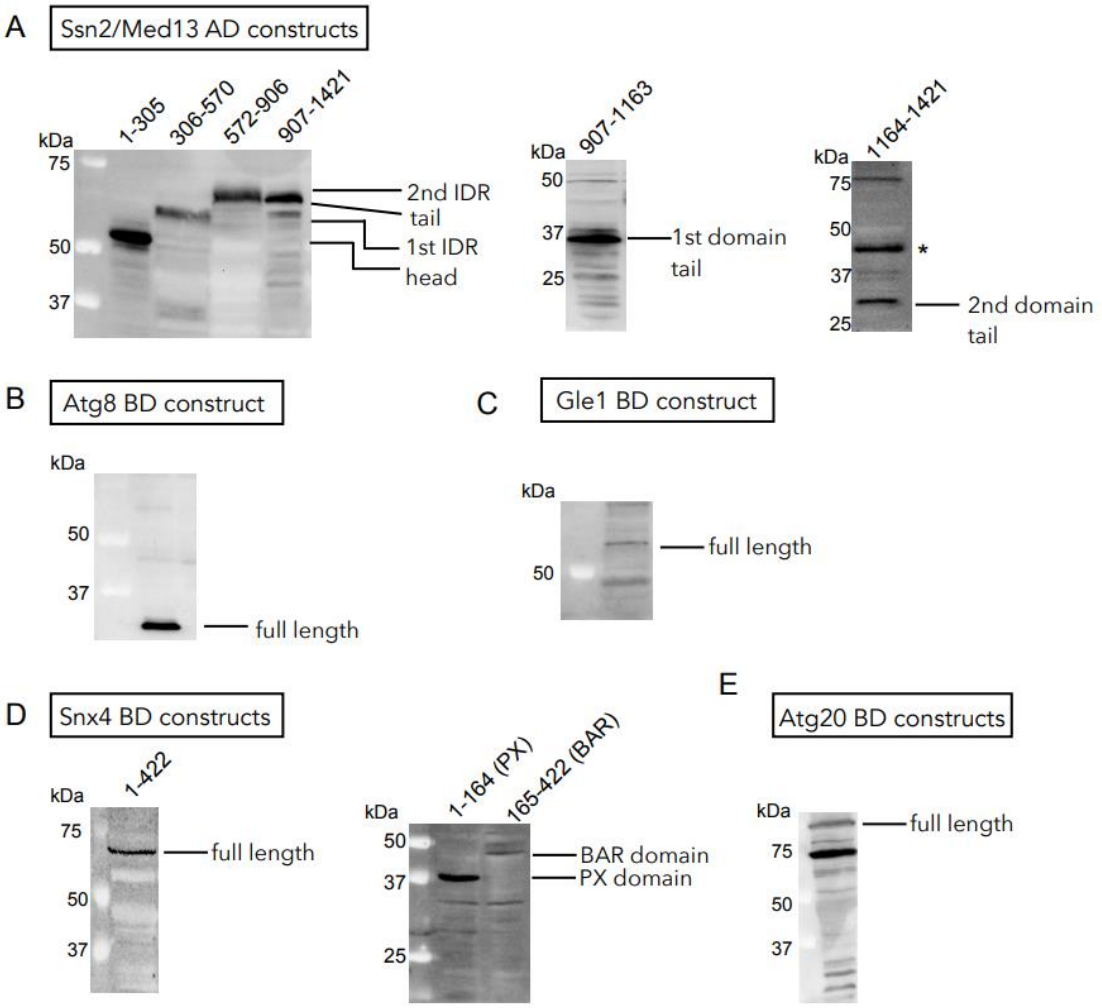

Figure S5. Western blot analysis of Y2H plasmids. **(A)** Western blot analysis of cells expressing indicated Med13 activating domain Y2H constructs. **(B and C)** Western blot analysis of cells expressing of Atg8 and Gle1 binding domain Y2H constructs respectively. **(D and E)** Western blot analysis of Snx4 and Atg20 binding domain Y2H constructs.

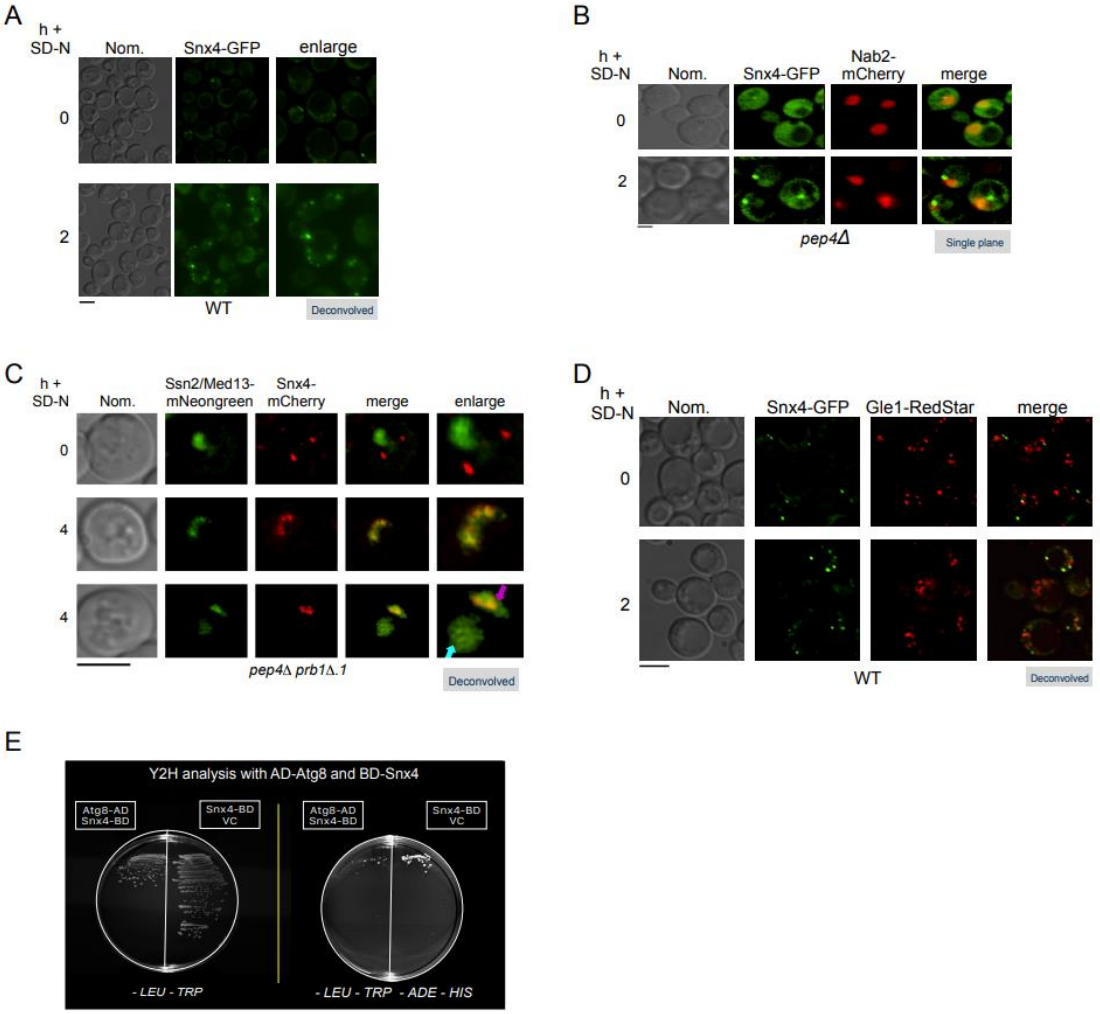

Figure S6. Snx4 localizes to the nuclear periphery following nitrogen starvation. **(A)** Fluorescence microscopy of GFP-Snx4 localization in wild-type cells following 2 h of nitrogen starvation. Bar: 5 μm. **(B)** Fluorescence microscopy of *pep4*Δ cells expressing GFP-Snx4 and harboring Nab2-mCherry (nuclear marker) before and after nitrogen starvation. Representative deconvolved images are shown. Bar: 5 μm. **(C)** Fluorescence microscopy of endogenous Med13-mNeongreen and mCherry-Snx4 in *pep4*Δ *prb1*Δ*.1* cells before and after nitrogen starvation. The vacuolar Med13 population is indicated by the blue arrow and perinuclear Med13-Snx4 colocalization is indicated by the pink arrow. Bar: 5 μm. **(D)** Y2H Gold cells harboring Gal4-BD-Snx4 and the indicated Gal4-AD-Atg8 construct or vector controls **(E)** Fluorescence microscopy of colocalization experiments performed in wild-type cells expressing GFP-Snx4 and endogenous Gle1-RedStar. Cells were grown to mid-log, washed, and resuspended in SD-N media for 2 h. Bar: 5 μm.

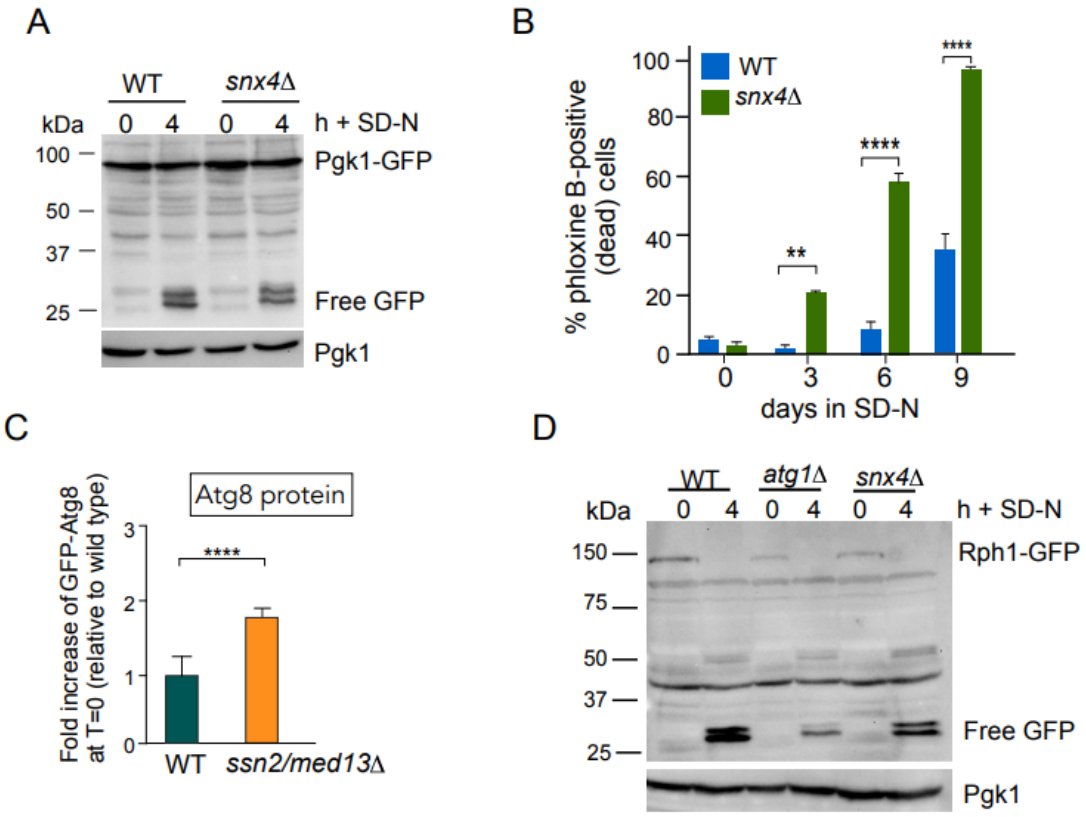

Figure S7. Snx4 is required for viability in long-term nitrogen starvation. **(A)** Western blot analysis of Pgk1- GFP cleavage assays in wild-type and *snx4*Δ cells following nitrogen starvation. **(B)** Wild-type and *snx4*Δ cells were grown to mid-log, washed, and resuspended in SD-N media for the indicated number of days. The percentage of inviable cells within the population was determined using pholxine B staining and fluorescence-activated cell analysis (FAC). Quantification of N=2 independent biological experiments. Data are mean ± S.D. ** P = 0.0012, **** P = <0.0001 **(C)** Quantification Atg8 protein levels in wild-type and *Med13*Δ cells relative to Pgk1 loading control. Quantification of N=3 biological samples. Data are mean ± S.D. **** P = <0.0001. **(D)** Western blot analysis of Rph1-GFP cleavage assays in wild-type, *atg1*Δ, and *snx4*Δ cells. Pgk1 levels were used as loading controls.

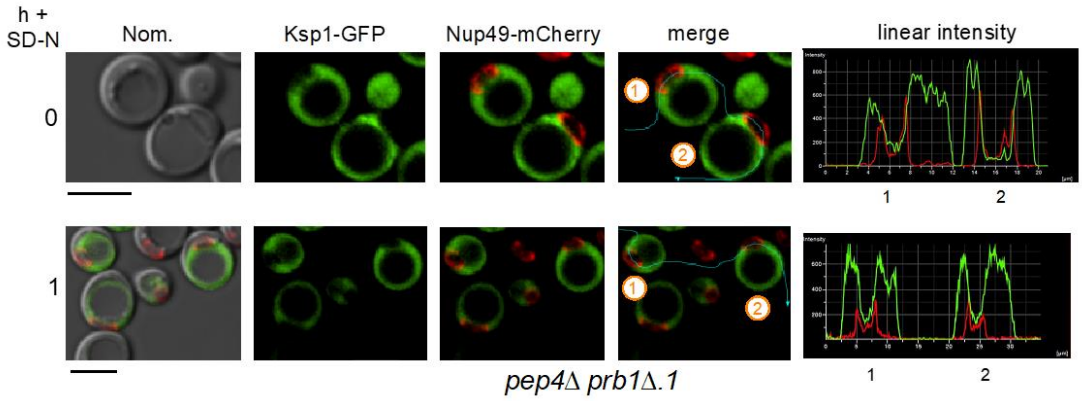

Figure S1. Fluorescence microscopy of Ksp1-GFP before and following nitrogen starvation in *pep4 prb1Δ.1* harboring the nuclear pore complex marker, Nup49-mCherry, using fluorescence microscopy. The numbered cells were further analyzed using linear quantification analysis. The green and red peaks represent the fluorescence intensity of Ksp1-GFP and Nup1-mCherry respectively. Scale bar = 5 μM

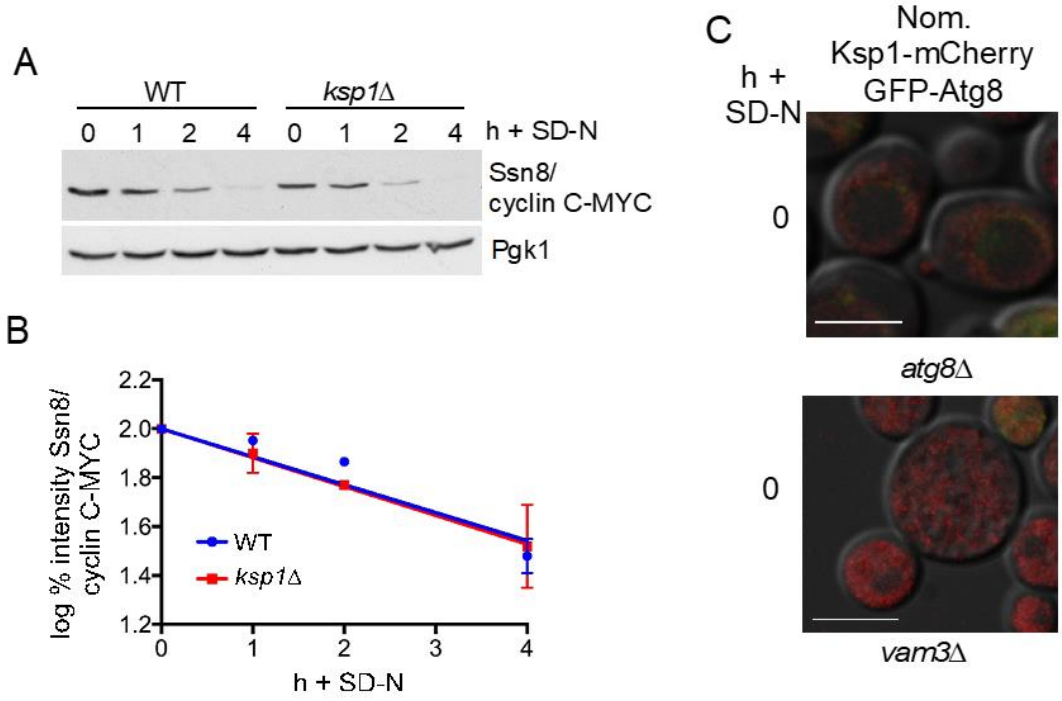

Figure S2. Ksp1 is not required to degrade cyclin C following nitrogen starvation. **(A)** Western blot analysis of Ssn8/cyclin C-MYC protein levels following nitrogen starvation in WT and *ksp1*Δ. Pgk1 protein levels were used as the protein loading control. **(B)** Degradation kinetics of Ssn8/cyclin C in WT and *ksp1*Δ. **(C)** Fluorescence microscopy in unstressed cells of Ksp1-mCherry and GFP-Atg8 in strains indicated. Bar = 5µM

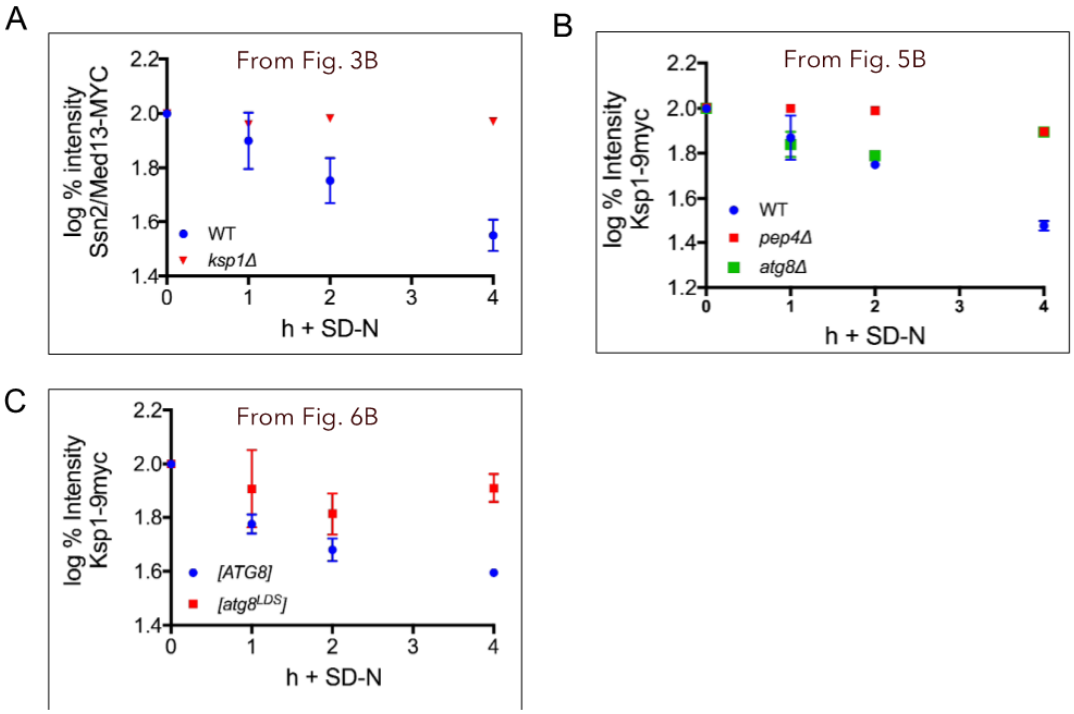

Figure S3. Degradation kinetics of proteins shown without the line of best fit. **(A)** Quantification of degradation kinetics of endogenous Ssn2/Med13-MYC levels following nitrogen starvation in wild type and *ksp1*Δ (**B and C**). Quantification of degradation kinetics of endogenous Ksp1-MYC levels following nitrogen starvation in wild type and *ksp1*Δ. The corresponding Figures that contain linear regression analysis are indicated.

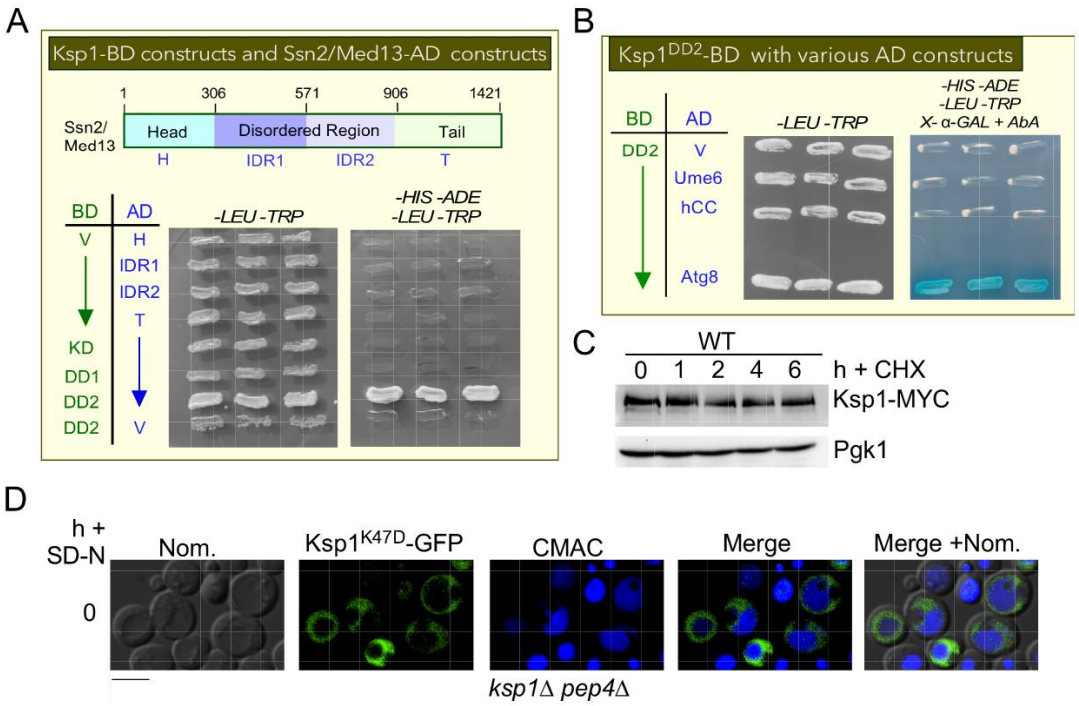

Figure S4. (A) Y2H analysis. Top panel: map of Ssn2/Med13 outlining its structure and the position of the Y2H activating domain constructs. Bottom panel: Y2H Gold cells harboring the indicated Gal4-BD-Ksp1 and Gal4-AD-Ssn2/Med13 constructs or vector control (V). Three biological replicates were plated on medium selecting for plasmid maintenance *(-LEU*, *-TRP*, left) or interaction by induction of the *ADE2* and *HIS3*, reporter genes (right). **(B)** Y2H analysis of Gal4-BD-Ksp1^{DD2} and Gal4-AD-Ume6 or Gal4-AD human cyclin C (hCC). The interaction between Gal4-BD-Ksp1^{DD2} and Gal4-AD-Atg8 was used as a positive control. Three biological replicates were plated on medium selecting for plasmid maintenance *(-LEU*, *-TRP*, left) or interaction by induction of all four reporter genes, *ADE2*, *HIS3*, *MEL1*, and *AUR1-C*, as described in the material and methods section. **(C)** Western blot analysis of endogenous Ksp1-MYC in mid-log cells following 50 µg/ml cycloheximide (CHX) treatment for the indicated times. **(D)** Fluorescence microscopy of Ksp1^{K47D}-GFP in unstressed cells. Vacuoles were labeled with CMAC. Bar =5µM.

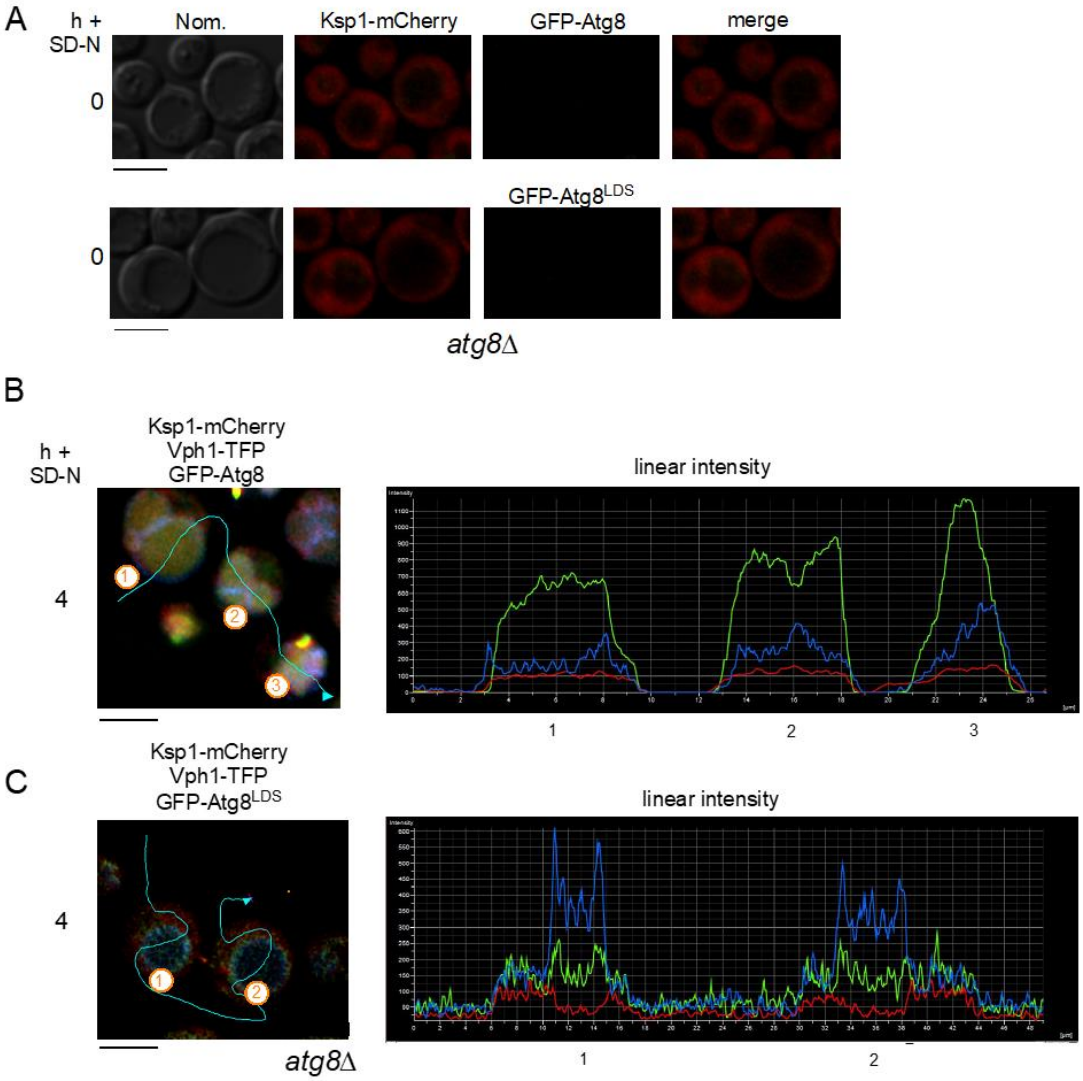

Figure S5. Ksp1 co-localizes with Atg8 following nitrogen starvation. **(A)** Fluorescence microscopy of cultures shown in unstressed cells. **(B)** Linear quantification analysis of Ksp1-mCherry in *atg8*Δ harboring GFP-Atg8 using fluorescence microscopy. Vph1-TFP was used to mark the vacuole. The blue line in the representative images correlates with the signal quantified and the cells analyzed are numbered. **(C)** As in B except that the *LDS*Δ allele of GFP-Atg8 was used. Scale bar = 5 μM.

A [ADEFGLPRSK][DEGMSTV][**WFY**][DEILQTV][ADEFHIKLMPSTV][**ILV**]

B

Start	End	Pattern	PSSM Score	AIM in Anchor	
16	21	NRYQKI	7	No	
27	32	GSYGYV	5	Yes	
167	172	DLYEAI	11	No	AIM2
277	282	IVFLNI	2	No	
318	323	YDFFQV	7	No	
355	360	EYYNNL	3	No	
405	410	FNFNNV	4	Yes	
649	654	NQFLRV	5	Yes	
1020	1025	NNWLIL	16	Yes	AIM1

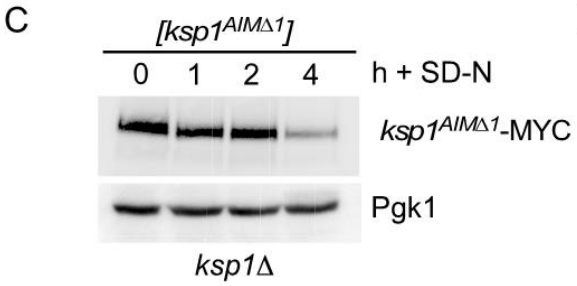

Figure S6. Ksp1 contains putative Atg8-interacting motifs (AIMs). **(A)** The extended AIM motif. Residues 3 and 6 correspond to the required aromatic and hydrophobic residues of the original central core motif conserved four amino acid motif ([**W/F/Y**]xx[**L/I/V**]) [58,69,73,74]. **(B)** Results from iLIR database [58] analysis of Ksp1 using the extended AIM motif. The position-specific scoring matrix (PSSM) score i.e., the highest conservation of pattern alignment when compared to verified AIM/LIR motifs is given. AIMs were scored positive for ANCHOR analysis if they overlapped with IDRs with the potential to transition to an ordered state. **(C)** Western blot analysis of *ksp1*$^{AIM\Delta1}$-9MYC protein levels in *ksp1*Δ cells following nitrogen starvation. Pgk1 protein levels are used as the protein loading control. **(D)** Degradation kinetics *ksp1*$^{AIM\Delta1}$-MYC protein levels obtained in C.

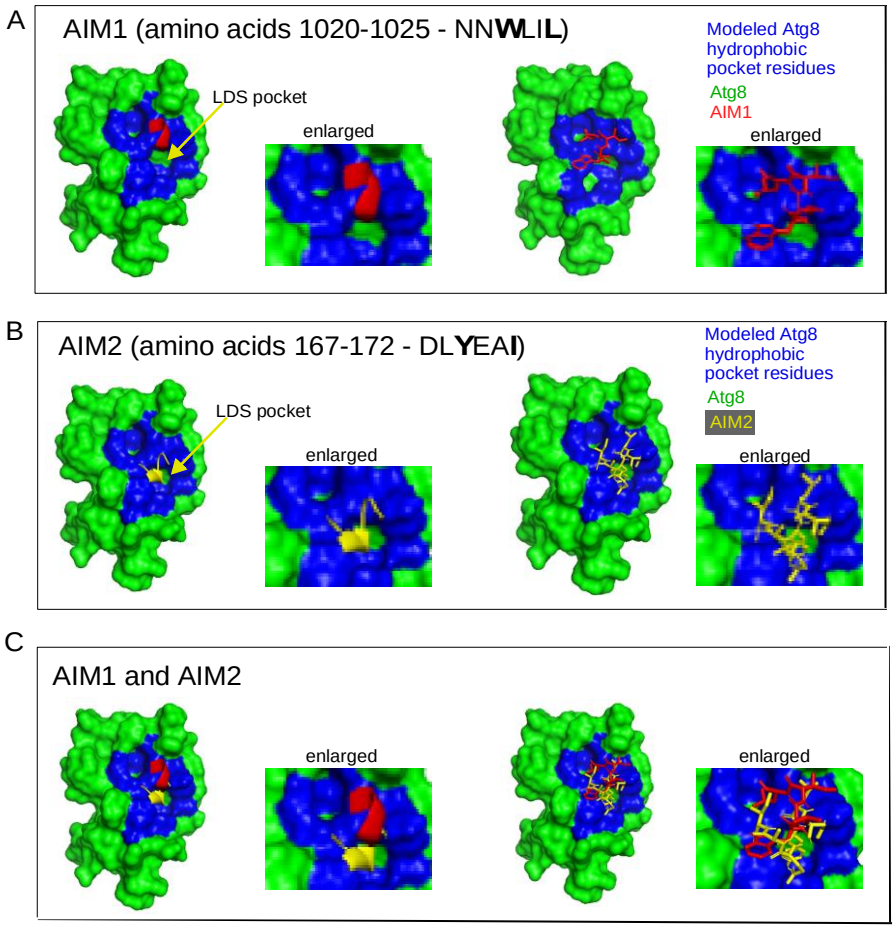

Figure S7. Representative stick and ribbon images of Ksp1^{AIM1} and Ksp1^{AIM2} modeled onto the hydrophobic binding pocket of Atg8. See text for details. **(A and B)** Ksp1^{AIM1} (red) and Ksp1^{AIM2} (yellow) were modeled onto the hydrophobic LDS residues (blue) of Atg8 (green) respectively**. (C)** Both Ksp1^{AIM1} and Ksp1^{AIM2} were modeled simultaneously demonstrating how they both can fit into the hydrophobic pocket.

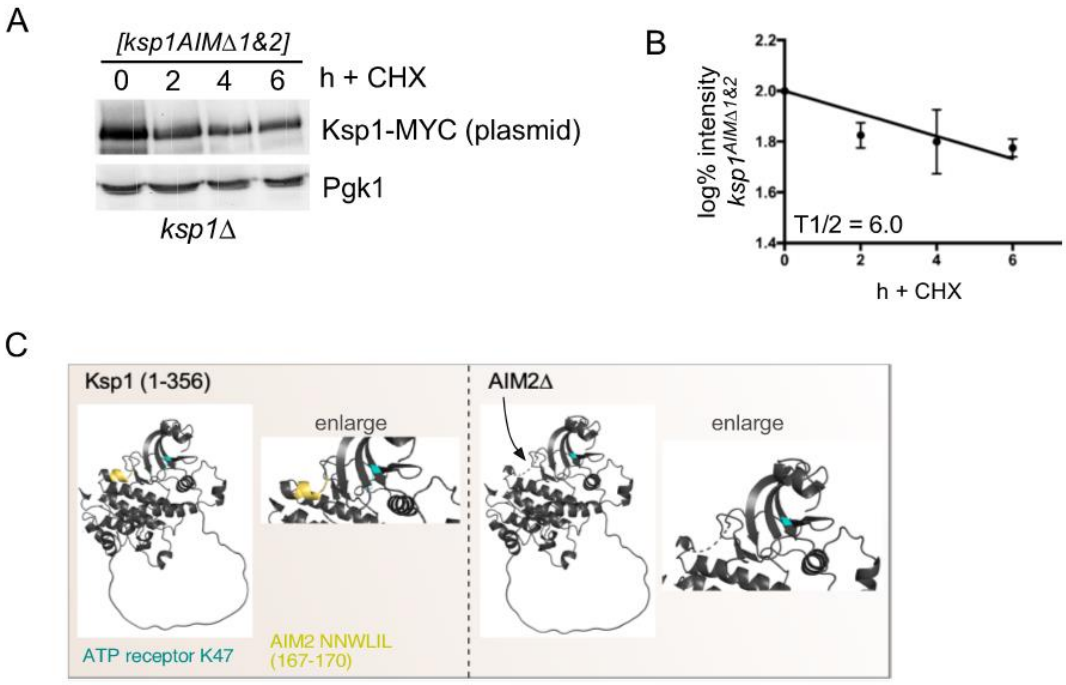

Figure S8. Deletion of AIM1 and AIM2 in Ksp1 only slightly changes protein stability. **(A)** Western blot analysis of *ksp1*Δ harboring the *ksp1*$^{AIM\Delta1\&2}$-9MYC plasmid in mid-log cells following 50 µg/ml cycloheximide (CHX) treatment for the indicated times **(B)** Quantification of A. N=2. **(C) Left panel.** Modeling of structured N terminal domain (amino acids 1-356) of Ksp1 showing the position of AIM2 and the kinase pocket (K47). Right pocket. The modeling was done using Ksp1$^{AIM2\Delta.}$ The original position of this motif is indicated by the arrow and dotted lines in the structure.

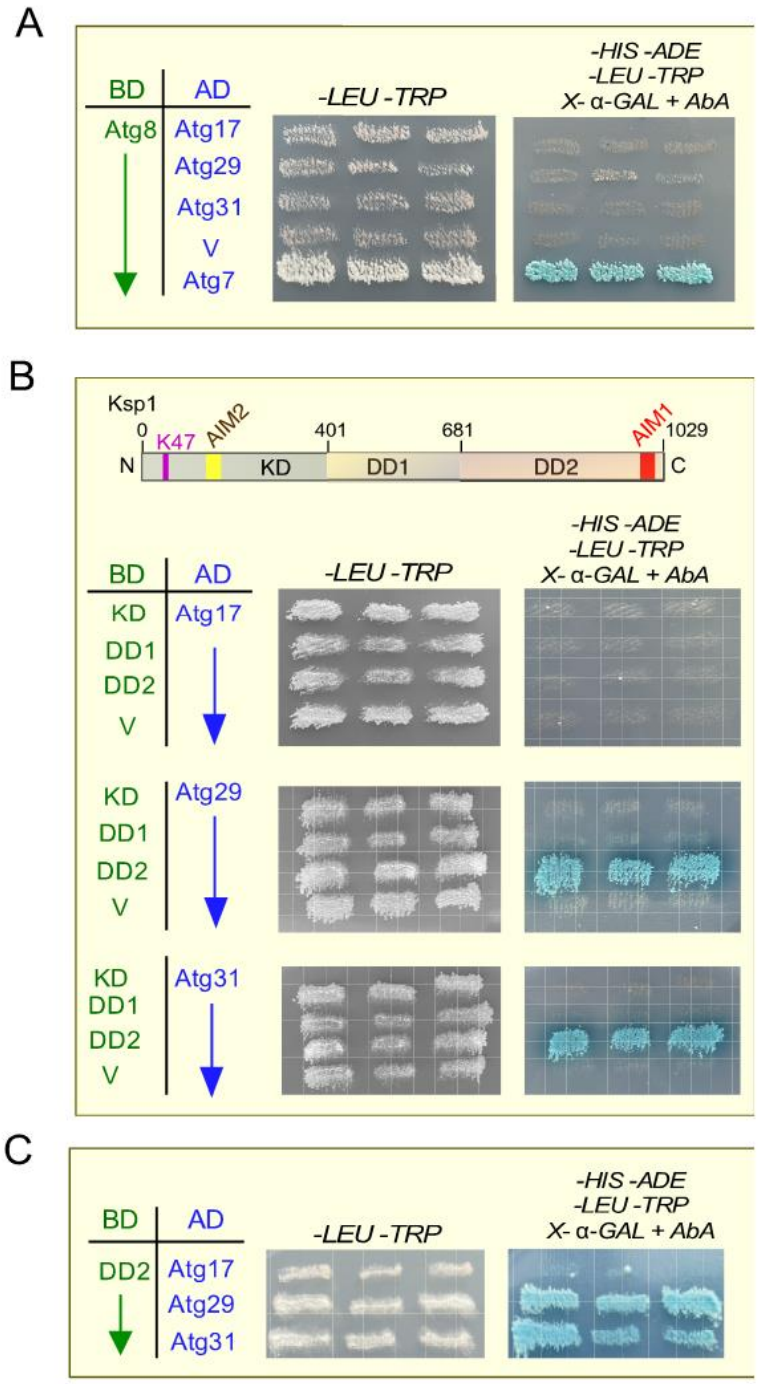

Figure S9. Y2H analysis of Ksp1 and 17C. Y2H analysis of the indicated Gal4-BD and Gal4-AD plasmids, or vector controls (V). Three biological replicates were plated on medium selecting for plasmid maintenance *(-LEU, -TRP*, left) or interaction by induction of all four reporter genes, *ADE2*, *HIS3*, *MEL1*, and *AUR1-C,* as described in the material and methods section.

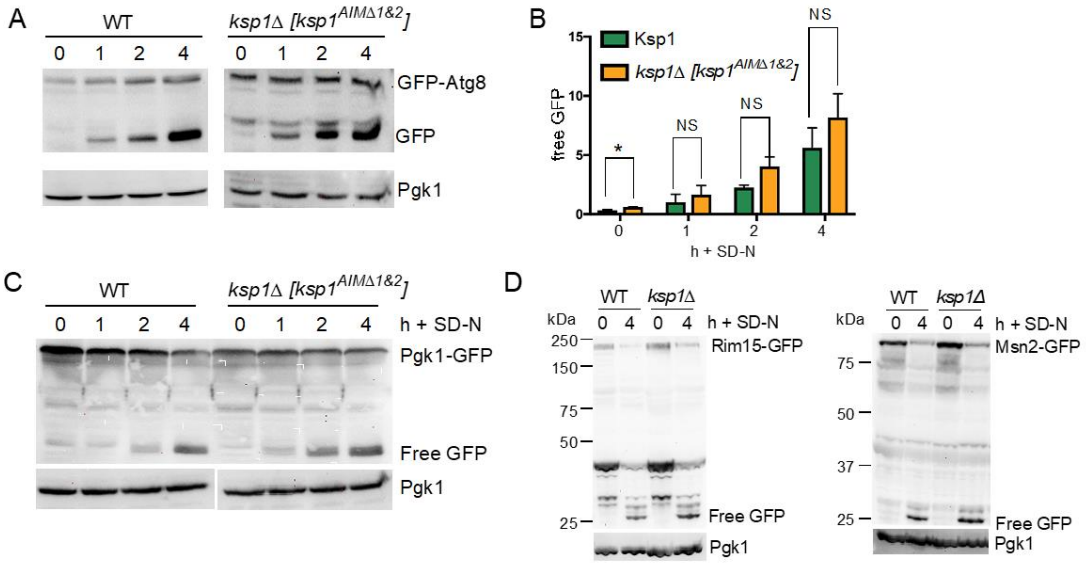

Figure S10. Precocious induction of autophagy in *ksp1*$^{\text{AIMΔ1&2}}$ **(A)** GFP-Atg8 cleavage assays after 4 h nitrogen starvation in the strains shown. **(B)** Quantification of free GFP from the assays in A. **(C)** Autophagic cleavage assays of Pgk1-GFP in the strains shown. **(D)** Autophagic cleavage assays of Rim15-GFP and Msn2-GFP in WT and *ksp1*Δ cells. For all assays, endogenous Pgk1 was used as a loading control.

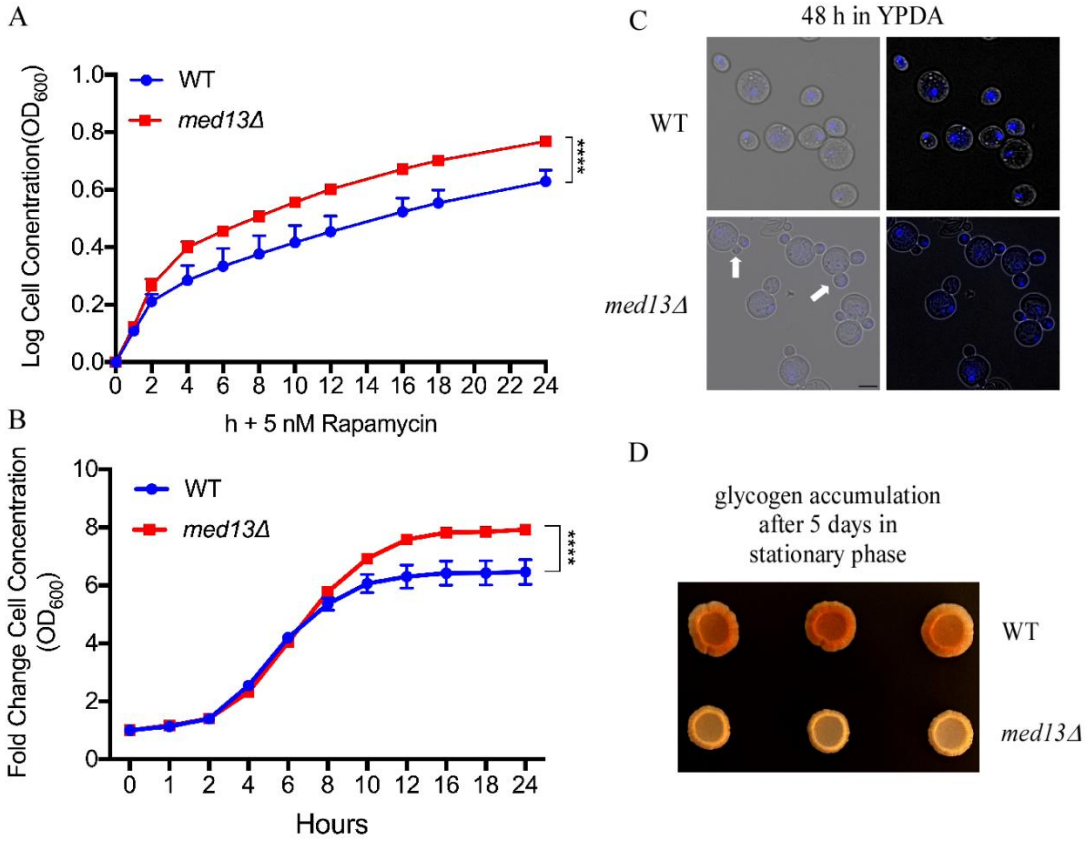

Figure S1. Med13 is required for efficient cell cycle arrest and quiescence entry following the transition from logarithmic cell growth to stationary phase**. (A)** Growth curves were performed in WT and *med13*Δ cells following treatment with low concentrations of rapamycin. Cell concentrations were monitored using absorbance readings analyzed by a plate reader. **(B)** Growth curves of indicated genotypes. Cells were grown to ~1 x 105 cells/mL and transferred to a 96-well plate. Cell concentrations were monitored using a plate reader. **(C)** Brightfield and fluorescence microscopy were used to monitor the budding index of the indicated genotypes. Cells were grown for 48 h in nutrient-replete media, stained with DAPI, and visualized. Scale bar = 5 μm. **(D)** Glycogen accumulation assays to assess carbohydrate storage during quiescence in the indicated genotypes. Three individual colonies of each genotype were grown overnight and were then plated onto a YPD plate in triplicate and grown for 5 days at 30ºC. The yeast colonies were then exposed to iodine vapors. Red/brown coloration signifies glycogen staining and was captured using the iBright FL1500 imaging system.

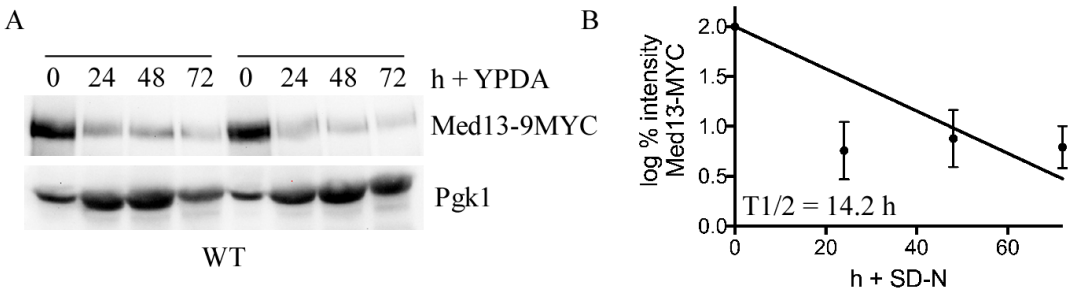

Figure S2. Med13 is degraded during stationary phase. **(A)** Western blot analysis of endogenous Med13-9MYC protein levels during stationary phase. Cells were grown in YPDA for the indicated time points. Two biological replicates are shown. **(B)** Quantification of A. Error bars indicate S.D. N=2 of biologically independent experiments.

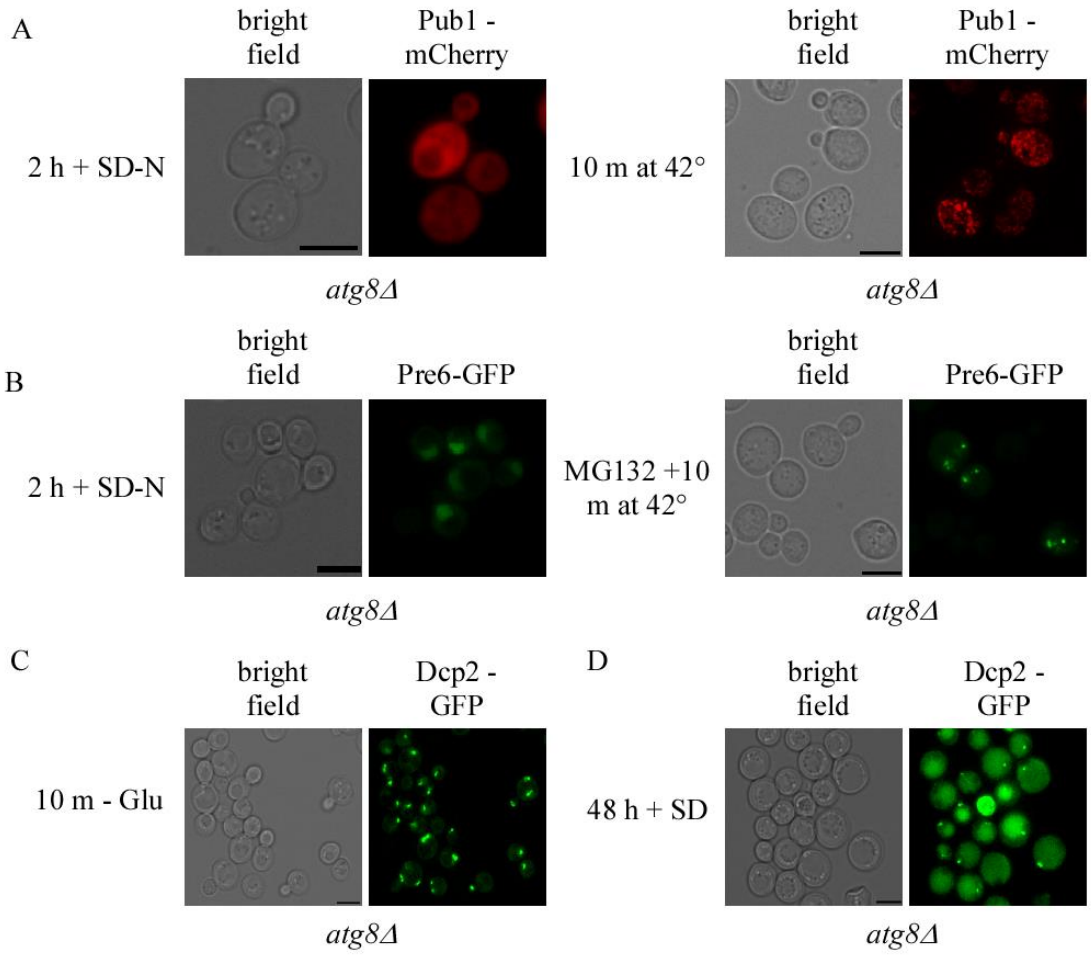

Figure S3. Stress granules and PSG do not form in nitrogen starvation**. (A** and **B)** Fluorescence microscopy was used to monitor the formation of stress granules and proteasome storage granules following nitrogen starvation (left panel). Pub1-mCherry and Pre6-GFP were used as markers for stress granules and PSGs respectively. Conditions that promote a robust SG and PSG response were used as positive controls (right panel). Representative images are shown. **(C** and **D)** Fluorescence microscopy was used to monitor the formation of P-bodies during glucose starvation and quiescence. Scale bar = 5 μm.

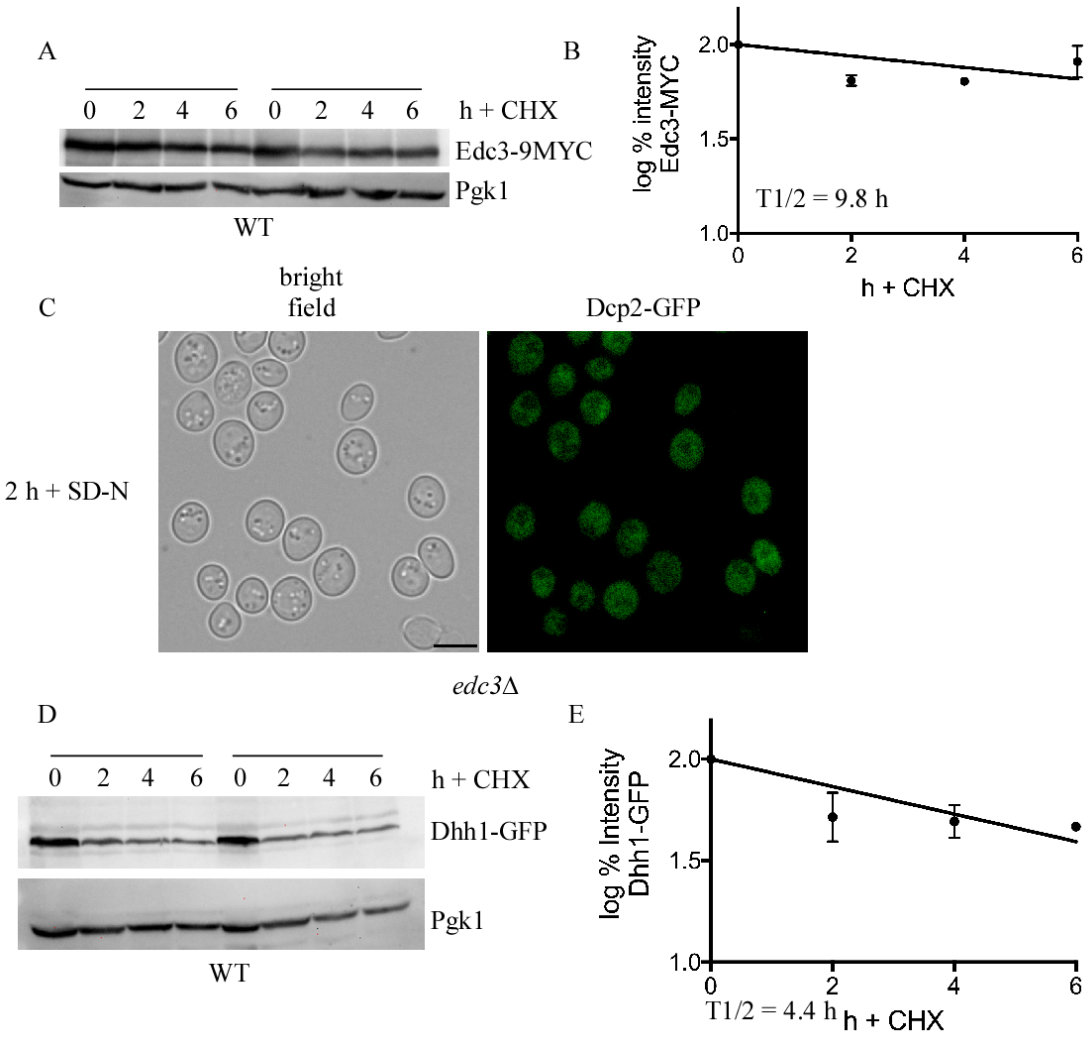

Figure S4. Edc3 and Dhh1 are actively degraded following nitrogen starvation. **(A)** Western blot analysis of endogenous Edc3-9MYC protein levels following cycloheximide treatment. Two biological replicates are shown. Pgk1 is used as the protein loading control. **(B)** Protein half-life quantification of A. (**C**) Fluorescence microscopy of P-body formation (Dcp2-GFP) in *edc3*Δ cells following nitrogen starvation. **(D)** Western blot analysis of endogenous Dhh1-GFP protein levels following cycloheximide treatment. Two biological replicates are shown. **(E)** Quantification of D.

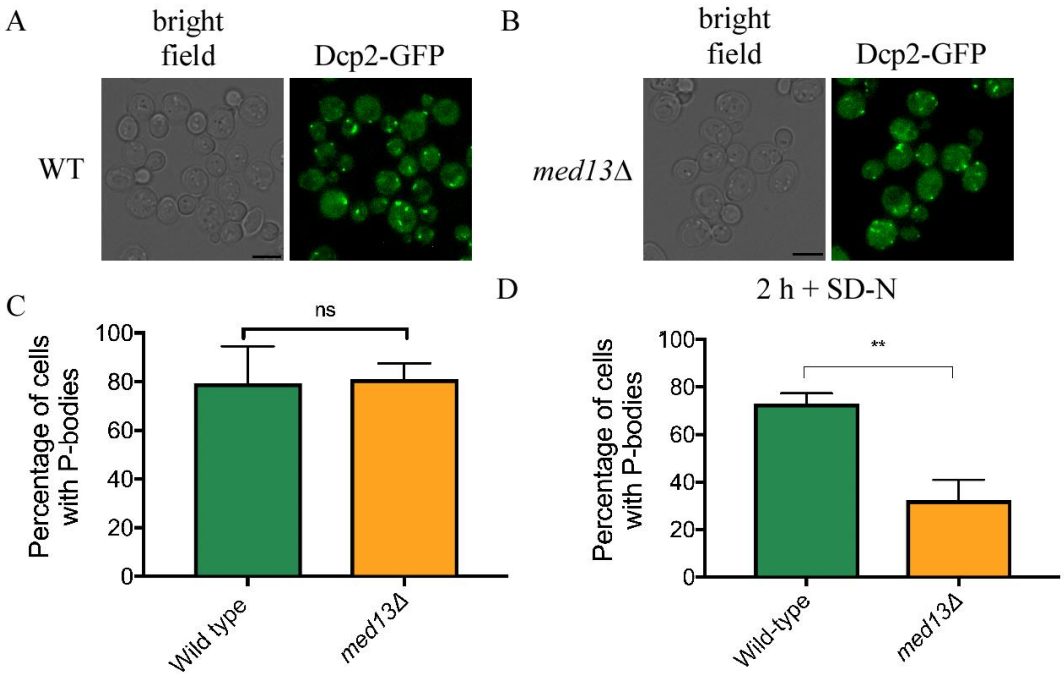

Figure S5. Med13 is not required for P-body formation. **(A)** The number of P-bodies following nitrogen starvation was quantified using fluorescence microscopy in WT and *med13*Δ cells expressing genomically-tagged Dcp2-GFP. **(B)** Images from A were analyzed using the image processing software Fiji. A graph depicting the total number of cells containing P-bodies is shown.

ABBREVIATIONS

AIM: Atg8 interacting motif
ATG: Autophagy-related genes
CKM: Cdk8 kinase module
IDR: intrinsically disordered region
LIR: LC3-interacting region
LDS: LIR/AIM docking site
NPC: nuclear pore complex
PAS: phagophore assembly site
RBP: RNA binding protein
UPS: ubiquitin-proteasome system
PDAC: pancreatic ductal adenocarcinoma
panNEN/NET/NEC: pancreatic neuroendocrine neoplasms/tumors/carcinomas
PanIN: pancreatic intraepithelial neoplasia
ADM: acinar ductal metaplasia
CQ: chloroquine
ROS: reactive oxygen species
SD-N: synthetic dextrose minus nitrogen
Y2H: Yeast-two hybrid
RNP: ribonucleoprotein
P-bodies: processing bodies
SRG: stress response genes
LLPS: liquid-liquid phase separation

ATTRIBUTES

Chapter 2
S.D. Willis at the Graduate School of Biomedical Sciences, Rowan University: RT-qPCR (Figure 9A); mass spectrometry experiments and analysis; K.F. Cooper at the Graduate School of Biomedical Sciences, Rowan University: microscopy (Figures 4 and 7).

Chapter 3
K.F. Cooper at the Graduate School of Biomedical Sciences, Rowan University: microscopy; S.J. Doyle at the Graduate School of Biomedical Sciences, Rowan University: modeling; S.D. Willis at the Graduate School of Biomedical Sciences, Rowan University: cloning

Chapter 4
S.D. Willis at the Graduate School of Biomedical Sciences, Rowan University: helped with Western blot analysis; B. Friedson at the Graduate School of Biomedical Sciences, Rowan University: helped with Western blot analysis; K.F.C. at the Graduate School of Biomedical Sciences, Rowan University: microscopy

Chapter 5
Dr. K.Q. Cai at the Institute for Cancer Research, Fox Chase Cancer Center: histopathology (Figures 3A, 3B, and 14); Vivarium staff at the Institute for Cancer Research, Fox Chase Cancer Center: metabolic tests (Figure 3C); S.D. Willis at the Graduate School of Biomedical Sciences, Rowan University: HCT116 work (Figure 11D). R. Strich at the Graduate School of Biomedical Sciences, Rowan University: genotyping (Figure 12).